

INFLATIONARY TRAJECTORIES

by

Pascal M. Vaudrevange

A thesis submitted in conformity with the requirements
for the degree of Doctor of Philosophy
Graduate Department of Physics
University of Toronto

Copyright © 2008 by Pascal M. Vaudrevange

Abstract

Inflationary Trajectories

Pascal M. Vaudrevange

Doctor of Philosophy

Graduate Department of Physics

University of Toronto

2008

The shapes of the primordial power spectra are the key quantities to unravel the physics of the inflationary epoch. We propose a new framework for parametrizing the spectra of primordial scalar and tensor perturbations, stressing the statistical trajectory nature of the relevant quantities. Of particular importance is the influence of priors which can lead to spurious results like an apparent detection of tensor modes. We clarify the impact of prior probabilities and demonstrate strategies to adjust the prior distributions.

The dependence on priors in inflation bears some resemblance to the landscape picture in string theory where a selection mechanism for the choice of compactified low energy limit describing the observable four dimensional universe is not available and the huge number of vacua can only be analyzed statistically, making the predictions of the theory highly dependent on the prior beliefs.

As an example we study two field inflation models based on the “large-volume” flux compactification of type IIB string theory representing a small corner of the full landscape. We find that even for a given realization of the potential, the details of inflation are heavily dependent on the initial conditions of the fields, adding an additional statistical element to the landscape. Instead of being able to reconstruct the full shape of this potential from inflation, only the path that the effective inflaton actually evolved along can be observationally determined, leaving the other areas of the potential inaccessible to exploration using the early universe as a laboratory.

Finally we investigate the trans-Planckian issue in the example of the Milne universe. In this FRW type universe, modes of a given physical wavelength are stretched due to the growths of the scale factor, implying that any given wavelength will at some point in the past have been

shorter than the Planck length and therefore requiring modifications due to trans-Planckian effects. However we argue that due to the fact that the Milne universe is a reparametrization of Minkowski space, no such effect should occur, as for an Minkowski observer only Unruh radiation should be visible.

Acknowledgements

Completing a thesis is quite a long process, and virtually impossible without the support of many people. A lot of people here in Toronto helped me in various ways during the past years, and now is the proper time to express my deepest gratitude to all of them.

I am greatly indebted to my adviser Professor Lev Kofman. Introducing me to the fascinating world of cosmology, his never ending enthusiasm, deep insights into physics and unparalleled intuition for physics taught me how to be a real physicist. It is my great pleasure to thank him for being such a superbly inspiring thesis adviser.

It is my pleasure to thank Professor J. Richard Bond for the many stimulating discussions on physics, showing me different approaches to approaching physical questions. I benefited tremendously from his deep insights into physics.

I would like to express my gratitude to my thesis advisory committee: Professor Erich Poppitz and Professor Charles Dyer for their continuous help and support along the way, Professor Katie Freese for kindly acting as the external appraiser and Professor Kentaro Hori for participating in my final oral examination.

I would also like to thank all the people at CITA for their friendship and advice, notably Neil Barnaby, Latham Boyle, Jonathan Braden, Carlo Contaldi, Jean-Francois Dufaux, Gary Felder, Carrie MacTavish, Dmitry Podolsky, Sergey Prokushkin, Jonathan Sievers, Peter Sloan, and last but not least special guest Jan Kratochvil who reminded me how much fun doing physics is.

I am pleased to thank my office mates past and present, who had to suffer through a lot of my ramblings and made the long hours of debugging really enjoyable: my present office mates Elizabeth Harper-Clark, Zhiqi Huang and Lawrence Mudryk and especially my former office mate Johannes Martin, for our great friendship.

I would like to thank my friends from the SDG: Elham Farahani, the most sincere person I know, to whom I will always be grateful for all the great talks we had, Shabnaz Pashapour, Xiongfeng Ma, Xun Ma and Ali Najmaie as well as my movie club friends Daniel Figueroa and Siew-Phang Ng for making the final weeks so much less stressful.

All the years in Toronto would have been only half as much fun without sports. I would like to thank all the members of the volleyball and ping pong crew for their friendship, especially captains Kuochieh Liao and Shengjun Yang, Cristen Adams, Yonggang Liu, Chiranjeeb Roy, April Yip and Yiqun Zhao.

Finally I would like to express my deepest gratitude to my family: My parent Jutta and Karl Vaudrevange as well as my brothers Dominik and Patrick. Without their continuous love and support it would not have been possible to complete this thesis.

Last but not least I would like to thank Siew Koon Chow, the person who grew closest to me, my ever faithful partner during this journey to the beginnings of time.

Contents

1	Introduction	1
1.1	Observational Probes Of The Early Universe	1
1.2	The Inflationary Paradigm	2
1.2.1	Scalar Perturbations	2
1.2.2	Tensor Perturbations and Polarization	3
1.2.3	Inflationary Model Building	3
1.2.4	Trajectories	5
1.2.5	The Trans-Planckian Problem - How Far Back Can We See?	6
1.2.6	Outline Of The Thesis	6
2	Scanning Inflationary Trajectories I: Power Spectra	8
2.1	Introduction	8
2.2	Inflationary trajectories and Observables	12
2.2.1	Basic Formalism	12
2.2.2	Prior prejudice and Bayesian Model Selection	16
2.3	Ensemble of Inflationary Trajectories	18
2.3.1	Properties of Trajectory Functions	19
2.3.2	Sample Trajectories for $V(\phi) = \lambda\phi^n$	20
2.3.3	Creating Random Trajectories	21
2.4	Trajectories and Traditional Observables	27
2.4.1	Priors in the Space of Traditional Observables	27
2.4.2	Priors in Linear Interpolation	27
2.4.3	Opening the Space of Observables	30
2.5	Observational Constraints on Trajectory Space	30
2.6	Reconstructing the Primordial Power Spectra from Simulated Data Sets	35
2.6.1	Cosmic Variance Limited Experiments	35
2.6.2	Planck and CMBPol Noise	36
2.7	Reconstructing the Primordial Power Spectra from Real Data Sets	39
2.7.1	Sampling with a uniform prior in $\ln \mathcal{P}_s, \ln \mathcal{P}_t$	39
2.7.2	Sampling with a uniform prior in $\ln \mathcal{P}_s, \mathcal{P}_t$	39

2.7.3	Sampling with a uniform prior on $\mathcal{P}_s, \mathcal{P}_t$	40
2.7.4	Sampling with uniform prior in $\mathcal{P}_s, \mathcal{P}_t$ and trajectory expansion in $\ln \mathcal{P}_s, \ln \mathcal{P}_t$	42
2.8	Summary and Conclusions	47
3	Scanning Inflationary Trajectories II: Acceleration Trajectories	50
3.1	Acceleration Trajectories	50
3.1.1	Enforcing the End of Inflation Condition with H and ϵ trajectories	51
3.1.2	Adjusting Priors	52
3.2	Sample trajectories for $V(\phi) = \lambda\phi^n$	55
3.3	Flow Equations	56
3.3.1	Comparison Chebyshev Polynomials vs. Flow trajectories	58
3.4	Physical Constraints on Trajectories	61
3.5	MCMC Reconstruction of Simulated CMB Data Sets	63
3.5.1	Simulated Data Sets	63
3.5.2	Reconstruction of the Simulated Spectra	63
3.6	MCMC Reconstruction from Real Data Sets	67
3.7	Degeneracy of the Potential Reconstruction	69
4	Roulette Inflation with Kähler Moduli and their Axions	73
4.1	Introduction	73
4.2	The Type IIB String Theory Model	76
4.3	Perturbative Corrections	80
4.4	Effective Potential and Volume Stabilization	81
4.5	Inflaton Potential	85
4.5.1	The Canonically-normalized Inflaton	88
4.6	Inflationary Trajectories	89
4.6.1	The Inflaton Equation of Motion	89
4.6.2	Stochastic Fluctuations and CMB and LSS Constraints	90
4.6.3	Trajectories with General Kähler modulus and Axion Initial Conditions	91
4.7	Stochastic Regime of Self-Reproduction	99
4.8	Discussion and Summary	101
5	Trans-Planckian Issue in the Milne Universe	105
5.1	Introduction	105
5.2	The Milne Universe	107
5.3	Quantum Field Theory in FRW space-times	108
5.4	$\langle 0_A T_\mu^{\nu(\text{Milne})} 0_A \rangle$ in contracting Milne universe	111
5.5	$\langle 0_C T_\mu^{\nu(\text{Milne})} 0_C \rangle$ in expanding Milne universe	112
5.6	Discussion: Challenge to the Trans-Planckian Challenge	113
6	Conclusions and Outlook	119

List of Tables

2.1	Cosmological parameters for the standard parametrization compared with equivalent $\ln \mathcal{P}_s$, $(\ln) \mathcal{P}_t$ trajectories	34
2.2	Naming convention for the various parametrizations	37
2.3	Effect of Planck/ CMBPol noise levels on the efficiency of reconstruction using the standard parametrization	37
2.4	Reconstructing simulated spectra using $\ln \mathcal{P}_s, \ln \mathcal{P}_t$	38
3.1	Comparison of run-time between the flow and the scanning approach	61
3.2	Naming convention for the various parametrizations	64
3.3	Reconstruction of acceleration trajectories from real data	67
4.1	Sample parameter sets for the T_2 inflation model	86

List of Figures

1.1	Angular CMB TT power spectrum	2
1.2	Schematic representation of a Calabi-Yau manifold	4
2.1	Flow of observables with varying N	9
2.2	Chebyshev polynomials to order 4	19
2.3	Chebyshev coefficients to order 5 for different potentials	22
2.4	Ensemble of valid trajectories $\mathcal{P}_s, \mathcal{P}_t$	23
2.5	Filter functions for the nodal point method	26
2.6	Prior distribution in $r - n_s$ space	28
2.7	Prior effect of a linear interpolation	29
2.8	1D posterior distribution of the cosmological parameters in the standard parametrization	33
2.9	Contribution to the total χ^2 ℓ by ℓ for BB	36
2.10	Expansion of $\mathcal{P}_s, \mathcal{P}_t$ to order 5 each	41
2.11	Prior distribution for monotonic and non-monotonic tensor power spectra	42
2.12	Prior distribution for sampling $\ln \mathcal{P}_s, \ln \mathcal{P}_t$ with uniform priors in $\mathcal{P}_s, \mathcal{P}_t$	43
2.13	Expansion of $\ln \mathcal{P}_s$, non-monotonic $\ln \mathcal{P}_t$ to order 5 each sampling with a uniform prior on $\mathcal{P}_s, \mathcal{P}_t$	44
2.14	Expansion of $\ln \mathcal{P}_s$, monotonic $\ln \mathcal{P}_t$ to order 5 each sampling with a uniform prior on $\mathcal{P}_s, \mathcal{P}_t$	45
2.15	Comparison of $\ln \mathcal{P}_s, \ln \mathcal{P}_t$	46
3.1	Ensemble of valid trajectories $H(N), \epsilon(N)$	51
3.2	Sample trajectories for ϵ and $\ln(-n_t)$ to order 5 each	54
3.3	Prior distribution of the values of ϵ at and in between nodal points in different parametrizations	55
3.4	Chebyshev coefficients for different potentials	57
3.5	Distributions of Chebyshev coefficients from CPNP and the flow method	59
3.6	Marginalized posterior distribution for the reconstruction of a standard parametrization simulated spectrum	64

3.7	Marginalized posterior distribution for the reconstruction of a simulated spectrum created using the ϵ parametrization	65
3.8	Reconstruction of the scalar-tensor ratio r	66
3.9	The reconstructed inflationary potential	69
3.10	The reconstructed inflationary potential	70
3.11	Degeneracy of the potential	72
4.1	Schematic illustration of the ingredients in Kähler moduli inflation	75
4.2	Uplifted potential $V(\tau_1, \tau_2)$	83
4.3	One dimensional sections of the uplifted potential for parameter set 1	85
4.4	The T_2 -potential surface $V(\tau, \theta)$ for the parameter set 1 of Table 4.5	87
4.5	Contour-plots of the potential including trajectories for several choices of initial values in field space (τ, θ) which are phenomenologically viable	92
4.6	Contour-plots of the potential including trajectories for several choices of initial values in field space (τ, θ) which are phenomenologically ruled out	93
4.7	3D plot of $V(\tau, \theta)$ for parameter set 4	93
4.8	Hubble parameter $H(\ln a)$ and deceleration parameter $\epsilon(\ln a)$ as functions of the number of e-folds for phenomenologically viable parameter sets 1-4	95
4.9	Hubble parameter $H(\ln a)$ and deceleration parameter $\epsilon(\ln a)$ as functions of the number of e-folds for phenomenologically ruled out parameter sets 5-6	96
4.10	Scalar and tensor power spectra for phenomenologically viable parameter sets 1-4	97
4.11	Scalar and tensor power spectra for phenomenologically ruled out parameter sets 1-4	98
4.12	Region of self-reproduction for parameter set 1	100
5.1	Redshift of the wavelength $\lambda = \frac{2\pi}{k}a(t)$ in the Milne universe	118
5.2	Patches of Minkowski space covered by the Milne metric	118

Chapter 1

Introduction

Early universe cosmology has come a long way. In its infancy a subject with only few experimental measurements, the past two decades have seen the quest for knowledge about the very first moments in time entering adolescence, unearthing a tremendous treasure-trove of data. From the first detection of cosmic microwave background radiation (CMB) by Penzias and Wilson [1] through the first detection of CMB anisotropies by the Cosmic Background Explorer (COBE)[2] to the high-precision measurements of the temperature anisotropies by the Wilkinson Microwave Anisotropy Probe (WMAP)[3], the observations of large scale structure surveys (LSS) contained in the incredibly voluminous catalogs of the Sloan Digital Sky Survey (SDSS)[4] and the Two Degree Field Galaxy Redshift Survey (2dFGRS)[5], the measurements of the Ly- α forest and the results of weak lensing observations, the ever increasing amount and quality of observational data makes cosmology a very exciting frontier of modern physics.

1.1 Observational Probes Of The Early Universe

The launch of the COBE satellite led to the first quantitative measurements of the CMB spectrum succeeded, and the detection of anisotropies on the order of 5×10^{-5} in the temperature distribution across the sky succeeded. The following years saw several balloon borne experiments, notably the Millimeter Anisotropy eXperiment IMaging Array (MAXIMA)[6] and the Balloon Observations Of Millimetric Extragalactic Radiation And Geophysics (BOOMERAnG)[7], detecting the first peak in the power spectrum of the temperature-temperature (TT) auto-correlation function across the sky. The WMAP satellite probe confirmed the presence of the first peak, detected a second peak, and sees hints of a third peak in the TT spectrum, while ongoing observations by other experiments also confirm the presence of a third peak (see Fig. 1.1¹). On the LSS side, the two major surveys SDSS and 2dFGRS provide deep insights into the structure of the universe, revealing the detailed shape of the matter power spectrum, the cosmic web of voids, clusters of galaxies and superclusters of galaxy clusters, while the

¹Plot from <http://lambda.gsfc.nasa.gov>

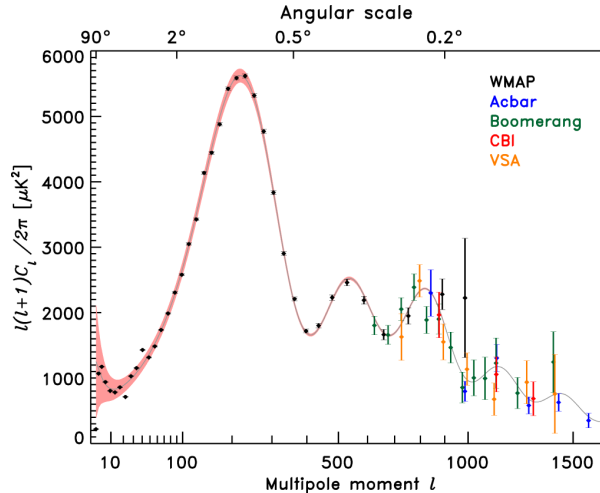


Figure 1.1: Angular CMB TT power spectrum showing the results of the Wilkinson Microwave Anisotropy Probe (WMAP3)[3], the Arcminute Cosmology Bolometer Array Receiver (Acbar)[8], the Balloon Observations Of Milimetric Extragalactic Radiation And Geophysics (BOOMERAnG)[7], the Cosmic Background Interferometer (CBI)[9] and the Very Small Array (VSA)[10]. Plot from <http://lambda.gsfc.nasa.gov> created by the WMAP science team.

universe remains homogeneous and isotropic on large scales.

The available information about the early universe can be roughly categorized into two realms. On the one hand the universe is strikingly isotropic and homogeneous, implying correlations across seemingly causally disconnected patches of the sky (the Horizon problem), with a flat Friedmann-Lemaître-Robertson-Walker (FLRW) metric describing the background evolution extremely well (the Flatness problem). On the other hand there were small perturbations around the observed isotropy and homogeneity of the universe, leading to the formation of all of the universe’s structure such as galaxies, clusters of galaxies and superclusters.

1.2 The Inflationary Paradigm

The inflationary paradigm, developed from pioneer works of [11, 12] in the beginning of the 1980’s, assumes an initial period of (quasi-)exponential expansion, which not only provides an explanation for the first “puzzles” about the background evolution of the early universe, like the Horizon and Flatness problem, but also provides a framework for generating the small anisotropies as observed by the precision measurements of the last decade.

1.2.1 Scalar Perturbations

During inflation, small quantum fluctuations of the scalar field driving the expansion induce fluctuations in the metric which are stretched to larger and larger wavelengths through the Hubble expansion until they are eventually frozen in after crossing the horizon. After inflation comes to an end, the universe reheats and becomes first radiation and then matter dominated.

The perturbations of the coupled photon baryon fluid enter the horizon, a mode at a time, and start to oscillate as the photon pressure resists gravitational compression. The velocity of the oscillations induces an additional Doppler shift which alters the observed pattern in the photon oscillations. The modes oscillate with diffusion damping reducing their amplitude until they reach the surface of last scattering, i.e. the moment in time when the baryon-photon fluid decouples, which is reached at different phases for the different wavelengths. The photons essentially free-stream through the universe, carrying an imprint of the above acoustic oscillations, redshifting with time, until they finally reach today's detectors and give valuable insight into the earliest history of the universe.²

With all the successes from the union of experiment and theory in cosmology, there are still several open questions.

1.2.2 Tensor Perturbations and Polarization

Of greatest current interest is the quest for a detection of the primordial gravitational waves predicted by inflation. By the same mechanism (amplification of quantum fluctuations) that produces perturbations in the scalar sector of the metric which in turn cause the anisotropy in the CMB temperature distribution across the sky, inflationary models generically produce perturbations in the tensor sector of the metric as well. The amplitude of the tensor fluctuations, which leave an imprint in both the temperature (TT) perturbations as well as in the polarization of the CMB, is directly related to the Hubble parameter and the energy scale of inflation, and determining it will significantly shrink the size of the zoo of possible inflationary models.

The polarization of the CMB is conveniently described by expanding it in E-modes and B-modes, which are related to the Stokes-Q and Stokes-U parameters. For cosmological considerations, the former basis is preferable to the latter because, while both the scalar and tensor perturbations of the metric contribute to the TT, TE, EE auto correlation functions, in a first approximation the B-modes are only sensitive to tensor fluctuations³.

With the amplitude of the BB power spectrum generically orders of magnitude lower than the TT power spectrum, the hunt for B-mode polarization is one of the most challenging and at the same time also most exciting endeavors in early universe cosmology.

Several upcoming experiments like Planck, Spider and CMBPol will increase the quality of CMB data, and CMBPol in particular will deliver pristine measurements of the CMB B-mode polarization.

1.2.3 Inflationary Model Building

On the inflationary model building side there is no shortage of proposals for the nature of the inflaton field. The development of inflationary models has gone hand in hand with advances

²For a more detailed introduction to the generation of CMB anisotropies see e.g. the textbooks [13, 14].

³Taking into account the effect of gravitational lensing, [15] showed that there is a conversion of E-modes into B-modes and vice versa; but it is possible to remove the lensing contamination to a certain extent [16].

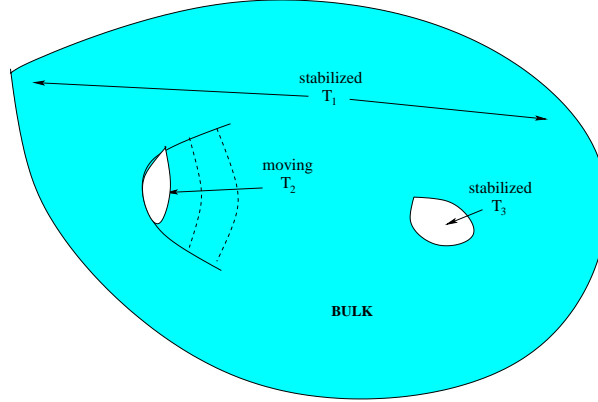


Figure 1.2: Schematic representation of a Calabi-Yau manifold

in theoretical particle physics, which provide a plethora of candidate models to describe the inflationary period. Old inflation, new inflation, chaotic inflation, SUGRA inflation, double inflation, power-law inflation, hybrid inflation, various SUSY and brane inflation models, inflation in string compactifications: this list presents only a fraction of all the candidates describing the inflationary stage that have been proposed in the past 25 years since the existence of an exponentially expanding phase in the early universe was first proposed. All these models operate at different energy scales, and can involve one or more fields (c.f. SUSY models, assisted inflation, \mathcal{N} -flation).

In recent years, a lot of effort has been put into attempts to realize inflation in the context of string theory, a candidate for a UV-complete quantum theory describing both particle physics and gravity. For example, in type IIB string theory, space-time is fundamentally 10 dimensional and must be reduced to 4 dimensions if it is to describe our reality. One possibility of doing so is compactifying the 6 extra dimension onto a Calabi-Yau manifold, which can be visualized as in Fig. 1.2. The sizes of the holes as well as the overall size of the manifold are described by so-called moduli fields. It proved very challenging to construct inflationary models in this setting because, on the one hand, these moduli fields need to be stabilized lest the manifold decompactifies which is phenomenologically forbidden. On the other hand, the potential of at least one of the moduli fields should be flat enough such that it allows for sufficient inflation. Finally, generic compactifications lead to a 4 dimensional anti-deSitter space-time. It is very challenging to obtain a positive cosmological constant and deSitter space in this setup. Only recently, string theorists [17, 18] discovered ways of compactifying the extra dimensions that lead to models with a small positive cosmological constant in four dimensions. Building on these compactifications, models were found by [19, 20, 21] with potentials that are sufficiently flat in the direction of at least one scalar field to allow for inflation to last for a sufficiently long time while at the same time all the other moduli fields describing the geometry of the compact manifold are stabilized. However despite many efforts, so far only explicit models with negligible production of gravitational waves during inflation have been found, with amplitudes

far below the threshold of even the most ambitious experiments, which – if these models were to describe the real world – would render useless all efforts to measure their gravitational wave imprint.

1.2.4 Trajectories

Because most models of inflation depend on (several) parameters (e.g. $V = m^2\phi^2 + \sigma\phi^3 + \lambda\phi^4$), the various realizations of inflation do not offer unique predictions, but cover a (sometimes huge) variety of power spectra with different shapes and amplitudes, with some clearly ruled out by current observations. Further adding to the complexity is the fact that in multiple field models, the initial conditions of the fields can also play a role, as demonstrated e.g. in [22].

It is standard practice to condense all information about the primordial power spectrum into 2 – 4 numbers, all determined at a pivot point in k -space, which are the amplitude A_s of the scalar power spectrum and its slope n_s , plus optionally the running of the slope n_{run} and/or the ratio of tensors to scalars r . These are then used to compare the model with the data.

There is a method (proposed by [23]) to generate inflationary flow trajectories and explore the space of observables, i.e. the space of parameters (n_s, r) , to investigate which region in parameter space is generically allowed by inflationary models. This approach is based on the truncated hierarchy of slow-roll parameters (3.9) and poses a rather strong prior towards small values of the tensor-scalar ratio r .

In contrast to the standard parametrization, we advocate the concept of trajectories. Inspired by the flow method, we developed a way to generate generic trajectories as a function of some time variable – be it the number of e-folds $N = -\int dt H$, where H is the Hubble parameter, or the wave number $\ln k$ – and relate them to the primordial power spectra. Examples for trajectory functions are $P_S(\ln k)$, $P_T(\ln k)$, the power spectra themselves, or more fundamental quantities like $\epsilon(\ln k) = -\dot{H}/H^2$ or $H(N)$ which require additional steps of either integration or differentiation to obtain the power spectra. The parameters of these trajectories – most conveniently the value of the trajectory at several points – are what we advocate as the new observables to make contact between model building and experiments, being in a sense more fundamental and less biased than previous attempts at reconstructing the primordial power spectra, and offering the additional benefit of a more universal control over the priors when performing Markov-Chain Monte Carlo (MCMC) parameter estimation. The only a priori constraint on a valid inflationary trajectory is that inflation happened inside the observational interval, as we cannot make any statements apart from the fact that inflation happened about the trajectory during the time period between the moment when the last mode for which reliable observations are available left the horizon and the end of inflation.

The trajectory picture in inflation resonates with the concept of the landscape [24] in string theory, where an enormous number of low energy models seem viable candidates for the description of our world, i.e. particle physics and gravity. The enormously huge number of vacua of string theory, differing e.g. in topology, field content and background fluxes, constitutes a

tremendous challenge for the prospect of ever unambiguously deriving the one and only low energy limit describing our four dimensional space-time, leading to the usage of stochastic arguments in the hope of progressing towards this goal.

Assuming that string theory is the correct theory of everything, the problems of the landscape have immediate consequences for model building in inflation. Instead of hoping to be handed a few models derived from string theory which offer distinctly different phenomenological consequences and filtering them through the observational eye of the needle to find the single theory that describes our universe, early universe cosmologists are finding themselves possibly faced with 10^{500} candidate theories describing the exponential expanding phase of the universe.

Observational data on the other hand so far offers only limited power to distinguish between different (and not even necessarily string inspired) models of inflation. The crucial element to be measured, the energy scale of inflation, can only unambiguously be determined through measurements of the B-mode polarization of the CMB. Due to its intrinsically small amplitude (typically orders of magnitude smaller than the amplitude of the temperature fluctuations) so far only upper limits have been determined, leaving prior effects to potentially dominate the measurements, possibly giving rise to spurious detections as observed in some parametrizations in the trajectory framework.

1.2.5 The Trans-Planckian Problem - How Far Back Can We See?

While the inflationary paradigm offers an explanation for all observables about the early universe, it also raises some conceptual issues, particularly the issue of the trans-Planckian problem[25, 26]. As mentioned above, during the inflationary stage fluctuations of a given physical wavelength are stretched outside the horizon, i.e. their wavelength increases with time. Looking at it the other way, it seems obvious what happens if we take an observable wavelength today and evolve it backwards in time, all the way back into the inflationary stage. The wavelength keeps shrinking and shrinking, until at some point, it crosses the Planck scale and becomes shorter than the Planck length. The same is also true for modes that leave the horizon during inflation if inflation lasted sufficiently long, therefore there could be imprints of trans-Planckian physics in the CMB. There is an extensive literature investigating the possibility of observing trans-Planckian effects in the CMB, using methods of quantum field theory in curved space-time to calculate the expected Trans-Planckian effects.

1.2.6 Outline Of The Thesis

Chapter 2 presents novel ways of parametrizing the primordial power spectra using the trajectories mentioned in Sec. 1.2.4 and is in the final stages of being written up as the paper “*Scanning Inflation I - Constraining the Power Spectra*”[27], written in collaboration with J. Richard Bond, Carlo Contaldi and Lev Kofman. We find that priors play a huge role when performing MCMC parameter estimation and can lead to spurious claims of a detection of

new features – in our case a spurious detection of tensor modes – if observational data is of insufficient quality.

Chapter 3 extends the trajectory method of chapter 2 to describe the time evolution of the ϵ parameter during inflation, encoding the dynamics of inflation driven by a single scalar field and allowing the reconstruction of the inflationary potential. Also in this case the choice of priors tremendously influences the results of MCMC parameter estimation runs with even stronger but still spurious detection of tensors. Finally we demonstrate the degeneracy of the reconstruction of the inflaton potential in the absence of information about the energy scale of inflation. This chapter will be published as the paper *”Scanning Inflationary Trajectories II: Constraining the Acceleration Trajectories”*[28] in collaboration with J. Richard Bond, Carlo Contaldi and Lev Kofman.

Chapter 4 investigates trajectories in the context of Kähler moduli inflation[21] as an example of a string theory model of inflation that intrinsically contains ensembles of trajectories of the dynamical fields, i.e. different realizations of inflation, for fixed parameters of the potential. We find that allowing the axionic partner of the Kähler modulus to participate in the dynamics, this model leads to a rich structure of various topologically distinct trajectories, adding another statistical element to the string theory landscape. Not only are there many different vacua that seem to be only treatable statistically so far – making the predictions highly dependent on the prior beliefs just as we found in Chapters 2 and 3 – even within a given vacuum we find another statistical element. The initial conditions of the fields greatly influence the phenomenological consequences, with e.g. just small variations in the initial conditions leading to huge variations in the number of e-folds that inflation in this model lasts. It is published in Phys. Rev. D. as *”Roulette Inflation”*[22], written in collaboration with J. Richard Bond, Lev Kofman and Sergey Prokushkin.

Chapter 5 studies the issue of observability of trans-Planckian physics due to the stretching of modes during inflation. It is submitted to Phys. Rev. D. available on the archive as the paper *”Trans-Planckian Issue in the Milne Universe”*[29], written in collaboration with Lev Kofman. We apply the trans-Planckian logic to the Milne universe, which is a FLRW-type metric with scale factor $a(t) = t$ and at the same time just a reparametrization of a quarter of Minkowski space. We find that while in Minkowski coordinates there clearly is no trace of any influence of Trans-Planckian physics, there can also be no such effect in Milne coordinates, as we show by performing the explicit renormalization of the energy-momentum tensor in Milne coordinates.

Chapter 6 contains the obligatory conclusions and outlook into the future for the field.

Chapter 2

Scanning Inflationary Trajectories I: Power Spectra

2.1 Introduction

Traditionally, inflationary model building moves along a well-trodden path from the top down: Finding a (physically motivated) potential, its logarithmic derivatives to various orders (a.k.a. slow roll parameters) at a given point in time map the predictions of the model into the space of traditional observables describing the shape of the power spectra $\mathcal{P}_s, \mathcal{P}_t$ of scalar and tensor perturbations. To be precise, instead of comparing predictions for all parameters of the power spectra (the scalar amplitude A_s , the scalar spectral index n_s , its running n_{run} and the tensor scalar ratio $r = \frac{\mathcal{P}_s}{\mathcal{P}_t}$), in most cases the predictions of the models are only tested against a subset of the above parameters, namely n_s and r [30]. Ignoring n_{run} can be justified as current measurements of the running of the scalar spectral index are still compatible with zero although there is an indication for non-zero running which would imply that the value of n_s is depending on the scale it is measured at.

Major efforts are undertaken to detect the tensor scalar ratio r for which so far only upper limits have been obtained. Observationally it is rather challenging to measure the amplitude of the only clean tracer of tensor modes, the B-mode polarization of the cosmic microwave background (CMB) radiation, which is orders of magnitude smaller than the amplitude of temperature fluctuations which is by itself already quite small. Obtaining an observational estimate for the magnitude of r is crucial for inflationary model building as this fixes the energy scale of inflation. So far, the only limits on the energy scale of inflation come from arguments from reheating, while the scalar power spectrum does not provide any information about the energy scale of inflation.

Just like the spectral index n_s , the tensor scalar ratio r is in principle a scale dependent quantity as the tensor spectral index n_T is related to r through the consistency relation $n_T = -\frac{r}{8}$ if inflation is driven by a single scalar field.

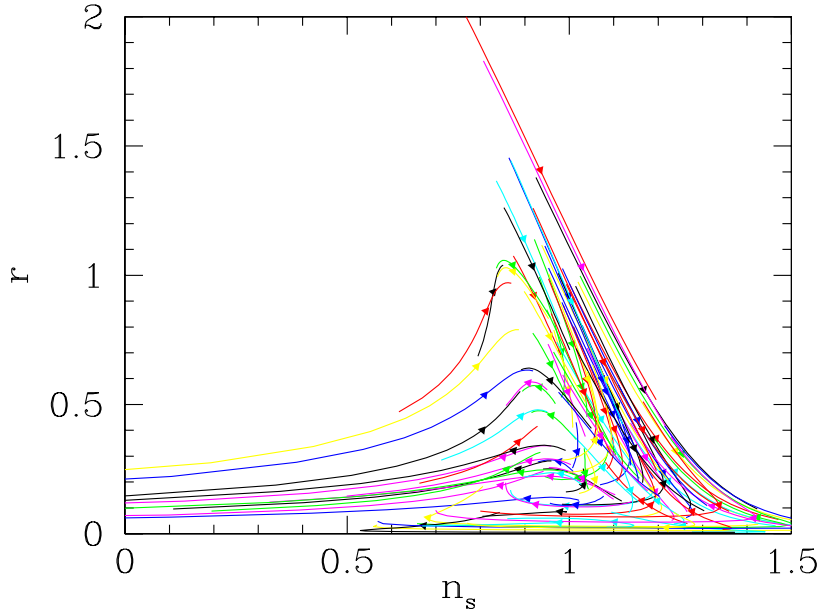


Figure 2.1: Flow along a random selection of the inflationary trajectories in the n_s vs. r plane during 10 e-folds. The trajectories were generated as seventh order Chebyshev expansions of $\epsilon(N)$.

With both n_s and r functions of the wave number k great care must be taken to use the same scale when comparing predictions from model building with observations. Fig. 2.1 shows the evolution during $\Delta N = 10$ ($N = \int_t^{t_{\text{end}}} H dt$ is the number of e-folds before the end of inflation) of n_s and r obtained for an ensemble of randomly generated trajectories, showing a substantial variation of these observables. However, the observational values for the parameters of the scalar and tensor power spectra are measured at a specific pivot point in k -space, usually taken to be $k_* = 0.05 \text{Mpc}^{-1}$ or $k_* = 0.002 \text{Mpc}^{-1}$. In contrast to this, the values of the logarithmic derivatives of the potential are generically taken at a specific point in time corresponding to a number of e-folds N_* before the end of inflation. In general, the mapping between the number of e-folds and the wave number k depends on the details of the inflationary dynamics and therefore on the parameters of the potential as well as the initial values in case of multiple field models. Also the relation between N and k is altered by the details of preheating after inflation, producing an uncertainty of ≈ 10 in the shift between these two quantities. Taking into account that n_s and r might well be time-dependent quantities, it is obvious that better strategies for relating theory with observations are needed.

Also, recently there has been a growing interest in models of inflation driven by the combined effect of several scalar fields which arise naturally in the context of e.g. minimal supersymmetric standard model (MSSM) and in string inspired models. With more than one field driving the dynamics, it is not at all clear that there should exist a unique attractor solution to which the trajectories from all initial values of the fields converge. Indeed, there are examples for models with several fields that offer several distinct attractor solutions[22], making the inflationary

dynamics heavily dependent on the initial values of the scalar fields.

In view of the above we suggest to work in a trajectory picture, a bottom-up approach to model building, in which all fundamental quantities such as the tensor and scalar power spectra or the Hubble parameter are regarded as trajectories, with a suitable choice of time variable such that there are no ambiguities about the location of observable quantities while at the same time capturing all essential dynamics. Instead of using the traditional parametrization to characterize the primordial power spectra, the trajectory functions are constrained directly using standard parameter estimation packages employing Markov Chain Monte Carlo (MCMC) methods. The trajectory function $f(x)$ is expanded in terms of Chebyshev polynomials $T_i(x)$ as

$$f(x) = \sum_{i=0}^{M-1} c_i T_i(x), \quad (2.1)$$

and is described either in the space of coefficients or in the space of function values at nodal points $x_k^M = \cos \frac{\pi(k+\frac{1}{2})}{M}$ (we will frequently suppress the index M for brevity), i.e. when creating an ensemble of trajectories, either the coefficients are drawn randomly or the value of the function at the nodal points of the Chebyshev expansion.

There are many possible choices for the trajectory function, the Hubble parameter H , ϵ , \mathcal{P}_s , \mathcal{P}_t , \dots , with the only criterion that one can map the trajectory function to the scalar and tensor power spectra. For example, the trajectory function ϵ (and also H) encodes all information about single field inflationary models as well as (neglecting the influence of isocurvature perturbations) gentle multiple field model in the sense that a sufficiently well-behaved dynamics can be cast in terms of an effective single field model. Mapping H trajectories to the power spectra requires differentiation to obtain ϵ , while mapping ϵ trajectories requires an integration step. Selecting the power spectra $\mathcal{P}_s, \mathcal{P}_t$ themselves as the trajectory functions offers more flexibility, not only allowing for a non-monotonic tensor power spectrum but also not relying on the single field approximation. In this paper we will focus on the choice of $\mathcal{P}_s, \mathcal{P}_t$ as trajectory functions while examining the choice of ϵ in the companion paper[28].

Different trajectory functions come with different priors. The Hubble parameter, \mathcal{P}_s and \mathcal{P}_t are constrained to be strictly positive, while ϵ is confined to lie in $\epsilon \in [0, 1]$. Using H or ϵ implies single field inflation, a rather complex prior on the allowed trajectories. Further on, the trajectory can be expanded in a non-linear mapping, e.g. logarithmically, as $\ln f(x) = \sum_{i=0}^{N-1} c_i T_i(x)$, imposing a different prior on the generated ensemble of trajectories.

All the different priors will bias the trajectories to varying degrees depending on the quality of observational data, and consequently alter the posterior distributions of the traditional observables, specifically the value of r which is strongly influenced by the choice of trajectory function and the prior distribution of the trajectory values. Even though one chooses a flat prior on the parameters, various effects can combine to implicitly change the prior away from flatness, in extreme cases even to a sharply peaked distribution. Generally, priors are to be chosen on various levels: from the prior that inflation should be driven by (a) scalar field(s) (resulting in

different choices for the consistency relation between the tensor and scalar power), over which parametrization to choose to which distribution should be used to draw the parameters of a given trajectory .

A natural choice for the time variable is the wave number k itself. As physical time evolves, modes of decreasing comoving wavelength are stretched outside the horizon, crossing into the super-horizon region when $k = aH$. This leads to the relation $d \ln k = (1 - \epsilon)H dt$, where k is the comoving wave number of the mode crossing the horizon, t is the physical time, and $\epsilon = -\frac{\dot{H}}{H^2}$ (where $\dot{H} = \frac{dH}{dt}$) which makes k a good time variable as long as the inflationary stage is not interrupted by periods of non-exponential expansion with $\epsilon \geq 1$.

The trajectory picture ultimately is a bottom-up approach to inflationary model building. With a proper choice of fundamental trajectory function, e.g. $\epsilon(\ln k)$, it becomes even possible to reconstruct the shape of the inflationary potential directly from observational data. In this paper, we focus on an unbiased reconstruction of the primordial scalar and tensor spectra, leaving the reconstruction of the inflationary potential to the accompanying paper[28].

We use the (suitably modified) Markov Chain Monte Carlo (MCMC) sampler COSMOMC [34] to obtain posterior distributions for the power spectra parameters as well as four other cosmological parameters, three of which are related to abundances: $\omega_b \equiv \Omega_b h^2$, the physical density of baryons, $\omega_c \equiv \Omega_c h^2$, the physical density of cold dark matter, $\theta \equiv 100 \ell_s^{-1}$, parametrizing the angular scale ℓ_s^{-1} associated with sound crossing at decoupling, which defines the overall position of the peak-dip pattern and from which the cosmological constant Ω_Λ can be derived. The fourth is an astrophysical parameter associated with the reionization of the Universe after recombination, τ , the Thomson scattering depth to decoupling. A flat Universe theoretical prior is reasonable to impose on inflation models, with the curvature energy $\Omega_k = 1 - \Omega_{tot} \approx 0$. In our analysis we include the following CMB data sets: WMAP3, CBI, ACBAR06, BOOMERANG03, DASI, MAXIMA and VSA. For large scale structure we include 2dFGRS and SDSS data sets. The treatment of the data is described in [7, 9].

There are data constraints beyond the CMB and LSS regions that are only loosely determined, i.e. “weak” prior probabilities, informed by broad brush stroke considerations, but still quite limiting. One is that the Universe underwent significant inflation, translating at lowest order to $0 < r < 16$ over the entire k range within the horizon. For the dynamical trajectories this corresponds to $0 < \epsilon < 1$, or equivalently an inflationary period that lasted for a sufficient number of e-folds N .

Enough inflation implies that scales of topological structures cannot be too small so that there is sufficient cosmic complexity to give rise to life. Also, the amplitude of the power spectrum at high k cannot be too large otherwise surviving primordial black holes (PBH) formed in abundance. Another weak prior driven by the CMB data is that the Compton “optical” depth cannot be too large or else there would be no CMB fluctuations on small scales. This reflects in the formation of the first ionizing stars and is more strongly restrictive than the PBH constraint. The epoch of galaxy formation is also a constraint, often used in

a very broad way in anthropic arguments. The data on high redshift galaxy abundances has improved enormously in recent years and even with the uncertainties associated with gas and radiation at early times can significantly constrain the power spectrum.

Improved observations narrow down the range of allowed variations. For example, in the eighties the upper limits on CMB fluctuations combined with a few LSS constraints already restricted the allowed possibilities. The COBE data further restricted what was allowed, and now in the era of WMAP and the higher resolution experiments, the possibilities for significant variation from the standard model are much more limited.

Using the traditional parametrizations of the primordial power spectra in terms of A_s and n_s , current CMB+LSS constraints on the basic 6-parameter model, are given in [8], with $n_s = 0.96^{+0.013}_{-0.014}$. Including either r or n_{run} , [7] finds $r < 0.36$ at the 95% confidence limit with $n_{\text{run}} = 0$ and $dn_s/d\ln k = -0.051^{+0.027}_{-0.026}$ with $r = 0$. Here we consider the two parameter r and $dn_s/d\ln k$ extension to the base model. After marginalizing over the other parameters, the current data give the contours in Fig. 2.6.

This paper is structured as follows. In Section 2.2 we describe the basic formalism of single field inflationary dynamics to settle the notation and comment on issues of model selection. Section 2.3 introduces the different possible parametrizations of background trajectories and describes various ways to generate ensembles of trajectories. Section 2.4 discusses the issue of priors in the space of traditional observables and provides an analytic explanation for the observed non-uniformity. Section 2.5 uses a specific trajectory parametrization that is equivalent to the standard parametrization to demonstrate the consistency of the scanning method. In Section 2.6 we use the reconstruction of simulated data sets to establish the influence of different priors and explores methods to compensate for the non-uniformity of the prior distributions. Section 2.7 confronts the trajectories with observational data, demonstrating the sensitivity to priors of the marginalized posterior distributions. In Section 2.8 we summarize our results.

2.2 Inflationary trajectories and Observables

In this section we review how the background dynamics is related to the power spectra of scalar and tensor cosmological fluctuations generated from inflation. We first introduce the basic formalism and notation describing single field inflation.

2.2.1 Basic Formalism

In the case of a single real scalar field driving inflation with potential $V(\phi)$ living in a FRW-type universe with the metric $ds^2 = dt^2 - a(t)^2(dx^2 + dy^2 + dz^2)$, the dynamics of the system of the scalar field $\phi(t)$ plus gravity $a(t)$ is described by the constraint equation

$$3H^2 = \frac{1}{M_p^2} \left(\frac{1}{2} \dot{\phi}^2 + V \right) , \quad (2.2)$$

and the equation of motion for the scalar field

$$\ddot{\phi} + 3H\dot{\phi} + V_{,\phi} = 0 , \quad (2.3)$$

where $H(t) = \frac{\dot{a}}{a}$ and $M_p = 1/\sqrt{8\pi G}$ is the reduced Planck mass (which we eventually will set to unity, $M_p = 1$). It is very convenient to introduce

$$\dot{H} = -\frac{1}{2} \left(\frac{\dot{\phi}}{M_p} \right)^2 , \quad (2.4)$$

which should be employed when numerically integrating the equations of motion while the Friedman equation (2.2) can be monitored to control the numerical stability.

An alternative formalism to deal with the scalar field/gravity system, which will be more suitable for this paper, is based on the Hamilton Jacobi equation [35]. It is based on the well-known Hamilton Jacobi formalism of classical mechanics. There the system is described in terms of canonical position and momentum coordinates (q, p) . Using the Hamilton Jacobi equation a canonical transformation to coordinates (Q, P) can be found that makes Hamiltonian \mathcal{H} vanish.

The Hamiltonian for the scalar/gravity system is given by the Hubble parameter as function of ϕ , $H = H(\phi)$, where the canonical momentum associated with variable ϕ is $\pi = \dot{\phi}$. The Hamilton-Jacobi equation arising from the constraint equation (2.2) reads

$$3H^2 = 2M_p^2 \left(\frac{\partial H}{\partial \phi} \right)^2 + \frac{V(\phi)}{M_p^2} . \quad (2.5)$$

The solutions of this equation $H = H(\phi)$ are families of trajectories differing by their initial conditions.

We will make use of the conventional hierarchy of slow-roll parameters defined with respect to derivatives of the function $H = H(\phi)$ namely

$$\epsilon_H \equiv -\frac{\dot{H}}{H^2} = 2M_p^2 \frac{H'^2}{H^2} , \quad \eta_H = 2M_p^2 \frac{H''}{H} , \quad \zeta_H = (2M_p^2)^2 \frac{H'''H'}{H^2} , \quad (2.6)$$

where $H' = \frac{dH}{d\phi}$ and higher orders are defined as

$${}^\ell \lambda_H = (2M_p^2)^\ell \frac{(H')^{\ell-1} d^{\ell+1} H}{H^\ell d\phi^{\ell+1}} , \quad (2.7)$$

for $\ell > 2$ as introduced by [36]. In the following we will drop the subscript H and use $\epsilon \equiv \epsilon_H$. It will also be useful to define the parameter $\sigma = 2\eta - 4\epsilon$, which corresponds to the value of the scalar spectral index $n_s - 1 = \sigma$ to lowest order in slow-roll.

The slow-roll regime is defined as the period during which the kinetic term $\ddot{\phi}$ in the equation of motion does not dominate and the slow-roll parameters as defined above are small which

ensures that the scalar field is rolling slowly down the potential towards the minimum. However, this is conceptually a different regime from the inflationary period, a point that we should elaborate on a bit further.

Inflation continues as long as $0 < \epsilon < 1$ and stops at $\epsilon = 1$. The values of η and the other slow-roll parameters in principle do not matter. Conventional wisdom has it that in practice, $\epsilon \approx 1$ at around the same time as $\eta \approx 1$. But from a theory point of view, this is not necessarily so. One could imagine for example that ϵ has some sharp spikes where $\eta \gg 1$, but stays within $[0, 1]$ even during those spikes. Now it might be quite a contrived potential for a single scalar field leading to this evolution, but who knows how baroque a model nature served us. The problem of models with large slow-roll parameters lies in the fact that in this case it is rather difficult to calculate the shape of the primordial power spectra of scalar and tensor perturbations. The expressions given in the literature (e.g. [37]) are usually derived assuming that ϵ is only slowly varying, and therefore are valid only if the slow-roll parameters are small.

But only the data can and shall decide whether such a model is permissible or not. A priori we should not exclude any model based on the values of the parameters of the slow-roll hierarchy alone. It is true that current observations favor models which have $n_s \approx 1$, but one can imagine – however not necessarily easily – a model in which the contributions of ϵ and η (and higher order terms) to the spectral index almost cancel, with each term individually being rather large.

The range of ϕ which corresponds to the observable horizon can vary significantly from model to model. However, one can use a different parametrization for the flow along the inflationary trajectory such as time t , the number of e -foldings $N = \int_t^{t_e} dt H(t)$ or even the wavelength $1/k$ of perturbations generated during inflation at horizon exit instead of the value of ϕ itself. The different parametrizations are all inter-related by the dynamics of the model, with a general non-linear mapping from one to the other.

It is convenient to relate the duration of inflation to the observable horizon which is almost the same in different models. The number of e -foldings N is counted backwards from the end of inflation

$$a(t) = a_e e^{-N}, \quad (2.8)$$

where a_e is the value of the scale factor at the time t_e at which inflation ends ($N = 0$) and preheating begins. The observable horizon corresponds to $N \approx 70$, and may vary by quite a few e -foldings between realizations, depending among other things on the energy scale of inflation.

Another good time variable is the wavelength $1/k$ of perturbations generated during inflation. In the uniform acceleration approximation we can equate $k = a(t_k)H(t_k)$, where t_k is the time when the mode k exceeds the horizon during inflation. The two parametrizations are related by $d \ln k / dN = -(1 - \epsilon)$ which can be integrated to give

$$\ln \left(\frac{k}{0.002 \text{Mpc}^{-1}} \right) = 62 + \Delta - N + \int_0^N dN' \epsilon(N'). \quad (2.9)$$

The term Δ is defined by the thermal history of the post-inflation cosmology, including (p)reheating, phase transitions and other sources of entropy generation. The connection between N and k is a matter of ongoing discussion [38, 39, 40, 41]. Typical values for Δ are $\Delta = 1 \dots 10$, derived recently from the theory of preheating after inflation, see [42, 43].

In the approximation of uniform acceleration (where $\dot{\epsilon} = 0$) the relation between $\ln k$ and N is straightforward, otherwise it depends on the trajectory itself through the term $\int_0^N dN' \epsilon(N')$. The contribution is small (for instance for the potential $V(\phi) \sim \phi^n$ the term gives a logarithmic correction $\int_0^N dN' \epsilon(N') \sim \ln(1+N)$), and only leads to small variations in the mapping between the observable wavelengths $1/k$ and e -foldings N .

The most convenient parametrization is the observable interval of k between the size of the horizon and scale of L_α clouds at redshift $z \sim 3$, $1/k \sim 1\text{Mpc}$.

We now turn to the amplitude and spectra $\mathcal{P}_s(k)$ and $\mathcal{P}_t(k)$ of scalar and tensor fluctuations generated in single field inflation models. These can be derived from the well known second order mode equations whose coefficients are functions of the background solution [44]. There are several frameworks for calculating the shape of the power spectra for inflation driven by a single real scalar field [45, 46] and multiple scalar fields [47, 48, 49]. However, assuming the observable fluctuations do not significantly depart from the scale free regime, we can proceed with a simpler formalism [37].

In the uniform acceleration approximation ($\epsilon = \text{const}$) the power spectra of scalar and tensor fluctuations as a function of the comoving momentum k are

$$\mathcal{P}_s = \frac{1}{8\pi^2\epsilon} \left(\frac{H}{M_p} \right)^2 e^{2u_s}, \quad (2.10)$$

$$\mathcal{P}_t = \frac{2}{\pi^2} \left(\frac{H}{M_p} \right)^2 e^{2u_t}, \quad (2.11)$$

where the values of ϵ and H are taken to be taken at $aH = k$ and u_s, u_t are small corrections that should be included for accuracy. For small slow roll parameters the spectra are expected to be mildly broken scale invariant, and well approximated by the power-law expressions

$$\mathcal{P}_s(\ln k) = A_s(k_{\text{pivot}}) \left(\frac{k}{k_{\text{pivot}}} \right)^{n_s-1}, \quad (2.12)$$

$$\mathcal{P}_t(\ln k) = A_t(k_{\text{pivot}}) \left(\frac{k}{k_{\text{pivot}}} \right)^{n_t}, \quad (2.13)$$

where $A_{s/t}(k_{\text{pivot}})$ is the amplitude at a pivot point and $n_{s/t}$ is the scalar spectral index at this point. Note that n_s is defined to be $n_s = 1$ for a flat spectrum, whereas $n_t = 0$ for a flat spectrum. When estimating parameters, the quantity that is usually determined is the tensor-scalar ratio $r = \frac{\mathcal{P}_t}{\mathcal{P}_s}$ instead of \mathcal{P}_t . We refer to the set of $\{A_s, n_s, n_{\text{run}} = dn_s/d\ln k, r\}$ as the standard or traditional parametrization.

The amplitude A_s , the spectral index n_s , its running n_{run} and the ratio of tensor and scalar

amplitudes r can be expressed in terms of slow roll parameters up to a selected order. The values for the spectral quantities are usually defined at an number of e-folds N corresponding to a choice of pivot scale k_{pivot} in Eq. 2.13. Including some small corrections for uniform acceleration in u_s, u_t , we have to second order for n_s, n_{run} and r

$$\begin{aligned} n_s - 1 &= \sigma - (5 - 3C)\epsilon^2 - \frac{1}{4}(3 - 5C)\sigma\epsilon + \frac{1}{2}(3 - C)\zeta^2, \\ n_{\text{run}} &= -2\zeta + 5\sigma\epsilon + 12\epsilon^2, \\ r &= \epsilon(1 - C(\sigma + 2\epsilon)), \end{aligned} \quad (2.14)$$

where $C = 4(\ln(2) + \gamma) - 5$ and the amplitude is given by

$$A_s = 2^{2\nu-3} \frac{\Gamma^2(\nu)}{\Gamma^2(\frac{3}{2})} (1 - \epsilon)^{2\nu-1} \frac{H^2}{\pi M_p^2 \epsilon}, \quad (2.15)$$

where $\nu = \frac{1-\eta+\epsilon}{1-\epsilon} + \frac{1}{2}$.

Common values for the position of the pivot point k_{pivot} are 0.05Mpc^{-1} and 0.002Mpc^{-1} . However one has to be careful when comparing theoretical predictions to the values at the pivot points: Even if n_{run} is only small but non-zero, the values of parameters A_s, n_s, r move around quite a bit within 10 e -folds, see Fig. 2.1. So one should make sure that one computes the prediction of the spectral index at the right k_{pivot} . In contrast to this, it seems a widespread practice to make predictions for observables at a fixed number of e-folds N before the end of inflation, which is usually taken to be around $N \approx 60$.

From a theoretical point of view, the running of the spectral index can generally be non-zero, $n_{\text{run}} = \frac{dn_s}{d\ln k} \neq 0$. Only recently observations have become sufficiently sensitivity to distinguish between running and non-running, with the 3-year WMAP results finding a non-zero n_{run} at 2σ .

The traditional parametrization of the power spectra is motivated by the fact that a pure deSitter stage of inflation has perfectly flat power spectra and that in most models of inflation driven by a scalar field ϵ is rather small, also giving rise to n_s being only slightly different from unity. But these two points are only a theoretical bias. Observational data should be the determining the parameters of the primordial power spectra as unbiased as possible. The only piece of unbiased information that we have at our disposal is the fact that $\epsilon \in [0, 1]$ during inflation. Therefore it is sensible to use a parametrization depending on ϵ for reconstructing the primordial power spectra (of course, one also needs an integration constant which we denote by H_1 to obtain the Hubble parameter as a function of k , $H(k)$) [28].

2.2.2 Prior prejudice and Bayesian Model Selection

Recently a lot of attention has been devoted to the question of model selection [50, 51]. Given several competing models with different numbers of parameters, the fundamental problem is to decide which one should be used to describe the data. If the likelihood of all models is the

same, one can simply invoke Occam's razor which prefers the model with the fewest parameter. However if the likelihoods for the models differ (and the model with the fewest parameters is not the most likely), there is a need to quantify the influence of Occam's razor, i.e. to quantify the penalty for the introduction of extra parameters. There are two different approaches to this. The first one uses information criteria like the Akaike Information Criterion [52],

$$AIC = -2 \ln \mathcal{L}_{\max} + 2k , \quad (2.16)$$

where \mathcal{L} is the best-fit likelihood and k is the number of parameters, or the Bayesian Information Criterion [53]

$$BIC = -2 \ln \mathcal{L}_{\max} + k \ln N \quad (2.17)$$

where \mathcal{L}, k are the same as above and N is the number of data points. It is easy to see that the AIC is equivalent to the familiar χ^2/dof method.

Under several strong assumptions, the BIC can be derived from the Bayesian evidence, which is the second approach to model selection, see e.g. [54] for details. In this method, the evidence E is calculated for each model, allowing for rank-ordering. The Bayesian evidence is defined by

$$E = \int d\theta \mathcal{L}(\theta) P(\theta) , \quad (2.18)$$

where θ is the parameter vector and $P(\theta)$ is the prior distribution which quantifies the belief in the range of possible parameters prior to looking at the data. This prior gives the Bayesian evidence a somewhat subjective touch, where one generally has to explicitly define the subjective prior beliefs when stating results. The rank-ordered set of models is then usually subjected to the interpretation scale from [55] assigning different significances to the various values of $\Delta \ln E$.

Based on this procedure, it has been argued by [51] that there is only very little evidence for a departure of the scalar spectral index n_s from unity, making the scale free Harrison Z'eldovich spectrum still a competitive candidate.

However, the issue of priors is somewhat more delicate than is usually stated. Very simply put, even going from sampling the parameter $\theta = \epsilon \in [0, 1]$ to sampling $\theta = \ln(\epsilon) \in [-\infty, 0]$ gives two different priors with vastly different parameter volume. It is not clear which form should be preferred. Also, using physically equivalent parametrizations in different variables, e.g.

$$\{\mathcal{P}_s(k_1), \mathcal{P}_s(k_2), \mathcal{P}_t(k_3)\} \in \{[0, \infty], [0, \infty], [0, \infty]\}, \quad (2.19)$$

instead of

$$\{A_s, n_s, r\} \in \{[0, \infty], [-\infty, \infty], [0, \infty]\}, \quad (2.20)$$

changes the volume of the prior space significantly while being physically equivalent. It is not

clear which parametrization should be the proper one. Therefore for now we choose to not put too much weight on considerations using Bayesian inference and model selection criteria. In Sec. 2.6 we will see the effect of different prior distribution on the posterior in practice, further illuminating some of the points raised here.

2.3 Ensemble of Inflationary Trajectories

We now introduce the ensemble of inflationary trajectories. Traditionally, the scalar field potential $V(\phi)$ is given by some theoretical motivation, generally containing several free parameters. Given the shape of the potential and assuming slow roll, it is easy to determine the values of ϵ and the slow roll parameter η through

$$\epsilon_H \approx \epsilon_V \equiv \frac{M_p^2}{2} \left(\frac{V'(\phi)}{V(\phi)} \right)^2, \quad \eta_H \approx \eta_V \equiv M_p^2 \left(\frac{V''(\phi)}{V(\phi)} - \frac{1}{2} \left(\frac{V'(\phi)}{V(\phi)} \right)^2 \right), \quad (2.21)$$

where $H^2(\phi) \approx \frac{1}{3M_p^2} V(\phi)$ has been used, calculate the values of the scalar spectral index n_s and of the scalar tensor ratio r using (2.14) and adjust the parameters to make the prediction for the observables compatible with observations. Also, inflation driven by a scalar field with the given potential should last for a sufficiently long time, i.e. for enough e -foldings, to accommodate uniformity on the scale of today's horizon H_0^{-1} . This procedure has an extensive record in the literature [30].

However, this method has several shortcomings that we would like to address. First of all, it puts a prior on the space of allowed models that is motivated not by physics but by aesthetic considerations such as the perceived simplicity or naturalness of the potential. This is biasing the reconstruction of the potential from observations in a way that could lead to the wrong conclusions about the naturalness of inflation. Secondly, comparing the predictions of a model with observations at only one scale, the pivot point, takes into account information available at different scales in a very restricted way, e.g. by allowing the scalar spectral index to run. The results of the 3 year data release of WMAP already indicate non-zero running. If future experiments strengthen this detection, new methods to compare theory with observations should be devised that allow for more freedom in the form of the power spectra.

Therefore we shall use $\mathcal{P}_s(\ln k)$ and $\mathcal{P}_t(\ln k)$ as trajectory functions describing the tensor and scalar curvature power spectrum of primordial perturbations. For reasons explained above it is more convenient to use $\ln k$, the wave number of perturbations, as time variable instead of the physical time t . The only priors we impose are positivity of both \mathcal{P}_s and \mathcal{P}_t , and monotonicity of \mathcal{P}_t (which we only relax where stated specifically).

As already indicated above, one way of judging the compatibility of a random ensemble of trajectories with observations is to map the ensemble of trajectories to the space of observables $S = \{A_s, n_s, n_{\text{run}}, r\}$ at a pivot point. While this method has the aforementioned drawbacks, a similar strategy with the same drawbacks is widely used in the literature especially in connection

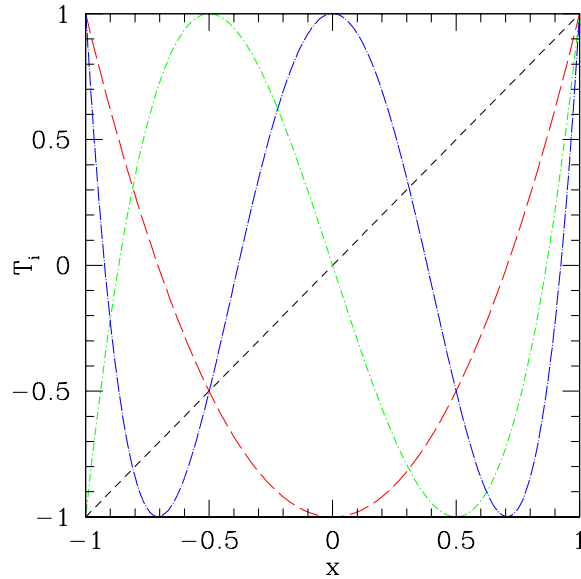


Figure 2.2: Chebyshev polynomials to order 4. At higher order, Chebyshev polynomials get increasingly similar to Fourier modes.

with the flow approach to inflation[56, 57, 58, 59].

Each pair of trajectories $(\mathcal{P}_s, \mathcal{P}_t)$ corresponds to a point in the space \mathcal{S} , the whole ensemble of trajectories to a scatter plot. A naive way to compare with observational data is to superimpose the scatter plot of trajectory predictions on the 2d posterior likelihood contours (n_s, r) obtained from MCMC parameter estimation, see Fig. 2.6.

What we actually need is to have effective ways to generate an ensemble of realizations of inflation with as few priors as possible. Our goal is to generate a multitude of inflationary trajectories in order to scan the space of inflationary models. These trajectories can be mapped into the traditional observables for the power spectrum of primordial scalar and tensor perturbations.

2.3.1 Properties of Trajectory Functions

If the argument (the “time” variable) of trajectory functions is the field ϕ , physical time t or number of e -folds N , the range of the argument corresponding to the same observable range in wave number $\ln k$ can significantly vary from trajectory to trajectory, as it is the case with the flow equations. Assuming that $\ln k$ accessible to observations ranges from $\ln k_{\min}$ to $\ln k_{\max}$, it will be convenient to construct the variable x

$$\ln k = \frac{\ln k_{\max} - \ln k_{\min}}{2}x + \frac{\ln k_{\max} + \ln k_{\min}}{2}, \quad (2.22)$$

which maps the range in $\ln k$ into the interval $[-1, 1]$. Thus, all inflationary models with inflationary trajectory within the observable interval in wave number of the fluctuations are

characterized by functions of x within the interval, $-1 \leq x \leq +1$. We want to scan over realizations of $\mathcal{P}_s, \mathcal{P}_t$ taken in the same interval of the argument (2.22).

Now we can address the problem of optimal approximation of functions in the interval $-1 \leq x \leq +1$ from a mathematical point of view, without any physical priors, and then optionally include the physical monotonicity constraint on \mathcal{P}_t , our goal being to scan over functions most uniformly.

From a mathematical perspective the most optimal uniform approximation of a function $f(x)$ in a finite interval $-1 \leq x \leq +1$ is given in terms of Chebyshev polynomials

$$f(x) = \sum_{j=0}^{M-1} c_j T_j(x) , \quad (2.23)$$

where $T_j(x)$ are the Chebyshev polynomials and c_j are the coefficients of the Chebyshev transform. The Chebyshev polynomials $T_j(x)$ are defined in the interval $-1 \leq x \leq +1$ in the following way

$$T_j(\cos(x)) = \cos(jx) . \quad (2.24)$$

Let us write down the first Chebyshev polynomials explicitly

$$T_0(x) = 1, \quad T_1(x) = x, \quad T_2(x) = 2x^2 - 1, \quad T_3(x) = 4x^3 - 3x, \quad \dots , \quad (2.25)$$

see Fig. 2.2 for a plot of the first 4 polynomials. A remarkable property of the Chebyshev decomposition is that it is the most accurate uniform decomposition of polynomials of a given degree

$$\|f(x) - \sum_{j=0}^{M-1} c_j T_j(x)\| = \min . \quad (2.26)$$

The sum (2.26) contains M polynomials with highest degree $M-1$. Therefore, an economic way to represent arbitrary functions $f(x)$ will be to scan over coefficients c_j up to a selected order $j_{max} = M-1$ and then use (2.23). An ensemble of trajectories generated by this procedure are shown in the Fig. 2.4.

2.3.2 Sample Trajectories for $V(\phi) = \lambda\phi^n$

It is instructive to get an insight into the form of trajectory functions for simple often used monomial potentials of the form $V(\phi) = \lambda\phi^n$. Assuming slow roll one has approximately

$$\begin{aligned} \phi^2 - \phi_0^2 &= 2nM_p^2(N - N_0) , \quad \epsilon = \frac{n^2}{4n(N - N_0) + 2(\phi_0/M_p)^2} , \\ H &= \frac{1}{M_p} \sqrt{\frac{\lambda}{3}} (2nM_p^2(N - N_0) + \phi_0^2)^{\frac{n}{4}} , \end{aligned} \quad (2.27)$$

where for simplicity we use the number of e -folds as time-variable. Using (2.10), these trajectories for H and ϵ can be mapped into trajectories for $(\mathcal{P}_s, \mathcal{P}_t)$. As a specific example consider simple chaotic inflation $V(\phi) = \frac{m^2}{2}\phi^2$, $m = 5 \times 10^{-6} M_p$. We can decompose expression $(\mathcal{P}_s, \mathcal{P}_t)$ obtained through (2.27) in terms of Chebyshev polynomials and find the spectrum of coefficients c_n for this model, using a slight alternation of the series (2.23)

$$P_{S/T}(N) = \sum_{j=0}^{M-1} c_j^{S/T} T_j(x) - \frac{1}{2} c_0^{S/T}, \quad (2.28)$$

where $M - 1 = j_{\max}$ is the maximum order of Chebyshev polynomials in the decomposition. This formally “unconventional” normalization of c_0 is rather convenient in practical use, e.g. see the Chebyshev code in Numerical Recipes [60], as it leads to a proper normalization of the orthogonality relation of the Chebyshev polynomials.

The coefficients of decomposition (2.28) for the function (2.27) is shown in Fig. 2.3 together with coefficients of the trajectories for the model $V = \frac{\lambda}{4}\phi^2$, $\lambda = 10^{-13}$. We see that with the chosen definition (2.28) the values of the c_j s for smooth monotonically increasing trajectories $\mathcal{P}_s, \mathcal{P}_t$ gradually decrease with j . However, possible features in $\mathcal{P}_s, \mathcal{P}_t$ would still be reflected in features in the Chebyshev “spectrum” c_j .

Since both $\mathcal{P}_s, \mathcal{P}_t$ and the polynomials $T_j(x)$ are dimensionless, all coefficients c_j are also dimensionless. For a typical realization we see that zero-order coefficient c_0 of (2.28) is responsible for a constant elevation of the trajectory. The first order coefficient c_1 , as follows from (2.25), reflects the overall slope of the trajectory. Then c_2 is related to its curvature, and so on. The expansion (2.28) up to low orders M describes relatively smooth trajectories $\mathcal{P}_s, \mathcal{P}_t$, while increasing the order of the polynomial expansion allows to catch smaller and smaller features.

2.3.3 Creating Random Trajectories

In this subsection we discuss how to numerically generate an ensemble of trajectories like those shown in Fig. 2.4, using both methods mentioned at the end of the previous section. We note that from now on we change the normalization $\mathcal{P}_s, \mathcal{P}_t \rightarrow 10^{10}\mathcal{P}_s, 10^{10}\mathcal{P}_t$ such that for e.g. an expansion of $\mathcal{P}_s = 2 \times 10^{-9}$ to order 1 we have $c_0 = 40$.

In order to create a random trajectory, one can either pick random numbers for the coefficients c_j of the Chebyshev expansion of the trajectory function or the values of the trajectory function at nodal points of the Chebyshev expansion which are then converted to the coefficients in a second step. This will generally lead to a different prior distribution than choosing the coefficients directly as we will see later. After that the trajectory has to be tested for viability.

Sampling coefficients

We will first explore the case of choosing the coefficient of the expansion, which we call Chebyshev Polynomial method of a certain order for a chosen trajectory, for instance, “CP method

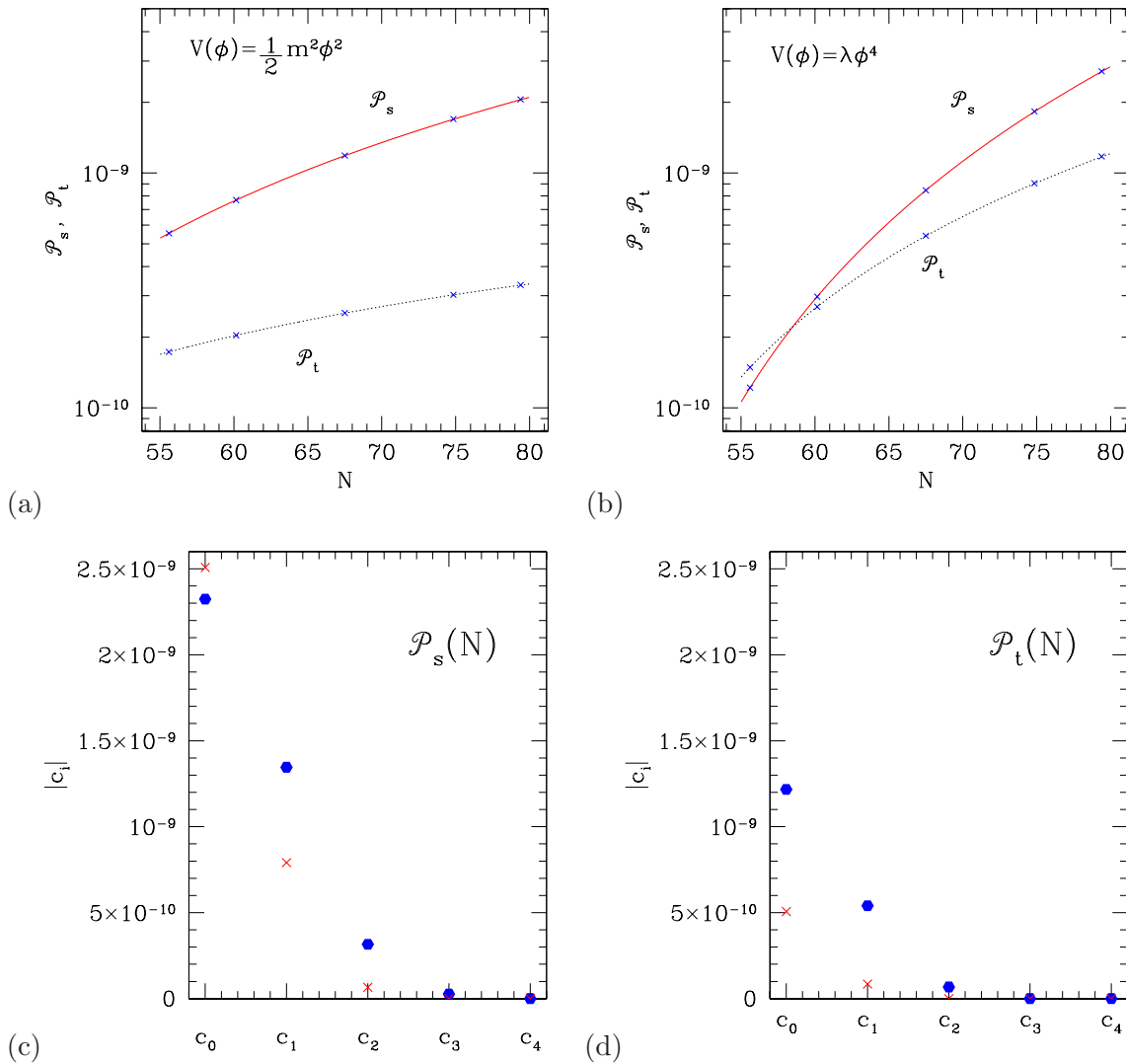


Figure 2.3: Chebyshev coefficients to order 5 each for the trajectories of \mathcal{P}_s , \mathcal{P}_t for (a) $V(\phi) = \frac{1}{2} m^2 \phi^2$ and (b) $V(\phi) = \lambda \phi^4$ of \mathcal{P}_s (solid line), \mathcal{P}_t (dotted line), with the positions of the nodal points indicated by blue crosses. The spectrum of coefficients is shown in (c) for $\mathcal{P}_s(N)$ and (d) for $\mathcal{P}_t(N)$ for $V(\phi) = \frac{m^2}{2} \phi^2$ (red crosses) and $V(\phi) = \lambda \phi^4$ (blue hexagons).

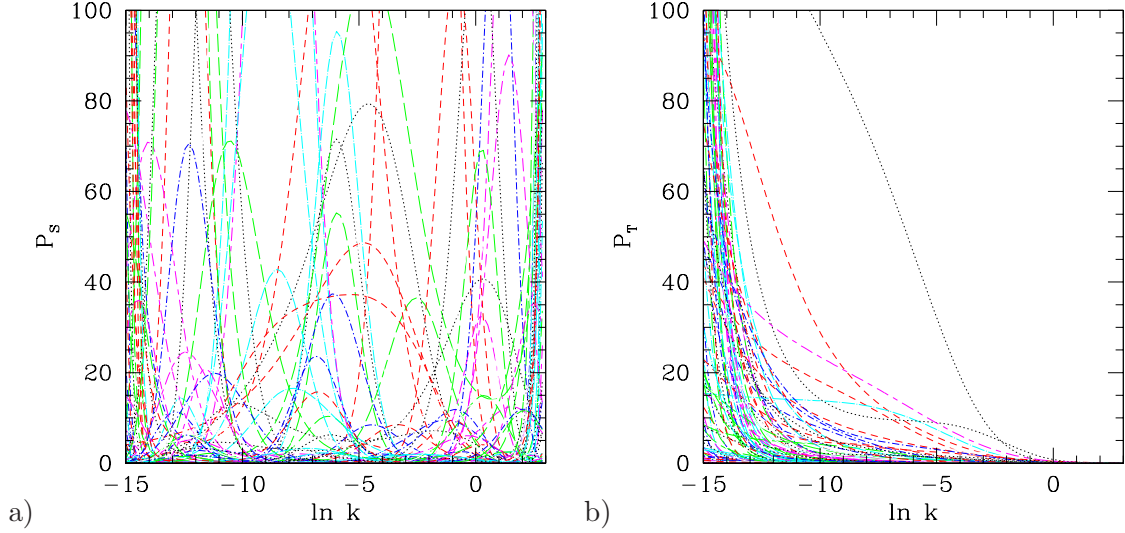


Figure 2.4: Ensemble of valid trajectories $\mathcal{P}_s, \mathcal{P}_t$ with a uniform prior on \mathcal{P}_s and a logarithmic prior and imposed monotonicity on \mathcal{P}_t .

to order 5 for $\mathcal{P}_s(N)$ ”, short “an order 5 expansion of \mathcal{P}_s ”, even shorter “ \mathcal{P}_s5 ”.

Generating pairs of trajectories $\mathcal{P}_s, \mathcal{P}_t$ by sampling the coefficients c_i is rather straightforward

1. draw $i_{\max} - 1$ random numbers $c_1, c_2, \dots, c_{i_{\max}-1}$ of the series (2.28) for \mathcal{P}_s ,
2. draw $j_{\max} - 1$ random numbers $c_1, c_2, \dots, c_{j_{\max}-1}$ of the series (2.28) for \mathcal{P}_t ,
3. optionally check for monotonicity of \mathcal{P}_t ,

producing trajectories that can easily be mapped to the classical observables (n_s, r, n_{run}) at a given pivot point N_* via

$$n_s = \frac{d\mathcal{P}_s}{d \ln k}, \quad n_{\text{run}} = \frac{d^2 \mathcal{P}_s}{d \ln k^2}, \quad r = \frac{\mathcal{P}_s}{\mathcal{P}_t}. \quad (2.29)$$

The expansion of $\ln \mathcal{P}_s$ to order 3 and $\ln \mathcal{P}_t$ to order 1 deserves special attention as this provides a smooth transition from traditional parametrization to the trajectory picture. Writing out the expansion explicitly,

$$\begin{aligned} \ln(\mathcal{P}_s)(\ln k) &= \frac{1}{2}c_0 + c_1 T_1(x) + c_2 T_2(x) \\ &= \frac{1}{2}c_0 + c_1 x + c_2 (2x^2 - 1) \\ &= \ln(A_s) + n_s \ln k + \frac{1}{2}n_{\text{run}}(\ln k)^2, \end{aligned} \quad (2.30)$$

where $x = \frac{1}{N_b - N_a} (2 \ln k - (N_b + N_a))$, it is obvious that there is a one-to-one correspondence between $c_0^{\mathcal{P}_t}, c_0^{\mathcal{P}_s}, c_1^{\mathcal{P}_s}, c_2^{\mathcal{P}_s}$ and $r, A_s, n_s, n_{\text{run}}$. In other words, the traditional parametrization

and $\ln \mathcal{P}_s3$, $\ln \mathcal{P}_t1$ sample the same space of inflationary models, albeit with slightly different priors on the parameters, especially the tensor scalar ration r .

Sampling values at nodal points

When using the CP method it is not easy to choose the ranges for the values of the coefficients to preferably create trajectories with a given amplitude of scalar and tensor perturbations in the $\ln k$ range of the traditional pivot points, i.e. around $k \approx 0.002\text{Mpc}^{-1}$ and $k = 0.05\text{Mpc}^{-1}$. When running Markov chains for MCMC parameter estimation, choosing the prior range of coefficients significantly wider than the posterior can considerably slow down convergence of the chains.

Therefore instead of choosing the CP coefficients c_j directly, we can choose the value of the trajectory functions at the nodal points of the Chebyshev transform. We will call this the ‘‘Chebyshev Polynomial Nodal Point’’ method, ‘‘CPNP’’, or short ‘‘choosing at nodal’’. Scanning the trajectories is then reduced to randomly generating the values of the trajectory at nodal points, with subsequent CP interpolation between them. This method provides significant flexibility with respect to specific choice of the trajectory functions. Indeed, for the \mathcal{P}_t trajectory we can generate random values PT_j and request that they are rank ordered with respect to the nodal points, and in this way guarantee monotonicity of $\mathcal{P}_t(x)$, thereby dropping the rejection rate to zero.

Suppose we want to find a polynomial expansion of an arbitrary function $f(x)$ which is *exact* at n points x_k ($k = 1, \dots, K$), that is the expansion

$$f_k \equiv f(x_k^M) = \sum_{j=0}^{M-1} c_j T_j(x_k^M), \quad (2.31)$$

which evaluates to the same values as the function $f(x)$ at points x_k , see Eq. (2.32). The position of the nodal points x_k^M depends on M , but we will drop the index M for transparency.

Finding c_j from (2.31) is actually a linear algebra problem, as is easily seen by introducing a $K \times M$ matrix $T_{kj} = T_j(x_k)$ of values of Chebyshev polynomials T_j at points x_k , and writing the sum (2.31) in vector notation $\mathbf{f} = T \cdot \mathbf{c}$. The necessary and sufficient condition for having a solution to this inhomogeneous system of linear equations is that $\text{rank } T = \text{rank } [T|\mathbf{f}]$, and the solution is unique if additionally $\text{rank } T = M$. In practice this means that (unless the matrices involved happen to be degenerate) the desired expansion can be found and is unique if the number of terms M in the expansion is the same as the number of points K . The coefficients of the expansion are then obtained from the vector of function values by a simple linear operation $\mathbf{c} = S \cdot \mathbf{f}$, where the matrix S is the inverse of the polynomial valued matrix $S = T^{-1}$.

Although one can construct a polynomial expansion which is exact on any set of points, what makes Chebyshev expansion special is the choice of points x_k which are zeroes of j -th

order Chebyshev polynomial $T_j(x)$

$$x_k^j = \cos \frac{\pi(k + \frac{1}{2})}{j} . \quad (2.32)$$

The points x_k^M are called *the nodal points* (we will frequently drop the index M for brevity). With this choice of points, the discrete orthogonality of Chebyshev polynomials comes into play

$$\sum_{k=1}^M T_i(x_k)T_j(x_k) = \begin{cases} 0 & , i \neq j \\ \frac{M}{2} & , i = j \neq 0 \\ M & , i = j = 0 \end{cases} \quad (2.33)$$

Applying (2.33) to (2.31), we get the coefficients of the Chebyshev expansions in the form

$$c_j = \frac{2}{M} \sum_{k=1}^M f(x_k)T_j(x_k) \quad (2.34)$$

(with $j = 0, \dots, M - 1$), which corresponds to the matrix S having components

$$S_{jk} = \frac{2}{M} \cos \frac{\pi(k - \frac{1}{2})j}{M} . \quad (2.35)$$

Thus, the relationship between the choice of coefficients of the Chebyshev expansion and the choice of function values at a set of points is a linear one, $\mathbf{c} = S \cdot \mathbf{f}$.

Having defined the matrix S_{jk} , it is instructive to examine some properties of the Chebyshev expansion of a trajectory $f(x)$ given the values $f_i \equiv f(x_i)$ of the trajectory at nodal points x_i . For this, we write

$$f(x) = \sum_{i,j} T_i(x)S_{ij}f_j \equiv \sum_i w_i(x)f_i . \quad (2.36)$$

where we introduced the *filter functions* $w_i(x) = T_j(x)S_{ji} = \frac{2}{M} \sum_j \cos \left(\frac{\pi j(i - \frac{1}{2})}{M} \right) T_j(x)$, plotted in Fig. 2.5. The function of order i is centered around the i^{th} nodal point x_i , denoted by the red “+” signs, and “feels out” away from this nodal point. The higher the order M of the Chebyshev expansion, the more localized each filter function, i.e. the influence of the f_i , becomes.

To summarize, we use the following procedure for generating random trajectories $\mathcal{P}_s, \mathcal{P}_t$ using the CPNP method

1. draw $i_{\max} - 1$ random values (PS_0, PS_1, PS_2, \dots) for \mathcal{P}_s ,
2. draw $j_{\max} - 1$ random values (PT_0, PT_1, PT_2, \dots) for \mathcal{P}_t
3. (optionally) sort them if monotonicity is desired

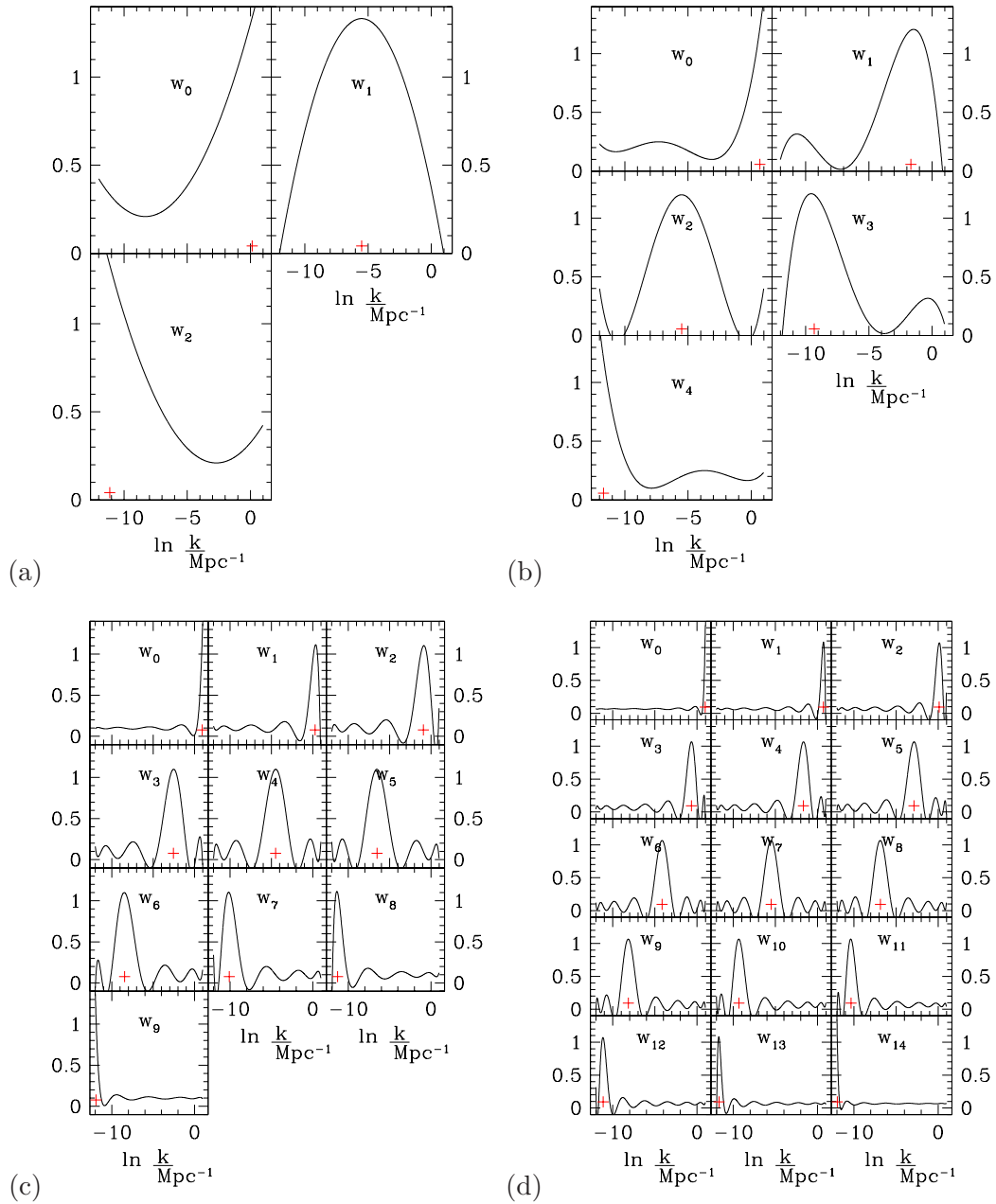


Figure 2.5: Filter functions $w_i(x)$ for the nodal point method at order M . The red “+” signs indicate the positions of the nodal point x_i . (a) $M = 3$, (b) $M = 5$, (c) $M = 10$, (d) $M = 15$. Note the degree of localization about the nodal points at high orders with non-trivial sidebands.

4. calculate Chebyshev expansion coefficients $\mathbf{c} = Q \cdot \mathbf{f}$

2.4 Trajectories and Traditional Observables

In this section we map the distribution of valid inflationary trajectories into the space of traditional observables. Traditionally the prior for inflationary models is that $V(\phi)$ is sufficiently smooth so that the slow roll parameters remain small in which case the scalar fluctuations have an only mildly broken scale invariant spectrum and can be parametrized by (n_s, n_{run}, r) . In the case of the CPNP method, the prior on the allowed trajectories is of a more complex nature depending on the details of the parametrization, manifesting itself in a non-uniform prior distribution in the $r - n_s$ plane.

2.4.1 Priors in the Space of Traditional Observables

First, we generate the ensemble of inflationary trajectories $\mathcal{P}_s, \mathcal{P}_t$ using the methods based on the Chebyshev decomposition described in Sec. 2.3. The nodal point method is numerically faster and offers more control over the details of the parametrization, so that below we mostly discuss the results obtained using the CPNP technique.

From a given ensemble $\mathcal{P}_s, \mathcal{P}_t$ we calculate the ensemble of points in the traditional space of observables (n_s, n_{run}, r) , evaluating the observables at the pivot point $k_\star = 0.002\text{Mpc}^{-1}$. The resulting scatter plot in the (r, n_s) plane is shown in Fig. 2.6. The green contours represent 1σ and 2σ likelihood contours of the CPNP method, and the 1σ and 2σ likelihood contours from CMB+LSS data are presented in yellow (see Sec. 2.5 for a description of the data sets used). Panel (a) shows $\ln \mathcal{P}_s$ to order 3, $\ln \mathcal{P}_t$ to order 1, panel (b) \mathcal{P}_s to order 3, \mathcal{P}_t to order 1, panel (c) $\ln \mathcal{P}_s$ to order 5, $\ln \mathcal{P}_t$ to order 5, and panel (d) shows \mathcal{P}_s to order 5, \mathcal{P}_t to order 5. When using the logarithmic expansion, the shape of the likelihood contours is fairly independent of the expansion order. In contrast to this, the distribution of observables varies significantly when using a linear expansion of $\mathcal{P}_s, \mathcal{P}_t$, owing to the fact that generically some trajectories have to be discarded as their interpolation produces values $\mathcal{P}_s < 0$ or $\mathcal{P}_t < 0$. In addition to this, the process of interpolating a function $f(x)$ will generally (heavily) modify the distribution of function values at different positions x , even in the case of linear interpolation.

2.4.2 Priors in Linear Interpolation

Naively one might expect that sampling uniformly a trajectory function at a number of nodal points in $\ln k$ and interpolating would also lead to a more or less uniform distribution of function values in between the sampled points. But this is only true for functions which do not have to fulfill any constraints. In case there are any restrictions on the functions, e.g. enforcing positivity of $\mathcal{P}_s, \mathcal{P}_t$, the prior will generally depend on the location in k -space, changing the picture dramatically. In case of constrained trajectory functions, the prior distribution becomes peaked away from zero despite being flat at nodal points. This can be understood in terms

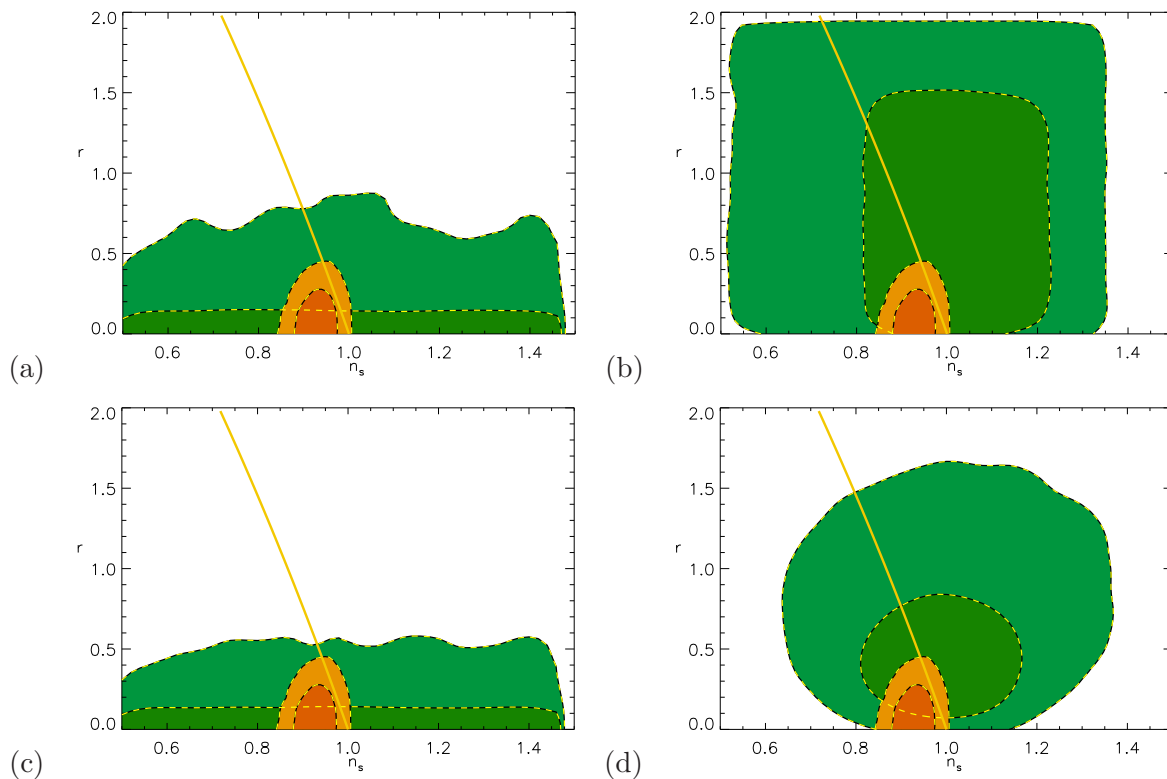


Figure 2.6: Prior distribution in $r - n_s$ space. The green shades are 1 and 2σ prior distributions for various choices of parametrization of the trajectories, the yellow shades show 68% and 95% contours of the current observational constraints from CMB+LSS data for a parametrization allowing for running of the spectral index. (a) $\ln \mathcal{P}_s$ to order 3, $\ln \mathcal{P}_t$ to order 1, (b) \mathcal{P}_s to order 3, \mathcal{P}_t to order 1, (c) $\ln \mathcal{P}_s$ to order 5, $\ln \mathcal{P}_t$ to order 5, (d) \mathcal{P}_s to order 5, \mathcal{P}_t to order 5. When using the logarithmic expansion, the distribution for the observables only varies mildly with the order of expansion. In contrast to this, the linear expansion results in a significantly different distribution. The solid yellow line shows the power law fix point with $n_s = 1 - \frac{2r}{16-r}$

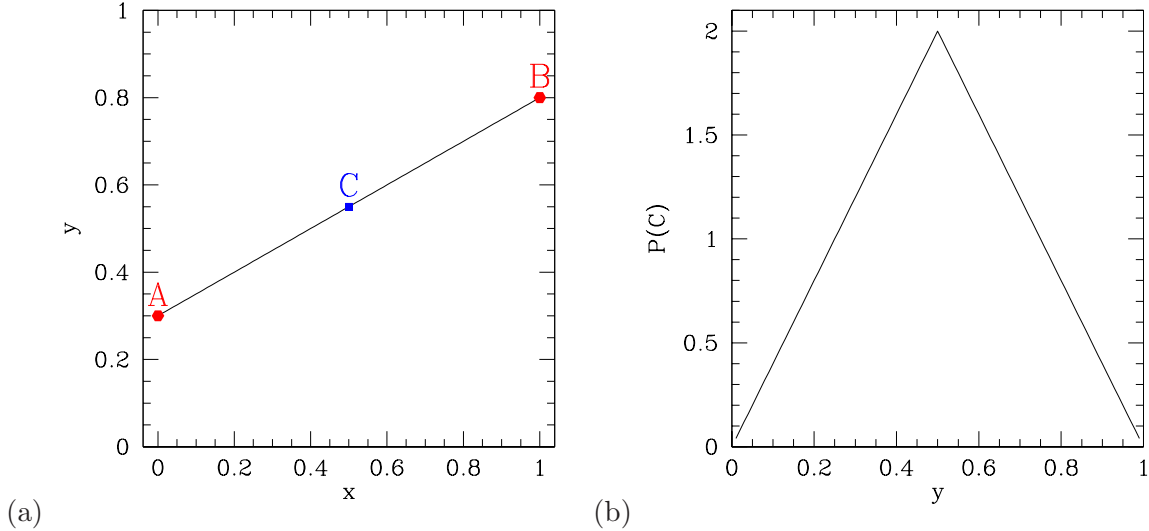


Figure 2.7: (a) Linear interpolation between two points A, B . A, B are drawn from $[0, 1]$ with uniform prior (b) The probability distribution of point C , located in the middle between A and B .

of a simple frequentist argument for example in a linear interpolation between two points $(A, y(A)), (B, y(B))$, denoted by the red dots in Fig. 2.7a. The vertical position of both points is chosen with a uniform prior $P(A) = P(B) = 1$, $(y(A), y(B)) \in [0, 1]$. For the value of $y(C)$ to be zero, both $y(A)$ and $y(B)$ have to be zero, whereas for say $y(C) = 0.5$, the pair $(y(A), y(B))$ can have values $(1.0, 0.0), (0.999, 0.001), \dots$, therefore it is much more likely for $y(C)$ to be 0.5 than to be zero.

Performing a more quantitative analysis of the situation, it is straightforward to calculate the prior distribution of the point $y(C)$ which is located in the midpoint between A and B ,

$$\begin{aligned}
 P(C) &= \int_0^1 dA \int_0^1 dB \delta(C - (A + (B - A)/2)) P(A)P(B) \\
 &= \begin{cases} 4(1 - C), & \frac{1}{2} < C \leq 1 \\ 4C, & 0 \leq C \leq \frac{1}{2} \end{cases}, \quad (2.37)
 \end{aligned}$$

to be shaped like a triangle, see Fig. 2.7(b). Using the Chebyshev expansion for interpolation, the prior distribution of trajectory functions in between nodal points therefore is not uniform either. This bias is responsible for the shift in the shape of the contours in Fig. 2.6(b), (d), changing the distribution to favor the tensor scalar ratio r at values larger than zero. The case of constant \mathcal{P}_t is more or less uniform in r direction (panel 2.6(b)), while the case of varying \mathcal{P}_t shows clearly the effect of the interpolation since the pivot point $k = 0.002\text{Mpc}^{-1}$ at which r is evacuated does not correspond to a nodal point at which the distribution would be uniform.

This effect can significantly alter the outcome of MCMC parameter reconstruction runs as we will see below. Most prominently it can lead to a spurious “detection” of tensors using the Chebyshev procedure as all trajectory functions \mathcal{P}_t related to the tensor-scalar ratio r are

constrained to be positive.

2.4.3 Opening the Space of Observables

We will now investigate how much of the model space is open and how the distribution of observables is to be interpreted. As mentioned previously, the question of an appropriate measure on the space of models is an ill-defined one at the moment. Even though the distribution of points is denser in some regions of the scatter plot than in others, this does not imply that some regions are favored by inflationary models while others are excluded and never reached. This can be seen in Fig. 2.6 where we plot the range of observables from the CPNP method using $((\ln)\mathcal{P}_s, (\ln)\mathcal{P}_t)$ to orders (3, 1) and (5, 5). The “allowed” space is varying significantly for the different choices.

In principle it is interesting to map all possible inflationary trajectories which are physically acceptable and cover the whole class of models where Eq. (2.14) are valid. Despite ambiguities in the density distribution of different parametrizations, it might be tempting to look for areas in the observable space (n_s, n_{run}, r) that cannot be reached by single field inflation models. Obviously, the borders are defined by the applicability of the slow roll approximation when calculating the observables. Each point in the observable space (n_s, n_{run}, r) can be mapped to the space of functions $\epsilon(N)$ (that can in principle be generated by the flow method) via its value and first and second derivatives $(\epsilon, \epsilon', \epsilon'')$ at the pivot point if the observables are calculated to second order in slow roll, i.e. including terms with ζ . But specifying ϵ and its first 2 derivatives (or more generally finitely many, say n derivatives) at one point does not uniquely specify the function $\epsilon(N)$ as one is always free to choose the value of the 3rd or generally $(n+1)^{\text{th}}$ derivative. So there is an infinite degeneracy between points in the observable space and the underlying inflationary model.

Now in principle this means that the space is only constrained by those points that are accessible when $0 < \epsilon < 1$. However in practice one is a bit more restricted in defining the area that is definitely accessible by inflationary models. The reason for this is that in order to make the mapping between observable and trajectory space, slow roll has to be valid. But let us stress that if slow roll is not valid at some points in observable space this only means that we cannot perform the mapping. By no means are these points excluded from being generated by valid inflationary models. It is just presently not possible to determine by which one.

2.5 Observational Constraints on Trajectory Space

As the precision and scope of cosmological observations increase the precision of the models being compared to the data will naturally have to increase and allow for more complexity. This move has already begun with the recent extension of the ‘basic’ parameter set to include deviations from simple power law spectra $P(k) \sim k^{n_s-1}$ in the form of a mild k -dependence parametrized by the parameter $n_{\text{run}} \equiv dn_s/d \ln k$. However a more general parametrization of

the shape of the initial power spectrum can be achieved with the techniques discussed above and we now introduce an initial attempt at constraining directly the Chebyshev coefficients of a generalized inflationary trajectory.

The advantage of such an approach is that we are not restricting ourselves to a particular model of inflation such as a choice of potential.

We have modified the publicly available `CAMB`¹[61] package to compute CMB angular power spectra and matter power spectra from initial perturbation spectra generated from m^{th} -order Chebyshev expansions of inflationary trajectories. In Sec. 2.6 we will give an overview over the various choices for trajectory functions and their advantages as well as disadvantages. Generally, the trajectory functions are chosen as functions of $\ln k$ as the power spectra are sampled in $\ln k$. This substitutes the paradigm of a power law spectrum of initial perturbations for both scalar and tensor modes. Thus the N Chebyshev coefficients take the place of the traditional parameters describing the initial perturbations such as the scalar and tensor spectral index n_s and n_t , the scalar amplitude A_s , the tensor/scalar ratio r , and any higher order spectral shape parameters such as the running of the scalar spectrum n_{run} .

The modified `CAMB` solver is inserted into the `COSMOMC`²[34] Markov Chain Monte Carlo (MCMC) parameter fitting package which is then set to sample the space of parameters.

Each Markov step in the chain draws a particular realization of the set of Chebyshev coefficients. If the resulting trajectory satisfies the conditions necessary for inflation in the observable interval, it is accepted and used in the computation of a C_ℓ spectrum from which a likelihood with respect to a combination of CMB and LSS data is computed. We use data sets from the following CMB experiments:

- Wilkinson Microwave Anisotropy Probe 3 data release [3, 58] (WMAP3) (see also the first year releases [62, 63])
- Cosmic Background Imager [64, 9] (CBI), $\ell \approx 400 \dots 3900$,
- Degree Angular Scale Interferometer [65] (DASI), $\ell \approx 140 - 800$,
- Millimeter Anisotropy eXperiment IMaging Array, [6] (MAXIMA), $\ell \approx 40 \dots 1000$,
- Very Small Array [10] (VSA), $\ell \approx 150 \dots 1400$,
- Balloon Observations Of Milimetric Extragalactic Radiation And Geophysics [7] (BOOMERAnG), $\ell \approx 80 \dots 1400$,
- Arcminute Cosmology Bolometer Array Receiver [66, 8] (ACBAR), $\ell \approx 350 \dots 2600$,

and from the Large Scale Structure (LSS) surveys

- Sloan Digital Sky Survey [4] (SDSS), $k/h \approx 0.015 \dots 0.3 \text{Mpc}^{-1}$,

¹<http://cosmologist.info/camb/>

²<http://cosmologist.info/cosmomc/>

- Two Degree Field Galaxy Redshift Survey [5] (2dFGRS), $k/h \approx 0.022 \dots 0.185 \text{Mpc}^{-1}$,

A typical run consists of 8 chains each with random initial positions in the full parameter space which consists of the Chebyshev coefficients and the remaining standard physical parameters. These consist of $\Omega_b h^2$, and $\Omega_c h^2$, the physical baryon and cold dark matter densities, the parameter θ describing the ratio of sound horizon at last scattering to the angular diameter distance to the last scattering surface, and the optical depth to last scattering τ . A standard set of external priors is assumed, these include an allowed range for the Hubble constant $40 \leq H_0 \leq 90 \text{ km s}^{-1} \text{Mpc}^{-1}$ and a minimum age constraint of 10 Gyrs. We also consider only flat models where $\Omega_{\text{tot}} = 1$.

In Table 2.1 we show the marginalized values for sampled parameters obtained from a combination of 8 chains from a run with trajectories expanded up to third order in \mathcal{P}_s and first order in \mathcal{P}_t . The total number of accepted samples in the chains was 48390 and the initial half was discarded to allow for burn-in of the Markov sampling and for automatic updating of the proposal density. The chains achieved a Gelman Rubin eigenvalue of $R - 1 \leq 0.07$ before they were considered converged.

For each sample of the Markov chains we can also re-derive the standard spectral parameters in order to compare with conventional parameter fits. In practice this is done by choosing a pivot scale at which the scalar spectral index n_s , ratio r and scalar running $dn_s/d \ln k$ are calculated using the first order slow-roll expansion. We choose a pivot scale of $k_\star = 0.05 \text{Mpc}^{-1}$ and assume the tensor mode spectral index is fixed by the tensor scalar ratio through $n_t = -r/8$.

Besides the parameters describing the primordial power spectra, we vary the parameters $\Omega_b h^2$ (baryon density), $\Omega_c h^2$ (dark matter density), θ ($100 \times$ the ratio of the sound horizon to the angular diameter distance) and τ (optical depth to the last scattering surface), where $h = H_0/100 \frac{\text{km}}{\text{sec}} \times \text{Mpc}$

Table 2.1 also shows the marginalized distributions for a number of derived parameters: $\Omega_m = \Omega_b + \Omega_c$ (total matter density), Ω_Λ (dark energy density, computed from the imposed constraint $\Omega_m + \Omega_\Lambda = \Omega_{\text{tot}} = 1$), σ_8 (scalar power on scales $k = 8h^{-1} \text{Mpc}$), z_{re} (redshift to reionization) and H_0 (Hubble parameter today).

Having obtained constraints on the space of allowed inflationary trajectories from the data we compare them with the results of the standard parametrization (Fig. 2.8) and find them in good agreement. In the following sections we will first investigate some issues with priors that are common to all different choices of parametrizations, and then demonstrate explicitly the impact priors do have on parameter estimation, especially on the ratio of tensor to scalar perturbations.

We denote the values of the trajectory coefficients by $c_i^{\mathcal{P}_s}, c_i^{\mathcal{P}_t}$, i.e. when sampling the coefficients as described in Sec. 2.3.3, and the values of the trajectories at the nodal points by PS_i, PT_i , i.e. when sampling the values at nodal points as described in Sec. 2.3.3.

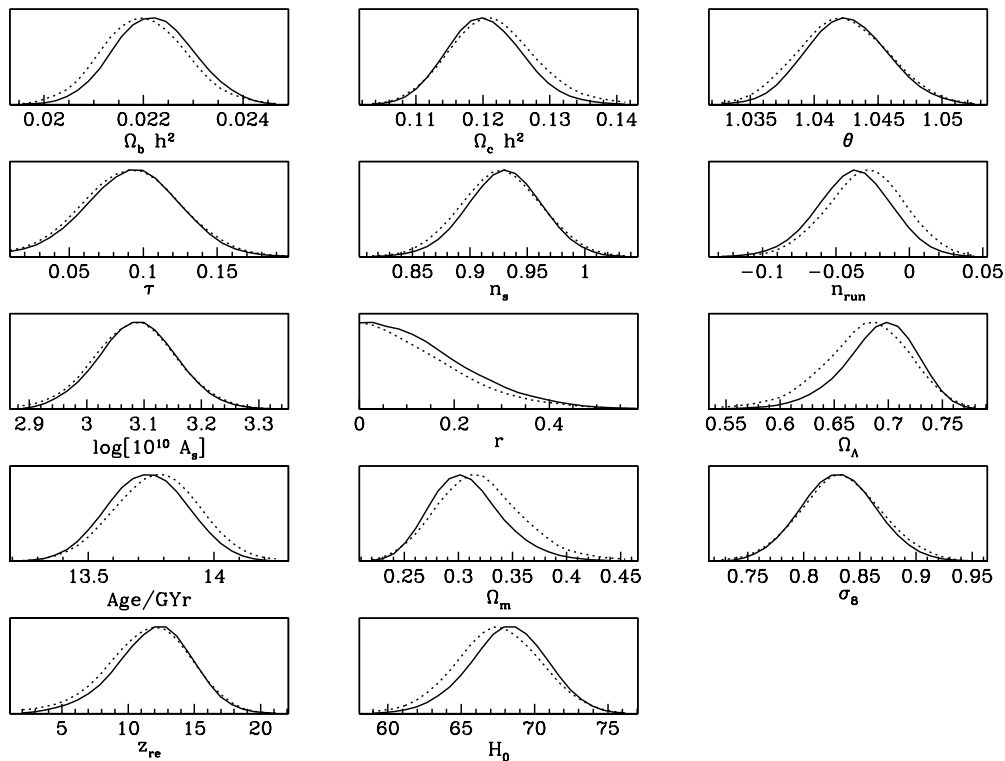


Figure 2.8: 1D posterior distribution of the cosmological parameters in the standard parametrization. $\Omega_b h^2$ is the baryon density, $\Omega_c h^2$ is the dark matter density, θ is $100\times$ the ratio of the sound horizon to the angular diameter distance, τ is the optical depth to the last scattering surface, Ω_Λ is the dark energy density (coming from the imposed constraint $\Omega_{\text{tot}} = 1$), $\Omega_m = \Omega_b + \Omega_c$ is the total matter density, σ_8 is the power on scales $k = 8h^{-1}\text{Mpc}$, z_{re} is the redshift of reionization, H_0 is the value of the Hubble parameter today.

Parameter	standard	$\ln \mathcal{P}_s, \ln \mathcal{P}_t$	$\ln \mathcal{P}_s, \mathcal{P}_t$
$\Omega_b h^2$	$0.0222^{+0.00078}_{-0.00077}$	$0.02183^{+0.00075}_{-0.00076}$	$0.02215^{+0.00078}_{-0.00075}$
$\Omega_c h^2$	$0.1205^{+0.0054}_{-0.0054}$	$0.1231^{+0.0063}_{-0.0062}$	$0.1221^{+0.0062}_{-0.006}$
θ	$1.0426^{+0.0031}_{-0.0031}$	$1.0419^{+0.0031}_{-0.003}$	$1.0428^{+0.0032}_{-0.0032}$
τ	$0.093^{+0.014}_{-0.014}$	$0.089^{+0.03}_{-0.031}$	$0.094^{+0.03}_{-0.03}$
$c_0^{\mathcal{P}_s}$	–	$2.33^{+0.41}_{-0.39}$	$2.29^{+0.4}_{-0.43}$
$c_1^{\mathcal{P}_s}$	–	$3.187^{+0.052}_{-0.053}$	$3.14^{+0.068}_{-0.067}$
$c_2^{\mathcal{P}_s}$	–	2.1^{+1}_{-1}	$1.6^{+1.2}_{-1.2}$
$c_0^{\mathcal{P}_t}$	–	$-9.58^{+3.6}_{-0.42}$	$2.93^{+0.86}_{-2.9}$
n_s	$0.93^{+0.031}_{-0.031}$	$0.919^{+0.034}_{-0.033}$	$0.926^{+0.034}_{-0.034}$
n_{run}	$-0.038^{+0.024}_{-0.024}$	$-0.031^{+0.024}_{-0.024}$	$-0.04^{+0.025}_{-0.026}$
$\ln[A_s]$	$-19.937^{+0.065}_{-0.065}$	$-19.942^{+0.066}_{-0.066}$	$-19.929^{+0.066}_{-0.069}$
r	$< 0.36(95\%CL)$	$< 0.044(95\%CL)$	$< 0.33(95\%CL)$
Ω_Λ	$0.691^{+0.032}_{-0.032}$	$0.672^{+0.039}_{-0.039}$	$0.682^{+0.037}_{-0.037}$
Age/GYr	$13.74^{+0.15}_{-0.16}$	$13.81^{+0.16}_{-0.16}$	$13.74^{+0.16}_{-0.16}$
Ω_m	$0.309^{+0.032}_{-0.032}$	$0.328^{+0.039}_{-0.039}$	$0.318^{+0.037}_{-0.037}$
σ_8	$0.831^{+0.032}_{-0.032}$	$0.836^{+0.032}_{-0.033}$	$0.839^{+0.033}_{-0.032}$
z_{re}	$11.9^{+2.8}_{-2.8}$	$11.7^{+2.9}_{-2.8}$	$12^{+2.7}_{-2.7}$
H_0	$68.2^{+2.5}_{-2.5}$	$66.7^{+2.8}_{-2.7}$	$67.7^{+2.8}_{-2.8}$

Table 2.1: Cosmological parameters for the standard parametrization compared with equivalent $\ln \mathcal{P}_s$, $(\ln) \mathcal{P}_t$ trajectories. $\Omega_b h^2$ is the baryon density, $\Omega_c h^2$ is the dark matter density, θ is $100 \times$ the ratio of the sound horizon to the angular diameter distance, τ is the optical depth to the last scattering surface, Ω_Λ is the dark energy density (coming from the imposed constraint $\Omega_{\text{tot}} = 1$), $\Omega_m = \Omega_b + \Omega_c$ is the total matter density, σ_8 is the power on scales $k = 8h^{-1} \text{Mpc}$, z_{re} is the redshift of reionization, H_0 is the value of the Hubble parameter today. The parameters are in good agreement, with the upper limit for the tensor scalar ratio r strongly depending on the prior.

2.6 Reconstructing the Primordial Power Spectra from Simulated Data Sets

In this section we gauge the potential performance of the different trajectory choices by reconstructing the shapes of known primordial spectra. The corresponding simulated C_ℓ 's include various levels of experimental noise, the noise levels expected of the upcoming Planck and CMBPol satellite experiments

We create simulated $C_\ell^{TT,TE,EE,BB}$ spectra using CAMB, optionally noise C_ℓ^{noise} to the simulated spectrum C_ℓ^{sim} by

$$C_\ell^{\text{obs}} = C_\ell^{\text{sim}} + C_\ell^{\text{noise}} , \quad (2.38)$$

and calculate the χ^2 via

$$\chi^2 = \sum_{\ell,i} \chi_i^2(\ell) \quad , \quad \chi_i^2(\ell) = f_{\text{sky}}(2\ell + 1) \left(\frac{C_i^{\text{obs}}(\ell)}{C_i^{\text{th}}(\ell)} - 1 + \ln \left(\frac{C_i^{\text{th}}(\ell)}{C_i^{\text{obs}}(\ell)} \right) \right) , \quad (2.39)$$

where $i \in \{TT, TE, EE, BB\}$ and f_{sky} is the fraction of the sky covered by observations (which we assume to be all sky). In order to simulate experimental noise we use a program written by A. Lewis that takes as input parameters the noise variance in μK^2 , the full width half maximum (FWHM) of the detector's beam in arc minutes and makes the simplified assumption that the noise in polarization is a factor of 2 larger than the noise in the temperature measurements. The noise in the C_ℓ 's is then calculated according to

$$C_\ell^{\text{noise}} = N e^{\ell(\ell+1)\sigma_\theta^2} , \quad (2.40)$$

where N is the noise variance, $\sigma_\theta = \frac{\theta\pi}{180\sqrt{8\ln 2}}$, and θ the beam FWHM in arc minutes.

2.6.1 Cosmic Variance Limited Experiments

In the first instance it seems tempting to simulate a cosmic variance limited experiment without any additional noise terms. However it turns out that in this case, the deviation in the high- ℓ BB measurements quickly come to dominate the total χ^2 , see Fig. 2.9. In contrast to this, the B-modes are getting very hard to measure as their amplitude drops dramatically and the effect of lensing begins to dominate for $\ell \gtrsim 200$. These in practice undetectable true modes give most of the contribution to the χ^2 make it very hard for the chains to find the proper extremum of the likelihood, leading to extremely slow convergence. In order to speed up convergence and to make the simulated data sets at least in principle obtainable we include noise in simulating an now ‘‘almost perfect experiment’’, while still ignoring lensing for computational speed reasons.

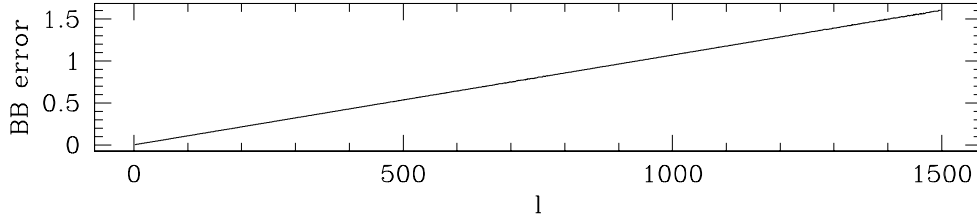


Figure 2.9: Contribution to the total χ^2 ℓ by ℓ for BB. Shown is the relative error between C_ℓ 's that were created with a 10% difference in the scalar tensor ratio. The amount contribution is growing with ℓ , just as one might expect. Note that this not taking into account the effects of lensing.

2.6.2 Planck and CMBPol Noise

Of great interest is the ability of present and future CMB experiments to detect primordial gravitational waves. While Planck is going to offer somewhat improved measurements of B-modes over WMAP, the upcoming CMBPol experiment will allow for the B-modes to be measured with excellent accuracy. However we do not investigate the discriminatory power of both Planck and CMBPol to detect the presence of a tensor component of the primordial power spectra but use their noise levels to demonstrate the influence of priors.

In order to simulate the experimental noise we make use of Eq. (2.40) with values for the noise variance and FWHM taken from the following table

Parameter	WMAP	Planck	CMBPol
Noise variance/ μK^2	3×10^{-2}	3×10^{-4}	1.7×10^{-6}
FWHM/ arcmin	13	7	7

where the noise variance for CMBPol was estimated by asserting that the experimental noise should equal the lensing signal in BB at about $\ell \approx 200$. Creating the simulated spectrum with the standard parametrization, the parameters $\Omega_b h^2, \Omega_c h^2, H_0, \tau, A_s, n_s, n_{\text{run}}$ for the initial data sets are set to the best fit values of [8], see Tab. 2.2. In order to gauge the ability of the different parametrizations to recover the presence of tensors, we vary the value of the tensor scalar ratio r from 0...0.5.

In order to speed up the reconstruction process, we only vary the parameters describing the primordial power spectra and keep the “late time” parameters fixed to their initial values. The simulated spectra are reconstructed remarkably well. Using the standard parametrization, the initial values are well reconstructed for simulated spectra with $r = 0.01$ and $r = 0.1$, the error bars being quite smaller in the simulations with CMBPol noise compared to the case of Planck noise, especially for r , see Table 2.3. When reconstructing the simulated spectra with using $\ln \mathcal{P}_s, \ln \mathcal{P}_t$ to order 5, each with uniform prior on $\ln \mathcal{P}_s, \ln \mathcal{P}_t$, the effect of the effective imposed prior on r can be clearly seen, c.f. Table 2.4. As the sampling with a uniform prior in $\ln \mathcal{P}_t$ heavily favors small values of \mathcal{P}_t , the reconstructed values for r are all systematically lower than the input values. Going to a uniform prior on $\mathcal{P}_s, \mathcal{P}_t$ instead, the effect of finding

(a)	Parameter	Value	(b)	standard_ns_nrun_r	
	$\Omega_b h^2$	0.0226	A_s	2.15×10^{-9}	
	$\Omega_c h^2$	0.115	n_s	0.96	
	H_0	70.4	n_{run}	-0.0551	
	τ	0.09	r	varying	

(c)	Parametrization	Parameters
	standard_ns_nrun_r	(A_s, n_s, n_{run}, r)
	$\ln \mathcal{P}_s$ order m , $\ln \mathcal{P}_t$ order n	$\ln PS_i, \ln PG_j$, with $i, j \in [0, n/m - 1]$
	\mathcal{P}_s order m , \mathcal{P}_t order n	PS_i, PG_j , $(i, j) \in [0, n - 1; 0, m - 1]$

Table 2.2: (a) and (b)Cosmological parameters of the simulated spectra. The values in a) are taken from [8]. The parameters of the primordial power spectra are depending on the chosen parametrization and are listed separately. c) Parametrizations used for reconstruction. If not indicated otherwise, the parameters listed are the values at nodal points. When sampling the coefficients instead of the values at the nodal points we will explicitly indicate it.

(a)	Initial	Planck	CMBPol
$\ln[A_s]$	-19.9678	$-19.951^{+0.036}_{-0.036}$	$-19.945^{+0.022}_{-0.021}$
n_s	0.96	$0.9593^{+0.0021}_{-0.0022}$	$0.9591^{+0.0012}_{-0.0012}$
n_{run}	-0.0551	$-0.0564^{+0.0047}_{-0.0047}$	$-0.0559^{+0.0025}_{-0.0024}$
r	0.01	$< 0.048(95\%CL)$	$0.01002^{+0.00062}_{-0.00062}$

(b)	Initial	Planck	CMBPol
$\ln[A_s]$	-19.9678	$-19.951^{+0.035}_{-0.035}$	$-19.945^{+0.023}_{-0.023}$
n_s	0.96	$0.9593^{+0.002}_{-0.002}$	$0.959^{+0.0013}_{-0.0013}$
n_{run}	-0.0551	$-0.0562^{+0.0048}_{-0.0049}$	$-0.0559^{+0.0025}_{-0.0025}$
r	0.1	$0.108^{+0.012}_{-0.016}$	$0.10005^{+0.00077}_{-0.00082}$

Table 2.3: Reconstruction of a simulated spectrum with the parameters for the primordial power spectra taken from [8] in column 2, the reconstructed values using Planck's/ CMBPol's projected noise in column 3 and 4 respectively. The simulated spectrum was created using the standard parametrization and the reconstruction used the standard parametrization (a) for $r = 0.01$ (b) for $r = 0.1$.

(a) Parameter	Initial	uniform prior on $\ln \mathcal{P}_s, \ln \mathcal{P}_t$		uniform prior on $\mathcal{P}_s, \mathcal{P}_t$	
		Planck	CMBPol	Planck	CMBPol
$\ln[PS_0]$	–	$1.91^{+0.97}_{-0.98}$	$2.01^{+0.61}_{-0.63}$	$3.5^{+0.88}_{-0.82}$	$2.83^{+0.35}_{-0.34}$
$\ln[PS_1]$	–	$2.825^{+0.049}_{-0.049}$	$2.829^{+0.022}_{-0.023}$	$2.903^{+0.052}_{-0.051}$	$2.858^{+0.017}_{-0.017}$
$\ln[PS_2]$	–	$2.943^{+0.027}_{-0.028}$	$2.94^{+0.018}_{-0.018}$	$2.911^{+0.038}_{-0.038}$	$2.936^{+0.018}_{-0.018}$
$\ln[PS_3]$	–	$1.5^{+1.4}_{-1.4}$	$1.6^{+1.4}_{-1.3}$	$2.72^{+0.71}_{-0.71}$	$3.22^{+0.46}_{-0.48}$
$\ln[PS_4]$	–	$-0.3^{+10}_{-9.7}$	$0.4^{+9.6}_{-10}$	$6.82^{+3.2}_{-0.7}$	$7.57^{+2.4}_{-0.49}$
$\ln[PT_0]$	–	$-7.9^{+1.9}_{-2.1}$	$-6.5^{+1}_{-3.5}$	$-3.4^{+1.4}_{-1.4}$	$-2.9^{+0.73}_{-0.74}$
$\ln[PT_1]$	–	$-5.3^{+1.8}_{-1.8}$	$-2.91^{+0.67}_{-0.63}$	$-2.1^{+1.1}_{-1.1}$	$-2.01^{+0.28}_{-0.27}$
$\ln[PT_2]$	–	$-3.2^{+1.7}_{-1.8}$	$-1.475^{+0.077}_{-0.075}$	$-1.03^{+0.87}_{-0.89}$	$-1.489^{+0.071}_{-0.068}$
$\ln[PT_3]$	–	0.3^{+2}_{-2}	$0.16^{+0.76}_{-0.81}$	$2^{+1.3}_{-1.2}$	$0.63^{+0.78}_{-0.83}$
$\ln[PT_4]$	–	$5^{+5}_{-1.5}$	$4.7^{+5.3}_{-1.9}$	$6.65^{+3.4}_{-0.98}$	$6.2^{+3.8}_{-1.1}$
n_s	0.96	$0.9595^{+0.0036}_{-0.0036}$	$0.959^{+0.0024}_{-0.0023}$	$0.9549^{+0.0043}_{-0.0044}$	$0.957^{+0.0022}_{-0.0022}$
n_{run}	-0.0551	$-0.0558^{+0.0065}_{-0.0067}$	$-0.0561^{+0.0034}_{-0.0033}$	$-0.0517^{+0.0084}_{-0.0086}$	$-0.0578^{+0.0028}_{-0.0028}$
$\ln[A_s]$	-19.9578	$-19.958^{+0.0017}_{-0.0017}$	$-19.9577^{+0.0012}_{-0.0011}$	$-19.9583^{+0.0023}_{-0.0023}$	$-19.9572^{+0.0011}_{-0.001}$
r	0.01	$< 0.0088(95\%CL)$	$0.0072^{+0.0014}_{-0.0015}$	$< 0.042(95\%CL)$	$0.00868^{+0.00092}_{-0.00092}$

(b) Parameter	Initial	uniform prior on $\ln \mathcal{P}_s, \ln \mathcal{P}_t$		uniform prior on $\mathcal{P}_s, \mathcal{P}_t$	
		Planck	CMBPol	Planck	CMBPol
$\ln[PS_0]$	–	$1.79^{+0.94}_{-0.94}$	$1.98^{+0.6}_{-0.61}$	$3.38^{+1}_{-0.99}$	$2.82^{+0.37}_{-0.37}$
$\ln[PS_1]$	–	$2.821^{+0.048}_{-0.046}$	$2.828^{+0.023}_{-0.023}$	$2.898^{+0.06}_{-0.059}$	$2.858^{+0.017}_{-0.018}$
$\ln[PS_2]$	–	$2.953^{+0.031}_{-0.031}$	$2.938^{+0.02}_{-0.019}$	$2.916^{+0.047}_{-0.047}$	$2.933^{+0.02}_{-0.02}$
$\ln[PS_3]$	–	$1.5^{+1.4}_{-1.4}$	$1.5^{+1.4}_{-1.5}$	$2.51^{+0.87}_{-0.87}$	$3.12^{+0.54}_{-0.55}$
$\ln[PS_4]$	–	$-0.6^{+11}_{-9.4}$	$-0.3^{+10}_{-9.7}$	$5.81^{+4.2}_{-0.91}$	$7.22^{+2.8}_{-0.46}$
$\ln[PT_0]$	–	$-6.4^{+2.8}_{-3.6}$	$-4.2^{+1.7}_{-5.8}$	$-2.3^{+1.6}_{-1.5}$	$-0.33^{+0.61}_{-0.62}$
$\ln[PT_1]$	–	$-2.4^{+1.5}_{-1.6}$	$-0.26^{+0.56}_{-0.57}$	$-0.71^{+0.95}_{-0.94}$	$0.44^{+0.19}_{-0.19}$
$\ln[PT_2]$	–	$0.24^{+0.53}_{-0.53}$	$0.817^{+0.033}_{-0.033}$	$0.56^{+0.54}_{-0.58}$	$0.817^{+0.034}_{-0.034}$
$\ln[PT_3]$	–	$2.9^{+1.2}_{-1.2}$	$2.47^{+0.7}_{-0.71}$	$3.3^{+1.2}_{-1.1}$	$2.47^{+0.63}_{-0.69}$
$\ln[PT_4]$	–	$6.6^{+3.4}_{-1.1}$	$6.1^{+3.9}_{-1.3}$	$7.09^{+2.9}_{-0.89}$	$6.75^{+3.2}_{-0.99}$
n_s	0.96	$0.9595^{+0.0035}_{-0.0035}$	$0.9591^{+0.0024}_{-0.0024}$	$0.9548^{+0.0051}_{-0.0052}$	$0.957^{+0.0023}_{-0.0023}$
n_{run}	-0.0551	$-0.055^{+0.0066}_{-0.0065}$	$-0.056^{+0.0034}_{-0.0034}$	$-0.0511^{+0.0094}_{-0.0095}$	$-0.0578^{+0.0028}_{-0.0029}$
$\ln[A_s]$	-19.9578	$-19.958^{+0.0016}_{-0.0017}$	$-19.9577^{+0.0011}_{-0.0011}$	$-19.9582^{+0.0028}_{-0.0026}$	$-19.9572^{+0.0011}_{-0.001}$
r	0.1	$< 0.077(95\%CL)$	$0.0852^{+0.0081}_{-0.008}$	$< 0.13(95\%CL)$	$0.0925^{+0.0047}_{-0.0047}$

Table 2.4: Reconstruction of simulated spectra with Planck and CMBPol noise using the parametrization $\ln \mathcal{P}_s, \ln \mathcal{P}_t$ to order 5 each with uniform priors on $\ln \mathcal{P}_s, \ln \mathcal{P}_t$. The recovered values of r are systematically lower than the input values owing to the fact that sampling in $\ln \mathcal{P}_t$ imposes a prior that greatly prefers small values of ϵ . (a) $r = 0.01$ (b) $r = 0.1$.

lower values of r is still present but less pronounced, underlining the influence of priors on the results.

While demonstrating the effectiveness of the trajectory method and also serving as a double check against errors in the programming, these results should not be taken as predictions for the data quality to be reached by Planck or CMBPol as we ignored lensing effects that pollute the B-modes and only varied the parameters of the primordial power spectra during the MCMC runs, keeping the “late time” parameters fixed to their initial values.

2.7 Reconstructing the Primordial Power Spectra from Real Data Sets

In this section we elaborate on the various parametrizations that can be used as trajectory functions. Although intuitively the most unbiased choice for a trajectory is to use $\mathcal{P}_s, \mathcal{P}_t$ and sample its values at nodal points, it turns out that for expansion orders greater or equal 2 of \mathcal{P}_t this choice implicitly imposes a prior on the tensor scalar ratio r , constraining it to be larger than zero almost everywhere despite a uniform prior distribution at the nodal points, see Sec. 2.4 for a discussion. We propose various methods of correctly taking this issue of priors into account, highlighting the advantages and disadvantages of each parametrization.

2.7.1 Sampling with a uniform prior in $\ln \mathcal{P}_s, \ln \mathcal{P}_t$

The perhaps simplest parametrization is expanding $\mathcal{P}_s, \mathcal{P}_t$ in Chebyshev polynomials up to a certain order independently of each other. Sampling the coefficients of the expansion of $\ln(\mathcal{P}_s)$ to order 3 and $\ln(\mathcal{P}_t)$ to order 1 in Chebyshev polynomials is equivalent to the standard parametrization with $A_s, r, n_s, n_{\text{run}}$, albeit with a slightly different prior on r , see Section 2.3.3. The results for the MCMC parameter estimation runs in good agreement with each other, see Tab. 2.1. Only the upper limit on the tensor scalar ratio r is heavily dependent on the prior imposed by the parametrization, with the logarithmic prior suppressing r considerably.

2.7.2 Sampling with a uniform prior in $\ln \mathcal{P}_s, \mathcal{P}_t$

The influence of priors on r is seen dramatically when expanding \mathcal{P}_t instead of $\ln(\mathcal{P}_t)$. In this case, the bounds on r are much weaker, allowing for r to be $\lesssim 0.17$ at 1σ , see Table 2.1. Changing the variable in which to sample from linear to logarithmic is equivalent to sampling with a logarithmic prior on \mathcal{P}_t

$$\prod_{i=0}^{N-1} P(\ln PT_i) d \ln PT_i = \prod_{i=0}^{N-1} P(\ln PT_i) \frac{d PT_i}{PT_i} \stackrel{!}{=} \prod_{i=0}^{N-1} P(PT_i) dPT_i \Rightarrow P(PT_i) = \frac{P(\ln PT_i)}{PT_i}. \quad (2.41)$$

In other words, sampling from $\ln PT_i$ uniformly at the nodal points, $P(\ln PT_i) = 1$, is equivalent to sampling PT_i at nodal points with a logarithmic prior, $P(PT_i) = \frac{1}{PT_i}$, favoring smaller values

for PT_i . While this suppresses the value of \mathcal{P}_t , the value of \mathcal{P}_s is determined rather well by the data, so that as a result the tensor-scalar ratio is also suppressed, leading to the difference in the constraint on r between sampling $\ln \mathcal{P}_t$ and \mathcal{P}_t , see Tab. 2.1.

2.7.3 Sampling with a uniform prior on $\mathcal{P}_s, \mathcal{P}_t$

Increasing the allowed complexity by expanding $\mathcal{P}_s, \mathcal{P}_t$ to order 5 each and sampling the trajectory values at nodal points, we now investigate the effect of more degrees of freedom on the reconstruction.

As shown in Fig. 2.10(d), some of the parameters PS_i, PT_i of the primordial spectra are not very well constrained. This is due to the fact that observational data of sufficient quality is not available over the full k -range. Observations stretch from about largest scales around $k \approx 10^{-4} \text{Mpc}^{-1}$ with large error bars due to cosmic variance to small scales of about $k \approx 0.1 \text{Mpc}^{-1}$ from measurements of Large Scale Structure.

It is surprising that increasing the order of the $(\mathcal{P}_s, \mathcal{P}_t)$ expansion from $(3, 1)$ to $(5, 5)$ has a huge impact on the tensor scalar ratio r , which now is found to be constrained away from zero at more than 3σ while still producing an angular power spectrum that fits the data remarkably well, c.f. Fig. 2.10(b). The upturn of the tensors towards lower k is compensated for by a downturn of scalar power (see Fig. 2.10(a)), giving the correct resulting amplitude for the TT C_ℓ 's.

Although quite exciting, this spurious detection of a non-zero tensor-scalar ratio is just driven by the chosen priors, c.f. Sec. 2.4. \mathcal{P}_t must be positive $\mathcal{P}_t > 0$ with a negative slope $\frac{d\mathcal{P}_t}{d \ln k} < 0$ because Hubble is a decreasing function of time. This implies that even though the values of \mathcal{P}_t at the nodal points are sampled with a uniform prior, the prior distribution of \mathcal{P}_t on and especially in between nodal points is rather complex and peaked at a value larger than zero, see Fig. 2.11. Panel (a) of this figure shows the prior probability distribution of a non monotonic \mathcal{P}_t trajectory to order 5 at a nodal point (black solid curve) and in between nodal points (red dashed curve). At the nodal point, the distribution should ideally be flat, however due to the positivity of \mathcal{P}_t the probability distribution falls off towards lower values of \mathcal{P}_t . In between nodal points, an interpolation effect is responsible for the peak of the probability distribution. To see this, assume for simplicity the linear interpolation between to points which are chosen with uniform prior from $[0, 1]$. Now examine the prior distribution at a position in the center between the two points. For the line at the center position to have the value 1, both random points must have the value 1. On the other hand, for the line at the center to have the value 0.5, there is a huge range of possible values for the 2 random points that will lead to the line crossing right through the middle of $[0, 1]$. Therefore, the probability distribution at the position in the middle between the two points will be shaped like a triangle, see Sec. 2.4 for a more detailed discussion.

The same effect is happening in the case of monotonic \mathcal{P}_t expansion in panel (b). The distribution in between nodal points (red dashed curve) is also peaked, however this is the

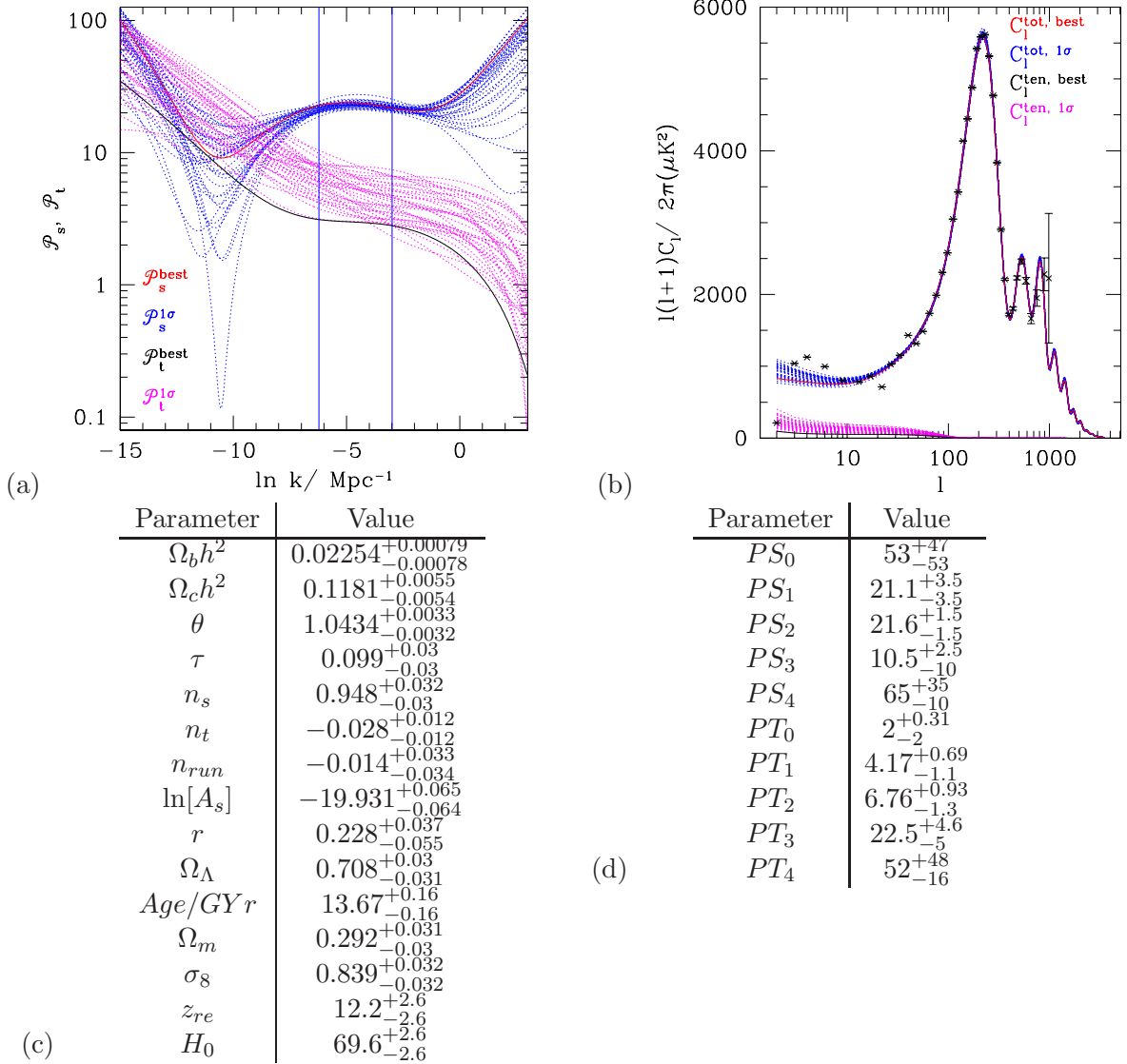


Figure 2.10: Expansion of $\mathcal{P}_s, \mathcal{P}_t$ to order 5 each. The plots of the primordial power spectra $\mathcal{P}_s, \mathcal{P}_t$ in panel (a) show that the ratio of scalar to tensor perturbations r is rather large. The red/ black line is the best-fit trajectory of $\mathcal{P}_s/ \mathcal{P}_t$ and the blue/ magenta lines are trajectories from the 1σ interval around the best-fit models for $\mathcal{P}_s/ \mathcal{P}_t$. Nevertheless the resulting angular power spectra in panel (b) show good compatibility with observational data. Shown is the best fit spectrum (red line for \mathcal{P}_s , black line for \mathcal{P}_t) together with a representative ensemble of spectra from the 1σ box around it in parameter space (blue for \mathcal{P}_s , magenta for \mathcal{P}_t). Panel (c) shows the marginalized values of traditional parameters, indicating a clear detection of a non-zero r . The parameters of the Chebyshev parametrization are presented in panel (d).

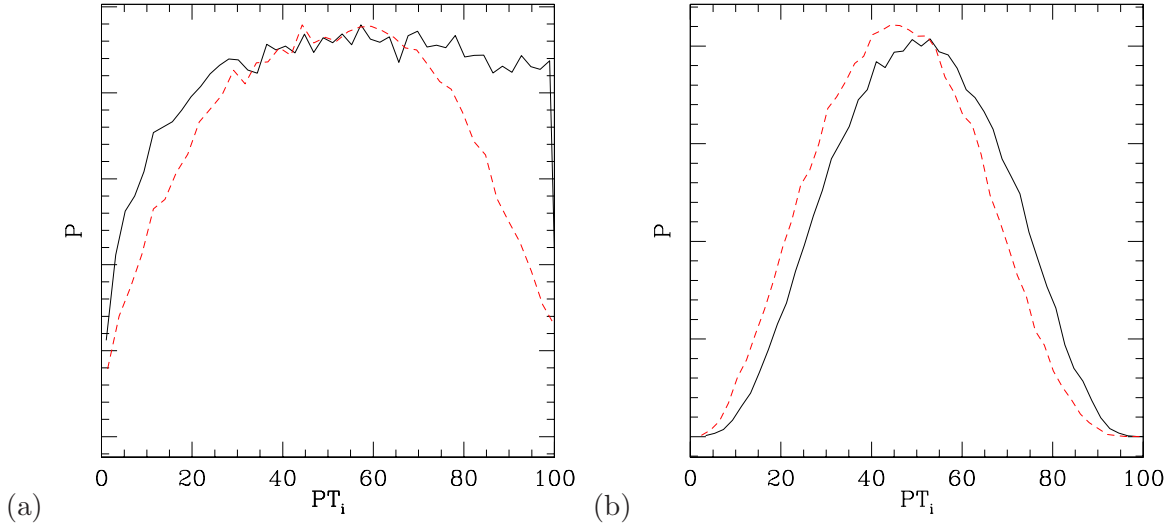


Figure 2.11: The prior probability distribution of \mathcal{P}_t to order 5 at a nodal point (black solid curves) and in between nodal points (red dashed curves) for (a) non monotonic and (b) monotonic \mathcal{P}_t . The fall-off of the distribution at lower values of \mathcal{P}_t even on the nodal point is due to the fact that \mathcal{P}_t is positive. In between nodal points, the effect discussed in Sec. 2.4 causes the distribution to be peaked. In the monotonic case, even at the nodal points enforcing monotonicity makes the distribution fall off at high values of \mathcal{P}_t , so that the distribution is peaked even at the nodal points, and the only effect of moving away from the nodal points is a slight shift in the position of the peak.

combined effect of the above interpolation effect together with the following. At a nodal point (black solid curve), the prior distribution is falling off due to positivity of \mathcal{P}_t towards low values of \mathcal{P}_t just as in the non monotonic case. Additionally, it is also falling off towards larger values of \mathcal{P}_t because \mathcal{P}_t is now enforced to be monotonic, making larger values of \mathcal{P}_t unlikely (unless it is the pivot point at the beginning of the expansion interval). The interpolation effect at this pivot merely produces a shift of the prior probability distribution.

Having identified the implicit priors as the cause for the apparent detection of tensor modes, we now turn towards looking for a parametrization that keeps the prior distribution flat on and in between nodal points. It turns out that sampling the trajectories with a uniform prior on \mathcal{P}_t at the nodal points but the performing the expansion in $\ln \mathcal{P}_t$ has exactly this property.

2.7.4 Sampling with uniform prior in $\mathcal{P}_s, \mathcal{P}_t$ and trajectory expansion in $\ln \mathcal{P}_s, \ln \mathcal{P}_t$

To overcome the prior-induced suppression of low values of \mathcal{P}_t away from the nodal points, the prior has to prefer small values of \mathcal{P}_t stronger than linearly. Obviously the most intuitive of such priors, the logarithmic one, produces a distribution at nodal points that is heavily skewed towards small values of \mathcal{P}_t , not uniform. However, combining the logarithmic expansion of $\ln \mathcal{P}_s, \ln \mathcal{P}_t$ with a uniform prior at the nodal points induces a prior that is only mildly suppressing small values of \mathcal{P}_t , see Fig. 2.12. The fall-off of the prior towards small values of \mathcal{P}_t in this case is by far not as severe as in the linear case of Fig. 2.11, but only a roughly 20%

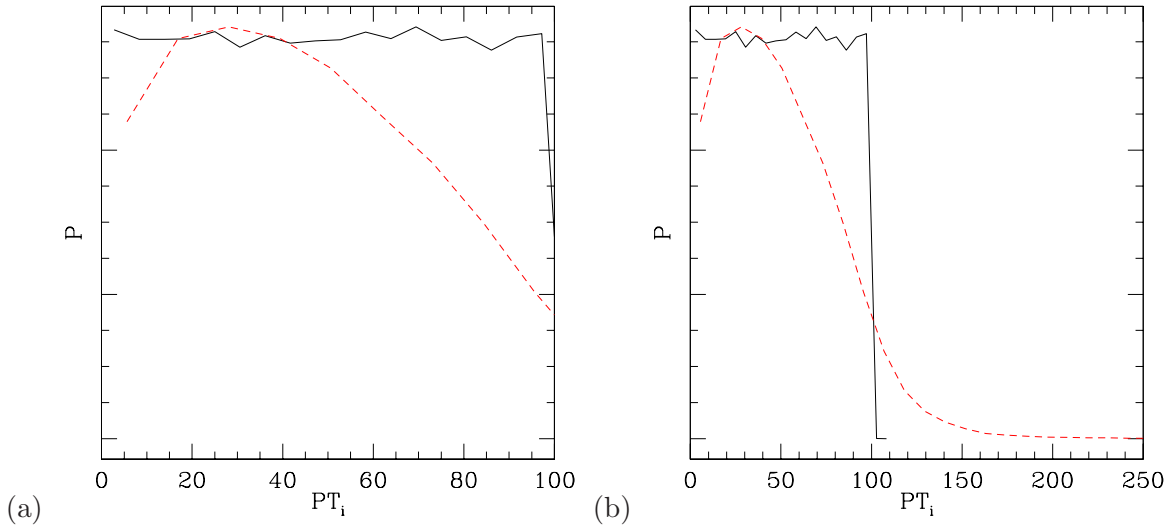


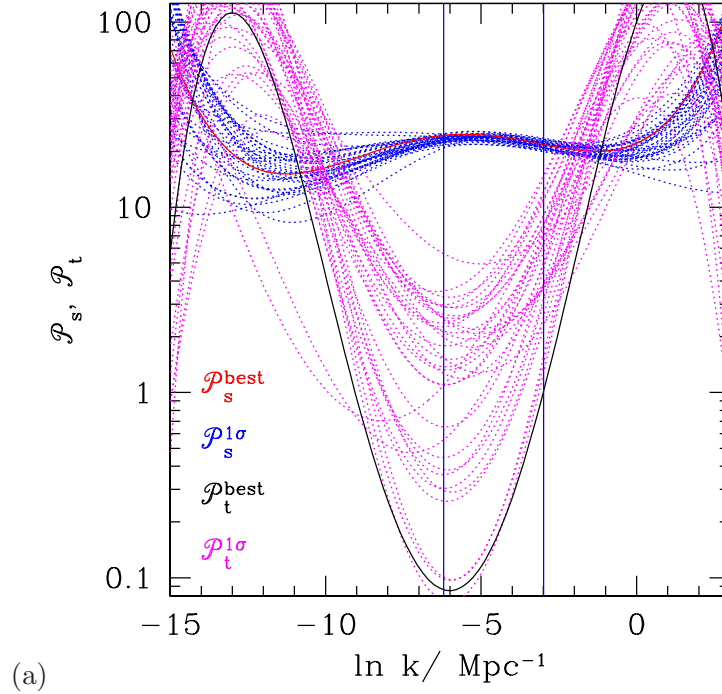
Figure 2.12: The prior distribution of a logarithmic expansion of $\ln \mathcal{P}_s, \ln \mathcal{P}_t$ with a uniform prior in $\mathcal{P}_t \in [0, 100]$ at the nodal points (black solid line) induces a prior in between nodal points (red dashed line) that only slightly disfavors small values of \mathcal{P}_t . Panel (b) is a zoomed out version of panel (a) demonstrating that the fall-off of the distribution towards larger values of \mathcal{P}_t is actually a “migration” towards larger values $\mathcal{P}_t > 100$.

reduction.

Choosing \mathcal{P}_t at nodal points from the interval $[0, 100]$, the distribution away from the nodal points is also falling off towards large values of \mathcal{P}_t . However this prior does not bias the results of the MCMC as in our units $\mathcal{P}_s(k = 0.002\text{Mpc}^{-1}) \approx 21$, i.e. a value of \mathcal{P}_t larger than that would give $r > 1$. The “missing” part of the prior distribution (the area between the black solid and red dashed line) is moved towards values $\mathcal{P}_t > 100$, see Fig. 2.12(b). Although there are certainly other prior choices that are even more uniform in between nodal points, we leave a thorough exploration of this to future work and proceed with the following prior: we expand the trajectories in $\ln \mathcal{P}_s, \ln \mathcal{P}_t$ while sampling uniformly in $\mathcal{P}_s, \mathcal{P}_t$ at the nodal points to perform an almost completely unbiased reconstruction of the primordial power spectra, with the results displayed in Fig. 2.13. There is no sign of a detection of gravity waves but only a (rather large) upper limits on the tensor scalar ratio r . However, as can be seen in panel (a) of Fig. 2.13, the reconstructed tensor power spectra are highly non-monotonic, owing to the fact that the available data offers upper limits the B-mode only in a small range around $k \approx 0.002\text{Mpc}^{-1}$ (indicated by the left vertical line in the figure) in k -space. Due to the lack of observational data outside of this range, the rise of tensor power can only be caused by the prior influence.

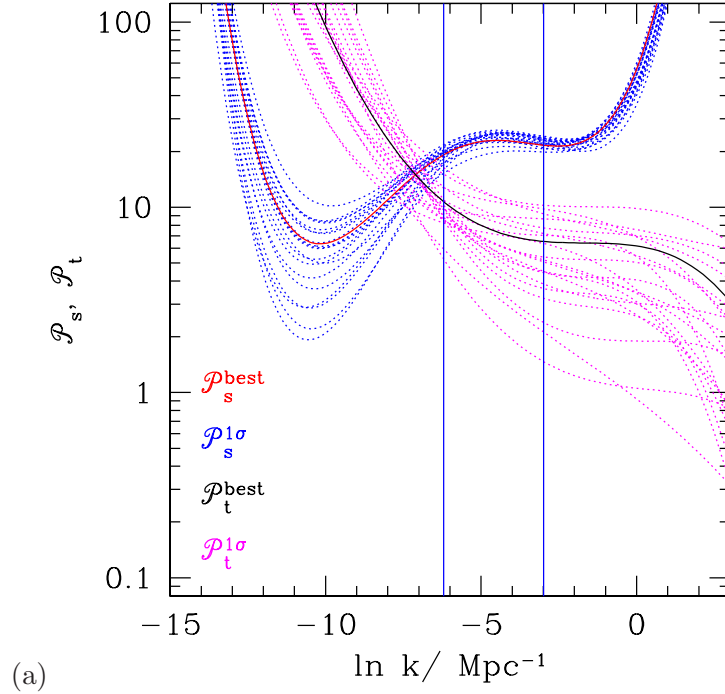
As a non-monotonic spectrum of tensor perturbation is rather difficult to obtain from a realistic model (although one could imagine models in which inflation is interrupted for short periods), it is beneficial to impose monotonicity on \mathcal{P}_t , trading the uniform prior on the values of \mathcal{P}_t for a more natural model, see Tab. 2.14.

Also in this case the effect of the non-uniform prior has been sufficiently weakened such that



Parameter	Value	Parameter	Value
$\Omega_b h^2$	$0.022^{+0.00075}_{-0.00078}$	$\ln[PR_0]$	57^{+43}_{-57}
$\Omega_c h^2$	$0.1202^{+0.0055}_{-0.0054}$	$\ln[PS_1]$	$19.7^{+2.4}_{-2.4}$
θ	$1.042^{+0.0032}_{-0.0033}$	$\ln[PS_2]$	$23.1^{+1.4}_{-1.5}$
τ	$0.094^{+0.03}_{-0.03}$	$\ln[PS_3]$	$15.2^{+6.8}_{-6.9}$
n_s	$0.933^{+0.032}_{-0.032}$	$\ln[PS_4]$	54^{+46}_{-54}
n_{run}	$-0.012^{+0.025}_{-0.024}$	$\ln[PT_0]$	51^{+49}_{-51}
$\ln[A_s]$	$-19.939^{+0.066}_{-0.067}$	$\ln[PT_1]$	51^{+49}_{-17}
r	$< 0.9(95\%CL)$	$\ln[PT_2]$	$2.67^{+0.62}_{-2.7}$
Ω_Λ	$0.689^{+0.034}_{-0.034}$	$\ln[PT_3]$	49^{+51}_{-49}
Age/GYr	$13.77^{+0.16}_{-0.16}$	$\ln[PT_4]$	50^{+50}_{-50}
Ω_m	$0.311^{+0.034}_{-0.034}$		
σ_8	$0.839^{+0.033}_{-0.033}$		
z_{re}	$12.1^{+2.8}_{-2.8}$		
H_0	$67.9^{+2.6}_{-2.7}$		

Figure 2.13: Expansion of $\ln \mathcal{P}_s$, non-monotonic $\ln \mathcal{P}_t$ to order 5 each sampling with a uniform prior on $\mathcal{P}_s, \mathcal{P}_t$. (a) Shape of the best fit trajectories for $\mathcal{P}_s, \mathcal{P}_t$ in red, black together with an ensemble of trajectories indicating the 1σ confidence interval in blue (for \mathcal{P}_s) and magenta (for \mathcal{P}_t). (b) Posterior distribution of the parameters including derived values for the traditional parametrization of the primordial power spectra. (c) Posterior distribution for the trajectory parameters



Parameter	Value	Parameter	Value
$\Omega_b h^2$	$0.02202^{+0.00079}_{-0.0008}$	PS_0	$9.2^{+0.8}_{-0.14}$
$\Omega_c h^2$	$0.1177^{+0.0058}_{-0.0061}$	PS_1	$3.37^{+0.14}_{-0.14}$
θ	$1.0422^{+0.0031}_{-0.0031}$	PS_2	$3.008^{+0.091}_{-0.093}$
τ	$0.107^{+0.034}_{-0.033}$	PS_3	$2^{+0.69}_{-0.68}$
n_s	$0.936^{+0.036}_{-0.035}$	PS_4	$9.32^{+0.68}_{-0.12}$
n_{run}	$0.034^{+0.03}_{-0.029}$	PT_0	$0.05^{+1}_{-0.96}$
$\ln[A_s]$	$-19.925^{+0.072}_{-0.072}$	PT_1	$1.12^{+0.66}_{-0.65}$
r	$< 0.41(95\%CL)$	PT_2	$2.06^{+0.37}_{-0.35}$
Ω_Λ	$0.703^{+0.034}_{-0.033}$	PT_3	$5.73^{+0.86}_{-0.89}$
Age/GYr	$13.76^{+0.16}_{-0.16}$	PT_4	$9.401^{+0.6}_{-0.095}$
Ω_m	$0.297^{+0.033}_{-0.034}$		
σ_8	$0.859^{+0.037}_{-0.037}$		
z_{re}	$13.1^{+2.9}_{-2.8}$		
H_0	$68.9^{+2.7}_{-2.6}$		

Figure 2.14: Expansion of $\ln \mathcal{P}_s$, monotonic $\ln \mathcal{P}_t$ to order 5 each sampling with a uniform prior on $\mathcal{P}_s, \mathcal{P}_t$. (a) Shape of the best fit trajectories for $\mathcal{P}_s, \mathcal{P}_t$ in red, black together with an ensemble of trajectories indicating the 1σ confidence interval in blue (for \mathcal{P}_s) and magenta (for \mathcal{P}_t). (b) Posterior distribution of the parameters including derived values for the traditional parametrization of the primordial power spectra. (c) Posterior distribution for the trajectory parameters.

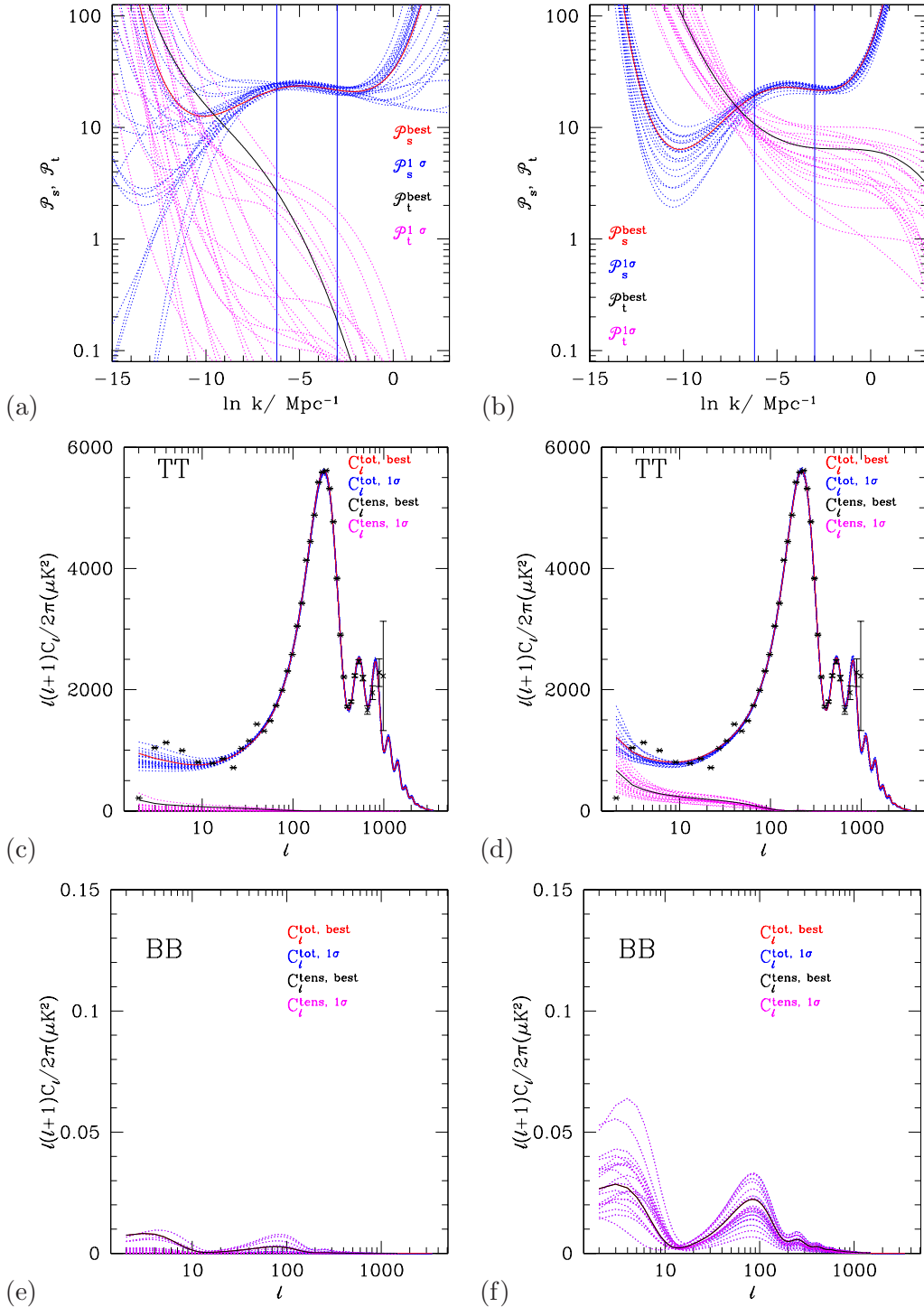


Figure 2.15: Comparison of $\ln \mathcal{P}_s, \ln \mathcal{P}_t$ with uniform sampling in $\ln \mathcal{P}$ (left panels) and \mathcal{P} (right panels). The linear power spectra in (a) and (b) clearly show the difference in reconstructed tensor power (black line is the best fit model, the purple lines are trajectories from the 1σ interval around it). The vertical blue lines indicate the scales $k = 0.002\text{Mpc}^{-1}$ and $k = 0.05\text{Mpc}^{-1}$. However the angular power spectra in (c) and (d) are both still in very good agreement with observations from WMAP3. The black data points are the binned results with the error bars not including cosmic variance. The red lines are the best fit for the total C_ℓ^{TT} (the blue lines are models from the 1σ interval), while the black line show the contribution of the tensors to the total C_ℓ^{TT} (with the purple lines again being models from the 1σ interval). The impact of the different priors is best seen in the difference of the BB signal in panels (e) and (f), making the detection of the amplitude of the B-modes the decisive factor in beating the influence of the priors.

for the tensor scalar ratio there is only an upper limit but without unphysical non-monotonicity of \mathcal{P}_t .

The parametrization using \mathcal{P}_s and \mathcal{P}_t independently is the most unbiased way to reconstruct the primordial power spectra. Ideally data alone should determine the shape of the spectra without any bias from theory like slow-roll evolution or the presence of only one single scalar field. However as long as the quality of available data is not strong enough, one has to very carefully take into account the effect of (implied) priors.

2.8 Summary and Conclusions

In this paper we study ways to scan over inflationary models in order to explore the range of primordial power spectra that can be generated. More importantly, we investigate the inverse problem of how to reconstruct the primordial power spectra of scalar and tensor perturbations from observational data.

While most of the previous studies on the ensemble of inflationary models used a diversity of potential functions $V(\phi)$, we focus instead on the trajectory functions during inflation, as described by the evolution of \mathcal{P}_s and \mathcal{P}_t during inflation, showing different ways of generating random trajectories.

If the time flow along of the inflationary trajectory is measured in terms of number of e -foldings N , then the interval of N for the observable universe generally depends on the inflationary model. The time interval during which the inflationary trajectories are examined can be made precisely independent of the model if time is measured in the comoving momenta of fluctuations $\ln k$. Thus we are dealing with an ensemble of trajectory functions over a fixed domain of the argument which can be conveniently expanded in Chebyshev polynomials, providing both an optimal approximation and numerically fast routines for evaluation and taking derivatives.

We demonstrate explicitly how the traditional parametrization using $A_s, n_s, n_{\text{run}}, r$ is exactly equivalent to a specific trajectory approach and show that the parameters reconstructed by both parametrizations are in very good agreement. As a further test of reliability, we show that simulated spectra smeared by Planck and CMBPol errors can be reconstructed with $\mathcal{P}_s, \mathcal{P}_t$ trajectories, but that there is still a residual uncertainty pertaining to the shape of the (implicit) prior distributions.

In contrast to existing methods like the flow equations, the scanning inflation approach as presented here does not involve any integration steps, making it numerically extremely fast. However the trajectory choice of $\mathcal{P}_s, \mathcal{P}_t$ does not respect the consistency relation connecting them in the case of inflation driven by a scalar field.

Incorporating the consistency relation naturally leads to taking another choice for the trajectory function, the deceleration parameter ϵ , where it becomes necessary to perform a single integration to obtain the Hubble trajectory needed to compute the power spectra. In this case,

one can describe all inflationary dynamics in terms of the evolution of e.g. $\epsilon(\ln k)$, also reconstructing the shape of the potential of the scalar field driving inflation. For details about this and other parametrizations we refer to the accompanying paper[28].

We identified the importance of priors and the ways their bias can change the outcome of MCMC parameter estimation. Even though parameters are sampled with flat priors, the prior distribution of the power spectra can be implicitly altered, a fact that is easy to overlook. Exploring various choices of priors, we demonstrated that it is possible to at least partially smooth the inhomogeneity of the priors, making the distribution uniform and only slightly depending on the position in k -space.

Using a uniform and homogeneous prior on \mathcal{P}_t in an expansion to order 5, the upper limit on $r < 0.41(95\%CL)$ is compatible with the limit $r < 0.36(95\%CL)$ obtained using the standard parametrization, given the fact that the \mathcal{P}_t parametrization allows for a low more degrees of freedom. Making the (somewhat unphysical) assumption that \mathcal{P}_t can be non-monotonic, the upper limits on $r < 0.9$ are even more less stringent. However we remark that this result is depending on the prior and therefore should be treated with caution. To put it into perspective, contrast this behaviour with the amplitude of scalar perturbations \mathcal{P}_s which is well constraint even when using a logarithmic prior. We conclude that in order to ultimately decide on the presence of gravitational waves, better observational data as e.g. promised by the CMBPol satellite is needed.

Let us finish with a final remark on the maximal amount of complexity that can be present in inflationary trajectories. In principle, one can increase the expansion order to arbitrarily high numbers, allowing for more and more structure in the trajectories. Here we conjecture³ that there is a natural limitation on the structure and fine details of the trajectories, namely that the details associated with features on time scales smaller than the inverse Hubble scale H^{-1} are irrelevant. This is to say only those features on a scale exceeding one e -folding are relevant. There are numerous examples in the literature with the calculations of the spectra from inflation with various features like breaks in the potentials, marginal inflation etc. All of them show that the features of the corresponding power spectra are smooth on scales less than H . Heuristically it can be understood by analogy with diffraction patterns in wave optics, where in our case the wavelength of interest is H^{-1} .

This conjecture implies that in order to exhaust all potential inflationary trajectories describing the physics in the k -range accessible to observations – i.e. about 10 e-folds – it is sufficient to consider trajectories only up to order 10, making inflation a science of only 10 numbers.

³We thank Andrei Linde for useful discussions of this point.

Acknowledgments

All computations were performed on the two computing clusters at CITA, McKenzie and Sunnyside. We gratefully acknowledge financial support by NSERC, CIAR and CFI.

Chapter 3

Scanning Inflationary Trajectories II: Acceleration Trajectories

3.1 Acceleration Trajectories

As the goal is to reconstruct the potential for a single scalar field driving inflation, we need to employ a trajectory function that encodes all information about the inflationary period. Specifically, the trajectory needs to fulfill the consistency relation $n_t = -\frac{r}{8}$, giving two obvious alternative choices each with its own set of priors, see Fig. 3.1.

The first, using the Hubble parameter $H(\ln k)$ as trajectory, is a natural candidate as all slow-roll parameters are related to it by simple differentiation, allowing an easy and fast computation of the primordial power spectra via Eq. (2.10). However, the priors implicitly imposed by this parametrization make Hubble not the best choice. The obvious prior, positivity of the trajectory function, was already encountered in [27] and leads to an avoidance of low values of H that could be overcome by using a logarithmic expansion of the trajectory function, i.e. working with $\ln H = \sum_{i=0}^{M-1} c_i T_i(x)$. The other prior, that the universe is inflating ($0 \leq -\frac{\dot{H}}{H^2} \leq 1$), is a more complex prior and hard to compensate for.

The second choice of trajectories, using $\epsilon(\ln k) = -\frac{\dot{H}}{H^2}$ as trajectory, offers a more easily tractable alternative. The prior of the inflationary condition – that ϵ is constraint to lie in the interval $\epsilon \in [0, 1]$ – and its implied avoidance of large and small values of ϵ can be easily dealt with by switching to a logarithmic expansion which we will elaborate in more detail below. While the choice of ϵ trajectories is the most unbiased one, given that a priori all we know about the inflationary period is that it happened, it has a slight disadvantage compared to choosing H , namely that numerical integration is required to relate ϵ to H so that the power spectra can be computed using Eq. (2.10).

$$\frac{d \ln H}{d \ln k} = -\frac{\epsilon}{1 - \epsilon}. \quad (3.1)$$

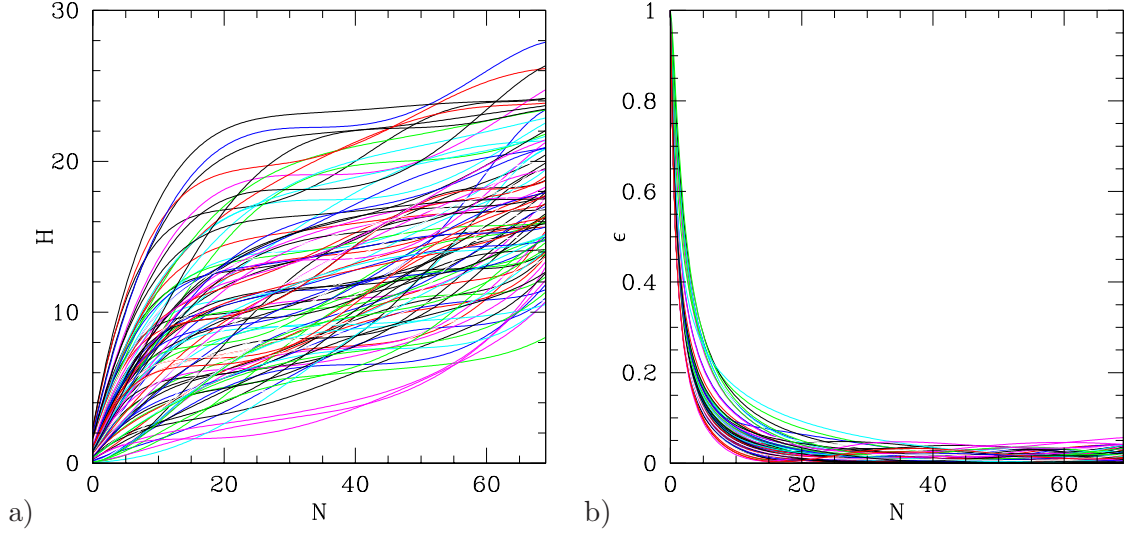


Figure 3.1: Ensemble of valid trajectories $H(N)$ and corresponding slow roll parameter $\epsilon(N)$.

3.1.1 Enforcing the End of Inflation Condition with H and ϵ trajectories

Even though the choice of the Hubble parameter H as trajectory function is implying a complicated prior, we briefly comment on the use of this parametrization to reconstruct the history of the whole inflationary period from $N \approx 70$ to $N = 0$.

If the trajectory is expanded over the whole inflationary interval, i.e. all the way from the beginning of the observable interval $N \approx 70$ to the end of inflation $N = 0$, the trajectory functions must obey the end of inflation condition $\epsilon = 1$ at $N = 0$. To obtain a random inflationary trajectory realization for the trajectory function, e.g. the Hubble parameter $H(N)$, we draw random values of H at M points along a trajectory, optionally sort them to obtain monotonically decreasing trajectories, and interpolate the entire trajectory using the Chebyshev polynomial expansion. In doing so, we must ensure that the trajectory is indeed inflationary (that is $0 < \epsilon < 1$ everywhere along the trajectory), and that inflation ends ($\epsilon = 1$) at the end point of the interval $N_{\text{end}} = 0$. While the inflationary requirement can be implemented as a simple cut (i.e. by just discarding the trajectories that do not satisfy it), the latter requirement is a specific constraint, and has to be dealt with when doing the draw. We will now explore how this can be done most economically for the trajectories ϵ and H .

For the trajectory choice ϵ with the CPNP method (see Sec. 2.3.3, it is straightforward to simply fix $\epsilon_0 = 1$ at the point $N = 0$.

For the trajectory choice H , the situation is more involved. We chose the $(M - 1)$ free parameters to be the values of H at the points which are furthest away from the end of the interval, and set the value at the end point to satisfy the end of inflation condition. This turns out to have a simple expression in the language of linear algebra.

The end of inflation condition $\epsilon = H_{,N}/H = 1$ can be equivalently written as $H_{,N} - H = 0$,

and upon expanding $H(x) = \sum c_j T_j(x)$, cast into a linear algebraic form $\mathbf{v} \cdot \mathbf{c} = 0$, which is just a condition that a vector \mathbf{c} of coefficients of Chebyshev expansion of H is orthogonal to some (known) vector \mathbf{v} with components $v_j = [T'_j(x_{\text{end}}) - T_j(x_{\text{end}})]$, where $T'_j = \frac{dT_j}{dN}$. As it is easy to check, the action of the matrix

$$P = 1 - \frac{\mathbf{p}\mathbf{v}^T}{\mathbf{p} \cdot \mathbf{v}} \quad (3.2)$$

will project the vector \mathbf{c} along the direction \mathbf{p} ($P \cdot \mathbf{c} = \mathbf{c} - \alpha \mathbf{p}$ with $\alpha = \frac{\mathbf{v} \cdot \mathbf{c}}{\mathbf{p} \cdot \mathbf{v}}$) to ensure

$$\mathbf{v} \cdot (P \cdot \mathbf{c}) \equiv 0, \quad (3.3)$$

that is, to ensure orthogonality to \mathbf{v} . Taking \mathbf{p} to be the direction in the coefficient vector space corresponding to adjusting the first function value $p_k = S_{k1}$ will give us the matrix \mathbb{P} that will project coefficients obtained from function values f_k with $k = 2, \dots, M$ to satisfy the end of inflation condition. One can combine this projection with the calculation of Chebyshev coefficients into a single step by simply defining a product matrix $Q = P \cdot S$.

To summarize, the algorithm implementing a random $H(N)$ trajectory draw that respects the end of inflation condition at $N = 0$ using the CPNP method is

1. draw $j_{\text{max}} - 1$ random values $\mathbf{f} = (0, f_2, \dots, f_n)$
2. (optionally) sort them if monotonicity is desired
3. calculate Chebyshev expansion coefficients $\mathbf{c} = Q \cdot \mathbf{f}$
4. perform cuts rejecting non-inflationary trajectories

Let us finally elaborate on the last point of this list, the rejection of trajectories. The CPNP method proves very flexible in that it is possible to reduce the rejection rate to be very small and even to be zero.

A general trajectory $H(N)$ will be rejected if either it is not monotonically increasing with N (decreasing with time) or if it is too steep in the sense that it reaches a point where $H' > H$. For the CPNP method using $H(N)$, one can in principle rank-order the values of $H(N)$ and in this way enforce monotonicity. This is very practical to generate points in (n_s, n_{run}, r) -space. However it is not viable in the context of MCMC parameter estimation, i.e. in the case that one wishes to constrain the shape of $H(N)$ by performing parameter estimation via Markov-Chain Monte Carlo algorithms for obvious reasons – switching the meaning of variables is rather detrimental to the idea of taking Markov steps, as it would make two successive steps completely uncorrelated with no hope of ever sampling from the target density.

3.1.2 Adjusting Priors

In the following we elaborate on different modifications to the ϵ trajectory functions which can be performed to compensate for the non-uniform prior in between nodal points that is induced by the inflation condition, see panel (a) in Fig. 3.3.

Renormalizing Trajectories

When using the CPNP method to create a $\epsilon(\ln k)$ trajectory it is very practical to consider renormalizing trajectories to constrain them to $[0, 1]$, so that all trajectories are valid and no rejections have to be performed. This can be accomplished by introducing two cut-off parameters $\epsilon^{(0)}, \epsilon^{(1)}$ to map ϵ to a function $g(x)$ which is then Chebyshev-expanded. In this way, we can map trajectories that would make excursions to $\epsilon < 0$ or $\epsilon > 1$ back into $0 < \epsilon < 1$ by defining the mapping of $\epsilon \leftrightarrow g(x)$.

$$\begin{aligned}
 g(\epsilon(x)) &= \begin{cases} 2\epsilon^{(0)} - \frac{(\epsilon^{(0)})^2}{\epsilon(x)}, & \epsilon(x) < \epsilon^{(0)} \\ \epsilon(x), & \epsilon^{(0)} < \epsilon(x) < \epsilon^{(1)} \\ 2\epsilon^{(1)} - 1 + \frac{(1-\epsilon^{(1)})^2}{1-\epsilon(x)}, & \epsilon(x) > \epsilon^{(1)} \end{cases} \\
 \epsilon(x) &= \begin{cases} \frac{(\epsilon^{(0)})^2}{2\epsilon^{(0)}-g(x)}, & g(x) < \epsilon^{(0)} \\ g(x), & \epsilon^{(0)} < g(x) < \epsilon^{(1)} \\ 1 - \frac{(1-\epsilon^{(1)})^2}{g(x)+1-2\epsilon^{(1)}}, & g(x) > \epsilon^{(1)} \end{cases} . \quad (3.4)
 \end{aligned}$$

This definition provides a continuous and smooth way of mapping ϵ with the values of the cut-off points controlling where the mapping should kick in. However, the prior on ϵ in between nodal points that is induced by this method is not uniform, see Fig. 3.3(a).

Nonlinear Mapping to $\ln(-n_t)$

One possibility to overcome the problem of keeping ϵ confined to the interval $[0, 1]$ without rejecting low tensors when choosing ϵ at nodal points is to sample the values of ϵ at nodal points but expand $\ln \epsilon$ in Chebyshev polynomials. However this can potentially still lead to boundary avoidance issues so that instead we use a parametrization that is equivalent to $\ln(-n_t)$ to lowest order in slow-roll, where the tilt of the tensor power spectrum is related to ϵ by

$$n_t = \frac{2\epsilon}{\epsilon - 1}. \quad (3.5)$$

$\epsilon = \{0, 1\}$ corresponds to $n_t = \{0, -\infty\}$, so during inflation n_t has to be negative. While this parametrization avoids the boundary at $\epsilon = 1$ (observations exclude extremely large values of ϵ close to unity), changing the parametrization to $\ln(-n_t)$ pushes the $\epsilon = 0$ boundary to ∞ and thereby avoids the rejection of low r . But at the same time it raises the problem of sampling from a non-compact interval if sampling is done in terms of the values of $\ln(-n_t)$ at nodal points.

A few sample trajectories are shown in Fig. 3.2, giving the visual impression that the distribution of values in between nodal points is more uniform when expanding in $\ln(-n_t)$ compared to ϵ . This is confirmed by Fig. 3.3 which shows the distribution of function values ϵ at and in between nodal points.

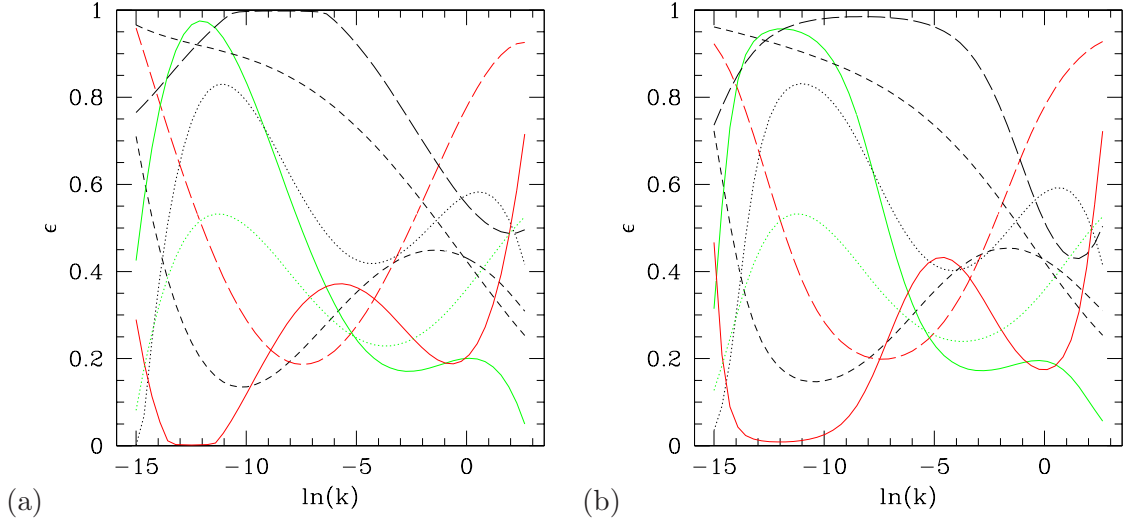


Figure 3.2: Sampling ϵ at 5 nodal points in $\ln k$. The same values of ϵ at the nodal points are interpolated (a) using ϵ (b) using $\ln(-n_t)$, with the same line styles corresponding to each other. The interpolation using $\ln(-n_t)$ is more uniform in between nodal points.

$\ln(-n_t)$ expansion with uniform prior in ϵ

As mentioned above, Fig. 3.3 suggests the following strategy to combine the advantages of both the ϵ and the $\ln(-n_t)$ expansion. Selecting the values of ϵ at nodal points with a uniform prior and then interpolating in between them using $\ln(-n_t)$, the interval to draw random numbers from stays compact, and at the same time issues of disfavoring small values of ϵ in between nodal points are avoided. As panel (c) in Fig. 3.3 shows, the distribution of trajectory values in between nodal points becomes much more uniform when using the expansion in $\ln(-n_t)$, making this choice of trajectory function the preferred one.

Instead of explicitly sampling uniformly in ϵ at the nodal points and subsequently transforming the values to $\ln(-n_t)$, one can alternatively perform the sampling uniformly in $\ln(-n_t)$ at nodal points and compensate for this by adjusting the likelihood by $\Delta\left(\frac{\chi^2}{2}\right)$, e.g. when performing MCMC parameter estimation.

We demonstrate the calculation of $\Delta\left(\frac{\chi^2}{2}\right)$ with the explicit example of going from a uniform prior on ϵ to a uniform prior in $\ln(-n_t)$. Adjusting the prior this way allows for great flexibility, making it very easy to test different choices of priors in practice.

$$\begin{aligned}
 P(\epsilon)d\epsilon &= P(\epsilon)\left|\frac{d\epsilon}{d\ln(-n_t)}\right|d\ln(-n_t) \stackrel{!}{=} P(\ln(-n_t))d\ln(-n_t), \\
 \Rightarrow P(\ln(-n_t)) &= \left|\frac{d\epsilon}{d\ln(-n_t)}\right| = \left|\frac{d\epsilon}{dn_t} \frac{dn_t}{d\ln(-n_t)}\right| = \frac{2}{(n_t + 2)^2}, \\
 \Rightarrow \Delta\left(\frac{\chi^2}{2}\right) &= \ln\left(\frac{2}{(n_T + 2)^2}\right), \tag{3.6}
 \end{aligned}$$

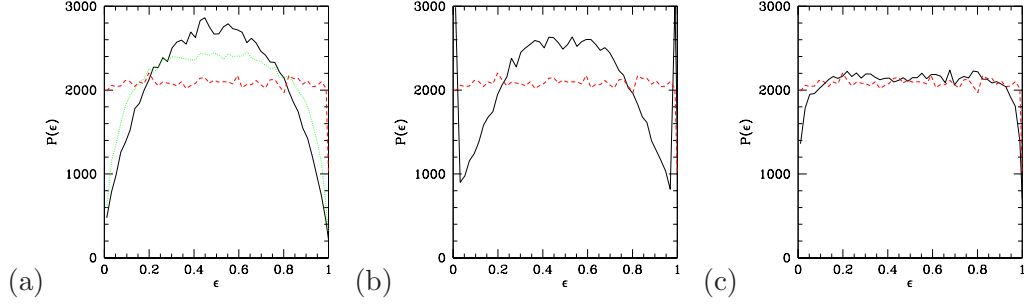


Figure 3.3: Prior distribution of values of ϵ at (red solid line) and in between (black solid line) nodal points in different parametrizations. At the nodal points, the distribution is flat. However the dotted green line in panel (a) shows the prior distribution at the nodal point when rejecting trajectories that do not support inflation over the whole observable interval, i.e. where ϵ wanders outside of $[0, 1]$. This does not occur when renormalizing ϵ or when expanding in $\ln(-n_t)$. (a) expansion in ϵ . (b) expansion ϵ with renormalization. (c) expansion in $\ln(-n_t)$ with uniform prior in ϵ .

where we used that $P(\epsilon)$ should be uniform and $\epsilon = \frac{n_t}{n_t+2}$, $\frac{d\epsilon}{dn_t} = \frac{2}{(n_t+2)^2}$, $\frac{d\ln(-n_t)}{dn_t} = -\frac{1}{n_t}$.

Adding this additional term for each nodal point to the $\log(\text{Likelihood})$ obtained from comparing the prediction of the specific realization of the trajectory with observational data adjusts the prior as desired, resulting in an effectively uniform distribution of ϵ along the nodal points.

3.2 Sample trajectories for $V(\phi) = \lambda\phi^n$

It is instructive to get an insight into the form of trajectory functions for simple, often used monomial potentials of the form $V(\phi) = \lambda\phi^n$, c.f. the analysis for $\mathcal{P}_s, \mathcal{P}_t$ trajectories in Chapter 2.3.2. Assuming slow roll, one has approximately

$$\begin{aligned} \phi^2 - \phi_0^2 &= 2nM_p^2(N - N_0), \quad \epsilon = \frac{n^2}{4n(N-N_0)+2(\phi_0/M_p)^2}, \\ H &= \frac{1}{M_p} \sqrt{\frac{\lambda}{3}} (2nM_p^2(N - N_0) + \phi_0^2)^{\frac{n}{4}}, \end{aligned} \quad (3.7)$$

where for simplicity we use the number of e -folds as time-variable.

As a specific example consider simple chaotic inflation $V(\phi) = \frac{m^2}{2}\phi^2$, $m = 10^{-6}M_p$. We can decompose expression (3.7) in terms of Chebyshev polynomials and find the spectrum of coefficients c_n for this model, using a slight alternation of the series (2.23)

$$\epsilon(N), H(N) = \sum_{j=0}^{M-1} c_j T_j(x) - \frac{1}{2}c_0, \quad (3.8)$$

where $M-1 = j_{\max}$ is the maximum order of Chebyshev polynomials in the decomposition. This formally “unconventional” normalization of c_0 is rather convenient in practical use, e.g. see the Chebyshev code in Numerical Recipes [60], as it leads to a proper normalization of the

orthogonality relation of the Chebyshev polynomials.

The result of decomposition (3.8) for the function (3.7) is shown in Fig. 3.4. Proceeding analogously for the model $V = \frac{\lambda}{4}\phi^2$, the spectrum for the trajectories for $\lambda = 10^{-13}$ is plotted in the same figure for comparison. We see that the values of c_j for smooth monotonically decreasing functions $H(x), \epsilon(x)$ gradually decrease with increasing jx . Since the polynomials $T_j(x)$ are dimensionless, all coefficients c_j have dimension of mass, so that we choose $10^{-5}M_p$ as units of c_j . For a typical realization we see that the 0th order coefficient c_0 of (3.8) is responsible for a constant elevation of H, ϵ , while the first order coefficient c_1 reflects the overall slope of the $H(x), \epsilon(x)$ fall-off and c_2 is related to its curvature, and so on. The expansion (3.8) with a low order polynomial describes a relatively smooth functions $H(x), \epsilon(x)$. Increasing the order of the polynomial expansion allows to catch smaller and smaller features of the trajectories $H(x), \epsilon(x)$.

3.3 Flow Equations

A different approach to generate inflationary trajectories uses the inflationary flow equations[23] which will be briefly sketched below.

Consider the set of slow roll parameters as defined in Eq. (2.6). Switching the argument of the parameters from the field ϕ to the number of e -folds N and successively differentiating the defining equations with respect to the number of e -folds, it is straight-forward to construct a hierarchy of first order ODEs

$$\begin{aligned} \frac{d\epsilon}{dN} &= \epsilon(\sigma + 2\epsilon) = 2\epsilon(\eta - \epsilon) , \\ \frac{d\sigma}{dN} &= -5\epsilon\sigma - 12\epsilon^2 + 2(2\lambda_H) , \\ \frac{d(\ell\lambda_H)}{dN} &= \left(\frac{1}{2}(\ell - 1)\sigma + (\ell - 2)\epsilon \right) (\ell\lambda_H) + (\ell+1\lambda_H) , \end{aligned} \quad (3.9)$$

where $\sigma = 2\eta - 4\epsilon$. After specifying random initial conditions for $\{\epsilon, \sigma, \ell\lambda_H\}$, trajectories are generated by solving the equations forwards in time (i.e. backwards in N) until either slow-roll breaks down, some preset maximum time has passed, or a fix-point is reached. Once slow roll breaks down (which is identified with the end of inflation at which $N = 0$), the equations are evolved backwards in time for a random number of e -folds between $N = 40, \dots, 70$. If inflation ends prematurely, i.e. if the model does not support inflation for the chosen number of e -folds, this model is not valid and rejected.

In practice, this infinite set of equations has to be truncated to be tractable on a computer. Generally the hierarchy is truncated at order of ≈ 7 , and the initial values for the $\ell\lambda_H$ are chosen from the interval $[-0.5 \times 10^{-\ell}, 0.5 \times 10^{-\ell}]$, imposing what is in effect a very smoothing prior on the allowed realizations of inflation.

The solutions of the flow equations differ by the choice of initial conditions. The process

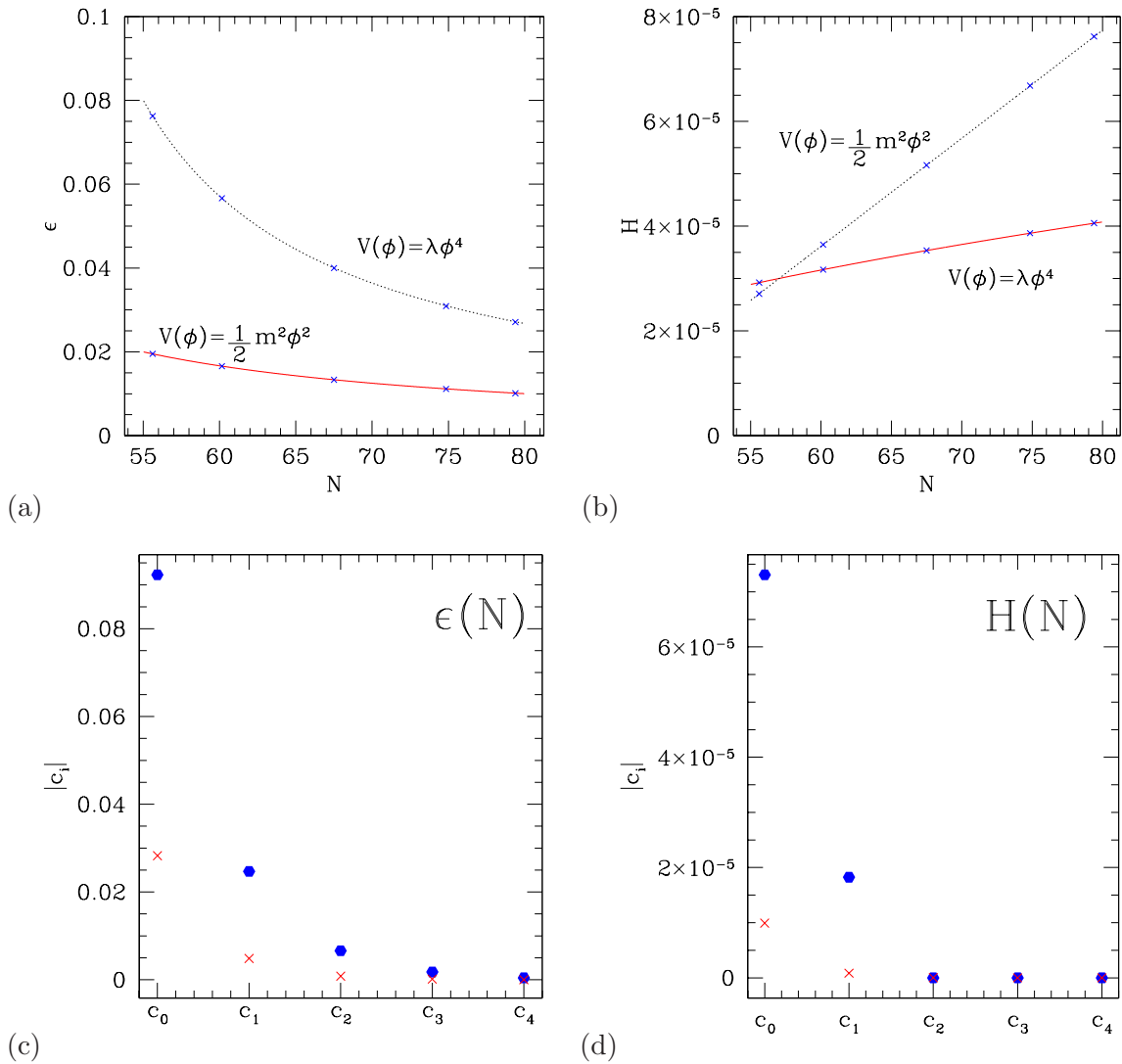


Figure 3.4: Chebyshev coefficients to order 5 each for the trajectories of (a) ϵ and (b) H for $V(\phi) = \frac{m^2}{2}\phi^2$ and $V(\phi) = \lambda\phi^4$ with the position of the nodal points indicated by blue crosses. The distributions of the coefficients is shown in (c) for $\epsilon(N)$ and (d) for $H(N)$ for $V(\phi) = \frac{m^2}{2}\phi^2$ (red crosses) and $V(\phi) = \lambda\phi^4$ (blue hexagons). The vertical axis is given in units of M_p .

of scanning over the models is thus controlled by the details of scanning over the range of initial conditions. The random choice of initial values for the ${}^\ell\lambda_H$ in some region is translated to scattering points across the space of observables (n_s, n_{run}, r) at some random value of N , resulting in plots like those shown Fig. 2.6 for the (n_s, r) -plane. Superimposing the WMAP χ^2 contours shows the degree of (in)compatibility between observational data and the realizations of inflation. Although the WMAP papers [67] correctly state that the theoretical flow equation points have no statistical weights at all, still one can be left with the incorrect impression that it is hard to make inflationary models to be compatible with the data, since most of the theoretical points obtained by the flow method are off the best fit observational area.

Let us scrutinize the flow approach further. First, we shall notice that the truncation of the set of flow equation at ${}^{\ell_{\text{max}}}\lambda_H$ means that the ${}^{\ell_{\text{max}}}$ th derivative of $H(\phi)$ is zero, i.e. $H(\phi)$ is a polynomial of $(\ell_{\text{max}} - 1)$ th order, see also [68]. This immediately means that assuming slow roll we are dealing with a specific class of inflaton potentials $V(\phi)$, namely those which can be expressed as the ratio of two polynomials. Second, the prescription how to define the small parameters ${}^\ell\lambda_H$ in terms of derivatives of $H(\phi)$ is ambiguous. We can introduce other combinations of higher derivatives of $H(\phi)$ which describe the same inflationary system. Therefore the hierarchy of flow equations is also ambiguous and does not reflect any physical dynamics of the system. Only truncating the system of ODEs and differences in the range of initial values introduces differences between the different ways to define the hierarchy of parameters. In fact the system of flow equations is nothing but one of many ways to generate a random ensemble of inflationary trajectories. One might even define the hierarchy in terms of $n_s, n_{\text{run}}, r, n_{\text{run}}^\ell$, which would result in filling the (n_s, r) -plane in Fig. 2.6 uniformly.

3.3.1 Comparison Chebyshev Polynomials vs. Flow trajectories

It is interesting to compare the efficiency of the sampling of inflationary trajectories by the scanning and flow method because ultimately, we are looking for a uniform sampling in the space of trajectories. For this, one needs to rigorously define uniform sampling on the space of all relevant functions – a task of functional analysis.

The Chebyshev polynomials are the best uniform approximation to a given function in a fixed interval (which always needs to be mapped to $[-1, +1]$ in practice), so they represent a natural candidate for the basis in function space in which to sample. However, it does not preclude other methods to be more successful for certain classes of functions, for instance exponential functions. Here we adopt a simple-minded practical approach to compare trajectory functions $\epsilon(N)$ generated by the different approaches of CP/ CPNP (see Sections 2.3.3 and 2.3.3) and flow equations in performing a Chebyshev transform of the functions and compare their “spectra”, the distribution of the coefficients c_j which is an analogue of the Fourier transform of the functions. We will compare the consequences for the scatter plots in the space of classical observables in the next section.

In order to obtain the “Chebyshevization” of a given function $f(x)$ defined in a finite domain

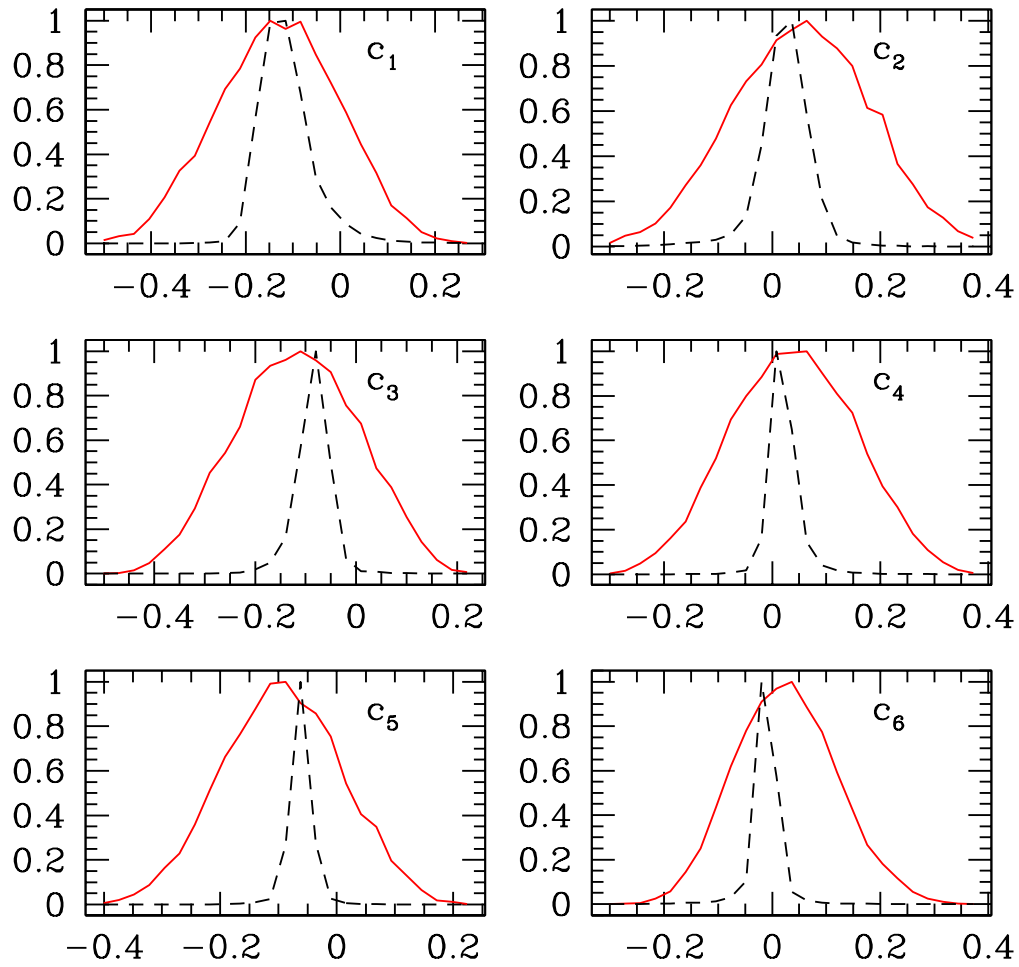


Figure 3.5: Comparison of Chebyshev coefficients c_1, \dots, c_6 of $\epsilon(N)$. The histograms show the distribution of coefficients obtained by the 7th order CPNP scanning method (solid curve) for $\epsilon(N)$ and by the 7th order flow method (dashed curve). The scanning method covers a wider range of coefficients, therefore sampling this function space more uniformly.

$x \in [-1, 1]$ it is fastest to use the orthogonality of the Chebyshev polynomials to obtain

$$c_j = \frac{2}{M} \sum_{k=0}^{M-1} f(x_k) T_j(x_k), \quad (3.10)$$

where the $x_k = \cos(\frac{\pi(k+\frac{1}{2})}{M})$ are the nodal points, see Eq. (2.32), which has the advantage that instead of an integration only a summation of a few terms has to be performed.

In order to perform the Chebyshev transformation on the output $\epsilon(N)$ of the flow algorithm, we have to compensate for the fact that the integration routine for the flow equations only gives results at a finite number of points. We used a cubic spline interpolation to obtain the values of $\epsilon(N)$ at the nodal points needed to calculate the c_j -s for the flow method. For the CP/CPNP method, we choose the order of Chebyshev expansion equal to the order of flow truncation.

However one should note that a given order of truncation in the flow equations does not really correspond to a Chebyshev expansion of the same order. Actually, the solution $\epsilon(N)$ for a given order of the flow equations has in principle infinitely many Chebyshev modes. This can be seen the following way: as mentioned in Sec. 3.3, the flow method corresponds to writing $H(\phi)$ in a truncated power series in ϕ , which corresponds to an infinite series in N through $\frac{d\phi}{dN} = \sqrt{2\epsilon} M_p$. Therefore a finite power series in ϕ corresponds to an infinite power series in N and vice versa. In practice this means that comparing the Chebyshev “spectra” of functions generated by the CP/CPNP method with the spectra of the functions generated by the flow approach should only be regarded as giving a qualitative picture.

Now we apply this procedure to the functions obtained from flow methods. We ran the flow equations at order 7 and produced 1000 valid trajectories. For the CPNP scanning method, we chose $\epsilon(N)$ at 7 nodal points and produced 1000 valid trajectories. As can be seen in the plot of the Chebyshev spectra of the functions Fig. 3.5, the scanning method covers a wider range of the coefficients, indicating that the CPNP method provides a more representative ensemble of trajectories in this function space. We omitted c_0 in the table as it is not drawn randomly but determined by the end of inflation condition.

In general, a broader spectrum of the c_j does not necessarily directly translate into a bigger area in the (r, n_s) -plane of observables for which the coefficients of each single trajectory should be uncorrelated. It turns out that in fact for the CPNP method a broader spectrum of the c_j corresponds to a larger area of points in the plane of observables which we will see explicitly below.

Let us finally comment on the computational efficiency and speed. The scanning approach is generally faster than the flow method, with the difference depending on the exact scanning method. On a 2.0GHz Pentium 4 at order 5, see Table 3.1 The direct CP method, choosing the coefficients of the Chebyshev expansion of $\epsilon(N)$ is only mildly faster than the flow method but if the size of the interval from which to sample the coefficients is decreased, the speed and efficiency increase.

Method	time/trajectory [s]
Flow	10^{-1}
CPNP $H(N)$	10^{-3}
CPNP $\epsilon(N)$	10^{-4}
CPNP $\epsilon(N)$ renormalized	3×10^{-5}

Table 3.1: Comparison of run-time between the flow and the scanning approach. All times measured on an 2.0GHz Intel Pentium 4.

The enormous difference in computational speed between the CPNP and the flow method is easy to understand. First of all, the CP based methods only require drawing random numbers and rejecting invalid trajectories. The main speed penalty is the generation of invalid trajectories which can be avoided when modifying the parametrization in a suitable way. This is in contrast to numerically evolving a system of differential equations in the flow approach, plus rejecting invalid trajectories.

There are several modifications of the scanning methods that affect the rejection ratio. For example, when performing CPNP at 2 nodal points for $H(N)$, there is a $\approx 50\%$ chance that the trajectory will be rejected because $H(N)$ will be increasing with time instead of decreasing. Instead of rejecting this trajectory, one could instead rank-order the values of $H(N)$ and in this way enforce monotonicity. In this case, only trajectories that have $\epsilon > 1$ can potentially be created, decreasing the rejection rate.

In the case of choosing ϵ at nodal points, the trajectory is already guaranteed to be inflationary for most of the time as the values at the nodal points are within the bounds $[0, 1]$, so only when the interpolation between two neighboring points “overshoots” outside of this interval the trajectory needs to be rejected.

Even these rejections can be avoided when renormalizing ϵ or expanding in $\ln(-n_t)$ (see Sec. (3.1.2)). These modification of the CPNP method reparametrize trajectories in such a way that by construction they do not leave the inflationary domain $\epsilon \in [0, 1]$, causing all created trajectories to be accepted, i.e. no cuts need to be performed to remove trajectories that do not inflate for a sufficiently long period.

To sum up, the CP scanning methods prove to be faster as generating invalid trajectories can be completely avoided and as they do not involve the numerically expensive integration of a set of differential equations but only a simple and fast evaluation of functions expressed through Chebyshev polynomials.

3.4 Physical Constraints on Trajectories

In this section we review physical constraints on the trajectory functions $H(x)$ and $\epsilon(x)$ related to their definitions, as well as constraints related to $V(\phi)$.

From the Einstein equations we have

$$\dot{H} = -\frac{1}{2M_p^2}(\rho + p) \leq 0, \quad (3.11)$$

for positive energy density ρ and equation of state $p \geq -\rho$. In particular for scalar fields ϕ_a this gives $\dot{H} = -\frac{1}{2M_p^2}\dot{\phi}_a^2 \leq 0$, making the Hubble parameter a decreasing function of time. Since $dt = -dN/H$, changing the time variable to the number of e-folds N gives

$$\frac{dH}{dN} \geq 0. \quad (3.12)$$

making the function $H(N)$ an increasing function of the argument. In the regime of self-reproduction, quantum effects may force H to become an increasing function of time for short periods of time, but we assume those effects to be negligible during the last 70 e -foldings of inflation.

Next, inflation takes place if

$$|\dot{H}| \leq H^2, \quad (3.13)$$

with equality corresponding to the end point of inflation, leading to a constraint on the parameter $\epsilon \equiv \frac{d \ln H}{dN}$ during inflation

$$0 \leq \frac{dH}{dN} \leq H \Leftrightarrow 0 \leq \epsilon \leq 1, \quad (3.14)$$

where $\epsilon(N=0) = 1$ at the end of inflation.

In principle, inflation may be interrupted by brief jumps of ϵ outside of the interval (3.12), but since this is accompanied by strongly broken scale invariance of the fluctuation spectra, we disregard these trajectories. The two conditions (3.14) exhaust the constraints on H and ϵ from general relativity.

The next level of constraints is related to the physical properties of scalar field potentials $V(\phi)$, leading to less general constraints than those from considerations of general relativity (3.14). Rewriting the HJ equation (2.5) in terms of functions of N and using (2.5) we get

$$\left(6 - \frac{d}{dN}\right) H^2 = \frac{2}{M_p^2} V[\phi(N)]. \quad (3.15)$$

From the positivity of V we obtain $\frac{dH}{dN} \leq 3H \Leftrightarrow \epsilon < 3$, which is weaker than (3.14). However, we also require that the function $V(\phi(N))$ is monotonically increasing as a function of N , without local minima within the interval $0 < N < 70$, $\frac{dV}{dN} > 0$. Then from (3.15) it follows that the slow roll parameter

$$\eta = 2 \frac{M_p^2}{H} \frac{d^2 H}{d\phi^2} = \frac{1}{\epsilon} \left(\frac{1}{H} \frac{d^2 H}{dN^2} - \frac{1}{2} \frac{d\epsilon}{dN} \right) \leq 3, \quad (3.16)$$

which is a new constraint on η that by definition is satisfied in the slow roll regime $\eta < 1$.

The final constraint is that inflation should last for a sufficient number of e -folds. Two different attitudes can be taken towards this condition. On the one hand, it is a desirable goal to reconstruct the whole acceleration history of the inflationary period from say $N \approx 70$ all the way to $N = 0$ in the context of surveying which possible trajectories are allowed or examining the problem of the measure of inflation (and of course also when doing model building). But if one would like to confront the trajectories with observations, reliable measurements are so far only obtainable in a limited range in k -space, from the size of today's horizon at $k \approx 10^{-4} \text{Mpc}^{-1}$ probed by full sky CMB observations to the scales of LSS measurements at $k \approx 1 \text{Mpc}^{-1}$. The corresponding interval in the number of e -folds is about $\Delta \approx 10$, the position of which can vary anywhere from $N \approx 30 \dots 100$ depending on the details of reheating, see Section 2.2.1. It would be technically very challenging to constrain a general trajectory over the whole range $N = 0 \dots 100$ if the only reliable constraints are available around $N = 90 \dots 100$. Therefore we focus on the reconstruction of the potential in the observable interval.

We denote the values of the trajectory coefficients by c_i , i.e. when sampling the coefficients as described in Sec. 2.3.3, and the values of the trajectories at the nodal points by ϵ_i , $\ln(-n_t)_i$, i.e. when sampling the values at nodal points as described in Sec. 2.3.3.

3.5 MCMC Reconstruction of Simulated CMB Data Sets

In this section we perform a check of the scanning method using ϵ trajectories to reconstruct simulated CMB data sets, using the same method as in Chapter 2.6 to simulate experimental noise from the upcoming satellites Planck and CMBPol.

3.5.1 Simulated Data Sets

Creating the simulated spectrum with the standard parametrization, the parameters $\Omega_b h^2$, $\Omega_c h^2$, H_0 , τ , A_s , n_s , n_{run} for the simulated data sets are set to the best fit values of [8], see Tab. 3.2. In order to gauge the ability of the different parametrizations to recover the presence of tensors, we vary the value of the tensor scalar ratio r from $0 \dots 0.5$.

When using the ϵ parametrization to create the simulated spectra, the primordial power spectra are encoded in the values of ϵ at nodal points, $\epsilon_i, i \in [0 \dots N]$, and the integration constant H_1 , see Eq. (3.1). We choose the values of ϵ_i to give values of r from $0.0001 \dots 0.5$, and adjust the integration constant H_1 such that the scalar amplitude is roughly $A_s \approx 2 \times 10^{-9}$ at $k = 0.002 \text{Mpc}^{-1}$. All other parameters are fixed to the same values as used for the standard parametrization, see Tab. 3.2.

3.5.2 Reconstruction of the Simulated Spectra

When performing the reconstruction we use several simplifying assumptions to keep the computational effort reasonable. First of all we keep all ‘‘late time’’ cosmological parameters fixed and vary only the parameters describing the primordial power spectra. Secondly we ignore the

(a) Parameter	Value	(b) standard parametrization	(c) ϵ_2, ϵ_3 (*)
$\Omega_b h^2$	0.0226	A_s	2.15×10^{-9}
$\Omega_c h^2$	0.115	n_s	0.96
H_0	70.4	n_{run}	-0.0551
τ	0.09	r	varying
			ϵ_i varying
			H_1 varying

Table 3.2: (a)-(c)Cosmological parameters of the simulated spectra (the definition of the parameters are given in Sec. 2.5). The values in (a) are taken from [8]. The parameters of the primordial power spectra are depending on the chosen parametrization and are listed separately. (*) The parameters for the ϵ parametrizations are adjusted such that the scalar amplitude A_s roughly has the value 2.15×10^{-9} . If not indicated otherwise, the parameters listed are the values at nodal points. When sampling the coefficients instead of the values at the nodal points we will explicitly indicate it.

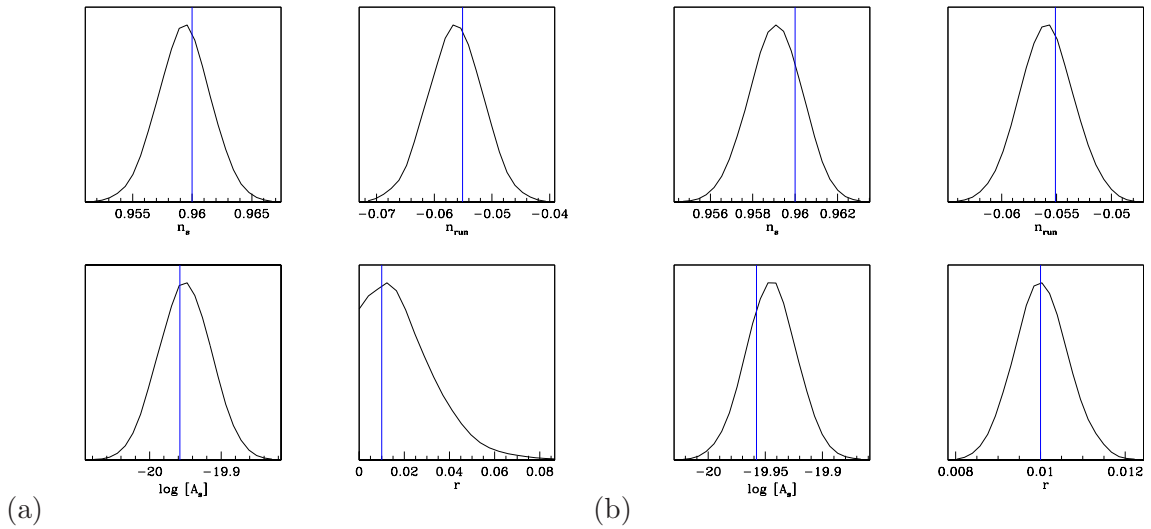


Figure 3.6: Marginalized posterior distribution for the parameters from the reconstruction of a simulated spectrum created using the standard parametrization. The blue vertical lines indicate the value of the input value of the simulated spectra. (a) Planck noise. (b) CMBPol noise.

effects of lensing. Therefore we do not claim to make any statements about the abilities of future experiments to detect for example $r > 0$, but merely use the reconstruction of simulated spectra as a test of correctness after modifying CAMB and COSMOMC to support the various parametrizations of the primordial power spectra and to demonstrate the prior dependence of the MCMC results.

First we reconstruct a spectrum generated by the traditional parametrization using the traditional parametrization. With the amplitude of the tensor to scalar ratio $r = 0.01$ and CMBPol's error bars, the reconstruction of the original values (indicated by the blue lines) works reasonably well (see Fig. 3.5.2)(b), whereas the simulated Planck data is too noisy to allow for a reconstruction of $r = 0.01$ (see Fig. 3.5.2(a)).

Also working with a spectrum generated by ϵ trajectories we reconstruct the initial values (indicated by blue lines) reasonably well, both at order 2 and 5(see Fig. 3.7(a) and Fig. 3.7(b)

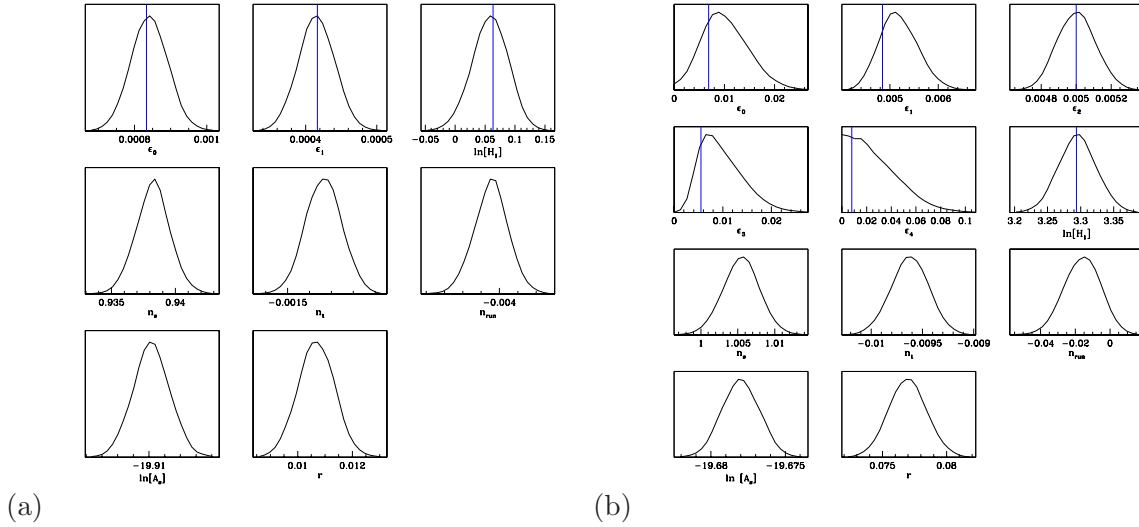


Figure 3.7: Marginalized posterior distribution for the parameters from the reconstruction of a simulated spectrum created using the ϵ parametrization. With CMBPol’s noise the parameters $\epsilon_0, \epsilon_1, \dots, H_1$ of the primordial power spectrum are perfectly recovered. The blue vertical line denotes the value used to create the simulated spectrum. The two bottom rows display the posterior distributions for the derived standard parameters $A_s, n_s, n_t, n_{\text{run}}, r$. (a) epsilon to order 2 (b) epsilon to order 5

respectively), where for comparison we also show the derived traditional parameters describing the primordial power spectra $A_s, n_s, n_{\text{run}}, r, n_t$. However in the order 5 reconstruction, the two values of ϵ_0, ϵ_4 , corresponding to the values of the ϵ trajectories at the borders of the reconstruction interval in $\ln k$ -space, are only poorly determined, which can be explained by the fact that these points are located in regions corresponding to scales where only limited observational data is available.

Finally we examine the influence of the implicit priors imposed by different parametrizations on the ability to reconstruct the value of the tensor scalar ratio r . Fig. 3.8 shows plots of initial values of r versus reconstructed values of r for a Planck type experiment (left column) and a CMBPol type experiment (right column), using the standard parametrization (top row), $\ln(\epsilon)$ to order 5 (middle row) and $\ln(\epsilon)$ to order 5 with uniform prior on ϵ at the nodal points (bottom row). The green line corresponds to $r_{\text{in}} = r_{\text{out}}$ and the red circles are the reconstructed values including error bars, while the red lines without circles are upper limits.

For a Planck type experiment, the different priors give vastly different results for $r_{\text{in}} < 0.05 \Leftrightarrow \log_{10}(r)_{\text{in}} = -1.3$, with the standard parametrizations and the logarithmic prior on ϵ to order 5 only giving upper limits for r while the sampling of $\ln(\epsilon)$ with a uniform prior on ϵ always gives a (spurious) detection.

Assuming a CMBPol type experiment, the influence of the different priors is negligible down to $r_{\text{in}} = 0.001 \Leftrightarrow \log_{10}(r)_{\text{in}} = -3$, owing to the quality of data. On the other hand, for $r < 0.001$ the parametrization sampling $\ln \epsilon$ with a uniform prior on ϵ reconstructs too large values of r while the other parametrizations find upper limits.

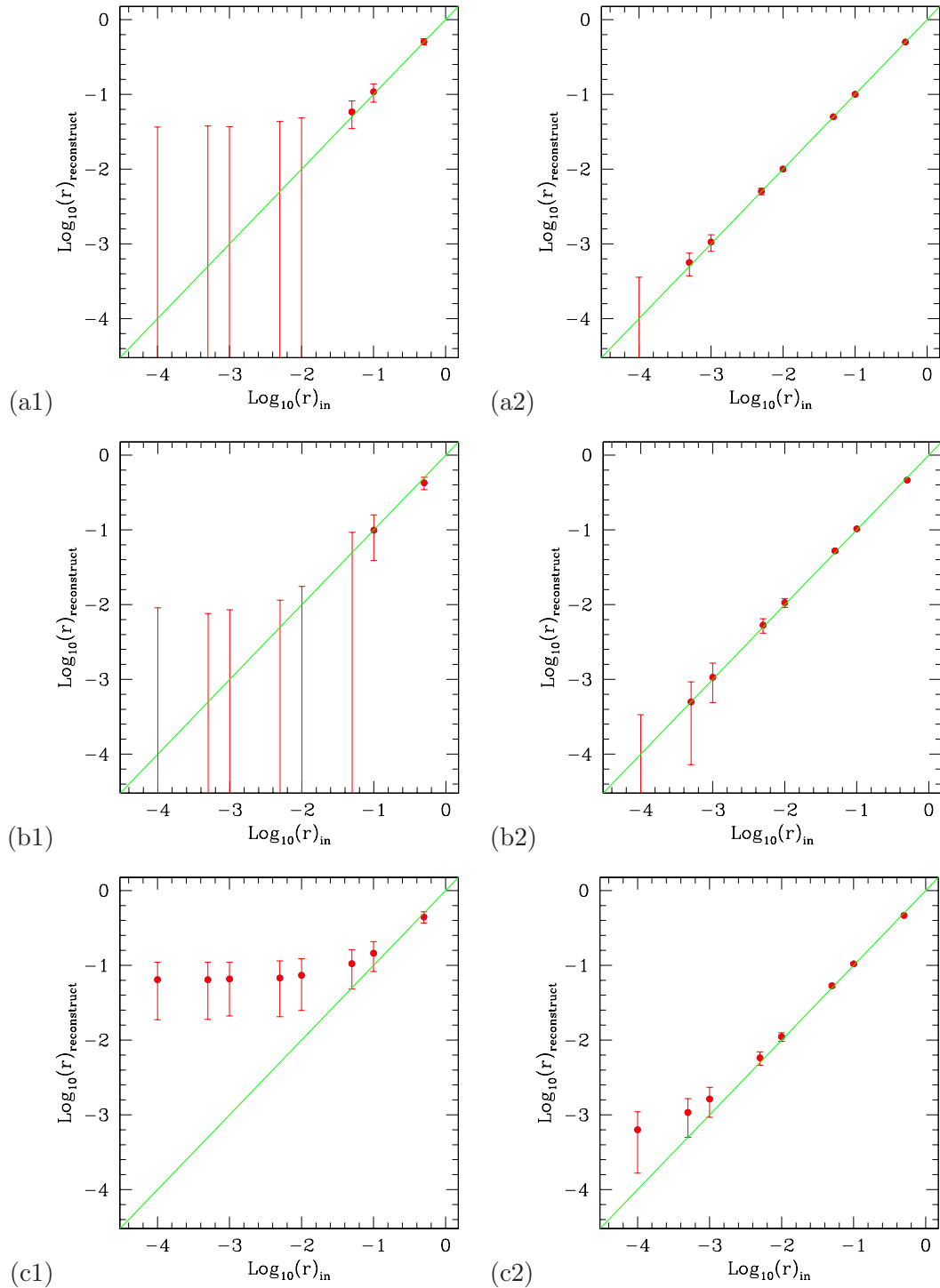


Figure 3.8: Reconstruction of simulated spectra created with the standard parametrization using different values of the tensor-scalar ratio $r = r_{\text{rin}}$ on the horizontal axis and reconstructed value $r_{\text{reconstruct}}$ on the vertical axis, using the following parametrizations: (a) standard (b) sampling $\ln \epsilon 5$ (c) sampling $\ln \epsilon 5$ with uniform ϵ prior. Note the influence of the implicit prior from the choice of parametrization on the reconstructed values of r for simulations with Planck errors (left column) compared to CMBPol errors (right column). Using the \ln parametrization with a uniform prior on ϵ gives systematically too large reconstructed values in the case of Planck errors (panel (c1)).

Parameter	order 1		order 5	
	uniform ϵ	uniform $\ln(-n_t)$	uniform ϵ	uniform $\ln(-n_t)$
$\Omega_b h^2$	$0.02309^{+0.00047}_{-0.00046}$	$0.02345^{+0.00052}_{-0.00055}$	$0.02234^{+0.00085}_{-0.00081}$	$0.02158^{+0.00077}_{-0.00079}$
$\Omega_c h^2$	$0.1148^{+0.0038}_{-0.0038}$	$0.1153^{+0.0037}_{-0.0037}$	$0.1263^{+0.0068}_{-0.0067}$	$0.1207^{+0.0074}_{-0.0078}$
θ	$1.0437^{+0.0028}_{-0.0027}$	$1.0456^{+0.0028}_{-0.0028}$	$1.045^{+0.0033}_{-0.0033}$	$1.0408^{+0.0033}_{-0.0033}$
τ	$0.082^{+0.028}_{-0.029}$	$0.103^{+0.031}_{-0.034}$	$0.1^{+0.03}_{-0.03}$	$0.097^{+0.032}_{-0.033}$
H_0	$71.3^{+1.4}_{-1.4}$	$72.1^{+1.5}_{-1.6}$	$13.67^{+0.17}_{-0.17}$	67^{+3}_{-3}
$\ln[-n_t]_0$	$-4.03^{+0.34}_{-0.33}$	$-7.449^{+4.1}_{-0.049}$	$0.2^{+1.1}_{-1.1}$	$-12.1^{+1.4}_{-7.9}$
$\ln[-n_t]_1$	–	–	$-2.35^{+0.32}_{-0.33}$	$-9.4^{+2.5}_{-1.6}$
$\ln[-n_t]_2$	–	–	$-3^{+0.35}_{-0.35}$	$-9.4^{+2.9}_{-11}$
$\ln[-n_t]_3$	–	–	$-1.1^{+0.67}_{-0.68}$	$-9^{+2.3}_{-1.6}$
$\ln[-n_t]_4$	–	–	$1.2^{+1.1}_{-1.1}$	$-10.8^{+2.8}_{-9.2}$
$\ln[H_1]$	$1.35^{+0.16}_{-0.15}$	$-0.3^{+2}_{-2.9}$	$-2.35^{+0.32}_{-0.33}$	$-1.3^{+2.2}_{-2.4}$
n_s	$0.9813^{+0.0067}_{-0.0068}$	$0.9925^{+0.0075}_{-0.0093}$	$0.885^{+0.04}_{-0.04}$	$0.913^{+0.045}_{-0.038}$
n_t	$-0.0185^{+0.0065}_{-0.0067}$	$-0.0074^{+0.0074}_{-0.0033}$	$-0.049^{+0.013}_{-0.012}$	$-0.0031^{+0.0031}_{-0.0017}$
$\ln[A_s]$	$-19.967^{+0.063}_{-0.065}$	$-19.912^{+0.068}_{-0.066}$	$-19.899^{+0.069}_{-0.071}$	$-19.939^{+0.07}_{-0.07}$
r	$0.148^{+0.053}_{-0.052}$	$< 0.086(95\%CL)$	$0.39^{+0.099}_{-0.1}$	$< 0.16(95\%CL)$

Table 3.3: Reconstruction of acceleration trajectories from real data to different orders using the $\ln(-n_t)$ parametrization and different priors. The definition of the “late-time” parameters is given in Sec. 2.5. A uniform prior on ϵ results in a spurious detection of $r > 0$ whereas a uniform prior on $\ln(-n_t)$ gives upper bounds on r that are tighter than the ones obtained by the standard parametrization. Both these results are purely driven by the prior.

3.6 MCMC Reconstruction from Real Data Sets

In this section we employ $\ln(-n_t)$ trajectories with different priors – in essence trajectories of the acceleration history of the universe which incorporate the consistency condition between the scalar and tensor power spectra – to reconstruct the shape of the primordial power spectra and ultimately the shape of the inflationary potential. As in Section 2.7 we again run a modified version of CAMB and COSMOMC to perform MCMC runs to constrain trajectories to various orders, using the same observational data sets.

Power Spectra and Acceleration Histories

Starting with the expansion of $\ln(-n_t)$ and a uniform prior on ϵ to order 1, there is an apparent 2σ detection of tensors (see Table 3.3) that cannot be explained by the prior issues we encountered before because an expansion to order 1 has $\epsilon = \text{const}$ and therefore the prior is completely uniform over the whole interval in k . To understand this apparent detection we need to make the connection explicit between choosing ϵ at a number of nodal points and the traditional parametrization.

A choice of constant ϵ , i.e. choosing ϵ at 1 nodal point, allows for a non-zero spectral index $n_s - 1 = -2\epsilon$ and non-zero tensor-scalar ration $r = 16\epsilon$. There are 2 degrees of freedom in the ϵ -parametrization: The value of ϵ and the integration constant H_1 . This corresponds to 2

degrees of freedom in the traditional parametrization: A_s, n_s, r , together with the constraint $r = -8(n_s - 1)$ which incorporates our assumption that there is a single scalar field driving inflation. The driving force for the tensor detection is not the data but the constraint between n_s and r with the well-constrained n_s forcing a detection of $r > 0$. Interestingly enough, when using a logarithmic prior on ϵ only an upper bound on r is found as well as only a negligible deviation of the scalar spectral index from unity, possibly indicating that observational data is not yet strong enough to clearly detect a deviation from a scale-invariant Harrison Zel'dovich spectrum.

Choosing ϵ at 2 nodal points allows for a non-zero running n_{run} in addition to non-zero n_s, r . One can express the running of the spectral index through ϵ and its derivatives with respect to $\ln k$, $\epsilon^{(n)} \equiv d^n \epsilon / d^n \ln k$, in the following way (for simplicity we ignore higher order slow roll parameters ζ, \dots)

$$n_{\text{run}} = \frac{dn_s}{d \ln k} = \frac{\epsilon - 1}{\epsilon} \epsilon'' + \left(\frac{\epsilon'}{\epsilon} \right)^2 - 2\epsilon'. \quad (3.17)$$

From this it is obvious that in the ϵ -parametrization with 2 nodal points (which means that $\epsilon' = \text{const}$, $\epsilon'' = 0$), n_{run} is varying with $\ln k$, albeit not freely but slaved to $\epsilon(\ln k)$. Counting free parameters, there is $\{H_1, \epsilon_0, \epsilon_1\}$ vs $\{A_s, n_s, n_{\text{run}}, r\}$ in the traditional parametrization. But as in the case of constant ϵ the latter set of parameters also entails a constraint between n_s, n_{run} and r which embodies the restriction to single field inflation models.

Also in the case of reconstructing ϵ at 2 nodal points, there is an apparent detection of tensors with $r \gtrsim 0.05$. However, it is not the data which is enforcing this, but an effect of the priors as outlined in Sec. 2.4, which is driving ϵ away from zero in between nodal points, creating a bias against small values of r .

Going to an expansion of $\ln(-n_t)$ to order 5 in the reconstruction (see Table 3.3), we find that using a uniform prior on ϵ results in a (spurious) detection of $r \approx 0.4$ which is purely due to the choice of prior. With a uniform prior on $\ln(-n_t)$, we find an upper limit on $r < 0.16(95\%CL)$ (somewhat tighter than the limit $r < 0.4$ obtained by using the standard parametrization) which is due to the preference of small values of ϵ caused by the choice of prior.

Reconstructing the Potential

Having obtained the posterior distributions of the parameters for the primordial power spectra, using the slow roll formula Eq. (2.13) and

$$V(\ln k) = 3H(\ln k)^2 \left(1 - \frac{1}{3} \epsilon(\ln k) \right), \quad (3.18)$$

$$\frac{d\phi}{d \ln k} = -\frac{\sqrt{2\epsilon}}{1 - \epsilon}, \quad (3.19)$$

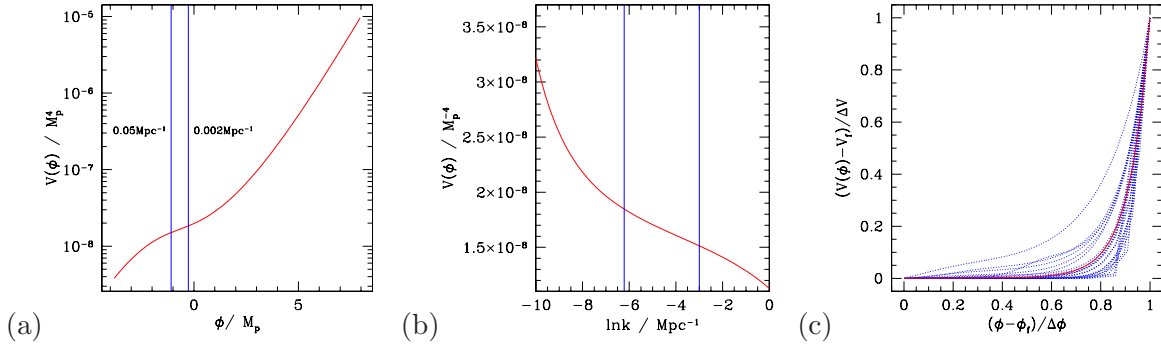


Figure 3.9: The reconstructed inflationary potential $V(\phi)$ using the $\ln(-n_t)$ parametrization with uniform prior on ϵ . Panel (a) shows the best fit potential with in red, with the positions of the field ϕ at $k = 0.05\text{Mpc}^{-1}$ and $k = 0.002\text{Mpc}^{-1}$ indicated by the blue vertical lines. Note in panel (b) that although the potential is varying over several orders of magnitude (owing to large values of ϵ over a wide range of k), on observable scales $V(\phi)$ varies only by little. Panel (c) shows the normalized reconstructed potential (solid red line) with potentials from the 1σ interval around it in (dotted blue lines) over normalized field values as the variation of ϕ is depending on the given trajectory.

allows to parametrically plot $(\phi(\ln k), V(\ln k))$, see Figs. 3.9 and 3.10. The positions of $k = 0.05\text{Mpc}^{-1}$ and $k = 0.002\text{Mpc}^{-1}$ are indicated by vertical blue lines in panels (a) and (b).

While the potential reconstructed using a parametrization with a uniform prior on ϵ in Fig. 3.9(a) is varying over several orders of magnitude owing to relatively large values of ϵ , the small values of r (and therefor ϵ) in the case of a uniform prior on $\ln(-n_t)$ induce only a small variation in $V(\phi)$ and also a lower energy scale of inflation, see Fig. 3.10. Note that the huge variation of V in the case of the uniform prior on ϵ happens outside the range in $\ln k$ where good data is available, c.f. Fig. 3.9(b).

3.7 Degeneracy of the Potential Reconstruction

In this section we make the important observation that the reconstruction of the scalar field potential $V(\phi)$ from the known spectrum of the scalar perturbations $\mathcal{P}_s(k)$ alone is strongly degenerate. It turns out that a given shape of $\mathcal{P}_s(k)$ corresponds to a whole one-parametric family of potentials $V(\phi)$, which can differ significantly in appearance, varying from concave to convex potentials, all giving identical spectra of scalar perturbations. In other words, potentials from new inflationary type to chaotic and all in between are all degenerate with respect to the scalar spectrum. A restricted form of ambiguity of the potentials with regards to the scalar power spectrum is well known in form of a duality between a pair of potentials. [69] found that the chaotic inflation model with potential $V(\phi) = \frac{1}{4}\lambda\phi^4$ and the new inflation type potential $V(\phi) = V_0 - \frac{1}{4}\lambda\phi^4$ give the same spectrum of fluctuations $\mathcal{P}_s(k) \sim \ln k^{3/2}$.

Here we make an even stronger statement, that not only pairs of potentials are degenerate with respect to the scalar spectrum, but an infinite number of potentials within a family of potentials produces identical power spectra of scalar perturbations. Moreover the continuous

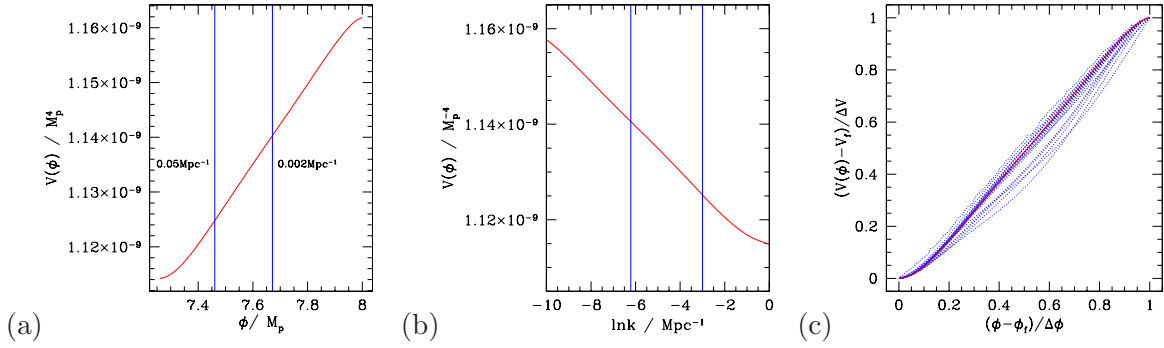


Figure 3.10: The reconstructed inflationary potential $V(\phi)$ using the $\ln(-n_t)$ parametrization with uniform prior on $\ln(-n_t)$. Panel (a) shows the best fit potential with in red, with the positions of the field ϕ at $k = 0.05\text{Mpc}^{-1}$ and $k = 0.002\text{Mpc}^{-1}$ indicated by the blue vertical lines. Note that in contrast to Fig. 3.9 the potential is varying only very little, owing to small values of ϵ . Panel (b) shows the variation of $V(\ln k)$. Panel (c) shows the normalized reconstructed potential (solid red line) with potentials from the 1σ interval around it in (dotted blue lines) over normalized field values as the variation of ϕ is depending on the given trajectory.

parameter which labels the members of the family is nothing but the amplitude of the tensor mode at a pivot point (which can be freely chosen), e.g. at the CMB quadrupole. Therefore knowledge of the amplitude of tensor fluctuations lifts the degeneracy of the potential reconstruction.

First we demonstrate the degeneracy of the potential reconstruction from the scalar spectrum of fluctuations in the uniform acceleration approximation for cosmological perturbations. Then we argue about the stability of this result for an exact calculation of the fluctuations. Finally, we show how this degeneracy appears in terms of the slow roll formalism of fluctuations.

The theory of scalar fluctuations from inflation in the uniform acceleration approximation gives the equation for the power spectrum as a function of comoving momentum k

$$\mathcal{P}_s(k) = \frac{1}{8\pi^2\epsilon} \left(\frac{H}{M_p} \right)^2 \Big|_{k=aH} = \frac{H^4}{16\pi^2 M_p^4 H'^2} \Big|_{k=aH}, \quad (3.20)$$

where we used the notation $H' = \frac{\partial H}{\partial \phi}$ and the right hand side is to be evaluated at the moment when $k = aH$.

Now recall the Hamilton Jacobi equation from which we can express the scalar field potential through $H(\phi)$ and its derivative $H'(\phi)$

$$V(\phi) = 3M_p^2 H^2 - 2M_p^4 H'^2 \quad (3.21)$$

where we seek to express the scalar potential through the known function $\mathcal{P}_s(k)$. Substituting H' from Eq. (3.20), we obtain

$$V(\phi) = H^2 M_p^2 \left(3 - \frac{1}{8\pi^2 \mathcal{P}_s} \left(\frac{H}{M_p} \right)^2 \right). \quad (3.22)$$

Finally we express the Hubble parameter H through the function \mathcal{P}_s , using (3.20) to find

$$\frac{dH}{d\phi} = \frac{1}{4\pi M_p^2} \frac{H^2}{\sqrt{\mathcal{P}_s}}. \quad (3.23)$$

We want to define H as a function of the momenta $\ln k$. For this we recall the relationship between $d\phi$ and $d \ln k$

$$d\phi = \frac{\sqrt{2\epsilon}}{1-\epsilon} M_p d \ln k, \quad (3.24)$$

or equivalently

$$\phi - \phi_0 = 4\pi M_p^2 \int_{\ln k_0}^{\ln k} d \ln k' \frac{H(k') \sqrt{\mathcal{P}_s(k')}}{H^2(k') - 8\pi^2 M_p^2 \mathcal{P}_s(k')}, \quad (3.25)$$

where we used $\epsilon = -\frac{\dot{H}}{H^2} = \frac{1}{8\pi^2 \mathcal{P}_s} \left(\frac{H}{M_p}\right)^2$. After we substitute (3.24) into (3.23), we obtain the following first order equation for the function $H(k)$

$$\frac{dH}{d \ln k} = \frac{H^3(k)}{H^2(k) - 8\pi^2 M_p^2 \mathcal{P}_s(k)}. \quad (3.26)$$

Thus, a given function $\mathcal{P}_s(k)$ defines a one parametric family of trajectories where the integration constant H_1 (not to be confused with the value of Hubble H_0 today) corresponds to the value of the Hubble parameter at a given wave number $\ln k_0$. The value of H_1 labels the members of the family of trajectories that produce identical scalar power spectra, see Fig. 3.11(a). Substituting the solution $H(H_1, k)$ in Eq. (3.22) and using Eq. (3.25) one can parametrically plot $\phi(\ln k), V(\ln k)$ to obtain the degenerate family of potentials $V(\phi)$, see Fig. 3.11(b) and (c), which contains both chaotic and new inflation types.

In order to break this degeneracy it is sufficient to determine the value of Hubble at any wave number e.g. by measurement of the tensor power spectrum

$$\mathcal{P}_t(k) = \frac{2}{\pi^2} \left(\frac{H}{M_p}\right)^2. \quad (3.27)$$

This will provide information about the scale of inflation and determine which of the trajectories $H(\ln k)$ is the one correctly describing the inflationary period.

It is interesting to see how the degeneracy manifests itself in terms of the slow roll parameters. At lowest order in slow roll, $n_s - 1 = 2\eta - 4\epsilon$. Assume that n_s is measured to be $n_s = \mu_1$. In the plane (η, ϵ) this defines the degeneracy line $2\eta = \mu_1 + 4\epsilon$. Adding the measurement of the running of the spectral index $n_{\text{run}} = -2\zeta + 5\sigma\epsilon + 12\epsilon^2$ introduces a higher order slow roll parameter ζ , see Eq. (2.6), so that fixing the running of the index at to $dn_s/d \ln k = \mu_2$ defines a hypersurface in the 3d parameter space (η, ϵ, ζ) . We can continue adding more freedom to n_s , but each higher derivative of n_s introduces an additional higher order slow-roll parameter. The bottom line is that for a given scalar spectrum in terms of the spectral index and its derivatives $(n_s, dn_s/d \ln k, \dots)$ there is a hypersurface which defines the degeneracy of the parameters

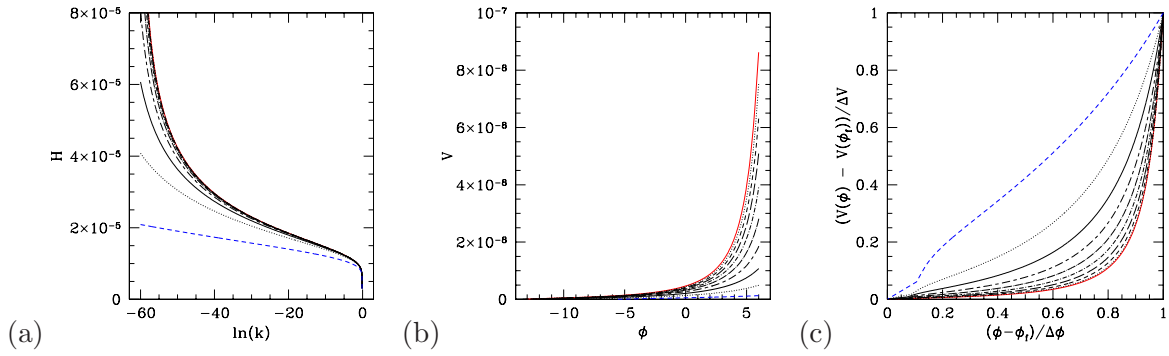


Figure 3.11: Degeneracy of the potential. All different trajectories for H shown in (a) – corresponding to the potentials in (b) – reproduce the same scalar power spectra. Panel (c) shows a plot of the normalized potential, which shows that both convex and concave potentials can describe the same scalar power spectrum.

$(\epsilon, \eta, \xi, \dots)$ which can only be resolved by measuring $r = \frac{P_{GW}}{P_s} = 16\epsilon$.

Chapter 4

Roulette Inflation with Kähler Moduli and their Axions

4.1 Introduction

The “top-down” approach to inflation seeks to determine cosmological consequences beginning with inflation scenarios motivated by ever-evolving fundamental theory. Most recent attention has been given to top-down models that realize inflation with string theory. This involves the construction of a stable six-dimensional compactification and a four-dimensional extended de Sitter (dS) vacuum which corresponds to the present-day (late-time) universe, *e.g.*, the KKLT prescription [17]. Given this, there is a time-dependent, transient non-equilibrium inflationary flow in four dimensions towards the stable state, possibly involving dynamics in both sectors.

Currently, attempts to embed inflation in string theory are far from unique, and indeed somewhat confused, with many possibilities suggested to engineer inflation, using different axionic and moduli fields [19, 20], branes in warped geometry [70], D3-D7 models [71, 72, 73], *etc.* [74, 75, 76, 77, 78, 79, 80]. These pictures are increasingly being considered within a string theory landscape populated locally by many scalar fields.

Different realizations of stringy inflation may not be mutually incompatible, but rather may arise in different regions of the landscape, leading to a complex statistical phase space of solutions. Indeed inflation driven by one mechanism can turn into inflation driven by another, *e.g.*, [81], thereby increasing the probability of inflation over a single mechanism scenario.

So far all known string inflation models require significant fine-tuning. There are two classes that are generally discussed involving moduli. One is where the inflaton is identified with brane inter-distances. To realize slow-roll inflation, the effective inflaton mass should be smaller than the Hubble parameter during inflation, $m^2 < H^2$. However, the brane position moduli fields ϕ are not minimally coupled but rather are conformally coupled and, therefore, acquire effective mass terms through $\frac{1}{12}R\phi^2$ with $R \sim H^2$ [82]. An example is warped brane inflation [70]. A possibility was discussed to make the coupling non-conformal, so the inflaton mass would be

below H but at the price of a fine-tuning [70]. The heavy inflaton mass is also a problem in supergravity inflation models. Another class is geometrical moduli such as Kähler moduli associated with 4-cycle volumes in an internal Calabi-Yau manifold as in [19, 20], which has been recently explored in [21] and which we extend here to illustrate the statistical nature of possible inflation histories.

Different models of inflation predict different spectra for scalar and tensor cosmological fluctuations. From cosmic microwave background and other large scale structure experiments one can hope to reconstruct the underlying theory that gave rise to them, over the albeit limited observable range. Introduction of a multiple-field phase space leading to many possible inflationary trajectories necessarily brings a statistical element prior to the constraints imposed by data. That is, a theory of inflation embedded in the landscape will lead to a broad theory “prior” probability that will be updated and sharpened into a “posterior” probability through the action of the data, as expressed by the likelihood, which is a conditional probability of the inflationary trajectories given the data. All we can hope to reconstruct is not a unique underlying acceleration history with data-determined error bars, but an ensemble-averaged acceleration history with data-plus-theory error bars [83].

The results will obviously be very dependent upon the theory prior. In general all that is required of the theory prior is that inflation occurs over enough e-foldings to satisfy our homogeneity and isotropy constraints and that the universe preheats (and that life of some sort forms) — and indeed those too are data constraints rather than a priori theory constraints. Everything else at this stage is theoretical prejudice. A general approach in which equal a priori theory priors for acceleration histories are scanned by Markov Chain Monte Carlo methods which pass the derived scalar and tensor power spectra through cosmic microwave background anisotropy data and large scale clustering data is described in [83]. But since many allowed trajectories would require highly baroque theories to give rise to them, it is essential to explore priors informed by theory, in our case string-motivated priors.

The old top-down view was that the theory prior would be a delta-function of *the* correct one and only theory. The new view is that the theory prior is a probability distribution on an energy landscape whose features are at best only glimpsed, with huge number of potential minima, and inflation being the late stage flow in the low energy structure toward these minima.

In the picture we adopt for this paper, the flow is of collective geometrical coordinates associated with the settling down of the compactification of extra dimensions. The observed inflaton would be the last (complex) Kähler modulus to settle down. We shall call this T_2 . The settling of other Kähler moduli associated with 4-cycle volumes, T_3, T_4, \dots and the overall volume modulus, T_1 , as well as “complex structure” moduli and the dilaton and its axionic partner, would have occurred earlier, associated with higher energy dynamics, possibly inflations, that became stabilized at their effective minima. The model is illustrated by the cartoon Fig. 4.1. We work within the “large volume” moduli stabilization model suggested in [84, 18, 85] in which the effective potential has a stable minimum at a large value of the compactified internal

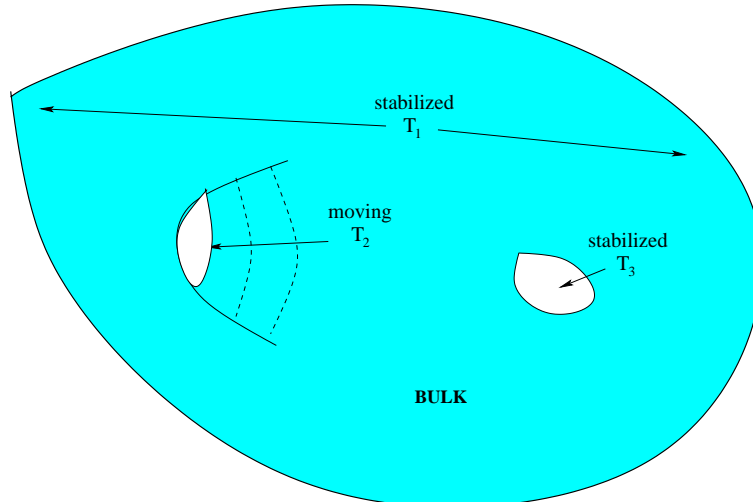


Figure 4.1: Schematic illustration of the ingredients in Kähler moduli inflation. The four-cycles of the CY are the Kähler moduli T_i which govern the sizes of different holes in the manifold. We assume T_3 and the overall scale T_1 are already stabilized, while the last modulus to stabilize, T_2 , drives inflation while settling down to its minimum. The imaginary parts of T_i have to be left to the imagination. The outer $3 + 1$ observable dimensions are also not shown.

volume, $\mathcal{V} \sim 10^5 - 10^{20}$ in string units. An advantage of this model is that the minimum exists for generic values of parameters, *e.g.*, of the flux contribution to the superpotential W_0 . (This is in contrast to the related KKLТ stabilization scheme in which the tree-level W_0 is fine-tuned at $\sim 10^{-4}$ in stringy units in order for the \mathcal{V} minimum to exist.)

In this paper, we often express quantities in the relatively small “stringy units” $m_s \propto M_P/\sqrt{\mathcal{V}}$, related to the (reduced) Planck mass

$$M_P = 1/\sqrt{8\pi G} = 2.4 \times 10^{18} \text{GeV}, \quad (4.1)$$

where G is Newton’s constant.

In this picture, the theory prior would itself be a Bayesian product of a number of conditional probabilities: (1) of manifold configuration defining the moduli; (2) of parameters defining the effective potential and the non-canonical kinetic energy of the moduli, given the manifold structure; (3) of the initial conditions for the moduli and their field momenta given the potentials. The latter will depend upon exactly how the “rain down” from higher energies occurs to populate T_2 initial conditions. An effective complication occurs because of the so-called eternal inflation regime, when the stochastic kicks that the inflaton feels in an e-folding can be as large as the classical drift. This T_2 -model is in fact another example of stringy inflation with self-reproduction. (See [19] for another case.) If other higher-energy moduli are frozen out, most inflationary trajectories would emerge from this quantum domain. However we expect other quantum domains for the higher-energy moduli to also feed the T_2 initial conditions, so we treat these as arbitrary.

The Kähler moduli are flat directions at the stringy tree level. The reason this picture works is that the leading non-perturbative (instanton) and perturbative (α') corrections introduce only an exponentially flat dependence on the Kähler moduli, avoiding the η -problem. Conlon and Quevedo [21] focused on the real part of T_2 as the inflaton and showed that slow-roll inflation with enough e-foldings was possible. A modification [86] of the model considered inflation in a new \mathcal{V} direction but with a negative result.

The fields T_i are complex, $T_i = \tau_i + i\theta_i$. In this paper we extend the model of [21] to include the axionic direction θ_2 . There is essentially only one trajectory if θ_2 is forced to be fixed at its trough, as in [21]. The terrain in the scalar potential $V(\tau_2, \theta_2)$ has hills and valleys in the θ_2 direction which results in an ensemble of trajectories depending upon the initial values of τ_2, θ_2 . The field momenta may also be arbitrary but their values quickly relax to attractor values. The paper [87] considered inflation only along the θ direction while the dynamics in the τ direction were artificially frozen. We find motion in τ always accompanies motion in θ .

In Kähler moduli models, there is an issue of higher order perturbative corrections. Even a tiny quadratic term would break the exponential flatness of the inflaton potential and could make the η -problem reappear. In this case, one will need to introduce a fine-tuning of the parameters in order for these corrections to have a limited effect on the crucial last sixty e-folds (see § 4.3 for details).

In § 4.2 we describe the model in the context of type IIB string theory. In § 4.3 we address whether higher (sub-leading) perturbative corrections introduce a dangerous mass term for the inflaton. In § 4.4 we discuss the effective potential for the volume, Kähler moduli and axion fields, showing with 3 moduli that stabilization of two of them can be sustained even as the inflaton T_2 evolves. Therefore in § 4.5 we restrict ourselves to $V(\tau_2, \theta_2)$ with the other moduli stabilized at their minima. § 4.6 explores inflationary trajectories generated with that potential, for various choices of potential parameters and initial conditions. In § 4.7 we investigate the diffusion/drift boundary and the possibility of self-reproduction. In § 4.8 we summarize our results and outline issues requiring further consideration, such as the complication in power spectra computation that follows from the τ_2, θ_2 freedom.

4.2 The Type IIB String Theory Model

Our inflationary model is based on the “large-volume” moduli stabilization mechanism of [84, 18, 85]. This mechanism relies upon the fixing of the Kähler moduli in IIB flux compactifications on Calabi-Yau (CY) manifolds M by non-perturbative as well as perturbative effects. As argued in [84, 18, 85], a minimum of the moduli potential in the effective $4d$ theory exists for a large class of models. The only restriction is that there should be more complex structure moduli in the compactification than Kähler moduli, i.e. $h^{1,2} > h^{1,1} > 1$, where $h^{1,2}, h^{1,1}$ are the Hodge numbers of the CY. (The number of complex structure moduli is $h^{1,2}$ and the number of Kähler moduli is $h^{1,1}$. Other Hodge numbers are fixed for a CY threefold.) The “large-volume” moduli

stabilization mechanism is an alternative to the KKLТ one, although it shares some features with KKLТ. The purpose of this section is to briefly explain the model of [84, 18, 85].

An effective 4d $\mathcal{N} = 1$ supergravity is completely specified by a Kähler potential, superpotential and gauge kinetic function. In the scalar field sector of the theory the action is

$$S_{\mathcal{N}=1} = \int d^4x \sqrt{-g} \left[\frac{M_P^2}{2} \mathcal{R} - \mathcal{K}_{,i\bar{j}} D_\mu \phi^i D^\mu \bar{\phi}^{\bar{j}} - V(\phi, \bar{\phi}) \right], \quad (4.2)$$

where

$$V(\phi, \bar{\phi}) = e^{\mathcal{K}/M_P^2} \left(\mathcal{K}^{i\bar{j}} D_i \hat{W} D_{\bar{j}} \bar{\hat{W}} - \frac{3}{M_P^2} \hat{W} \bar{\hat{W}} \right) + \text{D-terms}. \quad (4.3)$$

Here \mathcal{K} and \hat{W} are the Kähler potential and the superpotential respectively, M_P is the reduced Planck mass eq.(4.1), and ϕ^i represent all scalar moduli. (We closely follow the notations of [85] and keep M_P and other numerical factors explicit.)

The α'^3 -corrected Kähler potential [88] is

$$\frac{\mathcal{K}}{M_P^2} = -2 \ln \left(\mathcal{V} + \frac{\xi g_s^{\frac{3}{2}}}{2e^{\frac{3\phi}{2}}} \right) - \ln(S + \bar{S}) - \ln \left(-i \int_M \Omega \wedge \bar{\Omega} \right). \quad (4.4)$$

Here \mathcal{V} is the volume of the CY manifold M in units of the string length $l_s = 2\pi\sqrt{\alpha'}$, $\mathcal{V} = \mathcal{V}_s l_s^6$ and we set $\alpha' = 1$. The second term in the logarithm represents the α' -corrections with $\xi = -\frac{\zeta(3)\chi(M)}{2(2\pi)^3}$ proportional to the Euler characteristic $\chi(M)$ of the manifold M . $S = -iC_0 + e^{-\phi}$ is the IIB axio-dilaton with ϕ the dilaton component and C_0 the Ramond-Ramond 0-form. Ω is the holomorphic 3-form of M . The superpotential depends explicitly upon the Kähler moduli T_i when non-perturbative corrections are included

$$\hat{W} = \frac{g_s^{\frac{3}{2}} M_P^3}{\sqrt{4\pi}} \left(W_0 + \sum_{i=1}^{h^{1,1}} A_i e^{-a_i T_i} \right), \quad W_0 = \frac{1}{l_s^2} \int_M G_3 \wedge \Omega. \quad (4.5)$$

Here, W_0 is the tree level flux-induced superpotential which is related to the IIB flux 3-form $G_3 = F_3 - iSH_3$ as shown. The exponential terms $A_i e^{-a_i T_i}$ are from non-perturbative (instanton) effects. (For simplicity, we ignore higher instanton corrections. This should be valid as long as we restrict ourselves to $a_i \tau_i \gg 1$, which we do.) The Kähler moduli are complex,

$$T_i = \tau_i + i\theta_i, \quad (4.6)$$

with τ_i the 4-cycle volume and θ_i its axionic partner, arising from the Ramond-Ramond 4-form C_4 . The A_i encode threshold corrections. In general they are functions of the complex structure moduli and are independent of the Kähler moduli. This follows from the requirement that W is a holomorphic function of complex scalar fields and therefore can depend on τ_i only via the combination $T_i = \tau_i + i\theta_i$. On the other hand, W should respect the axion shift symmetry

$\theta_i \rightarrow \theta_i + \frac{2\pi}{a_i}$ and thus cannot be a polynomial function of T_i . (See [89, 90, 91] for discussion.)

The critical parameters a_i in the potential are constants which depend upon the specific nature of the dominant non-perturbative mechanism. For example, $a_i = \frac{2\pi}{g_s}$ for Euclidean D3-brane instantons and $a_i = \frac{2\pi}{g_s N}$ for the gaugino condensate on the D7 brane world-volume. We vary them freely in our exploration of trajectories in different potentials.

It is known that both the dilaton and the complex structure moduli can be stabilized in a model with a tree level superpotential W_0 induced by generic fluxes (see e.g. [92]) and the lowest-order (i.e. $\xi = 0$) Kähler potential, whereas the Kähler moduli are left undetermined in this procedure (hence are “no scale” models). Including both leading perturbative and non-perturbative corrections and integrating out the dilaton and the complex structure moduli, one obtains a potential for the Kähler moduli which in general has two types of minima. The first type is the KKLT minima [17] which requires significant fine tuning of W_0 ($\sim 10^{-4}$) for their existence. As pointed out in [85], the KKLT approach has a few shortcomings, among which are the limited range of validity of the KKLT effective action (due to α' corrections) and the fact that either the dilaton or some of the complex structure moduli typically become tachyonic at the minimum for the Kähler modulus. (We note, however, that [93] argued that a consistent KKLT-type model with all moduli properly stabilized can be found.) The second type is the “large-volume” AdS minima studied in [84, 18, 85]. These minima exist in a broad class of models and at arbitrary values of parameters. An important characteristic feature of these models is that the stabilized volume of the internal manifold is exponentially large, $\mathcal{V}_{min} \sim \exp(a\tau_{min})$, and can be $\mathcal{O}(10^5 - 10^{20})$ in string units. (Here τ_{min} is the value of τ at its minimum.) The relation between the Planck scale and string scale is

$$M_P^2 = \frac{4\pi\mathcal{V}_{min}}{g_s^2} m_s^2, \quad (4.7)$$

where \mathcal{V}_{min} is the volume in string units at the minimum of the potential. Thus these models can have m_s in the range between the GUT and TeV scale. Also, in these models one can compute the spectrum of low-energy particles and soft supersymmetry breaking terms after stabilizing all moduli (see [85, 94]). All these features make the “large-volume” compactification models especially attractive phenomenologically.

Conlon and Quevedo [21] studied inflation in these models and showed that there is at least one natural inflationary direction in the Kähler moduli space. The non-perturbative corrections in the superpotential eq.(4.5) depend exponentially on the Kähler moduli T_i , and realize by eq.(4.3) exponentially flat inflationary potentials. As mentioned in § 4.1, higher (sub-leading) α' and string loop corrections could, in principle, introduce a small polynomial dependence on the T_i which would beat exponential flatness at large values of the T_i . Although the exact form of these corrections is not known, we assume in this paper that they can be made unimportant for the values T_i take during the last stage of inflation. This may require fine tuning of the parameters or narrowing down of the class of working models in some other way (see § 4.3).

After stabilizing the dilaton and the complex structure moduli we can identify the string coupling as $g_s = e^\phi$, so the Kähler potential (4.4) takes the simple form

$$\frac{\mathcal{K}}{M_P^2} = -2 \ln \left(\mathcal{V} + \frac{\xi}{2} \right) + \ln g_s + \mathcal{K}_{cs}, \quad (4.8)$$

where \mathcal{K}_{cs} is a constant. Using this formula together with equations (4.3), (4.5), and (4.11), one can compute the scalar potential. In our subsequent analysis, we shall absorb the constant factor $e^{\mathcal{K}_{cs}}$ into the parameters W_0 and A_i .

The volume of the internal CY manifold M can be expressed in terms of the 2-cycle moduli t^i , $i = 1, \dots, n = h^{1,1}$:

$$\mathcal{V} = \frac{1}{6} \kappa_{ijk} t^i t^j t^k, \quad (4.9)$$

where κ_{ijk} is the triple intersection form of M . The 4-cycle moduli τ_i are related to the t^i by

$$\tau_i = \frac{\partial}{\partial t^i} \mathcal{V} = \frac{1}{2} \kappa_{ijk} t^j t^k, \quad (4.10)$$

which gives \mathcal{V} an implicit dependence on the τ_i , and thus \mathcal{K} through eq.(4.8). It is known [95] that for a CY manifold the matrix $\frac{\partial^2 \mathcal{V}}{\partial t^i \partial t^j}$ has signature $(1, h^{1,1} - 1)$, with one positive eigenvalue and $h^{1,1} - 1$ negative eigenvalues. Since $\tau_i = \tau_i(t^j)$ is just a change of variables, the matrix $\frac{\partial^2 \mathcal{V}}{\partial \tau_i \partial \tau_j}$ also has signature $(1, h^{1,1} - 1)$. In the case where each of the 4-cycles has a non-vanishing triple intersection only with itself, the matrix $\frac{\partial^2 \mathcal{V}}{\partial \tau_i \partial \tau_j}$ is diagonal and its signature is manifest. The volume in this case takes a particularly simple form in terms of the τ_i :

$$\mathcal{V} = \alpha \left(\tau_1^{3/2} - \sum_{i=2}^n \lambda_i \tau_i^{3/2} \right). \quad (4.11)$$

Here α and λ_i are positive constants depending on the particular model.¹ This formula suggests a “Swiss-cheese” picture of a CY, in which τ_1 describes the 4-cycle of maximal size and τ_2, \dots, τ_n the blow-up cycles. The modulus τ_1 controls the overall scale of the CY and can take an arbitrarily large value, whereas τ_2, \dots, τ_n describe the holes in the CY and cannot be larger than the overall size of the manifold. As argued in [18, 85], for generic values of the parameters W_0 , A_i , a_i one finds that $\tau_1 \gg \tau_i$ and $\mathcal{V} \gg 1$ at the minimum of the effective potential. In other words, the sizes of the holes are generically much smaller than the overall size of the CY.

The role of the inflaton in the model of [21] is the last modulus among the τ_i , $i = 2, \dots, n$, to attain its minimum. As noted by [21], the simplified form of the volume eq.(4.11) is not really necessary to have inflation. For our analysis to be correct, it would be enough to consider a model with at least one Kähler modulus whose only non-zero triple intersection is with itself,

¹For example, the two-Kähler-moduli model with the orientifold of $\mathbb{P}_{[1,1,1,6,9]}^4$ studied in [96, 18, 85] has $\alpha = 1/9\sqrt{2}$, $\lambda_1 = 1$, and $\lambda_2 = -1$.

i. e.,

$$\mathcal{V} = \alpha(\dots - \lambda_i \tau_i^{3/2}), \quad (4.12)$$

and which has its own non-perturbative term in the superpotential eq.(4.5).

4.3 Perturbative Corrections

There are several types of perturbative corrections that could modify the classical potential on the Kähler moduli space: those related to higher string modes, or α' -corrections, coming from the higher derivative terms in both bulk and source (brane) effective actions; and string loop, or g_s -corrections, coming from closed and open string loop diagrams.

As we mentioned before, α' -corrections are an important ingredient of the “large volume” compactification models of [84, 18, 85]. They are necessary for the existence of the large volume minimum of the effective potential in the models with Kähler moduli “lifted” by instanton terms in the superpotential. The leading α' -corrections to the potential arise from the higher derivative terms in the ten dimensional IIB action at the order $\sim \alpha'^3$,

$$S_{IIB} = -\frac{1}{2\kappa_{10}^2} \int d^{10}x \sqrt{-g^{(10)}} e^{-2\phi} [R + 4(\partial\phi)^2 + \alpha'^3 \frac{\zeta(3)}{3 \cdot 2^{11}} J_0 - \alpha'^3 \frac{(2\pi)^3 \zeta(3)}{4} Q + \dots], \quad (4.13)$$

where $J_0 \sim (R^{MN}{}_{PQ})^4$ and Q is a generalization of the six-dimensional Euler integrand,

$$\int_M d^6x \sqrt{g} Q = \chi. \quad (4.14)$$

Performing a compactification of (4.13) on a CY threefold, one finds α' -corrections to the metric on the Kähler moduli space, which can be described by the ξ -term in the Kähler potential (4.4) (see [97, 88]). We will see later that this correction introduces a positive term $\sim \xi W_0^2/\mathcal{V}^3$ into the potential. As discussed in [85], further higher derivative bulk corrections at $\mathcal{O}(\alpha'^4)$ and above are sub-leading to the $1/\mathcal{V}^3$ term and therefore suppressed. (Note that in the models we are dealing with, there is effectively one more expansion parameter, $1/\mathcal{V}$, due to the large value of the stabilized \mathcal{V} .) Also, α' -corrections from the D3/D7 brane actions depend on 4d space-time curvatures and, therefore, do not contribute to the potential. String loop corrections to the Kähler potential come from the Klein bottle, annulus and Möbius strip diagrams similar to those computed in [98, 99] for the models compactified on the orientifolds of tori. The Kähler potential including both leading α' and loop corrections can be schematically written as [98, 99]

$$\mathcal{K} = -2 \ln \mathcal{V} - \frac{\xi}{\mathcal{V}} + \frac{f_1}{\mathcal{V}^{2/3}} + \frac{f_2}{\mathcal{V}^{4/3}} + \dots \quad (4.15)$$

(We have dropped terms depending only on the brane and complex structure moduli.) Here f_1 and f_2 are functions of the moduli whose forms are unknown for a generic CY manifold. If they depend upon the inflaton τ_i polynomially, a mass term will arise for τ_i with the possibility of

an η -problem. For example, if one assumes $f_1(\tau_i) = F\tau_i^r$ with some constant F and a non-zero constant r , then the corresponding contribution to the potential will be

$$\delta V(\tau_i) \sim F\mathcal{V}^{-\frac{8}{3}}\tau_i^r \sim F\mathcal{V}^{\frac{2}{3}(r-4)}\varphi^{\frac{4}{3}r},$$

where φ , the canonically-normalized inflaton field, is related to τ_i as implicit in the equation (see § 4.5.1). In order for this correction to be smaller than the smallest φ -dependent term we find in the uncorrected potential derived in § 4.4, one needs to fine-tune the model-dependent coefficient F to fall faster than $\mathcal{O}(1/\mathcal{V}^{2r/3})$. For example, a quadratic mass term with $r = \frac{3}{2}$ would require F to fall faster than $1/\mathcal{V}$.

As well as τ -corrections there are possible θ -corrections. Non-perturbative effects modify the superpotential by breaking the shift symmetry, making it discrete. As noted we do include these. Although leading perturbative terms leave the Kähler potential θ -independent, subleading corrections can lead to θ -dependent modifications, which we ignore here.

Note also that, although the exact form of higher (sub-leading) corrections is unknown, any correction which introduces dependence on τ_i only via \mathcal{V} will not generate any new mass terms for τ_i . Nevertheless, these corrections can still affect the value of the stabilized volume \mathcal{V} . The reason for this is that any Kähler correction gives rise to a (\mathcal{V} -dependent) term $\sim W_0^2$ in the potential, as seen from (4.3), and W_0 is not necessarily small. Although in the “large volume” compactification models W_0 can take arbitrary values, we will keep it sufficiently moderate, to avoid having corrections bigger than the uncorrected potential.

In the rest of the paper, we study inflaton potentials that do not include the dangerous terms discussed above, assuming that one can find a class of models where these corrections are tuned away or absent.

4.4 Effective Potential and Volume Stabilization

In this Section, we sketch the derivation of the effective field theory potential starting from equations (4.3,4.5,4.8). We choose T_2 to be the inflaton field and study its dynamics in the 4-dimensional effective theory. We first have to ensure that the volume modulus \mathcal{V} and other Kähler moduli are trapped in their minima and remain constant or almost constant during inflation. For this we have to focus on the effective potential of all relevant fields.

Given the Kähler potential and the superpotential, it is straightforward but tedious to compute the scalar potential as a function of the fields T_i . To make all computations we modified the SUPERCOSMOLOGY Mathematica package [100] which originally was designed for real scalar fields to manipulate complex fields.

The Kähler potential (4.8) gives rise to the Kähler metric $\mathcal{K}_{i\bar{j}} = \frac{\partial^2 \mathcal{K}}{\partial T^i \partial \bar{T}^j}$, with

$$\mathcal{K}_{1\bar{1}} = \frac{3\alpha(4\mathcal{V} - \xi + 6\alpha(\sum_{k=2}^n \lambda_k \tau_k^{3/2}))}{4(2\mathcal{V} + \xi)^2 (\frac{\mathcal{V}}{\alpha} + \sum_{k=2}^n \lambda_k \tau_k^{3/2})^{1/3}}, \quad \mathcal{K}_{i\bar{j}} = \frac{9\alpha^2 \lambda_i \lambda_j \sqrt{\tau_i \tau_j}}{2(2\mathcal{V} + \xi)^2},$$

$$\mathcal{K}_{1\bar{j}} = -\frac{9\lambda_j\sqrt{\tau_j}(\alpha^5(\mathcal{V} + \alpha\sum_{k=2}^n\lambda_k\tau_k^{3/2}))^{1/3}}{2(2\mathcal{V} + \xi)^2}, \quad \mathcal{K}_{i\bar{i}} = \frac{3\alpha\lambda_i(2\mathcal{V} + \xi + 6\alpha\lambda_i\tau_i^{3/2})}{4(2\mathcal{V} + \xi)^2\sqrt{\tau_i}}. \quad (4.16)$$

This can be inverted to give

$$\begin{aligned} \mathcal{K}^{1\bar{1}} &= \frac{4(2\mathcal{V} + \xi)(\mathcal{V} + \alpha\sum_{k=2}^n\lambda_k\tau_k^{3/2})^{1/3}(2\mathcal{V} + \xi + 6\alpha\sum_{k=2}^n\lambda_k\tau_k^{3/2})}{3\alpha^{4/3}(4\mathcal{V} - \xi)}, \quad \mathcal{K}^{i\bar{j}} = \frac{8(2\mathcal{V} + \xi)\tau_i\tau_j}{4\mathcal{V} - \xi}, \\ \mathcal{K}^{1\bar{j}} &= \frac{8(2\mathcal{V} + \xi)\tau_j(\frac{\mathcal{V}}{\alpha} + \sum_{k=2}^n\lambda_k\tau_k^{3/2})^{2/3}}{4\mathcal{V} - \xi}, \quad \mathcal{K}^{i\bar{i}} = \frac{4(2\mathcal{V} + \xi)\sqrt{\tau_i}(4\mathcal{V} - \xi + 6\alpha\lambda_i\tau_i^{3/2})}{3\alpha(4\mathcal{V} - \xi)\lambda_i} \end{aligned} \quad (4.17)$$

This is the full expression for an arbitrary number of Kähler moduli T_i . The entries of the metric contain terms of different orders in the inverse volume. If we were to keep only the lowest order terms $\gtrsim \mathcal{O}(\frac{1}{\mathcal{V}^3})$, the shape of the trajectories we determine in the following sections and our conclusions would remain practically unchanged. Note that the kinetic terms for τ and θ are identical, appearing as $\mathcal{K}_{22}(\partial\tau\partial\tau + \partial\theta\partial\theta)$ in the Lagrangian.

The resulting potential is

$$\begin{aligned} V(T_1, \dots, T_n) &= \frac{12W_0^2\xi}{(4\mathcal{V} - \xi)(2\mathcal{V} + \xi)^2} + \sum_{i=2}^n \frac{12e^{-2a_i\tau_i}\xi A_i^2}{(4\mathcal{V} - \xi)(2\mathcal{V} + \xi)^2} + \frac{16(a_i A_i)^2\sqrt{\tau_i}e^{-2a_i\tau_i}}{3\alpha\lambda_i(2\mathcal{V} + \xi)} \\ &+ \frac{32e^{-2a_i\tau_i}a_i A_i^2\tau_i(1 + a_i\tau_i)}{(4\mathcal{V} - \xi)(2\mathcal{V} + \xi)} + \frac{8W_0 A_i e^{-a_i\tau_i} \cos(a_i\theta_i)}{(4\mathcal{V} - \xi)(2\mathcal{V} + \xi)} \left(\frac{3\xi}{(2\mathcal{V} + \xi)} + 4a_i\tau_i \right) \\ &+ \sum_{\substack{i,j=2 \\ i < j}}^n \frac{A_i A_j \cos(a_i\theta_i - a_j\theta_j)}{(4\mathcal{V} - \xi)(2\mathcal{V} + \xi)^2} e^{-(a_i\tau_i + a_j\tau_j)} [32(2\mathcal{V} + \xi)(a_i\tau_i + a_j\tau_j \\ &+ 2a_i a_j \tau_i \tau_j) + 24\xi] + V_{\text{uplift}}. \end{aligned} \quad (4.18)$$

We have to add here the uplift term V_{uplift} to get a Minkowski or tiny dS minimum. Uplifting is not just a feature needed in string theory models. For example, uplifting is done in QFT to tune the constant part of the scalar field potential to zero. At least in string theory there are tools for uplifting, whereas in QFT it is a pure tuning (see, *e.g.*, [17, 101] and references therein). We will adopt the form

$$V_{\text{uplift}} = \frac{\beta}{\mathcal{V}^2}, \quad (4.19)$$

with β to be adjusted.

We now discuss the stabilization of all moduli T_i plus the volume modulus. For this we have to find the global minimum of the potential eq.(4.18), which we do numerically. However, it is instructive to give analytic estimations. Following [18, 85], we study an asymptotic form of eq.(4.18) in the region where both $\mathcal{V} \sim \exp(a_i\tau_i)$, $i = 2, \dots, n$, and $\mathcal{V} \gg 1$. The potential is then a series of inverse powers of \mathcal{V} . Keeping the terms up to the order $\mathcal{O}(\frac{1}{\mathcal{V}^3})$ we obtain

$$V = \frac{1}{\mathcal{V}} \sum_{i=2}^n \frac{8(a_i A_i)^2\sqrt{\tau_i}}{\lambda_i\alpha} e^{-2a_i\tau_i} + \frac{4}{\mathcal{V}^2} \sum_{i=2}^n a_i A_i W_0 \tau_i e^{-a_i\tau_i} \cos(a_i\theta_i) + \frac{3\xi W_0^2}{4\mathcal{V}^3} + \frac{\beta}{\mathcal{V}^2}. \quad (4.20)$$

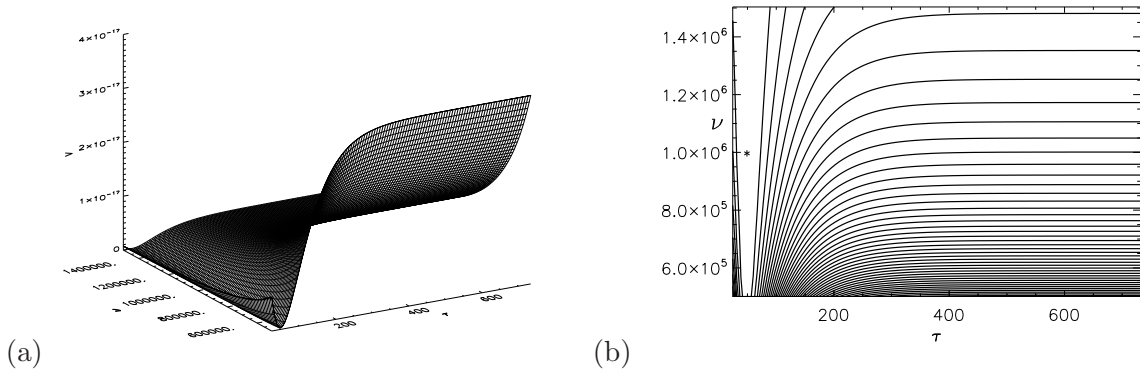


Figure 4.2: (a) The potential surface $V(\tau_1, \tau_2)$ in a two-Kähler model, with the axionic components θ_1 and θ_2 fixed at their minima. (b) shows the related contour plot of the volume \mathcal{V} against τ_2 . Although it may be possible to find a local (very shallow) minimum for the volume in this model (marked by a star), the generic situation is that both τ_1 and τ_2 will be dynamical, and indeed, the evolving τ_2 could force τ_1 out of a local minimum, thereby destabilizing what may have once been stabilized. For this reason, we have focused on models with three or more Kähler moduli, with all but one mutually enforcing their respective stabilizations, and in particular that of the volume. This large volume multi-Kähler approach to stabilization differs from the KKLT stabilization mechanism.

The cross terms for different τ_i do not appear in this asymptotic form, as they would be of order $1/\mathcal{V}^5$. Requiring $\frac{\partial V}{\partial \tau_i} = 0$ and $\cos(a_i \theta_i) = -1$ at the minimum of the potential eq.(4.20), we get

$$\mathcal{V}_{min} \sim \frac{W_0 \lambda_2}{a_2 A_2} \sqrt{\tau_{2,min}} e^{a_2 \tau_{2,min}} \sim \frac{W_0 \lambda_3}{a_3 A_3} \sqrt{\tau_{3,min}} e^{a_3 \tau_{3,min}} \sim \dots \sim \frac{W_0 \lambda_i}{a_n A_n} \sqrt{\tau_{n,min}} e^{a_n \tau_{n,min}} , \quad (4.21)$$

where $\tau_{i,min}$ are the values of the moduli at the global minimum. The expression (4.20) has the structure

$$V = \frac{C_1}{\mathcal{V}} + \frac{C_2}{\mathcal{V}^2} + \frac{C_3}{\mathcal{V}^3} , \quad (4.22)$$

where the coefficients C_1, C_2, C_3 are functions of τ_i and θ_i . C_1 and C_3 are positive but C_2 can be of either sign. However, the potential for the volume \mathcal{V} has a minimum only if $C_2 < 0$, which is achieved for $\cos(a_i \theta_i) < 0$; otherwise $V(\mathcal{V})$ would have a runaway character. Also if all τ_i are very large so that $e^{-a_i \tau_i} \rightarrow 0$, then $C_2 \rightarrow 0$ and \mathcal{V} cannot be stabilized. Therefore to keep C_2 non-zero and negative we have to require that some of the $i > 2$ Kähler moduli τ_i and their axionic partners are trapped in the minimum. For simplicity we assume all but T_2 are already trapped in the minimum.

It is important to recognize that trapping all moduli but one in the minimum cannot be achieved with only two Kähler moduli τ_1 and τ_2 , because τ_1 effectively corresponds to the volume, and τ_2 is the inflaton which is to be placed out of the minimum. The Fig. 4.2 shows the potential as a function of τ_1 and τ_2 for the two-Kähler model. One can see from this plot that a trajectory starting from an initial value for τ_2 larger than a critical value will have runaway behavior in the τ_1 (volume) direction. Thus, as shown by [21], one has to consider a model with three or more Kähler moduli.

By contrast, the “better racetrack” inflationary model based on the KKLT stabilization is achieved with just two Kähler moduli [20]. However, in our class of models with three and more Kähler moduli we have more flexibility in parameter space in achieving both stabilization and inflation. Another aspect of the work in this paper is that a “large volume” analog of the “better racetrack” model may arise.

We have learned that to be fully general we would allow all other moduli including the volume \mathcal{V} to be dynamical. This will lead to even richer possibilities than those explored here, where we only let T_2 evolve, and assume that varying it does not alter the values of the other moduli which we pin at the global minimum. To demonstrate this is viable, we need to show the contribution of T_2 to the position of the minimum is negligible. Following [21], we set all τ_i , $i = 2, \dots, n$, and their axions θ_i to their minima and use equations (4.20) and (4.21) to obtain the potential for \mathcal{V} :

$$V(\mathcal{V}) = -\frac{3W_0^2}{2\mathcal{V}^3} \left(\alpha \sum_{i=2}^n \left[\frac{\lambda_i}{a_i^{3/2}} \right] (\ln \mathcal{V})^{3/2} - \frac{\xi}{2} \right) + \frac{\beta}{\mathcal{V}^2}. \quad (4.23)$$

As one can see from eq.(4.20), the contribution of T_2 to the potential is maximal (by absolute value) when τ_2 and θ_2 are at their minimum, and vanishes as $\tau_2 \rightarrow +\infty$. This gives a simple criterion for whether the minimum for the volume \mathcal{V} remains stable during the evolution of T_2 : the functional form of the potential for \mathcal{V} (4.23) is insensitive to T_2 provided [21]:

$$\sum_{i=3}^n \frac{\lambda_i}{a_i^{3/2}} \gg \frac{\lambda_2}{a_2^{3/2}}. \quad (4.24)$$

For a large enough number of Kähler moduli this condition is automatically satisfied for generic values of a_i and λ_i . We conclude that with many Kähler moduli the volume does not change during the evolution of the inflaton T_2 because the other T_i stay at their minimum and keep the volume stable.

Now it is easy to show that the other T_i remain stable when T_2 moves. Indeed, in its asymptotic form (4.20) the potential is a sum of separate contributions from each modulus T_i independent of other T_i -s. Therefore, for a given stabilized value of \mathcal{V} , evolving T_2 will only change an additive constant in the potential for T_i , and thus will not affect the position of the minimum for T_i .

Note that the analysis above is purely classical and does not account for the quantum corrections to the effective potential for T_2 after integrating out all other T_i -s. To guarantee that these corrections are small during inflation one has to assume some hierarchy of the moduli masses. Since in this paper we focus on inflation driven only by T_2 , we assume that the masses of the other Kähler moduli T_i are larger than the inflationary energy scale.

Consider a toy model with three Kähler moduli in which T_2 is the inflaton and T_3 stays at its own minimum to provide an unvarying minimum for \mathcal{V} . We choose parameters as in set 1 in Table 1 (which will be explained in detail below in Sec. 4.5), and also let $a_3 = 2\pi/300$,

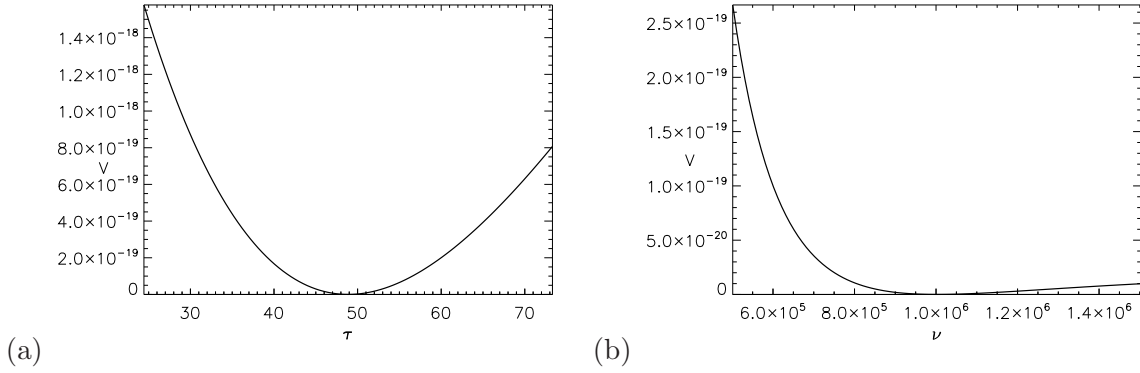


Figure 4.3: One dimensional sections of the uplifted potential for parameter set 1. We perform a proper uplift procedure by explicitly introducing the additional field τ_3 which is responsible for stabilizing the volume during inflation. The parameters for τ_3 are chosen in such a way that the stability condition is fulfilled and at the same time we recover the desired value of $\mathcal{V}_{min} \approx 10^6$. The minimum in τ_3 direction is clearly visible at $\tau_{3,min} \approx 49$.

$A_3 = 1/200$, and $\lambda_3 = 10$. Eq.(4.24) is strongly satisfied, $\frac{\lambda_2}{a_2^{3/2}} / \frac{\lambda_3}{a_3^{3/2}} = 10^{-4}$, under this choice of parameters. Therefore we can drop the τ_2, θ_2 -dependent terms in the potential (4.20) and use it as a function of the two fields \mathcal{V} and τ_3 to find their values at the minimum (after setting also $\theta_3 = \pi/a_3$ to its minimum). The minimization procedure should also allow one to adjust the uplift parameter β in a way that the potential vanishes at its global minimum. With our choice of parameters we found the minimum numerically to be at $\tau_3 = 49$ and $\mathcal{V} = 10^6$ with $\beta = 8.5 \times 10^{-6}$, as shown in Fig. 4.3.

4.5 Inflaton Potential

We now take all moduli T_i , $i > 3$, and the volume \mathcal{V} (hence T_1) to be fixed at their minima, but let T_2 vary, since it is our inflaton. For simplicity in the subsequent sections we drop the explicit subscript, setting $T_2 = \tau + i\theta$. The scalar potential $V(\tau, \theta)$ is obtained from eq.(4.18) with the other Kähler moduli stabilized:

$$V(\tau, \theta) = \frac{12W_0^2\xi}{(4\mathcal{V}_m - \xi)(2\mathcal{V}_m + \xi)^2} + \frac{D_1 + 12e^{-2a_2\tau}\xi A_2^2}{(4\mathcal{V}_m - \xi)(2\mathcal{V}_m + \xi)^2} + \frac{D_2 + \frac{16(a_2A_2)^2}{3\alpha\lambda_2}\sqrt{\tau}e^{-2a_2\tau}}{(2\mathcal{V}_m + \xi)} \quad (4.25)$$

$$+ \frac{D_3 + 32e^{-2a_2\tau}a_2A_2^2\tau(1 + a_2\tau)}{(4\mathcal{V}_m - \xi)(2\mathcal{V}_m + \xi)} + \frac{D_4 + 8W_0A_2e^{-a_2\tau}\cos(a_2\theta)}{(4\mathcal{V}_m - \xi)(2\mathcal{V}_m + \xi)} \left(\frac{3\xi}{(2\mathcal{V}_m + \xi)} + 4a_2\tau \right) + \frac{\beta}{\mathcal{V}_m^2}.$$

Here the terms D_1, \dots, D_4 contain contributions from the stabilized Kähler moduli other than the inflaton. We dropped cross terms between τ and other τ_i , $i > 3$, since these are suppressed by inverse powers of \mathcal{V}_m . Explicitly expanding to order $1/\mathcal{V}^3$ yields the simpler expression

$$V(\tau, \theta) = \frac{8(a_2A_2)^2\sqrt{\tau}e^{-2a_2\tau}}{3\alpha\lambda_2\mathcal{V}_m} - \frac{4W_0a_2A_2\tau e^{-a_2\tau}\cos(a_2\theta)}{\mathcal{V}_m^2} + \Delta V, \quad (4.26)$$

Parameter	W_0	a_2	A_2	λ_2	α	ξ	g_s	\mathcal{V}	$\Delta\varphi/M_p$
Parameter set 1	300	$2\pi/3$	0.1	1	$1/9\sqrt{2}$	0.5	1/10	10^6	2×10^{-3}
Parameter set 2	6×10^4	$2\pi/30$	0.1	1	$1/9\sqrt{2}$	0.5	1/10	10^8	1×10^{-3}
Parameter set 3	4×10^5	$\pi/100$	1	1	$1/9\sqrt{2}$	0.5	1/10	10^9	1.4×10^{-3}
Parameter set 4	200	π	0.1	1	$1/9\sqrt{2}$	0.5	1/10	10^6	1.5×10^{-3}
Parameter set 5	100	$2\pi/3$	0.1	1	$1/9\sqrt{2}$	0.5	1/10	10^6	1.9×10^{-3}
Parameter set 6	75	$2\pi/6$	1	1	$1/9\sqrt{2}$	0.5	1/10	10^8	4×10^{-4}

Table 4.1: Sample parameter sets for the T_2 inflation model. Sets 1 to 4 define models in which the primordial power spectra of perturbations are approximately compatible with observations, whereas sets 5 and 6 do not. There are approximate scaling relations which map one set of parameters without changing the power spectrum. The value of W_0 in sets 2 and 3 is so high that corrections to the potential seem likely to appear (see § 4.3). We note however that these large values can be reduced using the scaling transformation, but the undesirable cost is that τ can drop below the string scale or a_2 can become too large. The last column shows approximate values for the variation of the canonically-normalized inflaton eq.(4.29) over the observable e-fold range, appropriately small *cf.* the Planck scale.

where

$$\Delta V = \frac{3W_0^2\xi}{4\mathcal{V}_m^3} + \frac{D_2}{\mathcal{V}_m} + \frac{\beta - D_4}{\mathcal{V}_m^2} \quad (4.27)$$

is a constant term, since \mathcal{V} and τ_i , $i > 3$ are all stabilized at the minimum, and D_2 , D_4 depend only on these τ_i .

The potential eq.(4.26) has seven parameters W_0 , a_2 , A_2 , λ_2 , α , ξ , and g_s whose meaning was explained in § 4.2. We have investigated the shape of the potential $V(\tau, \theta)$ for a range of these parameters. W_0 , a_2 , A_2 control the low energy phenomenology of this model (see [94]) and are the ones we concentrate on here for our inflation application. We shall not deal with particle phenomenology aspects in this paper. Some choices of parameters W_0 , a_2 , A_2 seem to be more natural (see [94]). To illustrate the range of potentials, we have chosen the six sets of parameters given in Table 1. There is some debate on what are likely values of W_0 in string theory. We chose a range from intermediate to large. Since there are scaling relations among parameters, we can relate the specific ones we have chosen to others. An estimate of the magnitude of W_0 comes from a relation of the flux 3-forms F_3 and H_3 which appear in the definition of W_0 (eq.4.5) to the Euler characteristic $\tilde{\chi}$ of the F-theory 4-fold, which is $\tilde{\chi} \sim \int F_3 \wedge H_3$ from the tadpole cancellation condition. This suggests an approximate upper bound $W_0 \sim \sqrt{\tilde{\chi}}$ [84]. For typical values of $\tilde{\chi} \sim 10^3$, we would have $W_0 \sim 10 - 100$. There are examples of manifolds with $\tilde{\chi}$ as large as 10^6 , which would result in $W_0 \sim 10^3$. Further, the bound itself can be evaded by $F_3 \wedge H_3 = 0$ terms. However, we do not wish to push W_0 too high so that we can avoid the effects of higher perturbative corrections (see § 4.3 for explanation). We can use the scaling property for the parameters to move the value of W_0 into a comfortable range. This should be taken into account while examining the table.

The parameter sets in the table can be divided into two classes: Trajectories in sets 1...4 produce a spectrum of scalar perturbations that is comparable to the experimentally observed

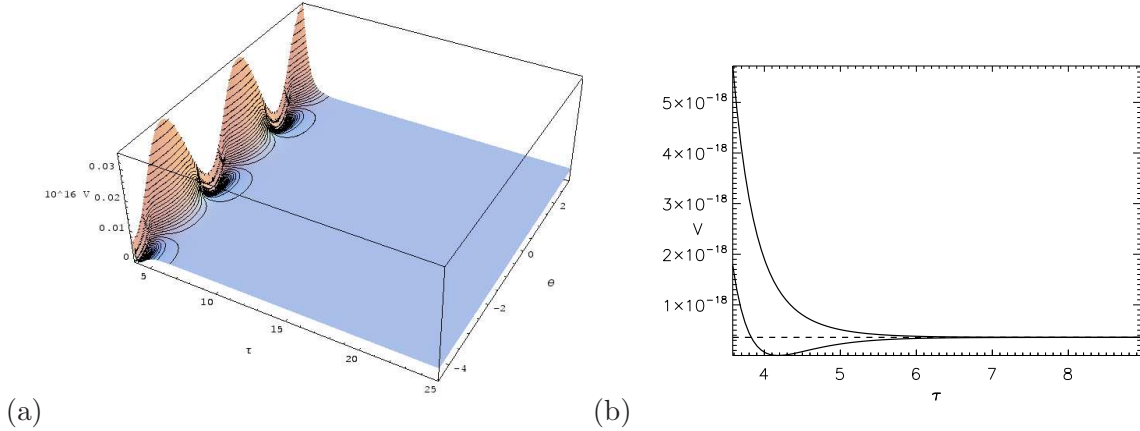


Figure 4.4: (a) The T_2 -potential surface $V(\tau, \theta)$ for the parameter set 1 of Table 4.5. Equipotential contour lines are superposed. Both τ and θ are multiplied by the characteristic scale a_2 . The surfaces for the other parameter sets in the Table are very similar when a_2 -scaled, even sets 5 and 6 with high W_0 . In all cases, we manually uplifted the potential to have zero cosmological constant at the minimum. The periodicity in the axionic direction and the constancy at large $a_2\tau$ are manifest. If instead of τ , we used the canonically-normalized field eq.(4.29) which is amplified by \sqrt{V} , the undulating nature in θ at large φ becomes more evident. However, the canonically-normalized inflaton is trajectory dependent and not a global function. (b) $V(\tau)$ for θ at $\cos(a_2\theta) = \pm 1$ shows how the flow for the positive value from large τ would be inward, but the flow would be outward for the negative value (and be unstable to θ perturbations). The dashed line is V_∞ , the $\tau \rightarrow \infty$ asymptote.

one (good parameter sets), whereas trajectories in parameter set 5 and 6 produce spectra whose normalization is in disagreement with observations (bad parameter sets). Sets 3 and 4 were chosen to large values of W_0 to illustrate how things change with this parameter, but we are wary that with such large fluxes, other effects may come into play for determining the potential over those considered here. A typical potential surface $V(\tau, \theta)$ is shown in Fig. 4.4 with the isocontours of $V(\tau, \theta)$ superimposed.

The hypersurface $V(\tau, \theta)$ has a rich structure. It is periodic in θ with period $2\pi/a_2$, as seen in Fig 4.4. Along $\theta = \frac{\pi(2l+1)}{a_2}$, where l is integer, the profile of the potential in the τ direction is that considered in [21]. It has a minimum at some $\tau = \tau_{min}$ and gradually saturates towards a constant value at large τ , $V(\tau) \rightarrow V_\infty(1 - Ca_2\tau e^{-a_2\tau})$, where C is a constant.² Along $\theta = \frac{2\pi l}{a_2}$, $V(\tau, \theta)$ falls gradually from a maximum at small τ towards the same constant value, $V(\tau) \rightarrow V_\infty(1 + Ca_2\tau e^{-a_2\tau})$. Trajectories beginning at the maximum run away towards large τ . Fig. 4.8(b) shows these two one-dimensional sections of the potential. For all other values of θ the potential interpolates between these two profiles. Thus, at large τ , the V surface is almost flat but slightly rippled. At small τ , the potential in the axion direction is highly peaked. Around the maximum of the potential it is locally reminiscent of the “natural inflation” potential involving a pseudo Goldstone boson [102, 103] (except that θ and τ must be simultaneously considered), as well as the racetrack inflation potential [19, 20].

²This type of potential is similar to that derived from the Starobinsky model of inflation [11] with a $\frac{M_p^2}{2} (R - \frac{1}{6M^2} R^2)$ Lagrangian via a conformal transformation, $V(\phi) = 6\pi M_p^2 M^2 [1 - \exp(-\frac{\phi}{\sqrt{12}\pi M_p})]^2$.

There are two approximate scaling symmetries in this model (in the asymptotics of (4.26) for $\mathcal{V} \gg \xi$), similar to those in [19],

$$\begin{aligned} a_i &\rightarrow u^{-1}a_i, (A_i, W_0, \xi) \rightarrow u^{3/2}(A_i, W_0, \xi), (\tau_i, \theta_i) \rightarrow u(\tau_i, \theta_i), (\lambda_i, \mathcal{P}_s, \epsilon) \rightarrow (\lambda_i, \mathcal{P}_s, \epsilon); \\ a_i &\rightarrow a_i, (A_i, W_0) \rightarrow v^{-3/2}(A_i, W_0), (\tau_i, \theta_i) \rightarrow (\tau_i, \theta_i), \mathcal{P}_s \rightarrow v^3\mathcal{P}_s, (\lambda_i, \xi, \epsilon) \rightarrow (\lambda_i, \xi, \epsilon) \end{aligned} \quad (4.28)$$

which can be used to generate families of models, trading for example large values of W_0 for small values of τ . For instance, applying the u scaling to parameter set 1, we can push the value of W_0 down to $W_0 \approx 2$, but at the same time pushing τ to lie in the range $\tau = 0.1 \dots 1.0$ during inflation, a range which is quite problematic since at such small τ higher order string corrections would become important.

More generally, for the supergravity approximation to be valid the parameters have to be adjusted to have τ_{min} at least a few: τ is the four-cycle volume (in string units) and the supergravity approximation fails when it is of the string scale. However, even if the SUGRA description in terms of the scalar potential is not valid at the minimum, it still can be valid at large τ , exactly where we wish to realize inflation. The consequence of small τ_{min} is that the end point of inflation, i.e. preheating, would have to be described by string theory degrees of freedom. We will return to this point in the discussion.

4.5.1 The Canonically-normalized Inflaton

If we define a canonically-normalized field φ by $d\varphi^2/2 = \mathcal{K}_{22}d\tau^2$, then

$$\varphi = \sqrt{\frac{4}{3} \frac{\alpha\lambda_2}{\mathcal{V} + \frac{\xi}{2}}} \tau^{3/4} M_p. \quad (4.29)$$

It is therefore volume-suppressed. For inflation restricted to the τ_2 direction, we identify φ with the inflaton. The field change $\Delta\varphi$ over the many inflationary e-foldings $N \equiv -\ln a/a_{end}$ is given in the last column in Table 1 for a typical radial (τ) trajectory. It is much less than M_p . (Here the scale factor at the end of inflation is a_{end} so N goes in the opposite direction to time.) The variations of the inflaton and the Hubble parameter *wrt* N ,

$$\frac{d\varphi/M_p}{dN} = \sqrt{2\epsilon}, \quad (4.30)$$

$$\frac{d \ln H/M_p}{dN} = \epsilon, \epsilon \equiv 1 + q, \quad (4.31)$$

suggest we must have a deceleration parameter q nearly the de Sitter -1 and the Hubble parameter H nearly constant over the bulk of the trajectories. This is shown explicitly in § 4.6 and Figures 4.8 and 4.9. The parameter $\epsilon(N)$ is the first “slow-roll parameter”, although it only needs to be below unity for inflation. With ϵ so small, we are in a *very* slow-roll situation until near the end of inflation when it rapidly rises from approximately zero to unity and beyond.

Equation (4.30) connects the change in the inflaton field to the tensor to scalar ratio $r = \mathcal{P}_t/\mathcal{P}_s$, since to a good approximation $r \approx 16\epsilon$. Since we find $\epsilon \ll 1$, we get very small r . The following relation [104, 105] gives a lower limit on the field variation in order to make tensor modes detectable

$$\frac{\varphi}{M_{\text{pl}}} \approx 0.46 \sqrt{\frac{r}{0.7}}. \quad (4.32)$$

We are not close to this bound. If φ/M_p is restricted to be < 1 in stringy inflation models, getting observable gravity wave signals is not easy. (A possible way out is to have many fields driving inflation in the spirit of assisted inflation [106].)

When the trajectory is not in the τ direction, the field identified with the canonically-normalized inflaton becomes trajectory-dependent as we describe in the next section and there is no global transformation. That is why all of our potential contour plots have focused on the Kähler modulus and its axion rather than on the inflaton.

4.6 Inflationary Trajectories

4.6.1 The Inflaton Equation of Motion

We consider a flat FRW universe with scalar factor $a(t)$ and real fields (τ, θ) . To find trajectories, we derive their equations of motion in the Hamiltonian form starting from the four dimensional Lagrangian (see [100] and references therein)

$$\mathcal{L} = \sqrt{-g} \left(R + G_{ij} \dot{\phi}^i \dot{\phi}^j - V \right), \quad (4.33)$$

with canonical momentum $P_i = \frac{\partial \mathcal{L}}{\partial \dot{\phi}^i} = 2a^3 G_{ij} \dot{\phi}^j$, where we used $\sqrt{-g} = a^3$ and ϕ_i , $i = 1, 2$ stands for (τ, θ) . (The usual field momentum is P_i/a^3 .) Here the non-canonical kinetic term is

$$G_{ij} = \mathcal{K}_{22} \delta_{ij}, \quad \mathcal{K}_{i\bar{j}} = \frac{\partial^2 \mathcal{K}}{\partial T^i \partial \bar{T}^j}. \quad (4.34)$$

The Hamiltonian is

$$\mathcal{H} = P_i \dot{\phi}^i - \mathcal{L} = \frac{1}{a^3} G^{ij} P_i P_j + V, \quad (4.35)$$

where $G^{ij} = G_{ij}^{-1}$. The equations of motion follow from $\dot{\phi}^i = \frac{\partial \mathcal{H}}{\partial P_i}$, $\dot{P}_i = -\frac{\partial \mathcal{H}}{\partial \phi^i}$, which reduce to

$$\dot{\phi}^i = \frac{1}{2a^3} G^{ij} P_j, \quad \dot{P}_i = -\frac{1}{4a^3} \frac{\partial G^{kl}}{\partial \phi^i} P_k P_l - a^3 \frac{\partial V}{\partial \phi^i}, \quad \dot{a} = aH, \quad \dot{H} = -\frac{1}{4a^6} G^{ij} P_i P_j. \quad (4.36)$$

We also use the constraint equation

$$M_P^2 H^2 = \frac{1}{3} \left(\frac{1}{4a^6} G^{ij} P_i P_j + V \right) = M_P^2 H^2 \epsilon/3 + V/3 \quad (4.37)$$

to monitor the accuracy of the numerical integration routine. Note that the deceleration, eq.(4.31), is related to the non-canonical kinetic term in the implicit manner indicated.

The inflaton is defined to be the field combination along the classical (unperturbed) trajectory. Isocurvature (isocon) degrees of freedom are those perpendicular to the classical trajectory. The kinetic metric in M_P units is $d\psi^2 = G_{ij}d\phi^i d\phi^j / M_P^2$. If θ is fixed, then ψ is related to φ introduced in § 4.5.1 by $\psi = \varphi / (\sqrt{2}M_P)$. More generally, the inflaton between the initial condition $\phi^i(N_0)$ and the value $\phi^i(N_1)$ is the distance along the path, $\int d\psi$. For our case with diagonal G_{ij} , it is

$$\psi = \int \sqrt{\mathcal{K}_{22}} d\tau (1 + d\theta^2/d\tau^2)^{1/2}. \quad (4.38)$$

4.6.2 Stochastic Fluctuations and CMB and LSS Constraints

The classical trajectory is perturbed by zero point fluctuations in all fields present, but only degrees of freedom with small mass will be relevant, hence in τ and θ , which in turn influence the scalar metric fluctuations encoded in $\ln a = -N$, and in the gravitational wave degrees of freedom. Structure formation depends upon the fluctuations in the scalar 3-curvature, which are related to those in $\ln a$ measured on uniform Hubble surfaces [107, 108], $\delta^{(3)}R = 4(k/a)^2 \delta \ln a|_H$. The usual result for single-field inflation is motivated by stochastic inflation considerations: the zero point fluctuations in the inflaton at “horizon crossing” when the three-dimensional wavenumber $k \approx Ha$ are $\delta\psi = [H/(2\pi M_P)]/\sqrt{2}$. Equation (4.30) gives the mapping, $\delta \ln a|_H = \delta\psi/\sqrt{\epsilon}$ along the inflaton direction. Thus the scalar power spectrum is

$$\mathcal{P}_s \equiv k^3/(2\pi^2) \langle |\delta \ln a|_H(k)|^2 \rangle = [H/(2\pi M_P)]^2/(2\epsilon) e^{2u_s}, \quad (4.39)$$

where u_s encodes small corrections to this simple stochastic inflation Hawking temperature formula.

The graviton zero point oscillations are, like those in a massless scalar field, proportional to the Hawking temperature at $k = Ha$,

$$\mathcal{P}_t(k) = 16 [H/(2\pi M_P)]^2/2 e^{2u_t}. \quad (4.40)$$

where u_t also encodes small corrections. The ratio $r(k)$ is therefore $\approx 16\epsilon$.

The scalar spectral index is given by $n_s - 1 = d \ln \mathcal{P}_s / d \ln k$. At lowest order, and for small ϵ , it is $n_s - 1 = -2\epsilon - \epsilon'/\epsilon$, where $\epsilon' \equiv d\epsilon/d \ln a$. To have ϵ nearly zero as our trajectories do, and yet have n_s differing at the 2-sigma level from unity as the current cosmic microwave background (CMB) and large scale clustering data indicate, imposes a constraint on ϵ'/ϵ which might seem to require a fine-tuning of the potential.

The current best estimate of n_s in flat universe models characterized by six parameters, in which gravity waves are ignored, is 0.96 ± 0.017 with CMB only, and 0.958 ± 0.015 with CMB and large scale structure (LSS) clustering data [8]. The errors are Bayesian 1-sigma ones. For

future reference, we note that the CMB data prefer a running of the scalar index at about the 2-sigma level, $dn_s/d\ln k = -0.047 \pm 0.021$ at a pivot point $k_p = 0.05 \text{ Mpc}^{-1}$. However, the 6 parameter case with no running is a very good fit, except in the low ℓ regime. The preferred amplitude of the scalar perturbations is $\mathcal{P}_s(k_p) = [21_{-1.0}^{+1.3}] \times 10^{-10}$. It is interesting to note that this number has been stable for a long time: the estimate from the COBE DMR experiment without the addition of any LSS or smaller scale CMB experiments was $[21 \pm 3] \times 10^{-10}$ when extrapolated with this $n_s = 0.96$ slope, and only slightly higher with no tilt [108].

The current constraint on the gravity wave contribution is $\mathcal{P}_t/\mathcal{P}_s < 0.6$ at the 95% confidence limit with CMB data (with the powers evaluated at the pivot point 0.002 Mpc^{-1}). When LSS data is added to the CMB, this drops to an upper limit of 0.28 but requires a single slope connection of the low k regime in which the tensors can contribute to the CMB signal and high k where the amplitude of LSS fluctuations is set. Relaxing this allows for higher values [83].

With the CMB-determined \mathcal{P}_s estimate, we have $[H/(2\pi M_P)] \approx 6.5 \times 10^{-5} \sqrt{\epsilon}$. If the acceleration ϵ were uniform over the observable range and gave rise to this n_s , we would have $\epsilon = 0.02$, $[H/(2\pi M_P)] \approx 10^{-5}$ and $r \sim 0.3$. But our trajectories have ϵ nearly zero and H almost flat, so to get the observed n_s the observable range would have to be well into the braking period towards preheating: *i.e.*, we would need $\epsilon'/\epsilon \approx 0.04$ over the CMB+LSS window, which seems like it would require a very finely-tuned potential. Rather remarkably, the first cases we tried gave values near this at the relevant number of e-foldings before the end of inflation. This point was also made by Conlon and Quevedo [21] for pure τ trajectories. We also find there is room for modest running of the scalar index over the observable window. (Note that the tensor slope $n_t \equiv d\ln \mathcal{P}_s/d\ln k$ is $\approx -2\epsilon$, hence very small.) A consequence of the small ϵ is $[H/(2\pi M_P)] \sim 10^{-10}$ and $V^{1/4} \sim 10^{14} \text{ GeV}$.

We caution that the single field model we used to estimate \mathcal{P}_s includes fluctuations only along the trajectory. There will also be fluctuations perpendicular to it, and fluctuations in the parallel and perpendicular directions can influence each other. The latter are isocurvature degrees of freedom. Although these will leave the \mathcal{P}_t formula unaffected, we expect modifications in the \mathcal{P}_s formula, a point we return to after making an inventory of the sorts of trajectories that will arise.

4.6.3 Trajectories with General Kähler modulus and Axion Initial Conditions

The τ -valley Attractor

We first restrict ourselves to trajectories in τ to connect with the Conlon and Quevedo [21] treatment. The stable flow is in the $\theta = \frac{2\pi l}{a_2}$ trough. As can be seen in Fig. 4.5(a), enough e-foldings for successful inflation are possible provided one starts at large enough τ . The dashed line in Fig. 4.8(a) shows ϵ is very small for this case, of order $\epsilon \approx 10^{-10}$. For the parameters we have considered, no effective inflation is possible if we start inward of τ_{min} rather than outward.

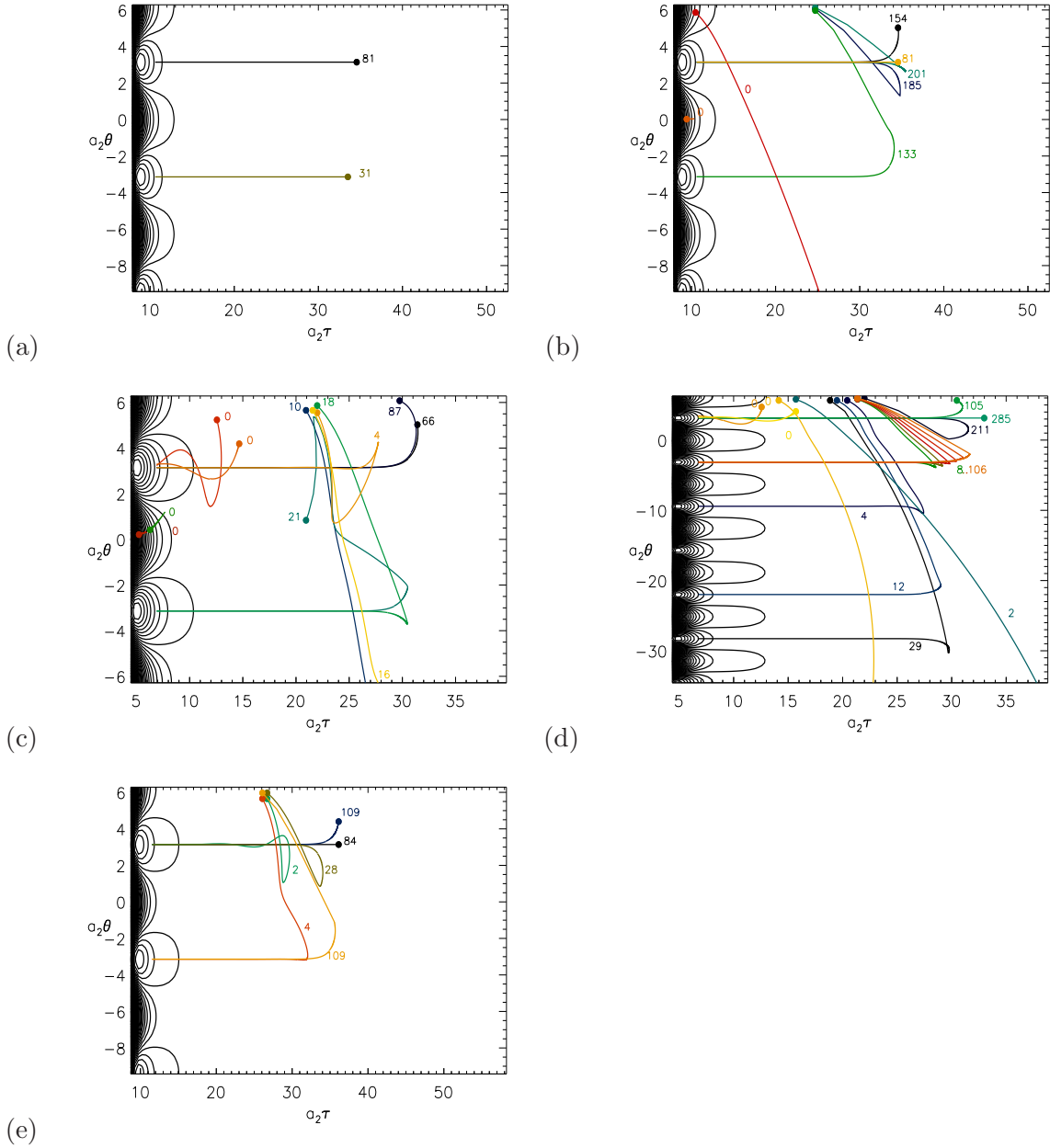


Figure 4.5: Contour-plots of the potential including trajectories for several choices of initial values (denoted by filled circles) in field space (τ, θ) . The trajectories are evolved numerically until inflation ends at $\epsilon = 1$. The number of e-folds is indicated next to the corresponding trajectory. During the last stages of inflation, the field always rolls along one of the valleys towards the minima which are located in the centre of the white circles. The maxima are located in the dark spots. Inflation in the axion direction can significantly enhance the amount of inflation over that obtained in pure τ inflation. Trajectories starting at large τ roll to the nearest valley, then to the minimum. But starting at intermediate τ with the axion sufficiently far from its minimum, we find the field can cross several θ -ridges before settling into a valley. Another manifestation is the run-away character for τ if the axion is placed close to its maximum. (a) shows the simple pure- τ inflation if θ is set to its minimum, as in Conlon and Quevedo, for parameter set 1. (b) shows the complex evolution for sample general starting conditions, for parameter set 1, (c), (d) and (e) show the same for sets 2, 3 and 4, respectively.

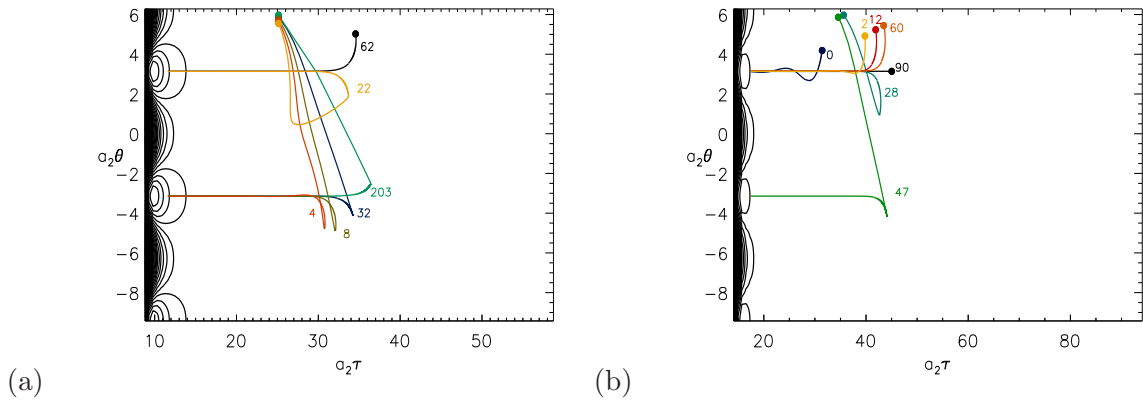


Figure 4.6: Sample trajectories for parameter sets 5 (a) and 6 (b), which have scalar power spectra amplitudes incompatible with the data. These still look similar to those in Fig. 4.5.

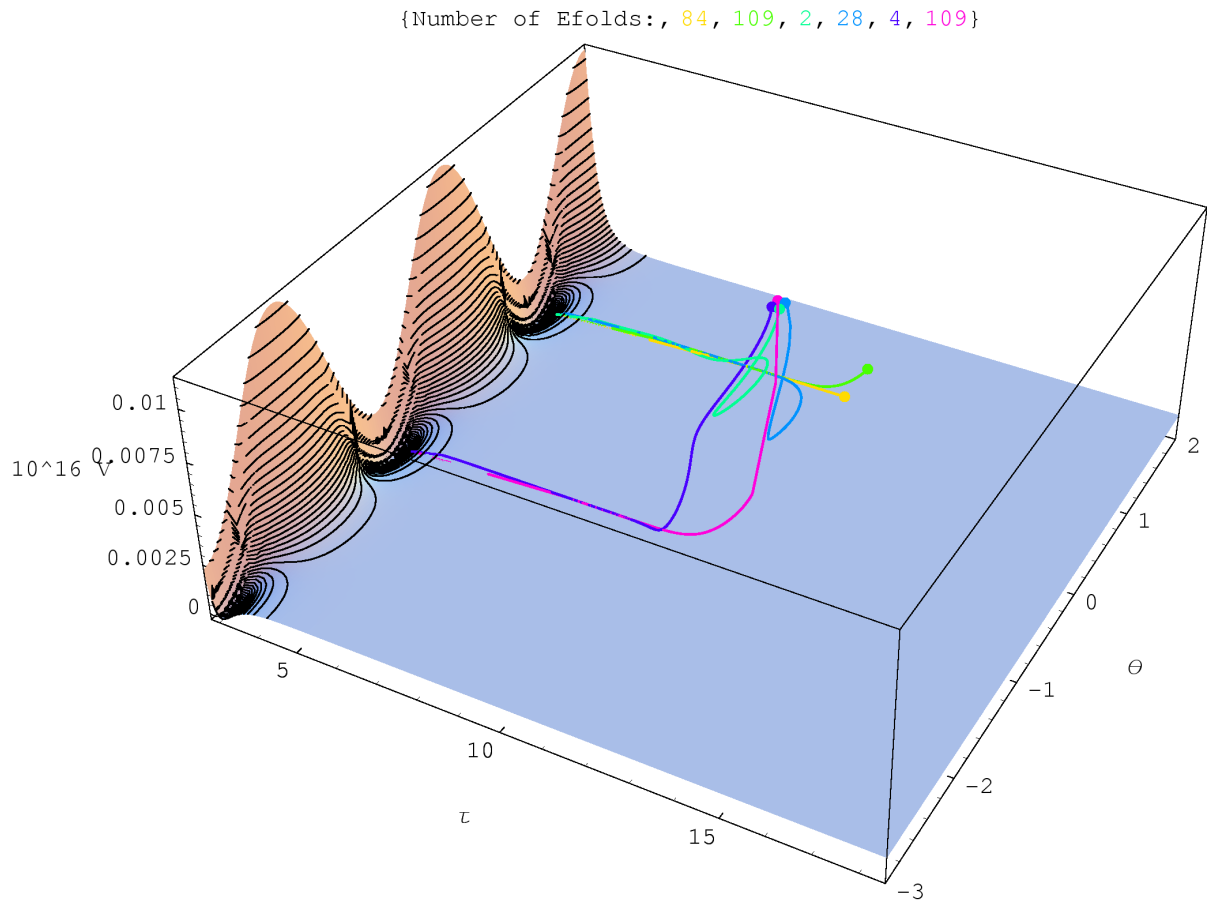


Figure 4.7: Potential with inflationary trajectories for parameter set 4. Shown is a plot of the potential in the (τ, θ) -plane, overlaid with equipotential contours. Note that for $\tau > 5$ there are no contours because the potential is exponentially flat but it still has the periodic structure in the θ -direction. The starting points of the trajectories are indicated by filled circles.

Another class of τ trajectories are those along the “ridge” where $\theta = \frac{2\pi l}{a_2}$ gives a positive contribution to the potential. These are unstable to small displacements in the axion direction.

The τ -trough trajectories serve as late-time attractors for initial conditions that begin with θ out of the trough. The very flat profile of the potential at large τ allows for a regime of self-reproducing inflation (§ 4.7). Trajectories which originate in the self-reproducing regime invariably flow to the τ -valley attractor and the observed e-folds would be just those of the Conlon and Quevedo sort.

The Variety of “Roulette” τ - θ Trajectories

When we allow the initial values of τ and θ to be populated with an equal a priori probability prior, given a set of parameters defining the $V(\tau, \theta)$ surface, we encounter a wide range of inflationary trajectories. Examples of the variety of behaviours for the parameter sets given in Table 1 are shown for $\tau(\ln a), \theta(\ln a)$ in Figures 4.5 and 4.6, and for $H(\ln a), \epsilon(\ln a)$ in Figures 4.8 and 4.9. Some of the trajectories are predominantly θ ones before settling into a τ -valley, similar to a roulette ball rotation before locking into a slot with a specific number, hence the name roulette inflation.

We began with the momenta of the fields set to zero, but the momenta are very quickly attracted to their slow-roll lock-in values, on of order an e-fold. We do not show this settling down phase in the trajectories we have plotted. We find a large fraction of trajectories are indeed inflating, and have the required $> 40 - 50$ e-folds of inflation (§ 4.6.3) to give homogeneity and isotropy over our observable Hubble patch. Large enhancements of the number of e-folds over τ -only inflation can occur because of significant flows in the θ -direction, while τ evolves slowly. As the figures show, initial values starting far out in τ generally roll towards the nearest τ -valley and then proceed along the τ -attractor. Trajectories starting at intermediate τ have enough energy to pass through the τ -valley in the axionic direction, but often turn around before reaching the neighbouring ridge, and roll back into the valley. They can move to larger τ while in the axion-dominated flow. If the initial values are chosen such that the initial potential energy is just a little higher, the inflaton can climb over the next ridge and settle in the adjacent valley, or the next one, or the next. Thus there exists bifurcation points which divide the phase space into solutions ending up in different valleys. Another feature in Fig. 4.5 is the existence of areas in which tiny changes in initial positions can lead to dramatic changes in the number of e-folds produced.

There are also cases in which the τ -attractor is not reached before the end of inflation. When starting from moderate values in τ , relatively far away from the valley, the field oscillates in the θ direction, albeit producing only a very small number of e-folds $N < 1$ (see Fig. 4.5 for examples).

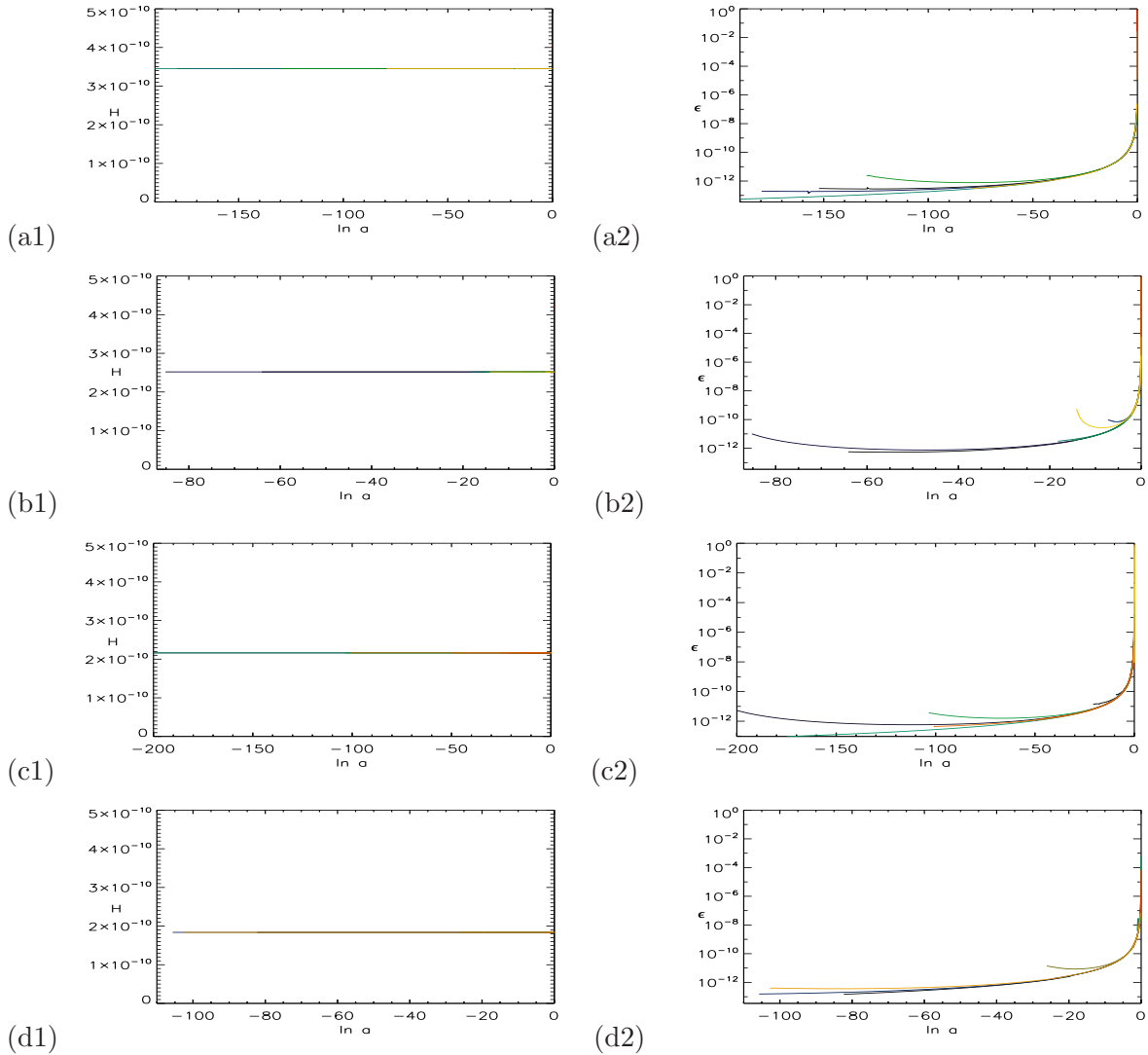


Figure 4.8: Hubble parameter $H(\ln a)$ (left column) and deceleration parameter $\epsilon(\ln a)$ (right column) as a function of the number of e-folds. $H(\ln a)$ is practically constant during inflation. ϵ during inflation is tiny and generally turns up towards the reheating phase rather rapidly. (a) Parameter set 1: the coloured trajectories are for general (τ, θ) inflation, the dashed trajectory is inflation strictly along τ (b,c,d) are the same for sets 2, 3, 4, respectively. Note that units along the x-axes are $\ln a = -N \approx \ln k$ here and in the plots for the power spectra. There is a very rapid phase in which the trajectory settles down to an attractor for the τ and θ field momenta which we do not show.

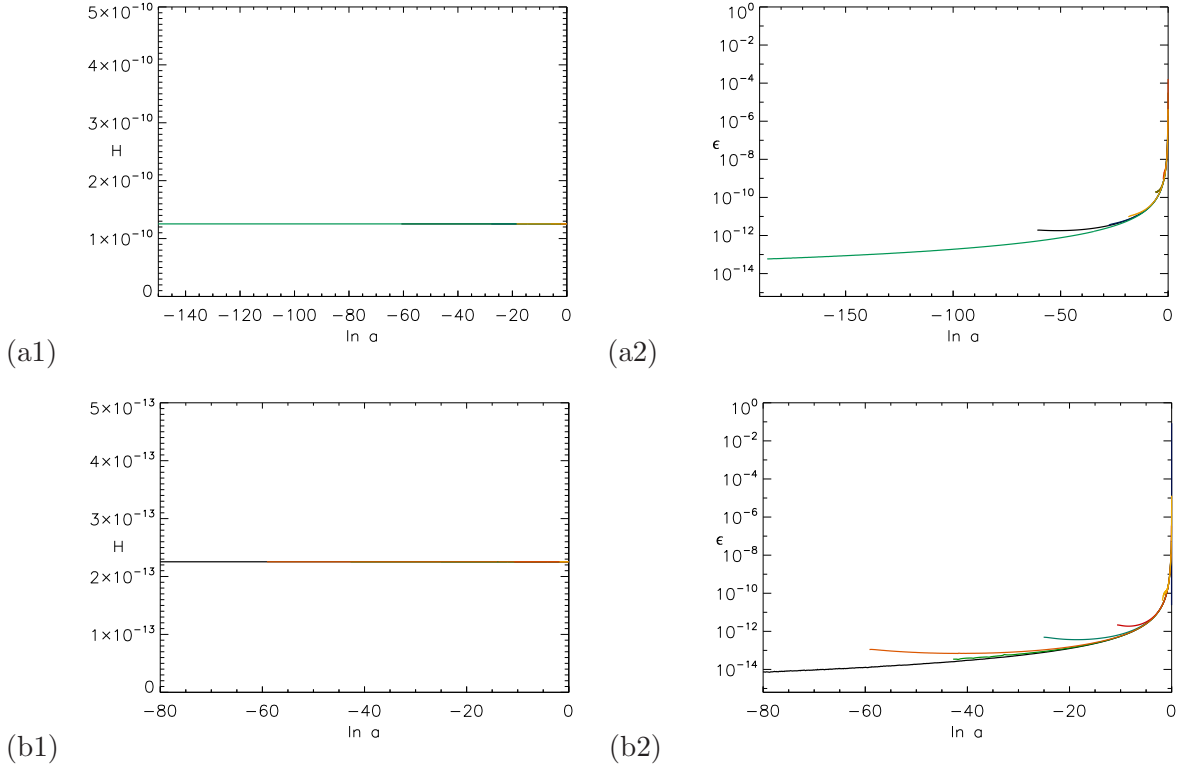


Figure 4.9: Same as Fig. 4.8, but for parameter sets 5 (a) and 6 (b).

The Scalar and Tensor Power Spectra and Isocurvature Effects

We estimate the power spectra $\mathcal{P}_s(k)$ using the single inflaton approximation, eq.(4.39), and $\mathcal{P}_t(k)$ using eq.(4.40), which only require H and ϵ for each trajectory. These are shown in Figures 4.10 and Figures 4.11. As expected from the very small ϵ 's we have encountered, to match \mathcal{P}_s and hence H^2/ϵ to the data would require small H , low energy inflation, and hence very small gravity wave power, $\mathcal{P}_t \propto [H/M_P]^2$.

For comparison, Figures 4.10 and Figures 4.11 also show the best-fit scalar power spectra that were obtained by the ACBAR collaboration [8] using CMB and LSS clustering data. The fixed power law case has $n_s = 0.96$. The spectrum with running has best-fits $n_s = 0.911$, $dn_s/d \ln k = -0.044$. Obviously the running model can at best be valid only over a limited number of e-foldings. We indicate the observable range of e-foldings by the heavy black line in the power spectrum figures. As we show below, the mapping of wavenumber to number of e-foldings is imprecise but because the energy of inflation is low, the relevant range for CMB+LSS observables is in the range $N = -\ln a \in [40, 50]$. For definiteness we take the pivot point k_p for running to be at $N = 45$.

To compute the scalar power spectra we assumed that the generation of fluctuations is driven by small perturbations along the trajectories, neglecting the effect of isocurvature fluctuations coming from perturbations perpendicular to this direction. We will now discuss why this might

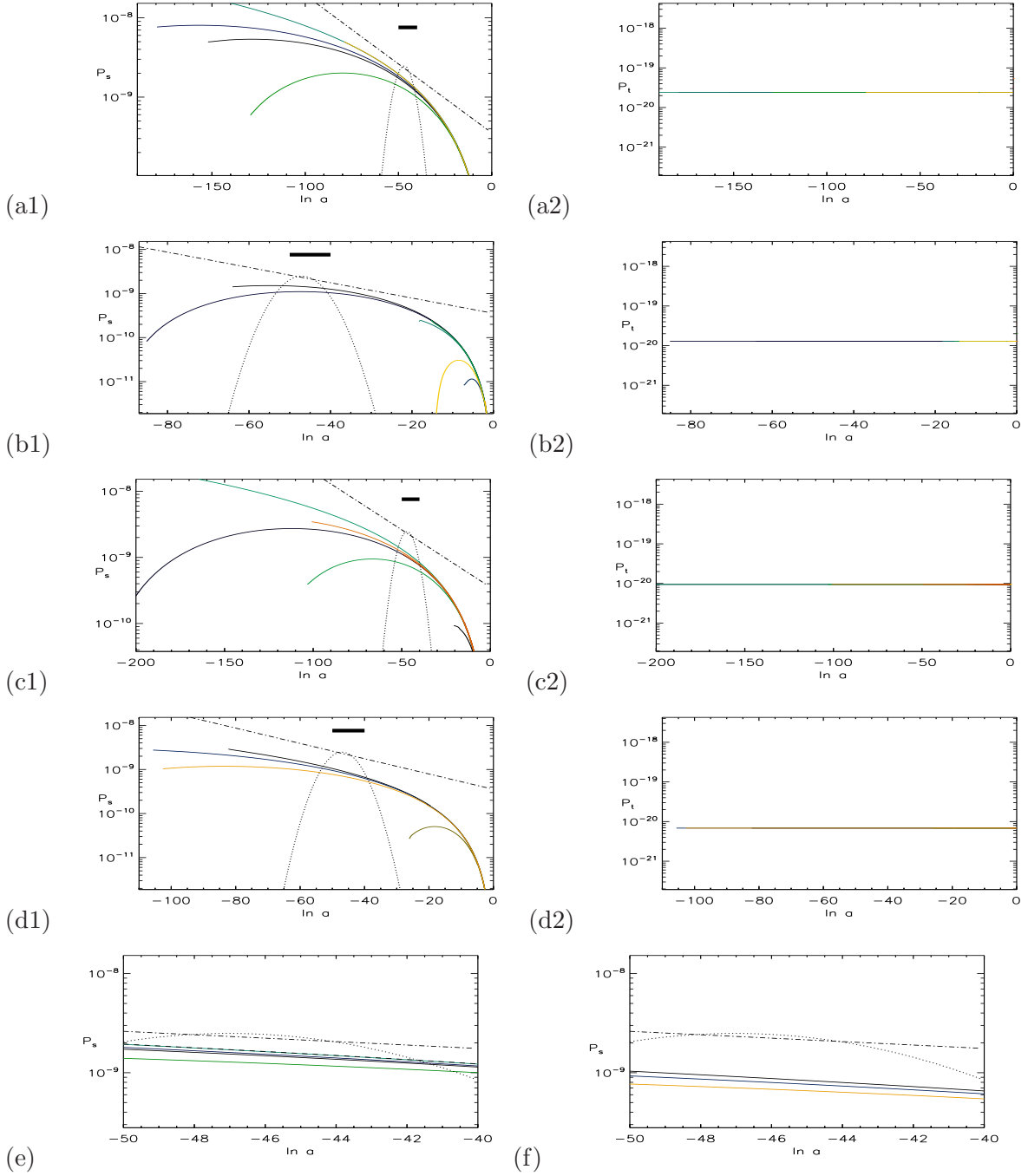


Figure 4.10: Power spectra for scalar \mathcal{P}_s and tensor \mathcal{P}_t fluctuations, derived assuming that only stochastic kicks along the trajectory are relevant for their determination, neglecting the influence of “isocurvature” fluctuations transverse to the inflaton trajectory. Both have amplitudes given by the instantaneous Hawking temperature. For comparison we present two template spectra: The dashed-dotted line shows a simple spectrum with no running of the spectral index $n_s = 0.96$. The dotted line is a simple spectrum with running of the spectral index $n_s = 0.91$, $dn_s/d \ln k = -0.044$, using values obtained by the ACBAR collaboration [8]. Both these spectra have the normalization set to $\mathcal{P}_s = 2.1 \times 10^{-9}$ at $N = 45$. (a,b,c,d) are for parameter sets 1, 2, 3 and 4. The dashed line corresponds to inflation with $\theta = \text{const}$ in the valley. Even though there is significant running for all models over large scales, the spectra are mostly featureless in the observable interval which panels (e) and (f) zoom into for sets 1 and 4.

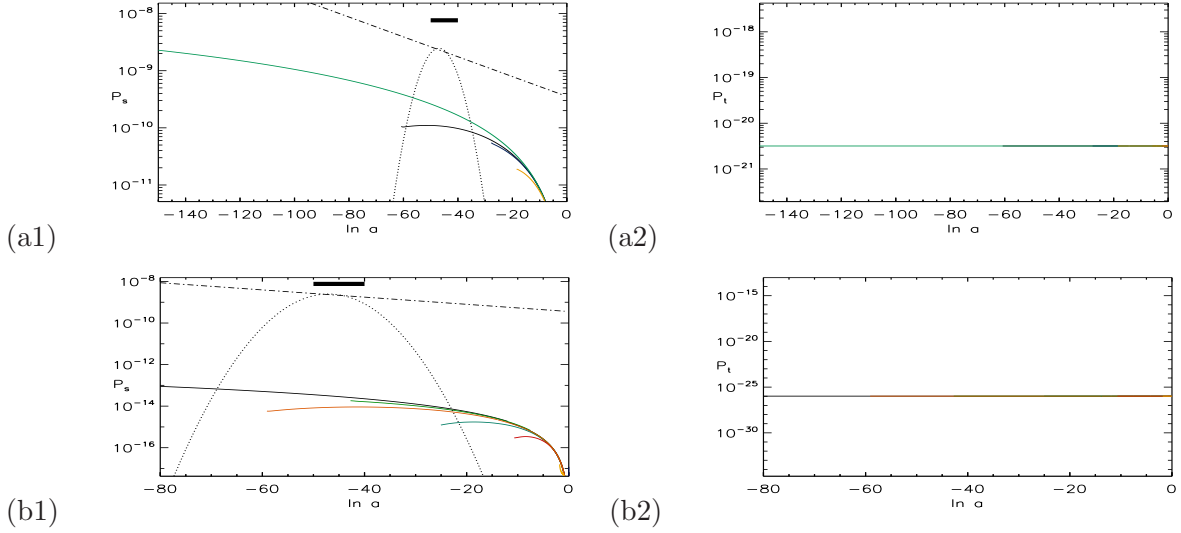


Figure 4.11: Power spectra for potentials with parameter sets 5 and 6 that do not give a scalar amplitude near to the observed value.

not necessarily catch the whole picture. In Fig 4.5d, there are a set of trajectories with initial values around $\tau \approx 21$ very close to each other where all fields end up in the second valley from the top. Two things are striking about those realizations of inflation: (1) the trajectories flange out when rolling down the axion towards larger τ 's during the first part of their evolution; (2) the number of e-folds of inflation varies tremendously from as little as $N \approx 8$ all the way to $N \approx 106$ when going towards larger initial θ 's while keeping τ fixed. The scalar spectra we compute for these flanging trajectories differ substantially, and make it clear that our simple single field algorithm will be unjustified in some regions of the space of initial conditions. Even though the transverse quantum jitter is characterized by very small H/M_P with width much smaller than the size of the curves in the figure, we recognize that tiny changes during the initial period of evolution in certain areas could produce big effects, an area for future investigation.

Number of e-folds N and the wavenumber of perturbations

Since our trajectory computations are in terms of $\ln a/a_{end}$, whereas the observables probe $k \sim Ha$ in Mpc^{-1} , we need to connect the two. The CMB+LSS probe k from $\sim 10^{-4} \text{Mpc}^{-1}$ to $\sim 1 \text{Mpc}^{-1}$, about 10 e-foldings. According to general lore (see e.g. [109]) the number of e-folds N as a function of k is given by

$$N(k) = 62 - \ln \frac{k}{6.96 \times 10^{-5} \text{Mpc}^{-1}} + \Delta, \quad (4.41)$$

where $6.96 \times 10^{-5} \text{Mpc}^{-1}$ is the inverse size of the present cosmological horizon and Δ is defined by the physics after inflation:

$$\Delta = -\ln \frac{10^{16} \text{GeV}}{V_k^{1/4}} + \frac{1}{4} \ln \frac{V_k}{V_{\text{end}}} - \frac{1}{3} \ln \frac{V_{\text{end}}^{1/4}}{\rho_{\text{reh}}}, \quad (4.42)$$

where ρ_{reh} is the energy density at the end of reheating, V_k is the value of the inflaton potential at the moment when the mode with the comoving wavenumber k exits the horizon at inflation and V_{end} is the value at the end of inflation. We will not go into any details about this formula or its derivation, but merely motivate some numbers for the individual terms.

Starting with Δ , we note that for its first term, $H \approx 3 \times 10^{-10} M_{\text{pl}}$ corresponds to $V_k^{1/4} \sim 10^{13}$ GeV. The second term can be neglected in our case, and the last term in the expression for Δ depends on the details of (p)reheating (which can be perturbative preheating, non-perturbative reheating or reheating involving KK-modes) which we put in the range of $1 < \Delta < 10$. Putting it all together we find that $\Delta \in [-17, -8]$. Therefore the observable range is about 10 e-folds inside the interval [35,55], with the exact location of the former depending on the details of reheating. For the purpose of our discussion, we take the observable $N \in [40, 50]$, and indicate this range by the black bar in Fig 4.10. We note that the required number of e-foldings is significantly lower than 65.

4.7 Stochastic Regime of Self-Reproduction

Our potential is flattening exponentially rapidly as τ increases. Therefore the velocity of the fields which are placed at large enough τ will be rather small. This opens the possibility for stochastic evolution of the fields due to their quantum fluctuations dominating over classical slow-roll [110, 107]. We now show that in the model (4.18) there is region of (τ, θ) space where the regime of self-reproduction operates. We distinguish this regime from the regime of eternal inflation due to bubble nucleations between different string vacua.

The criterion for self reproduction is actually that scalar perturbations are at least weakly nonlinear and that perturbation theory breaks down. The drift in each e-fold of the scalar ϕ^i is $\Delta\phi^i = G^{ij}(P_j/a^3)/(2H)$ where P_j/a^3 is the canonically-normalized field momentum. The corresponding drift in the normalized inflaton ψ is $\Delta\psi = \sqrt{\epsilon}$. The *rms* diffusion due to stochastic kicks is $\delta\psi = [H/(2\pi M_P)]/\sqrt{2}$, as given in § 4.6.2. The *rms* kick beats the downward drift when $\mathcal{P}_s^{1/2} \approx [H/(2\pi M_P)]/\sqrt{2\epsilon}$ exceeds unity, that is the fluctuations become non-perturbative. With such a flat nearly de Sitter potential, this is possible.

We now wish to consider this boundary as a function of θ as well as τ . In general it is impossible to bring both of their kinetic terms simultaneously into canonical form. However, when we consider the fluctuations of fields, we can revert to the approximation in which the Kähler metric stays approximately constant over the time-scales of the fluctuations. The result

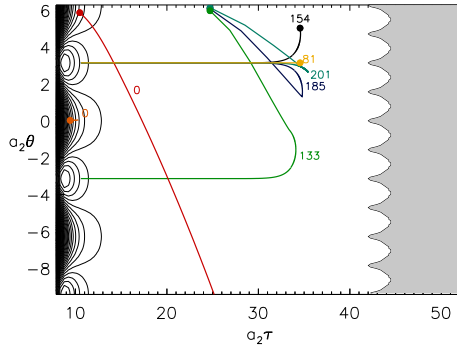


Figure 4.12: The self-reproduction region in which stochastic kicks dominate over the classical downward drift is indicated by the grey shaded area superposed upon the contour plot of the potential and some of its inflationary trajectories for parameter set 1. The most interesting trajectories start from outside of the quantum region. Those coming from the stochastic region will be attracted to the $\theta = \frac{2\pi l}{a_2}$ τ -trough trajectories.

is the following condition for the region where quantum fluctuations dominate over drift:

$$\frac{V}{12\pi^2} > \frac{1}{G_{\tau\tau}} \left(\frac{V_{,\tau}}{V} \right)^2, \quad \frac{V}{12\pi^2} > \frac{1}{G_{\theta\theta}} \left(\frac{V_{,\theta}}{V} \right)^2. \quad (4.43)$$

This result is consistent with starting from $\ddot{\phi}^i + 3H\dot{\phi}^i + \Gamma_{jk}^i \dot{\phi}^j \dot{\phi}^k + G^{ij} V_{,\phi^j} = 0$, using slow-roll to neglect terms of $O(\dot{\phi}^2, \ddot{\phi})$ and using the diagonality of G . In Fig. 4.12 we replot potential contours with various trajectories for parameter set 1, but with the drift/diffusion boundary now shown. Starting trajectories with arbitrary θ at the boundary should lead to large kicks in θ as well as τ , but ultimately a settling into a τ -trough well before the observable N range is approached. In that case, the θ complexity of trajectories would not manifest itself.

Will the universe truly be in a stochastic regime of self-reproduction – the scenario of eternal inflation [111] – within such a model? The picture is of the last hole jittering about in size at τ far from the potential minimum. If the last hole can jitter about far away from equilibrium, then the same phenomenon would be expected for other holes that we took to be stabilized before the last stages of T_2 settle-down. In that case, it is unclear how the initial conditions for T_2 would be fed, but the most probable source of trajectories would not necessarily be from the T_2 self-reproduction boundary. In all cases, it is unclear whether further corrections to the potential way out there will uplift it to a level in which drift steps exceed diffusion steps. Fortunately, we are not dependent on such an asymptotically flat potential for the inflation model explored here to work.

4.8 Discussion and Summary

We have investigated inflation in the “large volume” compactification scheme in the type IIB string theory model of [84, 18, 85]. Dynamics in the model are driven by Kähler moduli associated with four cycles and their axionic partners, $T_i = \tau_i + \theta_i$. We focused on the situation when all Kähler moduli/axions and the compact volume are stabilized at their minima except for a last modulus/axion pair $T_2 = (\tau, \theta)$ which we identified with the “observed” early universe inflaton. We showed that T_2 dynamics does not perturb the global minimum of the total potential if T_2 operates on a lower energy scale than that associated with the earlier stabilizations. To do this, three or more moduli were needed. We explicitly demonstrated stabilization with a three field example, T_1, T_2, T_3 . We also showed volume destabilization can occur even if it is initially stabilized if there are only two Kähler moduli, T_1, T_2 .

The two-dimensional potential $V(\tau, \theta)$ has a rich ridge-trough, hill-valley structure. We derived and solved the equations of motion of the (τ, θ) system appropriate to an expanding universe using the Hamiltonian formalism of [100]. The non-canonical nature of the kinetic terms played an important role in defining the evolution.

The ensemble of inflationary trajectories is a rich set. We first studied inflation in the τ direction, along the valleys of the potential surface, which are late-time attractors for most of the general trajectories. For example, trajectories originating in the region of self-reproduction we identified in § 4.6.2 — where stochastic diffusive kicks can beat classical field drift — would invariably finish in the τ -troughs. We calculated the number of e-folds N , the time variation of the Hubble parameter as a function of $\ln a$, $H(\ln a)$, the time variation of the acceleration history as encoded in the “first slow roll parameter” $\epsilon(\ln a)$, and the power spectrum for scalar \mathcal{P}_s and tensor \mathcal{P}_t fluctuations for many τ -trajectories in the different realizations of the potential we explored. We can use the tools of single field inflation with confidence to compute the spectra if we are only following evolution of the inflaton within the Kähler modulus valley. Our results support the conclusions of Conlon and Quevedo [21] who first suggested this model of inflation. In particular, trajectories exist in the “prior” ensemble which satisfy the CMB+LSS data.

Our main objective was to study inflation with general initial conditions for (τ, θ) . We found that trajectories originating in elevated parts of the potential (near its maxima or its ridges) with moderate to large initial τ values can pass over many valleys and hills in θ before settling into a final τ -valley approach to the end of inflation. These roulette wheel trajectories have an enhanced numbers of e-foldings relative to pure τ trajectories. It is also preferable to have 200 good trajectories with a single complex field rather than one good trajectory with 200 complex fields as occurs in the string version [80] of “assisted inflation” [106]. The power spectra of scalar fluctuations for trajectories along a general direction need to be calculated using tools appropriate to multiple-field inflation. In order to estimate the amplitude we used expression (4.39) for single field stochastic inflation. We found indications of weak running in the spectral index over the observable range for some trajectories, and no running for others. To the extent that these single-inflaton estimations are reasonable, we again found plenty of

roulette trajectories exist which satisfy the CMB+LSS data. Including the influence of the isocurvature degree of freedom on the observed power spectrum is needed to be completely concrete about such conclusions.

Although there can be pure τ -trajectories, we have not found pure θ trajectories to be possible. The “natural inflation” model explored in [102, 103] had a radial and an angular field, in a Mexican hat potential in which the Goldstone nature of the angular direction was broken into a $\cos(a_2\theta)$ type term only after the radial motion settled into the θ -trough with random θ values. (The a_2 was also associated with non-perturbative terms similar to those invoked here.) The radial motion could come from either the small or large direction, the latter being like a chaotic inflation scenario for a first (unobserved) stage of inflation. The observed inflaton was to be identified with the angular motion from near a θ maximum, where some fraction of the random θ would reside, towards a θ minimum. One of the features of the model was that near the maximum one could use the potential shape to get small gravity waves and yet significant scalar tilts.

Why is our model so different? In a \cos potential, inflation is possible in the immediate neighbourhood of the maximum, and so it is with our potentials if τ could be fixed. However we have found that beginning in the θ heights of our potentials near $\tau_{2,min}$ results in an outward radial flow, and, incidentally, insufficient e-folds to be of interest. These low τ heights are not populated from inward τ -flows. This is because angular dynamics are intimately tied to radial dynamics since the symmetry breaking of θ and τ are due to the same process, so hills and valleys in θ are at all radii, ultimately guiding θ trajectories to the τ -valleys. And our approach to the minimum is from a large radius flat potential rather than a growing chaotic inflation one. In general, we believe that our two-field Kähler modulus model gives a more natural inflation than natural inflation.

The inflaton potential at large τ is very shallow and in both the Kähler modulus and axion directions the motion rolls very slowly, even more so for larger τ . In both τ and θ quantum kicks in the (quasi) de Sitter geometry can dominate over the classical slow roll drift. We identified this regime of the self-reproducing universe in our models.

However, to have a self-reproduction regime depends on the immunity of the model against perturbative corrections, as we discussed in § 4.3. Corrections may lead to polynomial terms in τ in $V(\tau, \theta)$ which may spoil the flatness, and possibly even spoil inflation itself. This problem is specific to the models of inflation associated with large τ , as here. Models where inflation is realized with small values of the Kähler moduli, like “(better) racetrack inflation”, are not sensitive to the alteration of the potential at large τ .

The issue is unclear because the exact form of the corrections is not yet known, so we are left with exploring the worst and the best case scenarios. The best case scenario is that corrections are absent or suppressed by a large volume factor $1/\mathcal{V}$. The worst case scenario is where corrections generate significant terms for large τ . We note that inflation based on the potential $V(\tau, \theta)$ with two variables is more protected from the corrections than inflation based

solely upon the potential $V(\tau)$. Indeed, if the potential $V(\tau, \theta)$ is altered, the runaway character along the τ -ridges may be changed to give a shallow minimum along τ , and the region around this minimum might turn out to provide another suitable terrain for inflationary behaviour if there is slow roll in the θ direction. Although asymptotic flatness and self-reproduction may be destroyed by induced masses, the observable window at significantly smaller τ may still allow inflations with enough e-foldings. As often happens in the investigation of string theory cosmology, assumptions such as the gentle nature of the uplift imposed here have to be made. That a viable stringy inflation seems feasible should motivate further work by the string theory community on the corrections and their role in inflation model building.

In this paper, we did not treat the issues of reheating at the end of inflation and the relation of the model to the observed particle physics. We just assumed that all the inflaton energy is transferred to the energy of ultra relativistic particles of the Standard Model. We require that there should be no overproduction of dangerous particles such as other long-lived moduli or (non LSP) gravitinos. Such dangerous relics may “overclose the universe” or decay late enough to destroy the success of the Big Bang Nucleosynthesis of the light elements. Details of reheating depend on the Kähler moduli dynamics at the end of inflation and on the interactions of the Kähler moduli with other fields, including the Standard Model particles. The dynamics of τ depends on the character of the potential around the minimum. In our picture all the other moduli except the inflaton T_2 are stabilized and stay at the global minimum. If the value of $\tau_{2,min}$ exceeds the string scale, the supergravity description of the inflaton potential around the minimum will be valid, with the inflaton beginning to oscillate after slow roll ends. The coupling to other degrees of freedom, in particular those of the Standard Model, that appear in the reheating process is unclear. The canonically-normalized inflaton may have interaction via the gravitational coupling and this interaction must be sufficiently suppressed (*e.g.*, by the volume $1/\mathcal{V}$) to avoid significant radiative corrections to the inflaton potential. On the other hand, the oscillating inflaton should decay into Standard Model particles fast enough (in < 100 sec) to preserve successful Big Bang Nucleosynthesis. These requirements may put interesting constraints on the model for the couplings.

An alternative possibility is that $\tau_{2,min}$ is comparable to the string scale so that stringy effects play a direct role at the end of inflation. In this case one has to go beyond the supergravity description of the processes. We note that small $\tau_{2,min}$ does not constrain the Kähler modulus/axion inflation, since the observed e-folds take place at large τ : only the approach to, and consummation of, preheating would be affected, and would be quite different than in the supergravity case. One may envisage the following as a possible scenario: the Kähler modulus, which corresponds to the geometrical size of the four-cycles, shrinks to zero corresponding to the disappearance of a hole in a topological transition in the internal manifold. The energy of τ cascades first into the excited closed string loops, then further into KK modes in the bulk which interact with the Standard Model on the brane. Such a story is based on an analogy with the string theory reheating in warped brane inflation due to brane-antibrane annihilation

investigated in [112, 113, 114, 115]. In either the supergravity or stringy case, reheating in Kähler moduli/axion inflation in the large volume stabilization model is an interesting and important question worthy of further study.

Even within the context of the Kähler modulus/axion model explored here, the statistical element of the theory prior probability in the landscape of late stage moduli is unavoidable, so the terminology “roulette inflation” is quite appropriate — quite aside from the specific roulette trajectories we have identified that have a dominant angular motion before settling into a τ -trough on the way to the minimum. Within the landscape, we may have to be content with error bars on inflationary histories that have a very large “cosmic variance” due to the broad range of theory models and trajectories possible as well as the data errors due to cosmic microwave background and large scale structure observational uncertainties.

Acknowledgments

It is a pleasure to thank V. Balasubramanian, J. P. Conlon, K. Dasgupta, K. Hori, S. Kachru, A. Linde, F. Quevedo, K. Suruliz, L. Verde and S. Watson and especially R. Kallosh for valuable discussions and suggestions. This work was supported by NSERC and the Canadian Institute for Advanced Research Cosmology and Gravity Program. LK thanks SITP and KIPAC for hospitality at Stanford.

Chapter 5

Trans-Planckian Issue in the Milne Universe

5.1 Introduction

The quantum theory of cosmological fluctuations generated during the inflationary stage of the very early universe describes the time evolution of the scalar eigenmodes $\phi_k(t)e^{i\mathbf{k}x}$. The physical momentum of the eigenmodes $\mathbf{p} = \frac{\mathbf{k}}{a}$ is red-shifted in an expanding FRW universe with increasing scalar factor $a(t)$. If one takes a certain wavelength (of cosmological fluctuations) today and evolves it backwards in time, due to expansion this scale will shrink to smaller and smaller values and at one point will become smaller than the Planckian length. In other words, there are length scales visible today that have been below Planck length at some point in the past. This effect is especially dramatic during inflation, where the scalar factor increases exponentially. Ultimately, at some instance the physical momentum becomes equal to the Planckian mass scale M_p . After this point, the quantum field theory approach to fluctuations in an expanding universe (say, during inflation) should be replaced by a theory incorporating quantum gravity (say, string theory) which is not yet available. We found the earliest written traces of the trans-Planckian problem in [116]. The trans-Planckian challenge was articulated in [25], and discussed in many papers, see e.g [26, 117, 118, 119, 120, 121].

Suppose that trans-Planckian effects alter the result of the conventional QFT at inflation. Despite an unclear notion about the microscopic theory of the effect, there is, however, a convenient phenomenological encoding for it in terms of Bogolyubov coefficients [118]. Indeed, as far as the physical momentum of the mode is below M_p , QFT is applicable. Instead of the vacuum being the positive frequency eigenmode $f_k(\tau) = \frac{1}{2\omega_k}e^{-i\omega_k\tau}$, one can use the Bogolyubov coefficients A_k, B_k to describe the mode function of the initial state

$$f_k(\tau) \rightarrow A_k f_k(\tau) + B_k f_k^*(\tau) , \quad |A_k|^2 - |B_k|^2 . \quad (5.1)$$

UV physics, if any, is encoded in the B_k . The trans-Planckian effect looks pretty universal for

any expanding FRW universe. Consider the Milne universe which is a hyperbolic space with FRW type metric

$$ds^2 = dt^2 - a(t)^2 (dr^2 + \sinh^2 r (d\theta^2 + \sin^2 \theta d\phi^2)) , \quad (5.2)$$

where $a(t) = t$ is the scalar factor. This is the co-moving coordinate system of the kinematic Milne model, which represents a medium of probe particles without gravity freely moving from the origin in empty space-time.

In this model, physical wavelengths are red-shifted, so the reasoning for a trans-Planckian effect should also be applied here, see Figure 5.1. However, the Milne universe is in fact another coordinate system of flat Minkowski space-time, where QFT can be treated analytically in great details, see e.g. [122]. Therefore QFT in the Milne universe can be used as a convenient ground to address the trans-Planckian effect. We will focus on the VeV of the energy-momentum tensor of a test scalar field, $\langle T_\mu^\nu \rangle$, which can be calculated in both coordinate systems of the flat space-time: in the usual Minkowski coordinates, and in the Milne coordinates (5.2). For a given choice of vacuum the answer for the covariant energy-momentum tensor $\langle T_\mu^\nu \rangle$ should be the same. However, for the calculation of $\langle T_\mu^\nu \rangle$ in the Milne coordinates, trans-Planckian effects (in terms of A_k and B_k) can be included and can alter the result. We will consider this as a test to the trans-Planckian prescription.

Traditionally, the trans-Planckian problem is considered in the context of an expanding universe, where A_k and B_k are inherited from the past. However, we can also consider the trans-Planckian problem for a contracting universe, where the horizon is still much bigger than Planckian size while the wavelengths are already blue-shifted below the Planckian scale. This takes place in the contracting phase of the Milne universe (similar to the Figure 5.1 but with reverse time direction). For higher momenta ($k \gg 1$), the “trans-Planckian” moment of time where a given wavelength crosses the Planckian scale occurs at time $t \gg t_p \sim 10^{-42}$ sec, and where we expect QFT in flat space-time to be valid.

Therefore we can calculate the VeV of the energy-momentum tensor at the “trans-Planckian” time in Minkowski coordinates which obviously vanishes

$$\langle T_\mu^\nu \rangle = 0 . \quad (5.3)$$

Our goal is to calculate $\langle T_\mu^\nu \rangle$ in the contracting Milne universe (5.2) with and without trans-Planckian contribution and compare it to the correct result (5.3). The calculation of $\langle T_\mu^\nu \rangle$ in the contracting Milne universe is technically easier than that in the expanding Milne universe (although still quite tedious). Therefore we first consider the problem in the contracting Milne universe where methods of calculations will be introduced, and then extend the results for the expanding Milne universe. We credit [123] where $\langle T_\mu^\nu \rangle_{1/2}$ for the spin 1/2 field in the contracting Milne universe was calculated, and we will extend its method to the case of the scalar field, and the book [124], where $\langle T_\mu^\nu \rangle$ for a scalar field in the contracting Milne universe was calculated

by a different method.

We also consider $\langle T_\mu^\nu \rangle$ in the expanding Milne universe. Since the time t of the Milne coordinates and \tilde{t} of the Minkowski coordinates are connected by non-linear transformations, the vacuum choice for the expanding Milne universe is different from that in the contracting Milne universe. This is related to the choice of the conformal vacuum vs. adiabatic vacuum [122]. As a result, $\langle T_\mu^\nu \rangle$ in the Minkowski coordinates for this vacuum is non-zero and corresponds to an integration over the thermal spectrum of particles seen by an accelerating observer. On the other hand in an expanding Milne universe, in addition to this VeV, we may include a potential trans-Planckian contribution to A_k, B_k , which will alter the expected result.

The plan of this note is as follows. Section 2 contains a short introduction to the Milne universe. Section 3 is devoted to the general QFT in the FRW type universes, including the Milne universe. Section 4 gives a brief outline of the calculation of $\langle T_\mu^\nu \rangle$ in contracting Milne universe, while calculational details are collected in the appendix. Section 5 contains the extension of the results to the expanding Milne universe. In section 6 we discuss the challenge to the trans-Planckian challenge.

5.2 The Milne Universe

The metric of the Milne universe is a FRW type metric (5.2) or written in conformal coordinates

$$ds^2 = a(\eta)^2 (d\eta^2 - dr^2 - \sinh^2 r (d\theta^2 + \sin^2 \theta d\phi^2)), \quad (5.4)$$

$$a(\eta) = e^\eta,$$

where η is the conformal time. For the Milne metric the curvature tensor vanishes $R^\mu{}_{\nu\sigma\rho} = 0$, so it covers a portion of flat space-time. It is related to Minkowski space-time

$$ds^2 = d\tilde{t}^2 - d\tilde{r}^2 - \tilde{r}^2 (d\tilde{\theta}^2 + \sin^2 \tilde{\theta} d\tilde{\phi}^2), \quad (5.5)$$

by a coordinate transformation

$$\begin{aligned} \tilde{t} &= t \cosh r, & \tilde{r} &= t \sinh r, \\ \tilde{\theta} &= \theta, & \tilde{\phi} &= \phi, \end{aligned} \quad (5.6)$$

covering the patch $\tilde{t}^2 - \tilde{r}^2 > 0$. The upper cone $t > 0$ corresponds to an expanding universe, the lower one $t < 0$ corresponds to the contracting universe, see Figure 5.2.

The conformal properties of the Milne universe are important for the choice of the vacuum, which is related to global time-like Killing vectors. Indeed, there is a useful theorem [125, 122]: If for two conformally related conformally flat space-times M_1, M_2 with M_2 flat there exists a diffeomorphism between a global Cauchy hypersurface σ_1 of M_1 and a global Cauchy hypersurface σ_2 of M_2 , then there exists also a correspondence between the global time-like

Killing vector fields of M_1 and M_2 .

Taking the Milne Universe as M_1 , it was found [125] (through mapping both space-times to the Einstein Universe) that these conditions are fulfilled when taking M_2 to be Rindler space with metric

$$ds^2 = e^{2a\xi} (d\eta^2 - d\xi^2) - dy^2 - dz^2 \quad , \quad (5.7)$$

which possesses two global time-like Killing vector fields

$$\begin{aligned} & \partial_\eta, \\ & e^{-a\xi} \cosh(a\eta) \partial_\eta - e^{-a\xi} \sinh(a\eta) \partial_\xi, \end{aligned} \quad (5.8)$$

corresponding to the conformal vacuum and the adiabatic vacuum.

So we can deduce that there are also two global time-like Killing vector fields for the Milne Universe, one of them defining the conformal vacuum, and the other the adiabatic vacuum. The corresponding conformal Killing vector fields in the Milne metric (5.4) are

$$\begin{aligned} \Sigma_\mu^{(1)} & : \partial_\eta, \\ \Sigma_\mu^{(2)} & : e^{-\eta} \cosh r \partial_\eta - e^{-\eta} \sinh r \partial_r, \end{aligned} \quad (5.9)$$

where η, r are now the coordinates of the metric (5.4).

We are faced with the choice which vacuum to take. It turns out that natural choice of vacuum for the contracting Milne universe is the adiabatic vacuum, associated with the Killing vector $\Sigma_\mu^{(2)}$. The adiabatic vacuum also corresponds to the usual vacuum in the Minkowski coordinates. Indeed, this Killing vector $\Sigma_\mu^{(2)}$ is nothing but $\partial_{\tilde{t}}$. The conformal vacuum associated with the other Killing vector $\Sigma_\mu^{(1)}$ is the natural choice of vacuum for the expanding Milne universe.

5.3 Quantum Field Theory in FRW space-times

Let us recall the basics of the QFT of a free massive real scalar field in a FRW background. The equation of motion for the scalar field is given by

$$\left(\square + m^2 - \frac{R}{6} \right) \phi = 0, \quad (5.10)$$

where $\square = D_\mu D^\mu$, m is the mass of the scalar field and R is the Ricci scalar. Using conformal time in the FRW universe and making the Ansatz

$$\phi(x^\mu) = a(\eta)^{-1} \int d\mu(\lambda, l, m) u_\lambda(\eta) \Psi_J(\mathbf{x}), \quad (5.11)$$

where Ψ_J are eigenfunctions of the spatial Laplacian $\Delta^{(3)}\Psi_J = \lambda^2\Psi_J$ with quantum numbers $J = \{\lambda, l, m\}$ and $d\mu(J)$ is the measure over the quantum numbers, we obtain the following equation for the modes u_λ

$$\ddot{u}_\lambda + \omega^2 u_\lambda = 0, \quad \omega^2 = \lambda^2 + m^2 a^2, \quad (5.12)$$

where $\dot{u}_\lambda = \partial_\eta u_\lambda$ is the derivative with respect to conformal time. We quantize the field

$$\begin{aligned} \phi(x^\mu) = & \frac{1}{\sqrt{2}} \int \frac{d\mu(J)}{a(\eta)} \left(u_\lambda(\eta) \Psi_J(\mathbf{x}) a_J \right. \\ & \left. + u_\lambda^*(\eta) \Psi_J^*(\mathbf{x}) a_J^\dagger \right), \end{aligned} \quad (5.13)$$

where a_J^\dagger, a_J are the creation and annihilation operators for particles and antiparticles respectively. Using orthogonality relations for the eigenmodes of the spatial Laplacian it can be shown that the 00-component of the normal ordered energy momentum tensor for a scalar field is given by

$$\langle 0 | : T_0^0 : | 0 \rangle = \frac{1}{\pi^2 a^4} \int_0^\infty d\lambda \lambda^2 \omega s_\lambda, \quad (5.14)$$

where

$$s_\lambda = \frac{1}{2\omega} \left(|\dot{u}_\lambda|^2 + \omega^2 |u_\lambda|^2 - \omega \right). \quad (5.15)$$

Now we have to specify the vacuum $|0\rangle$ and the eigenmodes u_λ . The general solution to Equation (5.12) is

$$u_\lambda = c_1 H_{i\lambda}^{(1)}(\mu) + c_2 H_{i\lambda}^{(2)}(\mu), \quad (5.16)$$

where we defined $\mu = ma$ with $a = t = e^\eta$. $H_\nu^{(1,2)}(z)$ are the Hankel functions.

Now consider the contracting Milne universe. Initial conditions shall be defined at $t \rightarrow \infty$. For $\mu \rightarrow \infty$ we find a normalized positive energy solution

$$u_\lambda = \frac{\sqrt{\pi}}{2} e^{\frac{\pi}{2}\lambda} H_{i\lambda}^{(2)}(\mu). \quad (5.17)$$

The correct normalization follows from $(\phi_\lambda, \phi_\nu) = - \int_\Sigma d\Sigma^\mu \sqrt{-g_\Sigma} (\phi_\lambda \partial_\mu \phi_\nu^* - \phi_\nu^* \partial_\mu \phi_\lambda) \stackrel{!}{=} \delta_{\lambda,\nu}$ which translates into $u_\lambda \partial_t u_\nu^* - u_\nu^* \partial_t u_\lambda = i$ with Σ^μ being a time-like conformal Killing vector field orthogonal to the 3-surface of integration [126].

The choice (5.17) of the eigenmode corresponds to the adiabatic vacuum. Physically, the adiabatic vacuum corresponds to a vacuum which comes closest to being Minkowski, i.e. it should become Minkowski in the limit of a very slowly changing geometry. In general this

vacuum is associated with the WKB-type mode solutions of the equation of motion

$$u_\lambda = \frac{1}{\sqrt{2W_\lambda}} e^{-i \int^\eta d\eta' W_\lambda(\eta')} , \quad (5.18)$$

where W satisfies the non-linear equation

$$W_\lambda(\eta)^2 = \omega^2 - \frac{1}{2} \left(\frac{\ddot{W}_\lambda}{W_\lambda} - \frac{3 \dot{W}_\lambda^2}{2 W_\lambda^2} \right) . \quad (5.19)$$

Taking the limit of slowly varying scale factor a or rather equivalently the limit of large t (or η), we can approximate $\omega = m e^\eta = W_\lambda$, so that the adiabatic approximation to the WKB-type solution is given by

$$u_\lambda = \frac{1}{\sqrt{2m e^\eta}} e^{-i m e^\eta} , \quad (5.20)$$

which corresponds to the large η limit of the eigenmodes (5.17). Thus, the adiabatic vacuum $|0_A\rangle$ of the contracting Milne Universe is the same as the Minkowski vacuum [122].

Next, we consider the expanding Milne universe. Initial conditions shall be defined at $\eta = -\infty$ ($t = 0$). We have to select the solution

$$u_\lambda \rightarrow v_\lambda = \sqrt{\frac{\pi}{2}} \frac{1}{\sqrt{\sinh \pi \lambda}} J_{-i\lambda}(\mu) , \quad (5.21)$$

where $J_{i\lambda}(\mu)$ is the Bessel function. Its asymptotic form at $\eta \rightarrow -\infty$ is given by the normalized positive frequency solution $\frac{1}{\sqrt{2\lambda}} e^{-i\lambda\eta}$. This choice of eigenmode corresponds to the conformal vacuum.

Indeed, the conformal vacuum is obtained by performing a conformal transformation of the metric $g_{\mu\nu}$ to the metric $\tilde{g}_{\mu\nu}$, $g_{\mu\nu} = \Omega^2(x) \tilde{g}_{\mu\nu}$ which changes the equation of motion (5.10) to $\square \tilde{\Phi} = 0$, where $\tilde{\Phi} = \Omega^{-1} \Phi$. The vacuum state associated with the modes \tilde{u}_λ of $\tilde{\Phi}$ corresponds to the conformal vacuum $|0_C\rangle$.

It is instructive to compare the vacua of the contracting (adiabatic) and expanding (conformal) Milne universe. We can express the orthogonal set v_λ of normalized eigenfunctions of the expanding universe (5.21) in terms of the set of eigenfunctions u_λ of the contracting universe (5.17) introducing Bogolyubov coefficients

$$u_\lambda(\eta) = \alpha_\lambda v_\lambda(\eta) + \beta_\lambda v_\lambda^*(\eta) . \quad (5.22)$$

Using the relation between the Bessel and the Hankel functions (see (5.37)) we find

$$\alpha_\lambda = \frac{e^{\frac{\pi}{2}\lambda}}{\sqrt{2 \sinh \pi \lambda}} , \quad \beta_\lambda = \frac{e^{-\frac{\pi}{2}\lambda}}{\sqrt{2 \sinh \pi \lambda}} . \quad (5.23)$$

In particular, this means that the conformal vacuum in Minkowski space-time corresponds to

excitations of states related to the usual Minkowski adiabatic vacuum. In other words, in Minkowski coordinates $\langle 0_A | T_\mu^\nu | 0_A \rangle = 0$ but $\langle 0_C | T_\mu^\nu | 0_C \rangle \neq 0$.

5.4 $\langle 0_A | T_\mu^\nu(\text{Milne}) | 0_A \rangle$ in contracting Milne universe

In this section we outline the calculation of the energy momentum tensor $\langle 0_A | T_\mu^\nu(\text{Milne}) | 0_A \rangle$, in the contracting Milne universe. The starting point is expression (5.14) where we have to substitute the solution (5.17).

Formally the expression (5.14) for the mode functions in the Milne universe is divergent and needs to be regularized. Normal ordering in (5.14) takes care of the divergence coming from the zero point energy, but the energy momentum tensor in a curved space-time features more divergences which are attributed to vacuum polarization. In FRW type space-times it is most convenient to use the regularization method of Zel'dovich and Starobinsky [127], which we have adopted. The result is to replace s_λ in (5.14) by $s_\lambda - s_2 - s_4$ with (see (5.45) in the Appendix)

$$\begin{aligned} s_2 &= \frac{1}{16} \left(\frac{\dot{\omega}}{\omega^2} \right)^2, \\ s_4 &= -\frac{3}{256} \left(\frac{\dot{\omega}}{\omega^2} \right)^4 - \frac{1}{32} \frac{\dot{\omega}}{\omega^3} \frac{\partial}{\partial \eta} \left[\frac{1}{\omega} \frac{\partial}{\partial \eta} \left(\frac{\dot{\omega}}{\omega^2} \right) \right] \\ &\quad + \frac{1}{64} \left[\frac{1}{\omega} \frac{\partial}{\partial \eta} \left(\frac{\dot{\omega}}{\omega^2} \right) \right]^2. \end{aligned} \quad (5.24)$$

We illustrate the calculation for the energy density $\rho = T_{00}$, the other components of $T_{\mu\nu}$ can be either calculated similarly or from ρ , energy conservation $T_{\mu;\nu}^\mu$ and the vanishing of the conformal anomaly $\langle 0 | T_\mu^\mu | 0 \rangle = 0$.

For the renormalized energy density we have

$$T_0^{0(\text{ren})} = \rho_{\text{vac}} - \rho_0 - \rho_1 - \rho_2, \quad (5.25)$$

where

$$\begin{aligned} \rho_{\text{vac}} &= \lim_{\epsilon \rightarrow 0} \frac{1}{2\pi^2 a^4} \int_0^\infty d\lambda \lambda^2 \left(|\dot{u}_\lambda|^2 + \omega^2 |u_\lambda|^2 \right) e^{-\epsilon\lambda}, \\ \rho_0 &= \lim_{\epsilon \rightarrow 0} \frac{1}{2\pi^2 a^4} \int_0^\infty d\lambda \lambda^2 \omega e^{-\epsilon\lambda}, \\ \rho_{1,2} &= \frac{1}{\pi^2 a^4} \int_0^\infty d\lambda \lambda^2 \omega s_{2,4}. \end{aligned} \quad (5.26)$$

The first two terms ρ_{vac} and ρ_0 are divergent, but after regularization they contain finite contributions. The finite part ρ_{vac} can be interpreted as a contribution of particles, seen by the comoving observer in contracting Milne universe. Terms $\rho_{1,2}$ are finite, and together with the finite part of ρ_0 can be interpreted as the vacuum polarization seen by the comoving observer.

In order to extract divergences in ρ_{vac} and ρ_0 , we introduce the regularizer $e^{-\epsilon\lambda}$ with small dimensionless parameter ϵ . At the end of our calculations the final answer will not be dependent on it and we can send ϵ to zero. This technical trick is borrowed from [128].

The results of calculations of the integrals (5.26) detailed in the appendix are the following

$$\rho_{\text{vac}} = \frac{1}{\pi^2 a^4} \left(\frac{3}{\epsilon^4} + \frac{\mu^2}{4\epsilon^2} + \frac{\mu^4}{16} \log \frac{\epsilon\mu}{2} + \frac{\gamma\mu^4}{16} + \frac{\mu^4}{64} + \frac{\mu^2}{48} + \frac{1}{240} \right), \quad (5.27)$$

$$\rho_0 = \frac{1}{\pi^2 a^4} \left(\frac{3}{\epsilon^4} + \frac{\mu^2}{4\epsilon^2} + \frac{\mu^4}{16} \log \frac{\epsilon\mu}{2} + \frac{\gamma\mu^4}{16} + \frac{\mu^4}{64} \right), \quad (5.28)$$

$$\rho_1 = \frac{1}{\pi^2 a^4} \frac{1}{240}, \quad \rho_2 = \frac{1}{\pi^2 a^4} \frac{\mu^2}{48}. \quad (5.29)$$

In the net result (5.25) all divergences are canceled. However, all finite parts are also canceled so that we end up with

$$\langle 0_A | T_{0(\text{ren})}^{0(\text{Milne})} | 0_A \rangle = 0. \quad (5.30)$$

All other components of the energy momentum tensor are also zero.

5.5 $\langle 0_C | T_{\mu}^{\nu(\text{Milne})} | 0_C \rangle$ in expanding Milne universe

In this section we calculate the energy momentum tensor $\langle 0_C | T_{\mu}^{\nu(\text{Milne})} | 0_C \rangle$ in the expanding Milne universe. Again, we use the formula (5.14) where we substitute the solution (5.21).

Let us calculate energy density $\rho = \langle 0_C | T_{00}^{0(\text{Milne})} | 0_C \rangle$. We have an integral expression similar to (5.14), but with the eigenfunctions v_{λ} instead of u_{λ} . In principle, we can apply the method of the previous section to this case, including regularizing with $e^{-\epsilon\lambda}$ and extracting divergences. It is easier, however, to use relationship (5.22) between v_{λ} and u_{λ} . Then we obtain

$$\begin{aligned} \langle 0_C | T_0^{0(\text{Milne})} | 0_C \rangle &= \langle 0_A | T_0^{0(\text{Milne})} | 0_A \rangle \\ &+ \frac{1}{\pi^2 a^4} \int_0^{\infty} d\lambda \lambda^2 \omega |\beta_{\lambda}|^2 (2s_{\lambda} + 1) \\ &+ \Delta, \end{aligned} \quad (5.31)$$

where s_{λ} , constructed from $|u_{\lambda}|$, is defined in (5.15). The residual term Δ is defined in (5.52) and is constructed from $u_{\lambda}^2, u_{\lambda}^{*2}$. Before regularization all the divergences are in the first term $\langle 0_A | T_{00}^{0(\text{Milne})} | 0 \rangle$.

Expression (5.31) becomes transparent for large values of t (or η), where $s_{\lambda} \rightarrow 1$, $\Delta \rightarrow 0$. Regularizing expression (5.31) is reduced to regularizing the first term which we performed in

the previous section. Using (5.23) for β_λ , we have the final result

$$\langle 0_C | T_{0(\text{ren})}^{0(\text{Milne})} | 0_C \rangle = \frac{1}{\pi^2 a^4} \int_0^\infty d\lambda \lambda^2 \omega \frac{1}{e^{2\pi\lambda} - 1} . \quad (5.32)$$

As expected, in expanding Milne universe energy density is non-zero due to the choice of the conformal vacuum.

5.6 Discussion: Challenge to the Trans-Planckian Challenge

We will discuss all aspects of the UV physics which may emerge in the cosmological models, for instance, the impact of the horizon [129] on the trans-Planckian issue.

In an expanding/contracting flat universe, a given wavelength of the oscillator's eigenmode $e^{i\mathbf{k}\mathbf{x}}$ is red-shifted/blue-shifted. The Milne universe has hyperbolic three dimensional spatial slicing. The spatial eigenmode of this hyperbolic space is described by the function (5.35) (see Appendix). For simplicity we consider the high-frequency modes with $\lambda \gg 1$. In this limit the eigenmode (5.35) is reduced to simple standing waves $\sim \cos(\lambda r)$. For these modes we can use the intuitive red-shifting/blue-shifting picture.

In this section we will discuss how the results (5.30), (5.32) will be changed if we apply the trans-Planckian prescription for the eigenmodes with the wavelengths which were or will be below the Planckian scale in the contracting/expanding Milne universe.

In the contracting universe a given wavelength is blue-shifted and will be shorter than the Planckian scale at its “trans-Planckian” moment t_k . If trans-Planckian effects work in this model, then the value $\langle 0_A | T_{00(\text{ren})}^{(\text{Milne})} | 0_A \rangle$ will departure from zero. However, the moment t_k is much bigger than the Planckian time. The moment t_k is not special for observers in the usual Minkowski coordinate system, where $\langle 0_A | T_{00(\text{ren})}^{(\text{Mink})} | 0_A \rangle$ remains always zero. We conclude that the trans-Planckian effect does not emerge in the contracting Milne universe.

Now, let us apply the trans-Planckian prescription to the calculation of $\langle 0_C | T_{00(\text{ren})}^{(\text{Milne})} | 0_C \rangle$ for the expanding universe. We simply alter the eigenmode $u_\lambda(\eta)$ at the moment η_k , according to (5.1). Then the result (5.30) will be changed to

$$\langle 0_C | T_{0(\text{trans})}^{0(\text{Milne})} | 0_C \rangle = \frac{1}{\pi^2 a^4} \int_0^\infty d\lambda \lambda^2 \omega |\beta_\lambda + B_\lambda|^2 . \quad (5.33)$$

However, observers in the usual Minkowski coordinate system should not see any effects of B_λ . No trans-Planckian effects emerge in the expanding Milne universe.

It is clear that our consideration of the trans-Planckian issue in contracting/expanding cosmologies is much more general than the simple example of the Milne universe. Consider, for example, the expanding anisotropic Kasner universe

$$ds^2 = dt^2 - t^{2p_1} dx^2 - t^{2p_2} dy^2 - t^{2p_3} dz^2 , \quad (5.34)$$

with $\sum p_i = \sum p_i^2 = 1$, so that one of the p_i -s is non-positive. Suppose space is stretching in two directions while shrinking in the third direction, $p_3 < 0$. The component of the momentum k_3 of the quantum modes $e^{ik_3 z}$ associated with this third direction is blueshifting (while the universe as a whole is expanding), and at some point passes the Planckian scale. It is paradoxical to encounter quantum gravity effects in an expanding Kasner universe! Notice the special combination of parameters $p_1 = p_2 = 0, p_3 = 1$. In this case the Kasner metric (5.34) is the product of the two-dimensional Milne universe and R^2 and can be transformed to the Minkowski space-time, and we have another example where the trans-Planckian issue evaporates. The resolution of the paradox: the criterion for the UV (string) physics to become important is having large values of the curvature terms $C_{\mu\nu\rho\sigma}^{\mu\nu\rho\sigma}, R_{\mu\nu}^{\mu\nu}, R^2 \sim 1/l_p^4$ but not coordinate effects.

We can compare the situation with another apparent paradox of inflation, using the “trans-Planckian” value of the inflaton field $\phi \gg M_p$. There are no restrictions to use the large ϕ values, the physical restrictions are related to the energy density $V \ll M_p^4$ (where the curvature is sub-Planckian).

Acknowledgments

We are grateful to E. Kolb, A. Linde, V. Mostepanenko, V. Sahni and Yu. Shtanov for useful discussions. This research was supported by the University of Toronto and NSERC and CIAR.

Appendix

In this appendix we describe properties of the eigenfunctions $u_\lambda \Psi_J(\mathbf{x})$ of (5.10) and present some details of the renormalization procedure for the 0–0 component of the energy momentum tensor in the conformal and adiabatic vacuum.

Properties of Eigenfunctions

For the hyperbolic case of the open universe (as in the case of the Milne metric), $J = \lambda, l, m$. Ignoring non-normalizable super-horizon modes, we have $0 \leq \lambda \leq \infty$, $l = 0, 1, 2, \dots$, $m = -l, \dots, +l$. The explicit form of the normalized space-dependent part of the eigenfunction is

$$\Psi_J(\mathbf{x}) = \frac{1}{\sqrt{\sinh r}} \frac{\Gamma(i\lambda + l + 1)}{|\Gamma(i\lambda)|} P_{i\lambda-1/2}^{-l-1/2}(\cosh r) Y_{lm}(\theta, \phi), \quad (5.35)$$

where P_ν^μ are the associated Legendre polynomials, and Y_{lm} are the spherical harmonics. Let us focus on the high frequency ($\lambda \gg 1$) asymptotic of $\Psi_J(\mathbf{x})$. The asymptotic properties of $P_{i\lambda-1/2}^{-l-1/2}(\cosh r)$ imply [130]

$$P_{i\lambda-1/2}^{-l-1/2}(\cosh r) \sim \cos(\lambda r). \quad (5.36)$$

The time-dependent part of the eigenfunctions u_λ is reduced to the solution of the Bessel equation (5.12).

The two modes u_λ , corresponding to the adiabatic vacuum, and v_λ , corresponding to the conformal vacuum are related through

$$v_\lambda = \frac{e^{\frac{\pi}{2}\lambda}}{\sqrt{2 \sinh \pi \lambda}} u_\lambda + \frac{e^{-\frac{\pi}{2}\lambda}}{\sqrt{2 \sinh \pi \lambda}} u_\lambda^* , \quad (5.37)$$

which can be obtained by using the relation between the Bessel and the Hankel functions for $\lambda, \mu \in \mathbf{R}$

$$J_{-i\lambda}(\mu) = \frac{1}{2} \left((H_{i\lambda}^{(2)}(\mu))^* + e^{\pi\lambda} H_{i\lambda}^{(2)}(\mu) \right) . \quad (5.38)$$

This defines the coefficients $\alpha_\lambda, \beta_\lambda$ in (5.23).

Renormalizing $\langle 0_A | T_{00} | 0_A \rangle$

To compute the energy momentum tensor, we plug the solutions (5.17) of the mode equation (5.12) into the definition (5.14) of $\langle 0_C | T_{00} | 0_C \rangle$. Making use of the following properties of the Hankel functions [131]

$$\begin{aligned} \left(H_\nu^{(1)}(x) \right)^* &= H_{\nu^*}^{(2)}(x) , \\ H_{-\nu}^{(1)}(z) &= e^{\nu i \pi} H_\nu^{(1)}(z) , \\ \frac{2\nu}{z} H_\nu^{(i)}(z) &= H_{\nu-1}^{(i)}(z) + H_{\nu+1}^{(i)}(z) , \end{aligned} \quad (5.39)$$

we find

$$\begin{aligned} |\dot{u}_\lambda|^2 &= \frac{\pi}{4} \left[\frac{\mu^2}{2} \left(H_{i\lambda+1}^{(1)} H_{i\lambda+1}^{(2)} + H_{i\lambda-1}^{(1)} H_{i\lambda-1}^{(2)} \right) \right. \\ &\quad \left. + \lambda^2 H_{i\lambda}^{(1)} H_{i\lambda}^{(2)} \right] , \\ |u_\lambda|^2 &= \frac{\pi}{4} H_{i\lambda}^{(1)} H_{i\lambda}^{(2)} . \end{aligned} \quad (5.40)$$

Now we apply

$$H_\nu^{(1)} H_\nu^{(2)} = \frac{4}{\pi^2} \int_0^\infty dx K_0(2\mu \sinh x) \left(e^{2\nu x} + e^{-2\nu x} \right) , \quad (5.41)$$

where $K_0(z)$ is the MacDonald function, and introduce the regularizing factor $e^{-\epsilon\lambda}$ to get

$$\begin{aligned} \rho_{\text{vac}} &= \frac{1}{2\pi^2 a^4} \int_0^\infty d\lambda \lambda^2 (|\dot{u}_\lambda|^2 + \omega^2 |u_\lambda|^2) \\ &= \frac{2}{\pi^3 a^4} \int_0^\infty dx K_0(2\mu \sinh x) \\ &\quad \times \left[\mu^2 \cosh(x)^2 \int_0^\infty d\lambda \lambda^2 \cos(2\lambda x) e^{-\epsilon\lambda} \right. \\ &\quad \left. + \int_0^\infty d\lambda \lambda^4 \cos(2\lambda x) e^{-\epsilon\lambda} \right] \end{aligned}$$

$$\begin{aligned}
&= \frac{2}{\pi^3 a^4} \int_0^\infty dx K_0(2\mu \sinh x) \\
&\quad \times \left[\mu^2 \cosh(x)^2 \underbrace{\epsilon \frac{\epsilon^2 - 12x^2}{(\epsilon^2 + 4x^2)^3}}_{=:f} \right. \\
&\quad \left. + 12 \epsilon \underbrace{\frac{\epsilon^4 - 40\epsilon^2 x^2 + 80x^4}{(\epsilon^2 + 4x^2)^5}}_{=:h} \right].
\end{aligned} \tag{5.42}$$

Multiplying the fractions f, h by a power of x^n will result in a zero contribution for $n \geq 3$ and $n \geq 5$ respectively. Therefore we expand $K_0(2\mu \sinh x) \cosh^2 x$ to $O(x^3)$ and $K_0(2\mu \sinh x)$ to order $O(x^5)$ and perform the integrations to obtain

$$\begin{aligned}
\rho_{\text{vac}} &= \frac{1}{\pi^2 a^4} \left(\frac{3}{\epsilon^4} + \frac{\mu^2}{4\epsilon^2} + \frac{\mu^4}{16} \log \frac{\epsilon}{2} \right. \\
&\quad \left. + \frac{\mu^4 \log \mu}{16} + \frac{\gamma \mu^4}{16} + \frac{\mu^4}{64} + \frac{\mu^2}{48} + \frac{1}{240} \right),
\end{aligned} \tag{5.43}$$

The energy momentum tensor contains divergences even after subtracting the vacuum energy ρ_0 which calculates to

$$\begin{aligned}
\rho_0 &= \frac{1}{\pi^2 a^4} \int_0^\infty d\lambda \lambda^2 \frac{\omega}{2} e^{-\epsilon \lambda} \\
&= \frac{1}{\pi^2 a^4} \\
&\quad \times \left(\frac{3}{\epsilon^4} + \frac{\mu^2}{4\epsilon^2} + \frac{\mu^4}{16} \log \frac{\epsilon}{2} + \frac{\mu^4 \log \mu}{16} + \frac{\gamma \mu^4}{16} + \frac{\mu^4}{64} \right).
\end{aligned} \tag{5.44}$$

To deal with the remaining divergences, we employ the Zel'dovich-Starobinsky regularization scheme [127] which amounts to introducing the variables $s_\lambda = |\beta_\lambda|^2$ and $u_\lambda - iv_\lambda = \pm 2\alpha_\lambda \beta_\lambda e^{-2i \int_{\eta_0}^\eta d\eta \omega}$ obeying

$$\begin{aligned}
\dot{s}_\lambda &= \frac{1}{2} \frac{\dot{\omega}}{\omega} u_\lambda, \\
\dot{v}_\lambda &= 2\omega u_\lambda, \\
\dot{u}_\lambda &= \frac{\dot{\omega}}{\omega} (1 \pm 2s_\lambda) - 2\omega v_\lambda.
\end{aligned} \tag{5.45}$$

We set $\lambda \rightarrow h\lambda, m \rightarrow hm, \omega \rightarrow h\omega$, expand $s_\lambda, u_\lambda, v_\lambda$ in a series

$$s_{h\lambda} = \sum_{\ell=1} \frac{1}{h^\ell} s_\ell, \quad u_{h\lambda} = \sum_{\ell=1} \frac{1}{h^\ell} u_\ell, \quad v_{h\lambda} = \sum_{\ell=1} \frac{1}{h^\ell} v_\ell, \tag{5.46}$$

and plug them into (5.45) to find after some algebra

$$s_4 = -\frac{3}{256} \left(\frac{\dot{\omega}}{\omega^2} \right)^4 - \frac{1}{32} \frac{\dot{\omega}}{\omega^3} \frac{\partial}{\partial \eta} \left[\frac{1}{\omega} \frac{\partial}{\partial \eta} \left(\frac{\dot{\omega}}{\omega^2} \right) \right]$$

$$+\frac{1}{64} \left[\frac{1}{\omega} \frac{\partial}{\partial \eta} \left(\frac{\dot{\omega}}{\omega^2} \right) \right]^2, \quad s_2 = \frac{1}{16} \left(\frac{\dot{\omega}}{\omega^2} \right)^2, \quad (5.47)$$

with all other $s_\ell = 0$. Now we can easily calculate

$$\begin{aligned} \rho_1 &= \frac{1}{\pi^2 a^4} \int_0^\infty d\lambda \lambda^2 \omega s_2 = \frac{1}{\pi^2 a^2} \frac{\mu^2}{48}, \\ \rho_2 &= \frac{1}{\pi^2 a^4} \int_0^\infty d\lambda \lambda^2 \omega s_4 = \frac{1}{\pi^2 a^2} \frac{1}{240}. \end{aligned} \quad (5.48)$$

Adding up all terms gives

$$\langle 0_A | T_0^{0(\text{ren})} | 0_A \rangle = \rho_{\text{vac}} - \rho_0 - \rho_1 - \rho_2 = 0. \quad (5.49)$$

Renormalizing $\langle 0_C | T_{00} | 0_C \rangle$

In order to compute $\langle 0_C | T_{00} | 0_C \rangle$ we plug the conformal eigenmodes (5.21) into (5.15), express the modes v_λ, v_λ^* in terms of the modes u_λ, u_λ^* (5.17) and find after some algebra

$$\begin{aligned} \bar{s}_\lambda &= \frac{1}{2\omega} (|\dot{v}_\lambda|^2 + \omega^2 |v_\lambda|^2 - \omega) \\ &= s_\lambda + \frac{e^{-\pi\lambda}}{\sinh \pi\lambda} \left(s_\lambda + \frac{1}{2} \right) + \tilde{\Delta}, \end{aligned} \quad (5.50)$$

where we can identify the second term as $|\beta_\lambda|^2(2s_\lambda + 1)$ and

$$\tilde{\Delta} = \frac{1}{4\omega \sinh \pi\lambda} (\dot{u}_\lambda^2 + \omega^2 u_\lambda^2 + \dot{u}_\lambda^{*2} + \omega^2 u_\lambda^{*2}). \quad (5.51)$$

This gives rise to expression (5.31) for $\langle 0_C | T_0^0 | 0_C \rangle$ with

$$\Delta = \frac{1}{\pi^2 a^4} \int d\lambda \lambda^2 \omega \tilde{\Delta}. \quad (5.52)$$

At late times, the integrand $\tilde{\Delta}$ is rapidly oscillating so that $\lim_{t \rightarrow \infty} \Delta = 0$ as can be seen by using the large argument asymptotics of the Hankel functions

$$\begin{aligned} \lim_{\mu \rightarrow \infty} H^{(1)}(\mu) &= \sqrt{\frac{2}{\pi\mu}} e^{i(\mu - \frac{1}{2}\nu\pi - \frac{\pi}{4})}, \\ \lim_{\mu \rightarrow \infty} H^{(2)}(\mu) &= \sqrt{\frac{2}{\pi\mu}} e^{-i(\mu - \frac{1}{2}\nu\pi - \frac{\pi}{4})}. \end{aligned} \quad (5.53)$$

The late time behaviour of $(2s_\lambda + 1) \rightarrow 1$ can be easily seen from (5.40) using the asymptotic behaviour of the Hankel functions (5.53).

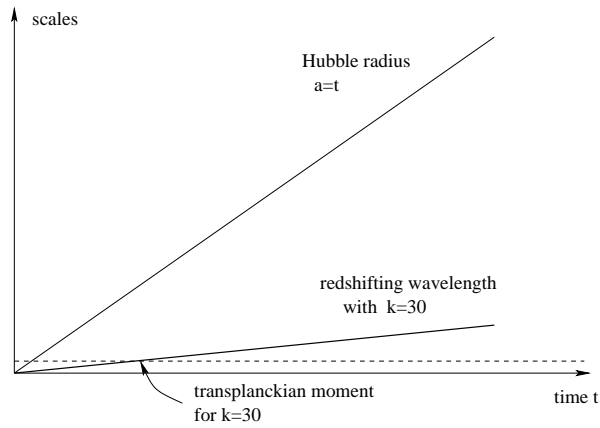


Figure 5.1: Redshift of the wavelength $\lambda = \frac{2\pi}{k}a(t)$ in the Milne universe. The horizontal dashed line represents the Planck scale l_p . A given wavelength for example $k = 30$ crosses the Planckian scale at its trans-Planckian moment t_k .

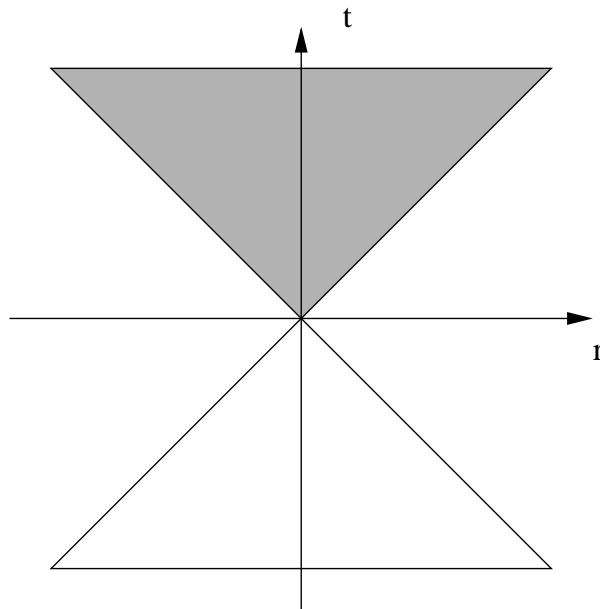


Figure 5.2: The patches of Minkowski space covered by the Milne metric. Upper (shadow) patch corresponds to the expanding universe, while the lower (empty) patch corresponds to the contracting universe

Chapter 6

Conclusions and Outlook

We investigated the statistical character of the ensemble of inflationary acceleration trajectories both on the experimental/ data analysis side and on the theoretical/ model building side.

On the data analysis side, using the trajectory framework we examined the impact of theoretical priors on the reconstruction of the parameters of the primordial power spectra, finding a strong dependence on the parametrization of the trajectories. Not surprisingly, especially experimentally not well determined quantities like the tensor scalar ratio are most sensitive to the – sometimes even only implicit – choice of priors.

We offered different strategies to compensate the effect of the priors when performing MCMC parameter reconstruction by varying the form of the parametrization and explicitly adjusting the prior in the calculation of the likelihood of a given model. Performing some simplified preliminary explorations of resolving power of the upcoming satellites Planck and CMBPol we showed that – depending on the amplitude of the tensor fluctuations – priors will always play a role when reconstructing information about the inflationary potential.

On the theoretical side we examined the properties of the inflationary period in an explicit large volume compactification of type IIB string theory, finding another example of the landscape where not only the parameters of the potential (corresponding to different choices for the details of the compactification and background fluxes) but also the initial conditions of the two dynamical fields greatly impact the evolution of the resulting universes, leading to wildly varying observational consequences: tiny variations in the initial conditions around certain points in field space result in inflation lasting from just a few e-folds of inflation to hundreds of e-folds. Instead of each point in the string landscape of vacua corresponding to a unique observational prediction it turns out that also within a given vacuum the choice of initial condition adds another statistical element. Observations can only hope to reconstruct the slice of the underlying potential corresponding to the actual trajectory of the dynamical fields.

On the surface, the situation for early universe cosmology appears somewhat tedious, with the ultimate goal of uniquely determining the inflaton potential seemingly completely out of reach. Intrinsic uncertainties from the data as well as from the theory side appear to be turning inflationary model building into a game of prior belief.

But the situation need not necessarily be as hopeless depending on what future measurements will see. For example if upcoming observations determine the inflationary energy scale by measuring the amplitude of gravity waves which would immediately rule out the known inflationary models derived from string theory. Models based on the KKLT construction so far seem to contain only very tiny tensor scalar ratios of $r \approx 10^{-10}$, far below the values of $r \approx 10^{-2} \dots 10^{-3}$ that the most optimistic experiments hope to be able to detect. Therefore any experimental signal of gravity waves produced during inflation would pose somewhat of a challenge to string theory, but we should stress that there is no no-go theorem forbidding large values for the amplitude of the tensor power spectrum in those kinds of models.

Also on the theory side much about string theory is still unknown. Maybe some as of now still unknown mechanism other than statistics will provide a guiding principle for determining which valley in the landscape of string vacua is the most “fundamental” one. It might even turn out that alternative UV complete theories of gravity like loop quantum gravity will be able to provide better fits to the data.

In the end, the ultimate factor deciding which vacuum/ valley/ theory is the right one must be observational data and not a theoretical prior belief in the beauty of a theory. In this sense, the next years promise to be a very exciting time for cosmologists as more and more experiments are providing better and better data and nobody knows which unexpected observational results will be obtained in the future.

We investigated the trans-Planckian issue in the Milne universe, arguing that there should be no trans-Planckian effects in this FRW-type reparametrization of (a quarter of) Minkowski space despite the fact that in Milne coordinates the scale factor is growing with time leading to any given mode to originate from below Planckian size. However, for a Minkowski coordinate observer, the point in time – at which for a Milne observer a given mode is crossing the Planck size – is not different from any other, with no expansion of modes in time. The only effect associated with a change of observers is the appearance of Unruh radiation.

Bibliography

- [1] Arno A. Penzias and Robert Woodrow Wilson. A measurement of excess antenna temperature at 4080-mc/s. *Astrophys. J.*, 142:419–421, 1965.
- [2] D. J. Fixsen et al. The cosmic microwave background spectrum from the full coBE/firas data set. *Astrophys. J.*, 473:576, 1996, astro-ph/9605054.
- [3] D. N. Spergel et al. Wilkinson microwave anisotropy probe (wmap) three year results: Implications for cosmology. 2006, astro-ph/0603449.
- [4] Patrick McDonald et al. The linear theory power spectrum from the lyman-alpha forest in the sloan digital sky survey. *Astrophys. J.*, 635:761–783, 2005, astro-ph/0407377.
- [5] Shaun Cole et al. The 2df galaxy redshift survey: Power-spectrum analysis of the final dataset and cosmological implications. *Mon. Not. Roy. Astron. Soc.*, 362:505–534, 2005, astro-ph/0501174.
- [6] S. Hanany et al. Maxima-1: A measurement of the cosmic microwave background anisotropy on angular scales of 10 arcminutes to 5 degrees. *Astrophys. J.*, 545:L5, 2000, astro-ph/0005123.
- [7] C. J. MacTavish et al. Cosmological parameters from the 2003 flight of boomerang. *Astrophys. J.*, 647:799, 2006, astro-ph/0507503.
- [8] Chao-Lin Kuo et al. Improved measurements of the cmb power spectrum with acbar. 2006, astro-ph/0611198.
- [9] Jonathan L. Sievers et al. Implications of the cosmic background imager polarization data. 2005, astro-ph/0509203.
- [10] Clive Dickinson et al. High sensitivity measurements of the cmb power spectrum with the extended very small array. *Mon. Not. Roy. Astron. Soc.*, 353:732, 2004, astro-ph/0402498.
- [11] Alexei A. Starobinsky. A new type of isotropic cosmological models without singularity. *Phys. Lett.*, B91:99–102, 1980.

- [12] Alan H. Guth. The inflationary universe: A possible solution to the horizon and flatness problems. *Phys. Rev.*, D23:347–356, 1981.
- [13] Scott Dodelson. *Modern cosmology*. Amsterdam, Netherlands: Academic Pr., 2003. 440 p.
- [14] V. Mukhanov. *Physical foundations of cosmology*. Cambridge, UK: Univ. Pr., 2005. 421 p.
- [15] Matias Zaldarriaga and Uros Seljak. Gravitational lensing effect on cosmic microwave background polarization. *Phys. Rev.*, D58:023003, 1998, astro-ph/9803150.
- [16] Lloyd Knox and Yong-Seon Song. A limit on the detectability of the energy scale of inflation. *Phys. Rev. Lett.*, 89:011303, 2002, astro-ph/0202286.
- [17] Shamit Kachru, Renata Kallosh, Andrei Linde, and Sandip P. Trivedi. De sitter vacua in string theory. *Phys. Rev.*, D68:046005, 2003, hep-th/0301240.
- [18] Vijay Balasubramanian, Per Berglund, Joseph P. Conlon, and Fernando Quevedo. Systematics of moduli stabilisation in calabi-yau flux compactifications. *JHEP*, 03:007, 2005, hep-th/0502058.
- [19] J. J. Blanco-Pillado, C. P. Burgess, J. M. Cline, C. Escoda, M. Gomez-Reino, R. Kallosh, A. Linde, and F. Quevedo. Racetrack inflation. *JHEP*, 11:063, 2004, hep-th/0406230.
- [20] J. J. Blanco-Pillado, C. P. Burgess, J. M. Cline, C. Escoda, M. Gomez-Reino, R. Kallosh, A. Linde, and F. Quevedo. Inflating in a better racetrack. *JHEP*, 09:002, 2006, hep-th/0603129.
- [21] Joseph P. Conlon and Fernando Quevedo. Kaehler moduli inflation. *JHEP*, 01:146, 2006, hep-th/0509012.
- [22] J. Richard Bond, Lev Kofman, Sergey Prokushkin, and Pascal M. Vaudrevange. Roulette inflation with kaehler moduli and their axions. *Phys. Rev.*, D75:123511, 2007, hep-th/0612197.
- [23] William H. Kinney. Inflation: Flow, fixed points and observables to arbitrary order in slow roll. *Phys. Rev.*, D66:083508, 2002, astro-ph/0206032.
- [24] Michael R. Douglas. The statistics of string / m theory vacua. *JHEP*, 05:046, 2003, hep-th/0303194.
- [25] Robert H. Brandenberger and Jerome Martin. The robustness of inflation to changes in super-planck- scale physics. *Mod. Phys. Lett.*, A16:999–1006, 2001, astro-ph/0005432.
- [26] Alexei A. Starobinsky. Robustness of the inflationary perturbation spectrum to trans-planckian physics. *Pisma Zh. Eksp. Teor. Fiz.*, 73:415–418, 2001, astro-ph/0104043.

- [27] J. Richard Bond, Carlo Contaldi, Lev Kofman, and Pascal M. Vaudrevange. Scanning inflationary trajectories i: Constraining the power spectra. *in prep.*
- [28] J. Richard Bond, Carlo Contaldi, Lev Kofman, and Pascal M. Vaudrevange. Scanning inflationary trajectories ii: Constraining the acceleration trajectories. *in prep.*
- [29] Pascal M. Vaudrevange and Lev Kofman. Trans-planckian issue in the milne universe. 0600, arXiv:0706.0980 [hep-th].
- [30] Milan B. Mijic, Michael S. Morris, and Wai-Mo Suen. The r^{*2} cosmology: Inflation without a phase transition. *Phys. Rev.*, D34:2934, 1986.
- [31] Lisa Randall, Marin Soljatic, and Alan H. Guth. Supernatural inflation: Inflation from supersymmetry with no (very) small parameters. *Nucl. Phys.*, B472:377–408, 1996, hep-ph/9512439.
- [32] C. Armendariz-Picon, T. Damour, and Viatcheslav F. Mukhanov. k-inflation. *Phys. Lett.*, B458:209–218, 1999, hep-th/9904075.
- [33] G. R. Dvali and S. H. Henry Tye. Brane inflation. *Phys. Lett.*, B450:72–82, 1999, hep-ph/9812483.
- [34] Antony Lewis and Sarah Bridle. Cosmological parameters from cmb and other data: a monte- carlo approach. *Phys. Rev.*, D66:103511, 2002, astro-ph/0205436.
- [35] D. S. Salopek and J. R. Bond. Nonlinear evolution of long wavelength metric fluctuations in inflationary models. *Phys. Rev.*, D42:3936–3962, 1990.
- [36] Andrew R. Liddle, Paul Parsons, and John D. Barrow. Formalizing the slow roll approximation in inflation. *Phys. Rev.*, D50:7222–7232, 1994, astro-ph/9408015.
- [37] Ewan D. Stewart and David H. Lyth. A more accurate analytic calculation of the spectrum of cosmological perturbations produced during inflation. *Phys. Lett.*, B302:171–175, 1993, gr-qc/9302019.
- [38] V. Barger, Hye-Sung Lee, and Danny Marfatia. Wmap and inflation. *Phys. Lett.*, B565:33–41, 2003, hep-ph/0302150.
- [39] Andrew R Liddle and Samuel M Leach. How long before the end of inflation were observable perturbations produced? *Phys. Rev.*, D68:103503, 2003, astro-ph/0305263.
- [40] Scott Dodelson and Lam Hui. A horizon ratio bound for inflationary fluctuations. *Phys. Rev. Lett.*, 91:131301, 2003, astro-ph/0305113.
- [41] Michael Malquarti, Samuel M. Leach, and Andrew R. Liddle. From the production of primordial perturbations to the end of inflation. *Phys. Rev.*, D69:063505, 2004, astro-ph/0310498.

- [42] Lev Kofman, Andrei D. Linde, and Alexei A. Starobinsky. Reheating after inflation. *Phys. Rev. Lett.*, 73:3195–3198, 1994, hep-th/9405187.
- [43] Lev Kofman, Andrei D. Linde, and Alexei A. Starobinsky. Towards the theory of reheating after inflation. *Phys. Rev.*, D56:3258–3295, 1997, hep-ph/9704452.
- [44] Viatcheslav F. Mukhanov, H. A. Feldman, and Robert H. Brandenberger. Theory of cosmological perturbations. part 1. classical perturbations. part 2. quantum theory of perturbations. part 3. extensions. *Phys. Rept.*, 215:203–333, 1992.
- [45] Kevork Abazajian, Kenji Kadota, and Ewan D. Stewart. Parameterizing the power spectrum: Beyond the truncated taylor expansion. *JCAP*, 0508:008, 2005, astro-ph/0507224.
- [46] Shuichiro Yokoyama, Takahiro Tanaka, Misao Sasaki, and Ewan D. Stewart. Wronskian formulation of the spectrum of curvature perturbations. *JCAP*, 0606:020, 2006, astro-ph/0605021.
- [47] Hyun-Chul Lee, Misao Sasaki, Ewan D. Stewart, Takahiro Tanaka, and Shuichiro Yokoyama. A new delta n formalism for multi-component inflation. *JCAP*, 0510:004, 2005, astro-ph/0506262.
- [48] S. Groot Nibbelink and B. J. W. van Tent. Scalar perturbations during multiple field slow-roll inflation. *Class. Quant. Grav.*, 19:613–640, 2002, hep-ph/0107272.
- [49] S. Groot Nibbelink and B. J. W. van Tent. Density perturbations arising from multiple field slow-roll inflation. 2000, hep-ph/0011325.
- [50] Pia Mukherjee, David Parkinson, and Andrew R. Liddle. A nested sampling algorithm for cosmological model selection. *Astrophys. J.*, 638:L51–L54, 2006, astro-ph/0508461.
- [51] Andrew R. Liddle, Pia Mukherjee, and David Parkinson. Cosmological model selection. *Astron. Geophys.*, 47:4.30–4.33, 2006, astro-ph/0608184.
- [52] H. Akaike. A new look at the statistical model identification. *IEEE Transactions on Automatic Control*, 19 (6):716–723, 1974.
- [53] G. Schwarz. Estimating the dimension of a model. *Annals of Statistics*, 6 (2):461–464, 1978.
- [54] D. J. C. MacKay. *Information Theory, Inference and Learning Algorithms*. Cambridge University Press, 2003.
- [55] H. Jeffreys. *Theory of Probability*. Clarendon Press, 1998.
- [56] William H. Kinney, Edward W. Kolb, Alessandro Melchiorri, and Antonio Riotto. Wmapping inflationary physics. *Phys. Rev.*, D69:103516, 2004, hep-ph/0305130.

- [57] Richard Easther and William H. Kinney. Monte carlo reconstruction of the inflationary potential. *Phys. Rev.*, D67:043511, 2003, astro-ph/0210345.
- [58] Hiranya Peiris and Richard Easther. Recovering the inflationary potential and primordial power spectrum with a slow roll prior: Methodology and application to wmap 3 year data. *JCAP*, 0607:002, 2006, astro-ph/0603587.
- [59] Hiranya Peiris and Richard Easther. Slow roll reconstruction: Constraints on inflation from the 3 year wmap dataset. *JCAP*, 0610:017, 2006, astro-ph/0609003.
- [60] W. Press, S. Teukolsky, W. Vetterling, and Flannery B. *Numerical Recipes in Fortran*. Cambridge University Press, 1992. p. 184.
- [61] Antony Lewis, Anthony Challinor, and Anthony Lasenby. Efficient computation of cmb anisotropies in closed frw models. *Astrophys. J.*, 538:473–476, 2000, astro-ph/9911177.
- [62] G. Hinshaw et al. First year wilkinson microwave anisotropy probe (wmap) observations: Data processing methods and systematic errors limits. *Astrophys. J. Suppl.*, 148:63, 2003, astro-ph/0302222.
- [63] H. V. Peiris et al. First year wilkinson microwave anisotropy probe (wmap) observations: Implications for inflation. *Astrophys. J. Suppl.*, 148:213, 2003, astro-ph/0302225.
- [64] A. C. S. Readhead et al. Extended mosaic observations with the cosmic background imager. *Astrophys. J.*, 609:498–512, 2004, astro-ph/0402359.
- [65] N. W. Halverson et al. DASI first results: A measurement of the cosmic microwave background angular power spectrum. *Astrophys. J.*, 568:38–45, 2002, astro-ph/0104489.
- [66] Chao-lin Kuo et al. High resolution observations of the cmb power spectrum with acbar. *Astrophys. J.*, 600:32–51, 2004, astro-ph/0212289.
- [67] Licia Verde et al. First year wilkinson microwave anisotropy probe (wmap) observations: Parameter estimation methodology. *Astrophys. J. Suppl.*, 148:195, 2003, astro-ph/0302218.
- [68] Andrew R Liddle. On the inflationary flow equations. *Phys. Rev.*, D68:103504, 2003, astro-ph/0307286.
- [69] Andrei D. Linde. *Particle Physics and Inflationary Cosmology*. Chur, Switzerland: Harwood, 1990, hep-th/05032.
- [70] S. Kachru, R. Kallosh, A. Linde, J. Maldacena, L. McAllister, and S. P. Trivedi. Towards inflation in string theory. *JCAP*, 0310:013, 2003, hep-th/0308055.
- [71] Keshav Dasgupta, Carlos Herdeiro, Shinji Hirano, and Renata Kallosh. D3/d7 inflationary model and m-theory. *Phys. Rev.*, D65:126002, 2002, hep-th/0203019.

- [72] Jonathan P. Hsu, Renata Kallosh, and Sergey Prokushkin. On brane inflation with volume stabilization. *JCAP*, 0312:009, 2003, hep-th/0311077.
- [73] Keshav Dasgupta, Jonathan P. Hsu, Renata Kallosh, Andrei Linde, and Marco Zagermann. D3/d7 brane inflation and semilocal strings. *JHEP*, 08:030, 2004, hep-th/0405247.
- [74] Alex Buchel and Radu Roiban. Inflation in warped geometries. *Phys. Lett.*, B590:284–294, 2004, hep-th/0311154.
- [75] Mohsen Alishahiha, Eva Silverstein, and David Tong. Dbi in the sky. *Phys. Rev.*, D70:123505, 2004, hep-th/0404084.
- [76] C. P. Burgess, J. M. Cline, H. Stoica, and F. Quevedo. Inflation in realistic d-brane models. *JHEP*, 09:033, 2004, hep-th/0403119.
- [77] Oliver DeWolfe, Shamit Kachru, and Herman L. Verlinde. The giant inflaton. *JHEP*, 05:017, 2004, hep-th/0403123.
- [78] Norihiro Iizuka and Sandip P. Trivedi. An inflationary model in string theory. *Phys. Rev.*, D70:043519, 2004, hep-th/0403203.
- [79] S. Dimopoulos, S. Kachru, J. McGreevy, and Jay G. Wacker. N-flation. 2005, hep-th/0507205.
- [80] Richard Easther and Liam McAllister. Random matrices and the spectrum of n-flation. *JCAP*, 0605:018, 2006, hep-th/0512102.
- [81] L. A. Kofman, Andrei D. Linde, and Alexei A. Starobinsky. Inflationary universe generated by the combined action of a scalar field and gravitational vacuum polarization. *Phys. Lett.*, B157:361–367, 1985.
- [82] Nathan Seiberg and Edward Witten. The d1/d5 system and singular cft. *JHEP*, 04:017, 1999, hep-th/9903224.
- [83] J. R. Bond, C. Contaldi, L. Kofman, and P. M. Vaudrevange. Scanning inflation. *in preparation*.
- [84] Vijay Balasubramanian and Per Berglund. Stringy corrections to kaehler potentials, susy breaking, and the cosmological constant problem. *JHEP*, 11:085, 2004, hep-th/0408054.
- [85] Joseph P. Conlon, Fernando Quevedo, and Kerim Suruliz. Large-volume flux compactifications: Moduli spectrum and d3/d7 soft supersymmetry breaking. *JHEP*, 08:007, 2005, hep-th/0505076.
- [86] Joan Simon, Raul Jimenez, Licia Verde, Per Berglund, and Vijay Balasubramanian. Using cosmology to constrain the topology of hidden dimensions. 2006, astro-ph/0605371.

- [87] R. Holman and Jimmy A. Hutasoit. Axionic inflation from large volume flux compactifications. 2006, hep-th/0603246.
- [88] Katrin Becker, Melanie Becker, Michael Haack, and Jan Louis. Supersymmetry breaking and alpha'-corrections to flux induced potentials. *JHEP*, 06:060, 2002, hep-th/0204254.
- [89] Ian Affleck, Michael Dine, and Nathan Seiberg. Dynamical supersymmetry breaking in four-dimensions and its phenomenological implications. *Nucl. Phys.*, B256:557, 1985.
- [90] Michael Dine, N. Seiberg, X. G. Wen, and Edward Witten. Nonperturbative effects on the string world sheet. *Nucl. Phys.*, B278:769, 1986.
- [91] Edward Witten. Non-perturbative superpotentials in string theory. *Nucl. Phys.*, B474:343–360, 1996, hep-th/9604030.
- [92] Steven B. Giddings, Shamit Kachru, and Joseph Polchinski. Hierarchies from fluxes in string compactifications. *Phys. Rev.*, D66:106006, 2002, hep-th/0105097.
- [93] Paul S. Aspinwall and Renata Kallosh. Fixing all moduli for m-theory on $k3 \times k3$. *JHEP*, 10:001, 2005, hep-th/0506014.
- [94] Joseph P. Conlon, Shehu S. Abdussalam, Fernando Quevedo, and Kerim Suruliz. Soft susy breaking terms for chiral matter in iib string compactifications. *JHEP*, 01:032, 2007, hep-th/0610129.
- [95] P. Candelas and X. C. de la Ossa. Moduli space of calabi-yau manifolds. Prepared for XIII International School of Theoretical Physics: The Standard Model and Beyond, Szczyrk, Poland, 19-26 Sep 1989.
- [96] Frederik Denef, Michael R. Douglas, and Bogdan Florea. Building a better racetrack. *JHEP*, 06:034, 2004, hep-th/0404257.
- [97] Philip Candelas, Xenia C. De La Ossa, Paul S. Green, and Linda Parkes. A pair of calabi-yau manifolds as an exactly soluble superconformal theory. *Nucl. Phys.*, B359:21–74, 1991.
- [98] Marcus Berg, Michael Haack, and Boris Kors. String loop corrections to kaehler potentials in orientifolds. *JHEP*, 11:030, 2005, hep-th/0508043.
- [99] Marcus Berg, Michael Haack, and Boris Kors. On volume stabilization by quantum corrections. *Phys. Rev. Lett.*, 96:021601, 2006, hep-th/0508171.
- [100] Renata Kallosh and Sergey Prokushkin. Supercosmology. 2004, hep-th/0403060.
- [101] C. P. Burgess, R. Kallosh, and F. Quevedo. de sitter string vacua from supersymmetric d-terms. *JHEP*, 10:056, 2003, hep-th/0309187.

- [102] Fred C. Adams, J. Richard Bond, Katherine Freese, Joshua A. Frieman, and Angela V. Olinto. Natural inflation: Particle physics models, power law spectra for large scale structure, and constraints from coBE. *Phys. Rev.*, D47:426–455, 1993, hep-ph/9207245.
- [103] Katherine Freese, Joshua A. Frieman, and Angela V. Olinto. Natural inflation with pseudo - nambu-goldstone bosons. *Phys. Rev. Lett.*, 65:3233–3236, 1990.
- [104] George Efstathiou and Katherine J. Mack. The lyth bound revisited. *JCAP*, 0505:008, 2005, astro-ph/0503360.
- [105] David H. Lyth. What would we learn by detecting a gravitational wave signal in the cosmic microwave background anisotropy? *Phys. Rev. Lett.*, 78:1861–1863, 1997, hep-ph/9606387.
- [106] Andrew R. Liddle, Anupam Mazumdar, and Franz E. Schunck. Assisted inflation. *Phys. Rev.*, D58:061301, 1998, astro-ph/9804177.
- [107] D. S. Salopek and J. R. Bond. Stochastic inflation and nonlinear gravity. *Phys. Rev.*, D43:1005–1031, 1991.
- [108] J. Richard Bond. Theory and observations of the cosmic background radiation. Lectures at Summer School on Cosmology and Large Scale Structure, Les Houches, France, Aug 1-22, 1993.
- [109] Dmitry I. Podolsky, Gary N. Felder, Lev Kofman, and Marco Peloso. Equation of state and beginning of thermalization after preheating. *Phys. Rev.*, D73:023501, 2006, hep-ph/0507096.
- [110] Andrei D. Linde, Dmitri A. Linde, and Arthur Mezhlumian. From the big bang theory to the theory of a stationary universe. *Phys. Rev.*, D49:1783–1826, 1994, gr-qc/9306035.
- [111] Andrei D. Linde. Eternal chaotic inflation. *Mod. Phys. Lett.*, A1:81, 1986.
- [112] N. Barnaby, C. P. Burgess, and J. M. Cline. Warped reheating in brane-antibrane inflation. *JCAP*, 0504:007, 2005, hep-th/0412040.
- [113] Andrew R. Frey, Anupam Mazumdar, and Robert Myers. Stringy effects during inflation and reheating. *Phys. Rev.*, D73:026003, 2006, hep-th/0508139.
- [114] Lev Kofman and Piljin Yi. Reheating the universe after string theory inflation. *Phys. Rev.*, D72:106001, 2005, hep-th/0507257.
- [115] Xingang Chen and S. H. Henry Tye. Heating in brane inflation and hidden dark matter. *JCAP*, 0606:011, 2006, hep-th/0602136.
- [116] G. V. Chibisov and Yu. V. Shtanov. Structural anisotropy in a chaotic inflationary universe. *Sov. Phys. JETP*, 69:17–22, 1989.

- [117] Robert H. Brandenberger and Jerome Martin. On signatures of short distance physics in the cosmic microwave background. *Int. J. Mod. Phys.*, A17:3663–3680, 2002, hep-th/0202142.
- [118] Ulf H. Danielsson. A note on inflation and transplanckian physics. *Phys. Rev.*, D66:023511, 2002, hep-th/0203198.
- [119] Richard Easther, Brian R. Greene, William H. Kinney, and Gary Shiu. A generic estimate of trans-planckian modifications to the primordial power spectrum in inflation. *Phys. Rev.*, D66:023518, 2002, hep-th/0204129.
- [120] Jerome Martin and Robert Brandenberger. On the dependence of the spectra of fluctuations in inflationary cosmology on trans-planckian physics. *Phys. Rev.*, D68:063513, 2003, hep-th/0305161.
- [121] Edward W. Kolb, A. A. Starobinsky, and I. I. Tkachev. Trans-planckian wimpzillas. 2007, hep-th/0702143.
- [122] N. D. Birrell and P. C. W. Davies. *Quantum Fields In Curved Space*. Cambridge University Press, 1982.
- [123] V. Sahni. Regularized quantum energy momentum tensor for spinor fields in the chitre-hartle and milne metrics. *Class. Quant. Grav.*, 1:579–590, 1984.
- [124] A. A. Grib, S. G. Mamaev, and V.M. Mostepanenko. *Vacuum Quantum Effects in Strong Fields*. Friedmann Lab Publishing, St Petersburg, 1994.
- [125] P. Candelas and J. S. Dowker. Field theories on conformally related space-times: Some global considerations. *Phys. Rev.*, D19:2902, 1979.
- [126] S.G. Mamaev. Vacuum expectation values of the energy-momentum tensor of quantized fields in a homogeneous isotropic space-time. *Teor. i Mat. Fiz.*, 42:350, 1980.
- [127] Ya. B. Zeldovich and Alexei A. Starobinsky. Particle production and vacuum polarization in an anisotropic gravitational field. *Sov. Phys. JETP*, 34:1159–1166, 1972.
- [128] L. A. Kofman, V. Sahni, and Alexei A. Starobinsky. Anisotropic cosmological model created by quantum polarization of vacuum. *Sov. Phys. JETP*, 58:1090–1095, 1983.
- [129] Nemanja Kaloper, Matthew Kleban, Albion E. Lawrence, and Stephen Shenker. Signatures of short distance physics in the cosmic microwave background. *Phys. Rev.*, D66:123510, 2002, hep-th/0201158.
- [130] H. Bateman and A. Erdelyi. *Higher Transcendental Functions*. New York: McGraw-Hill, 1953-55.

- [131] M Abramowitz and I. A. Stegun. *Handbook of mathematical functions with formulas, graphs, and mathematical tables*. Washington U.S. Govt. Print. Off., 1964.